Modélisation numérique tridimensionnelle de l'interaction sol-structure avec prise en compte des effets de site

Zouhair Adnani

université PARIS-SACLAY

NNT : 2018SACLY006

Modélisation numérique tridimensionnelle des effets de site en Interaction Sol-Structure par une méthode adaptée aux problèmes sismiques de très grande taille

Thèse de doctorat de l'Université Paris-Saclay
préparée à L'ENSTA ParisTech

École doctorale n°579: Sciences mécaniques et énergétiques, matériaux et géosciences (SMEMaG)
Spécialité de doctorat: Génie Mécanique

Thèse présentée et soutenue à Palaiseau, le 25/05/2018, par

Zouhair ADNANI

Composition du Jury :

Jean-François SEMBLAT Professeur, ENSTA (Unité de Mécanique)	Président
Attilio FRANGI Professeur, Politecnico di Milano (Department of Civil and Environmental Engineering)	Rapporteur
Geert DEGRANDE Professeur, KU Leuven (Department of Civil Engineering)	Rapporteur
Marc BONNET Directeur de recherche, ENSTA (POEMS)	Directeur de thèse
Stéphanie CHAILLAT Chargé de recherche, ENSTA (POEMS)	Co-directeur de thèse
Vinicius ALVES FERNANDES Ingénieur de recherche, EDF R&D	Examinateur

Thèse de doctorat

Titre : Modélisation numérique tridimensionnelle des effets de site en Interaction Sol-Structure par une méthode adaptée aux problèmes sismiques de très grande taille

Keywords : Interaction Sol-Structure, Effets de site, Méthode des éléments de frontière, Méthode multipôles rapide, Méthode des éléments finis.

Résumé : Les études récentes ont montré l'influence de la géométrie et de la lithologie du site sur l'amplification de l'onde sismique incidente. Disposer d'outils de simulation est nécessaire pour l'analyse du risque sismique des ouvrages. Néanmoins, les effets de site sont souvent découplés des calculs d'interaction sol-structure vu la taille des domaines à considérer et de la complexité des modèles. L'objectif de cette thèse est de développer une stratégie de calcul numérique d'interaction sol-structure permettant de prendre en compte les effets de site dans un contexte industriel. Pour ce faire, un couplage entre la méthode des éléments finis (FEM) et la méthode des éléments de frontière accélérée par la méthode multipôle rapide (FM-BEM) est développé dans ce travail. La BEM permet de modéliser des problèmes dans des domaines de très grande taille ou infinis mais est gourmande en temps de calculs. Avec la méthode accélérée, il est possible de considérer des géologies plus complexes et d'accéder à des gammes de fréquences plus élevées par rapport à des approches classiques (purement FEM ou couplage BEM-FEM), grace à l'accélération du produit matrice-vecteur dans la résolution par un solveur itératif. La mise en place de cette approche s'appuie sur le code FEM industriel *Code_Aster* (EDF R&D) et le code FM-BEM *Coffee* (CNRS) développé par S. Chaillat.

La FM-BEM est d'abord utilisée pour la modélisation de cas de sols réalistes afin de valider ses paramètres pour une utilisation dans un cadre industriel. Une stratégie de couplage FM-BEM/FEM est ensuite développée à l'aide d'une technique de sous-structuration dynamique où la structure (et éventuellement le sol proche) est modélisée par la FEM, alors que le sol infini est représenté par un opérateur d'impédance et des forces sismiques, construits avec la méthode FM-BEM. L'opérateur d'impédance et les forces sismiques, qui sont calculés sur une base réduite afin d'en réduire le coût de calcul, sont validés sur des cas canoniques (demi-espace homogène, bassin à géométrie variable...). L'influence sur la réponse de la structure de la forme du bassin, de l'angle d'incidence des ondes ainsi que du rapport de célérité des ondes entre les couches est alors étudiée et la réponse de la structure comparée aux cas où les effets de site seraient absents. Enfin, la méthodologie de couplage mise en place est utilisée pour effectuer des calculs d'interaction sol-structure sur des structures dans le bassin de Grenoble.

Title : Three-dimensional numerical modeling of site effects in Soil-Structure Interaction for large scale seismic problems

Keywords : Soil-Structure Interaction, Site effects, Boundary element method, Fast multipole method, Finite element method.

Abstract : Recent studies have shown the influence of the geometry and lithology of the site on the amplification of the incident seismic wave. Having simulation tools is necessary to seismic risk analysis of structures. Nevertheless, site effects are often decoupled from soil-structure interaction computations given the size of the domains to be considered and the complexity of the models. The objective of this work is to develop a numerical method to simulate soil-structure interaction, that also takes into account site effects. To this aim, a coupling strategy between the finite element method (FEM) and the fast multipole accelerated boundary element method (FM-BEM) is proposed. The BEM is well suited to deal with large-scale or infinite domains but is very expensive in terms of memory requirements or computational time. Once accelerated with the Fast Multipole Method, the FM-BEM allows to model more complex geologies and to consider a higher frequency range compared to classical approaches (purely with the FEM or with a standard BEM-FEM coupling) thanks to the acceleration of the matrix-vector product needed in the iterative solver. The implementation of this strategy is based on the FEM code *Code_Aster* (EDF R&D) and the FM-BEM code *Coffee* (CNRS) developed by S. Chaillat.

In this work, FM-BEM is first used to model soils with realistic mechanical characteristics and to validate the parameters of the method in an industrial context. An FM-BEM/FEM coupling strategy is then proposed using a dynamic substructuring technique where the structure (and possibly the near soil) is modelled by the FEM, while the infinite soil is represented by an impedance operator and seismic forces, computed with the FM-BEM. The impedance operator and the seismic forces, which are computed on a reduced basis in order to reduce computational costs, are then validated on canonical cases (homogeneous half-space, basin with variable geometry ...). The influence on the response of the structure of the shape of the basin, the angle of incidence of the waves as well as the ratio of the wave velocities between the layers is then studied and the response of the structure is compared to cases where the site effects are absent. Finally, the proposed coupling methodology is used to simulate soil-structure interaction on a configuration such as structures in the Grenoble basin.

To Sofia, Jude, and Imane,
light of the lights

Contents

Remerciements v

Contents vii

List of Figures ix

List of Tables xvii

1. Introduction 1

1.1. Site effects and Soil-Structure Interaction 2
1.2. Causes of site effects 3
1.3. Seismic wave propagation and amplification in an elastic medium 6
1.4. Numerical methods to model elastic wave propagation in soils 8
1.5. Main ingredients of the boundary element method 11
1.6. Fast multipole accelerated boundary element method 13
1.7. Aim and outline of this work 19

2. Capabilities of the fast multipole accelerated boundary element method to model elastic soils 23

2.1. Analysis of the numerical efficiency: benefits of the FM-BEM 24
2.2. Transition between the BEM and the FM-BEM 25
2.3. Choice of the density of points in an industrial context 26
2.4. Effects of the artificial truncation of the free surface 28
2.5. Speed-up of the multi-frequency computations 30
2.6. Fourier synthesis to obtain results in the time domain 31
2.7. Conclusions 33

3. Fast methods to model Soil-Structure Interaction 35

3.1. Coupling between fast BEMs and FEM 36
3.2. Variational formulation of Soil-Stucture Interaction 37

3.3. Efficient computation of Soil-Structure Interaction problems 40

4. Validation of the impedance operator and seismic force for reference case studies 43
4.1. Evaluation of the impedance operator in the case of a homogeneous half-space 44
4.2. Impedance operator for hemispherical basin in half-space with material contrasts . . 59
4.3. Seismic force for a homogeneous basin 71
4.4. Seismic force in the case of a heterogeneous basin 73
4.5. Conclusion 77

5. Structural response for piecewise homogeneous media 79
5.1. Definition of the test case 80
5.2. Influence of the basin shape on the response of the structure 84
5.3. Effect of an obliquely incident wave on the response of the structure 92
5.4. Conclusion 104

6. Application on realistic configuration of Soil Structure Interaction 107
6.1. Modelling of the Grenoble valley 108
6.2. Illustration of site effects due to geological and topographical structure 110
6.3. Illustration of the site effects on the response in the presence of buildings 116
6.4. Conclusion 120

7. Conclusions and directions for future work 121
7.1. Conclusions 121
7.2. Directions for future work 123

Appendices 125

A. Analytic solutions: diffraction of incident plane waves 125
A.1. Case of an incident plane P-wave 125
A.2. Case of an incident plane SV-wave 127

Bibliography 129

List of Figures

1.1. Propagation of a wave from the source to the site [59]. 2
1.2. Recorded accelerations during the 1985 Mexico earthquake. 3
1.3. Interference between two waves in the case of a concave topography. 4
1.4. Illustration of the amplification of SH-waves in a homogeneous medium (model of Caracas from [25]). 4
1.5. Trapping of waves in a stratified medium. The softest soil is in light green, while the stiffest soil is in dark green. 5
1.6. Site effect due to the basin shape and velocity contrast. The alluvial basin is depicted in pink. The bedrock is depicted in brown. 6
1.7. Motion induced by a P-wave (left) and a S-wave (right). 7
1.8. FMM: illustration of the position of points and of poles. 14
1.9. FMM: definition of the adjacent cells [7]. 16
1.10. Comparaison of necessary elementary operations between FM-BEM and classical BEM [7]. 17
1.11. Multi-level subdivision of the domain [32]. 18

2.1. Hemispherical basin in a elastic half-space. 24
2.2. Computational time per iteration with respect to the number of degrees of freedom for the standard and Fast Multipole accelerated BEM. 25
2.3. Relative errors with respect to the analytic solution for the FM-BEM (red and blue lines) and BEM (black and green symbols) to solve incident plane wave propagation problems. 26
2.4. Relative errors for different meshing criterion. 27
2.5. Total computational time per computation for the two meshing criteria: six or ten points per S-wavelength. 27
2.6. Number of iterations with respect to the frequency for the two meshing criteria: six or ten points per S-wavelength. 28
2.7. Relative error for different truncation error. 29

2.8. Total computational time per computation, with respect to the frequency for different size of the free surface. 30
2.9. Impact of the use of an initial guess on the number of iterations. 31
2.10. Test case considered to check the accuracy of the Fourier synthesis to obtain results in the time domain. The point in red corresponds to the point where the surface displacement is evaluated. 31
2.11. Input Ricker signal for the Fourier synthesis. 32
2.12. Amplitude of the vertical displacement at the post-processing with respect to the frequency. 32
2.13. Amplitude of the vertical displacement at the post-processing point with respect to time. 33

3.1. Subdomain method: schematic and notation. 38

4.1. Illustration of the two configurations considered for the validation of the impedance operator for a homogeneous half-space: surface (right) and embedded (left) footings. 44
4.2. Illustration of the rigid body modes of a circular surface footing. 45
4.3. Example of a mesh of a surface circular footing on a homogeneous half-space. 46
4.4. Circular surface footing on a homogeneous half-space: Validation of the computation of the impedance of the horizontal mode K_{11} (Eq 3.7): comparison between the FM-BEM solution (denoted COFFEE), the solution given by the standard BEM using Miss3D code (denoted Miss3D) and the solution extracted from [60] (denoted Sieffert). 47
4.5. Circular surface footing on a homogeneous half-space: Validation of the computation of the impedance of the vertical mode K_{33s} (Eq 3.7): comparison between the FM-BEM solution (denoted COFFEE), the solution given by standard BEM using Miss3D code (denoted Miss3D) and the solution extracted from [60] (denoted Sieffert). . . . 48
4.6. Circular surface footing on a homogeneous half-space: Validation of the computation of the impedance of the rocking mode K_{44} (Eq 3.7): comparison between the FM-BEM solution (denoted COFFEE), the solution given by standard BEM using Miss3D code (denoted Miss3D) and the solution extracted from [60] (denoted Sieffert). . . . 49
4.7. Circular surface footing on a homogeneous half-space: Validation of the computation of the impedance of the torsion mode K_{66} (Eq 3.7): comparison between the FM-BEM solution (denoted COFFEE), the solution given by standard BEM using Miss3D code (denoted Miss3D) and the solution extracted from [60] (denoted Sieffert). . . . 50
4.8. Influence of the truncation radius on the oscillations reported in the impedance computed with the FM-BEM. 51
4.9. Impedance for an interface in a bounded domain: model considered. 52
4.10. Computation of the impedance for the horizontal and the vertical modes of an interface in a bounded domain. Comparison of the solution with FM-BEM (denoted COFFEE) and FEM (denoted *Code_Aster*). 53
4.11. Example of a mesh of an embedded cylindrical footing on a homogeneous half-space. 54

4.12. Embedded cylindrical footing: Validation of the computation of the impedance of the horizontal mode K_{11} (Equation 3.7): comparison between the FM-BEM solution (denoted COFFEE), the solution given by standard BEM using Miss3D code (denoted Miss) and the solution extracted from [60] (denoted Sieffert). 55

4.13. Embedded cylindrical footing: Validation of the computation of the impedance of the vertical mode K_{33} (Equation 3.7): comparison between the FM-BEM solution (denoted COFFEE), the solution given by standard BEM using Miss3D code (denoted Miss) and the solution extracted from [60] (denoted Sieffert). 56

4.14. Embedded cylindrical footing: Validation of the computation of the impedance of the rocking mode K_{44} (Eq 3.7): comparison between the FM-BEM solution (denoted COFFEE), the solution given by standard BEM using Miss3D code (denoted Miss) and the solution extracted from [60] (denoted Sieffert). 57

4.15. Embedded cylindrical footing: Validation of the computation of the impedance of the torsion mode K_{66} (Eq 3.7): comparison between the FM-BEM solution (denoted COFFEE), the solution given by standard BEM using Miss3D code (denoted Miss) and the solution extracted from [60] (denoted Sieffert). 58

4.16. Embedded cylindrical footing: Validation of the computation of the impedance of the coupling of the rocking mode and the torsion mode K_{15} (Eq. 3.7): comparison between the FM-BEM solution (denoted COFFEE), the solution given by standard BEM using Miss3D code (denoted Miss) and the solution extracted from [60] (denoted Sieffert). 59

4.17. Surface and embedded circular footings in the case (i) of a hemispherical basin in a half-space. 60

4.18. Coupling FEM-BEM strategy for the case of a surface or embedded footings (case of a hemispherical basin in a half-space). 61

4.19. Circular surface footing on a homogeneous half-space. Validation of the computation of the impedance of the horizontal mode K_{11} (Eq 3.7): comparison between the FM-BEM solution (denoted COFFEE), the solution given by the FEM-BEM coupling (*Code_Aster*) and the solution extracted from [60] (denoted Sieffert). 62

4.20. Circular surface footing on a homogeneous half-space. Validation of the computation of the impedance of the vertical mode K_{33} (Eq 3.7): comparison between the FM-BEM solution (denoted COFFEE), the solution given by the FEM-BEM coupling (*Code_Aster*) and the solution extracted from [60] (denoted Sieffert). 62

4.21. Circular surface footing on a homogeneous half-space. Validation of the computation of the impedance of the rocking mode K_{44} (Eq 3.7): comparison between the FM-BEM solution (denoted COFFEE), the solution given the FEM-BEM coupling (*Code_Aster*) and the solution extracted from [60] (denoted Sieffert). 63

4.22. Circular surface footing on a homogeneous half-space. Validation of the computation of the impedance of the torsion mode K_{66} (Eq 3.7): comparison between the FM-BEM solution (denoted COFFEE), the solution given by the FEM-BEM coupling (*Code_Aster*) and the solution extracted from [60] (denoted Sieffert). 63
4.23. Comparison of K_{33} for two different wave velocities. 64
4.24. Circular surface footing on a multi-domain basin. Validation of the computation of the impedance of the horizontal mode K_{11} (Eq 3.7): comparison between the FM-BEM solution (denoted COFFEE), the solution given by the FEM-BEM coupling (*Code_Aster*) and the solution extracted from [60] (denoted Sieffert homogeneous) in the case of a homogeneous half-space. 65
4.25. Circular surface footing on a multi-domain basin. Validation of the computation of the impedance of the vertical mode K_{33} (Eq 3.7): comparison between the FM-BEM solution (denoted COFFEE), the solution given by the FEM-BEM coupling (*Code_Aster*) and the solution extracted from [60] (denoted Sieffert homogeneous) in the case of a homogeneous half-space. 66
4.26. Circular surface footing on a multi-domain basin. Validation of the computation of the impedance of the rocking mode K_{44} (Eq 3.7): comparison between the FM-BEM solution (denoted COFFEE), the solution given by the FEM-BEM coupling (*Code_Aster*) and the solution extracted from [60] (denoted Sieffert homogeneous) in the case of a homogeneous half-space 66
4.27. Circular surface footing on a multi-domain basin. Validation of the computation of the impedance of the horizontal mode K_{66} (Eq 3.7): comparison between the FM-BEM solution (denoted COFFEE), the solution given by the FEM-BEM coupling (*Code_Aster*) and the solution extracted from [60] (denoted Sieffert homogeneous) in the case of a homogeneous half-space 67
4.28. Embedded cylindrical footing on a homogeneous half-space. Validation of the computation of the impedance of the horizontal mode K_{11} (Eq 3.7): comparison between the FM-BEM (denoted COFFEE), FEM-BEM coupling (*Code_Aster*) solutions. 68
4.29. Embedded cylindrical footing on a homogeneous half-space. Validation of the computation of the impedance of the vertical mode K_{33} (Eq 3.7): comparison between the FM-BEM (denoted COFFEE), FEM-BEM coupling (*Code_Aster*) solutions. 68
4.30. Embedded cylindrical footing on a homogeneous half-space. Validation of the computation of the impedance of the rocking mode K_{44} (Eq 3.7): comparison between the FM-BEM solution (denoted COFFEE), the solution given by the FEM-BEM coupling (*Code_Aster*). 69
4.31. Embedded cylindrical footing on a homogeneous half-space. Validation of the computation of the impedance of the torsion mode K_{66} (Eq 3.7): comparison between the FM-BEM solution (denoted COFFEE), the solution given by the FEM-BEM coupling (*Code_Aster*). 69

4.32. Embedded cylindrical footing on a multi-domain basin. Validation of the computation of the impedance of the horizontal mode K_{11} (Eq 3.7): comparison between the FM-BEM (denoted COFFEE) and the FEM-BEM coupling (*Code_Aster*) solutions. . . . 70
4.33. Embedded cylindrical footing on a multi-domain basin. Validation of the computation of the impedance of the vertical mode K_{33} (Eq 3.7): comparison between the FM-BEM (denoted COFFEE) and the FEM-BEM coupling (*Code_Aster*) solutions. . . . 70
4.34. Embedded cylindrical footing on a multi-domain basin. Validation of the computation of the impedance of the rocking mode K_{44} (Eq 3.7): comparison between the FM-BEM (denoted COFFEE) and the FEM-BEM coupling (*Code_Aster*) solutions. . . . 71
4.35. Embedded cylindrical footing on a multi-domain basin. Validation of the computation of the impedance of the torsion mode K_{66} (Eq 3.7):comparison between the FM-BEM (denoted COFFEE) and the FEM-BEM coupling (*Code_Aster*) solutions. 71
4.36. Surface footing on a homogeneous half-space. 72
4.37. Validation of the computation of the seismic force for the coupling of SV-wave with the horizontal mode f_{11}: comparison between the FM-BEM solution (denoted COFFEE) and the solution given by classical BEM (denoted Miss3D). 72
4.38. Validation of the computation of the seismic force for the coupling of P-wave with the vertical mode f_{33}: comparison between the FM-BEM solution (denoted COFFEE) and the solution given by classical BEM (denoted Miss3D). 73
4.39. Surface and embedded footings in the case of a hemispherical basin in half-space. . . 73
4.40. Surface and embedded footings in the case of a hemispherical basin in half-space. . . 74
4.41. Validation of the computation of the seismic force for the coupling of SV-wave with the horizontal mode f_{11}: comparison between the FM-BEM solution (denoted COFFEE) and the solution given by the FEM-BEM coupling (*Code_Aster*). 74
4.42. Validation of the computation of the seismic force for the coupling of P-wave with the vertical mode f_{33}: comparison between the FM-BEM solution (denoted COFFEE) and the solution given by the FEM-BEM coupling (*Code_Aster*). 75
4.43. Validation of the computation of the seismic force for the coupling of SV-wave with the horizontal mode f_{11}: comparison between the FM-BEM solution (denoted COFFEE), the solution given by *Code_Aster*. 75
4.44. Validation of the computation of the seismic force for the coupling of P-wave with the horizontal mode f_{33}: comparison between the FM-BEM solution (denoted COFFEE), the solution given by *Code_Aster*. 76
4.45. Embedded cylindrical footing. Validation of the computation of the seismic force for the coupling of SV-wave with the horizontal mode f_{11}: comparison between the FM-BEM (denoted COFFEE) and the FEM-BEM coupling (*Code_Aster*) solutions. 76
4.46. Embedded cylindrical footing. Validation of the computation of the seismic force for the coupling of SV-wave with the horizontal mode f_{33}: comparison between the FM-BEM (denoted COFFEE) and the FEM-BEM coupling (*Code_Aster*) solutions. 77

5.1. Types of basin used: Case (a) hemispherical basin in homogeneous half-space (left) and Case (b) horizontally stratified basin (right). 80
5.2. Types of basin used: Case (a) hemispherical basin in homogeneous half-space (left) and Case (b) horizontally stratified basin (right). 84
5.3. Polarization of the plane waves. 85
5.4. Free field displacements along the (**a**) X-, (**c**) Y- and (**e**) Z-direction; and displacements along the (**b**) X-, (**d**) Y- and (**f**) Z-direction at the base of the structure. A vertical incident unit plane SV-wave is imposed as a loading. 87
5.5. Free field displacements along the (**a**, **b**) X-, (**c**, **d**) Y- and (**e**, **f**) Z-direction. A vertical incident unit plane SH-wave is imposed as a loading. 89
5.6. Free field displacements along the (**a**) X-, (**c**) Y- and (**e**) Z-direction; and displacements along the (**b**) X-, (**d**) Y- and (**f**) Z-direction at the base of the structure. A vertical incident unit plane P-wave is imposed as a loading. 91
5.7. Oblique incident plane wave. 92
5.8. Horizontal displacement along the X-direction at the base of the structure. An incident unit plane SV-wave is imposed as a loading for various angle of incidence. . 93
5.9. Horizontal displacement along the Y-direction at the base of the structure. An incident unit plane SV-wave is imposed as a loading for various angle of incidence. . 94
5.10. Vertical displacement along the Z-direction at the base of the structure. An incident unit plane SV-wave is imposed as a loading for various angle of incidence. 95
5.11. Total displacement at the base of the structure. An incident unit plane SV-wave is imposed as a loading for various angle of incidence. 96
5.12. Horizontal displacement along the X-direction at the base of the structure. An incident unit plane SH-wave is imposed as a loading for various angle of incidence. . 97
5.13. Horizontal displacement along the Y-direction at the base of the structure. An incident unit plane SH-wave is imposed as a loading for various angle of incidence. . 98
5.14. Vertical displacement along the Z-direction at the base of the structure. An incident unit plane SH-wave is imposed as a loading for various angle of incidence. 99
5.15. Total displacement at the base of the structure. An incident unit plane SH-wave is imposed as a loading for various angle of incidence. 100
5.16. Horizontal displacement along the X-direction at the base of the structure. An incident unit plane P-wave is imposed as a loading for various angle of incidence. . . 101
5.17. Horizontal displacement along the Y-direction at the base of the structure. An incident unit plane P-wave is imposed as a loading for various angle of incidence. . . 102
5.18. Vertical displacement along the Z-direction at the base of the structure. An incident unit plane P-wave is imposed as a loading for various angle of incidence. 103
5.19. Total displacement at the base of the structure. An incident unit plane P-wave is imposed as a loading for various angle of incidence. 104

6.1. Grenoble basin: layers and shape of the basin. 108

6.2. Top and bottom view of the mesh of Grenoble basin, with the chosen location for the center and border points are indicated in red. 110
6.3. Displacement at the free surface of the basin. A vertical incident unit plane SV-wave is imposed as a loading. 112
6.4. Displacement at the free surface of the basin. A vertical incident unit plane SH-wave is imposed as a loading. 113
6.5. Displacement at the free surface of the basin. A vertical incident unit plane P-wave is imposed as a loading. 114
6.6. Displacement at the free surface of the basin in the X-direction. A vertical incident unit plane SV-wave is imposed as a loading. 115
6.7. Displacement at the free surface of the basin in the Y-direction. A vertical incident unit plane SH-wave is imposed as a loading. 115
6.8. Displacement at the free surface of the basin in the Z-direction. A vertical incident unit plane P-wave is imposed as a loading. 116
6.9. Displacement at the free surface of the basin. A vertical incident unit plane SV-wave is imposed as a loading. 118
6.10. Displacement at the free surface of the basin. A vertical incident unit plane SH-wave is imposed as a loading. 119
6.11. Displacement at the free surface of the basin. A vertical incident unit plane P-wave is imposed as a loading. 120

A.1. Diffraction of an incident plane P-wave by a free surface. 126
A.2. Diffraction of an incident plane S-wave by a free surface. 127

List of Tables

4.1. Static stiffness of a circular surface footing of radius R on a homogeneous half-space of Poisson's ratio ν. 46

5.1. Frequencies, unit effective mass and cumulated effective mass for the eigenmodes in u_x direction. The most important modes in this direction are indicated in blue. . . . 82
5.2. Frequencies, unit effective mass and cumulated effective mass for the eigenmodes in u_y direction. The most important modes in this direction are indicated in blue. . . . 82
5.3. Frequencies, unit effective mass and cumulated effective mass for the eigenmodes in u_z direction. The most important modes in this direction are indicated in blue. . . . 83

6.1. Mechanical parameters used to model the layers of the bedrock. 108
6.2. Mechanical parameters used to model the layers of the sedimentary basin. 109
6.3. Depth of the layer under the center point of the basin 6.2. 111
6.4. Depth of the layer under the border point of the basin 6.2. 111
6.5. Frequencies, unit effective mass and cumulated effective mass for the eigenmodes in u_x direction. 117
6.6. Frequencies, unit effective mass and cumulated effective mass for the eigenmodes in u_y direction. 117
6.7. Frequencies, unit effective mass and cumulated effective mass for the eigenmodes in u_z direction. 117

Chapter 1

Introduction

Contents

1.1. Site effects and Soil-Structure Interaction 2
1.2. Causes of site effects 3
1.2.1. Topographic site effects 4
1.2.2. Lithologic site effects 4
1.2.3. Geometric site effects of sedimentary basins 5
1.3. Seismic wave propagation and amplification in an elastic medium . . . 6
1.4. Numerical methods to model elastic wave propagation in soils 8
1.4.1. Finite Element Method 8
1.4.2. Discontinuous Galerkin Method 9
1.4.3. Spectral Element Method 9
1.4.4. Boundary Element Method 10
1.4.5. Conclusions 10
1.5. Main ingredients of the boundary element method 11
1.5.1. Boundary integral equations 11
1.5.2. The boundary element method (BEM) 12
1.5.3. Conclusions 13
1.6. Fast multipole accelerated boundary element method 13
1.6.1. Foundations of the fast multipole method 14
1.6.2. The single level FMM 15
1.6.3. The multi-level FMM 18
1.6.4. Conclusions 19
1.7. Aim and outline of this work 19

1.1. Site effects and Soil-Structure Interaction

The regulations on the seismic design of structures are often based on safety factors that ensure, more or less conservatively, the mechanical resistance of the structure. In order to quantify seismic design margins, more realistic models are becoming more and more common. The increasing use of non-linear behaviour models is a significant proof of this. In this context, it is important to work on a better characterisation not only of the non-linear dynamic behaviour of the structures, but also of the seismic loading used in the studies. To this end, in the recent years, collaborative projects have been organised with a strong desire to increase exchanges between seismologists and earthquake engineering specialists (see for example the projects E2VP [45] and QUEST [38]).

Defining the seismic loading consists in evaluating three different phenomena (Figure 1.1): (i) the effect of the seismic source inherent to the properties of the fault, (ii) the propagation of the seismic wave from the fault to the site, and finally (iii) the site effects related to the topography and lithology of the site. A rigorous definition of the seismic loading requires an advanced grasp of each of these phenomena.

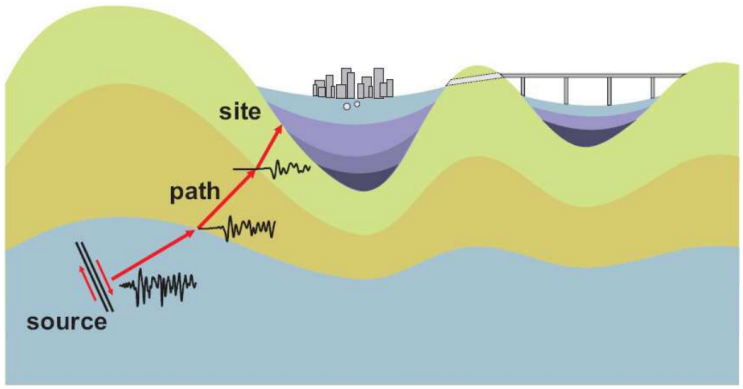

Figure 1.1.: *Propagation of a wave from the source to the site [59].*

The scope of this work is the evaluation of the site effects in Soil-Structure Interaction. The motion induced in a structure by an earthquake depends on the intensity and the frequency content of the seismic wave in general, but also, more locally, on the geological properties of the soil around the structure. Therefore, assessing the importance of the topography, heterogeneities between soil layers (induced by the velocity contrast between layers) and the shape of the sedimentary basin is necessary for better predicting the response of the structure to an earthquake.

Soil-Structure Interaction (SSI) is the study of the interaction between the soil and the structure under a seismic loading. It consists in evaluating how the ground motion affects the structural response and how the structure motion affects the incident seismic wave. Solving such a coupled system requires, in most cases, a numerical solution. Models that incorporate the necessary physical mechanisms can be costly both in time and memory requirements. The numerical simulation of the response of a structure to a seismic wave requires to consider two different components of the model:

the soil and the structure. It is a multi-scale problem: the structure has a characteristic length of few tens meters, and the soil has a characteristic length that can reach few kilometers.

In addition to SSI, it is known that the topography of the bassin, its different layers (i.e. heterogeneities) can affect the frequency content of a seismic wave, as well as induce in certain configurations an amplification or attenuation of the wave, locally around the structure. The 1985 Mexico earthquake exhibited such effects. On Figure 1.2, an attenuation of the wave amplitude is noted in the Teacalco and UNAM stations in comparison with the accelerations recorded in the Campos station located near the epicentre of the earthquake. However the site effects abruptly caused seismic wave amplification in the sedimentary basin (station SCT). Even if the city of Mexico was located at 400km from the earthquake epicenter, the accelerations recorded in Mexico were larger than the ones recorded near the epicentre.

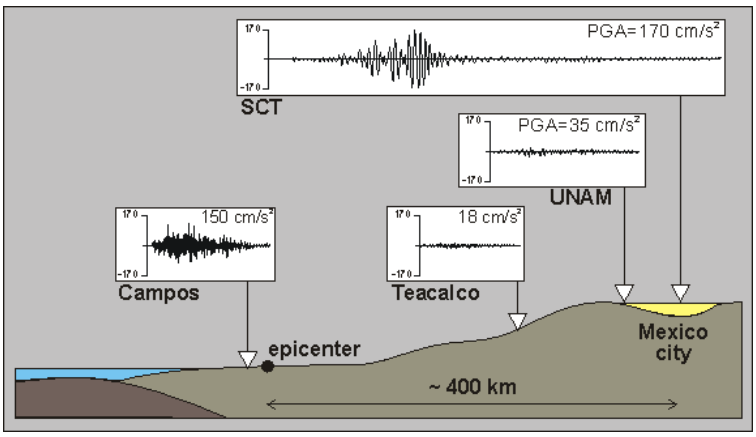

Figure 1.2.: *Recorded accelerations during the 1985 Mexico earthquake.*

It is then essential to predict the occurrence of these phenomena by numerically simulating site effects when considering Soil-Structure Interaction. The number of parameters influencing the structure response being too wide, e.g. the characteristics of the soil, of the seismic fault and the geology around the structural, only the effects of the most important parameters can be taken into account [31]. In the following, only the topography and the lithology parameters are considered.

1.2. Causes of site effects

Site effects are related to the mechanical properties of the different layers of soil and to the geological distribution of the strata and topography of a given site. In this Section, these different aspects are recalled.

1.2.1. Topographic site effects

The topography of a site influences directly the incident seismic wave, causing an amplification or an attenuation of the wave amplitude.

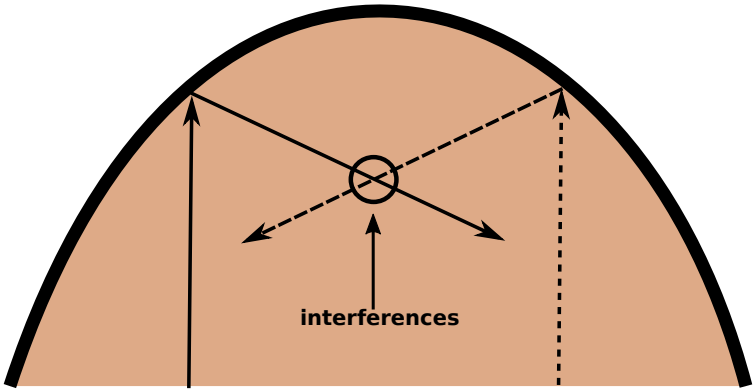

Figure 1.3.: *Interference between two waves in the case of a concave topography.*

Concave topographies cause an amplification (for example in the case of mountains and hills), whereas convex topographies can cause attenuation of the wave amplitude. Figure 1.3 illustrates graphically the origin of these constructive and destructive interferences. A more complex example is the model of Caracas from [25]. Figure 1.4 presents the results for a homogeneous model with a topographic relief. Results show that the wave amplitude at the top of the mountain is equal to twice the amplitude of the incident wave, due to the amplification of the seismic wave because of the concave topography of the basin in this location.

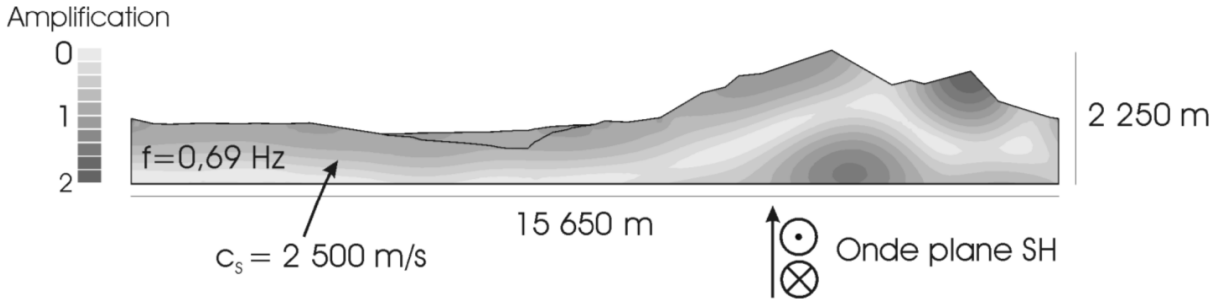

Figure 1.4.: *Illustration of the amplification of SH-waves in a homogeneous medium (model of Caracas from [25]).*

1.2.2. Lithologic site effects

The stratification of the sedimentary layers exhibits in general a decrease of the wave velocity in the upper layers. Deeper layers are subjected to higher confining stresses, therefore presenting higher elastic modulus. For engineering porpuses, the bedrock is considered as the uppermost layer which presents shear wave velocity higher than 800 m/s. This contrast of wave velocities causes a

trapping of the waves and thus an amplification of the motion. This phenomenon depends on the wave velocity contrast, layer's thickness and the frequency content of the incident wave. This effect tends also to extend the duration of the free-field signal. Figure 1.5 illustrates this phenomenon in the case of two horizontal layers, where the light green soil is softer than the dark green soil, and thus causes wave trapping in the softer layer.

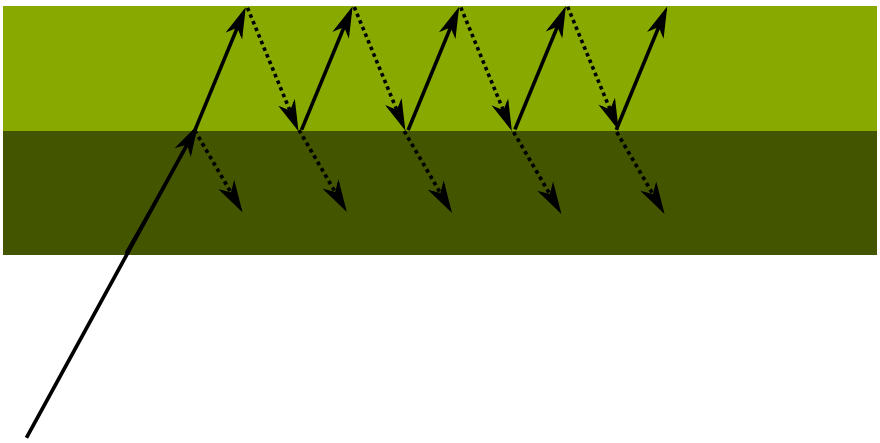

Figure 1.5.: *Trapping of waves in a stratified medium. The softest soil is in light green, while the stiffest soil is in dark green.*

A sedimentary basin can also filter high frequencies in some cases. Indeed, high frequencies being generally dominant in the bedrock while lower frequencies dominate the response of the softer soils, the stratigraphy of the soils causes an amplification of the amplitude of the low frequencies and an attenuation of the high frequencies due to the filtering effect of soft soils [35].

1.2.3. Geometric site effects of sedimentary basins

The shape of the sedimentary basin itself may cause a decrease or amplification of waves (Figure 1.6). These effects, coupled with the lithological effects, can lead to the focusing of waves and the generation of surface waves [25].

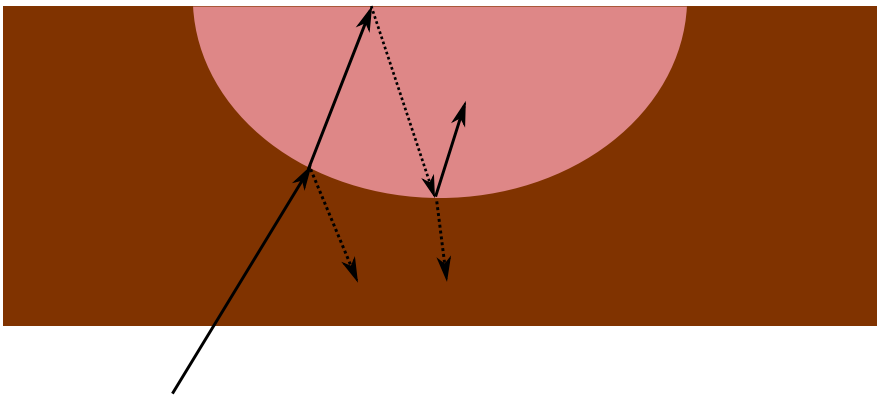

Figure 1.6.: *Site effect due to the basin shape and velocity contrast. The alluvial basin is depicted in pink. The bedrock is depicted in brown.*

Modeling the site effects is based on modeling the propagation on a wave in the considered medium. This thesis is within the framework of elastodynamic soils. The following Section presents the theoritical aspects of the wave propagation in elastodynamics.

1.3. Seismic wave propagation and amplification in an elastic medium

In the following, Ω denotes an elastic medium. The fundamental equation of elastodynamics in the time-domain writes:

$$\underline{div}(\underline{\underline{\sigma}}) + \underline{f}_d = \rho \underline{\ddot{u}}, \ \forall\, t, \ \forall\, \underline{x} \ \in \ \Omega \tag{1.1}$$

where $\underline{u}$ is the displacement vector, $\underline{\ddot{u}}$ is the second time derivative of the displacement, $\underline{\underline{\sigma}}$ is the stress tensor, $\underline{f}_d$ is the body force vector and ρ is the density.

Under the hypothesis of small perturbations (SPH), the stress tensor writes: $\underline{\underline{\sigma}} = \underline{\underline{\underline{C}}} : \underline{\underline{\varepsilon}}$, with $\underline{\underline{\varepsilon}}$ the infinitesimal strain tensor that can be written as a function of the displacement vector $\underline{u}$ as: $\underline{\underline{\varepsilon}} = \frac{1}{2}(\underline{\underline{grad}}(\underline{u}) + (\underline{\underline{grad}}(\underline{u}))^t)$, $\underline{\underline{\underline{C}}}$ the stiffness tensor, $()^t$ the transpose operator and $grad$ is the gradient operator.

In this work, soils with a linear viscoelastic isotropic constitutive law, and constant characteristics per layer are considered. This is a first approximation of the behaviour of the soil. It is used for large models where the computational cost of more complex constitutive law is prohibitive or when there is little knowledge on the properties of the soil. In this context, within each soil layer, the stiffness tensor $\underline{\underline{\underline{C}}}$ depends of only two parameters. Expressing equation (1.1) in terms of Lamé parameters (λ and μ) and displacement writes:

$$(\lambda + 2\mu)\ \underline{grad}(div(\underline{u})) - \mu\ \underline{curl}(\underline{curl}(\underline{u})) + \underline{f}_d = \rho \underline{\ddot{u}}, \tag{1.2}$$

where $grad$, div and $curl$ denotes the gradient, divergence and curl operators respectively.

To simplify equation (1.2), the Helmholtz decomposition [34] is used, under the assumption of smoothness and decay of $\underline{u}$. It consists in introducing a scalar potential Φ and a vector potential $\underline{\Psi}$ that satisfy $\underline{u} = \underline{grad}(\Phi) + \underline{curl}(\underline{\Psi})$ with $div(\underline{\Psi}) = 0$. The potentials Φ et $\underline{\Psi}$ are uniquely determined as the solutions of equations (1.3) and (1.4) with:

$$\Delta\Phi = div(\underline{u}), \tag{1.3}$$

$$and\ \Delta\underline{\Psi} = -\underline{curl}(\underline{u}). \tag{1.4}$$

Introducing this decomposition in equation (1.2) gives:

$$\underline{grad}((\lambda + 2\mu)\Delta\Phi - \rho\ddot{\Phi}) + \underline{curl}(\mu\Delta\underline{\Psi} - \rho\ddot{\underline{\Psi}}) = \underline{0}. \tag{1.5}$$

From equation (1.5), the unicity of the decomposition leads to the separation of the potentials Φ and $\underline{\Psi}$:

$$(\lambda + 2\mu)\Delta\Phi = \rho\ddot{\Phi}, \tag{1.6}$$

$$\mu\Delta\underline{\Psi} = \rho\ddot{\underline{\Psi}}. \tag{1.7}$$

Both equations (1.6) and (1.7) take the form of a wave equation. Since $\Delta\Phi = div(\underline{u})$, the potential Φ can be regarded as a particle traveling in the direction parallel to the direction of propagation with a velocity $C_p = \sqrt{\frac{\lambda+2\mu}{\rho}}$. Waves resulting from the potential Φ are called compression waves or P-waves, because they cause compression and dilatation of the medium they propagate through (Figure 1.7, left). Since $\Delta\underline{\Psi} = -\underline{curl}(\underline{u})$, the potential $\underline{\Psi}$ can be regarded as a particle traveling in the direction orthogonal to the direction of propagation with a velocity $C_s = \sqrt{\frac{\mu}{\rho}}$. Waves resulting from the potential $\underline{\Psi}$ are called shear waves or S-waves (Figure 1.7, right).

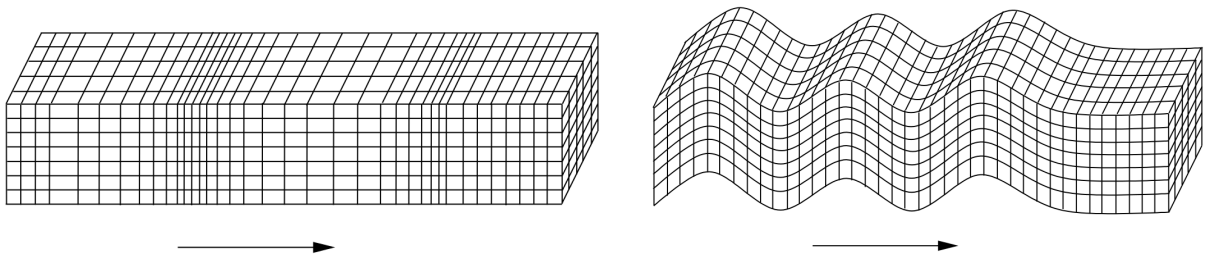

Figure 1.7.: *Motion induced by a P-wave (left) and a S-wave (right).*

The shear and compression waves are called body waves because they are three dimensional waves that propagate through material volume, contrary to the surface waves that propagate on interfaces between layers of the material or in the free surface.

In this work, the solution of elastodynamic problems in the Fourier domain is considered. The fundamental equation of elastodynamics in the Fourier domain writes:

$$\underline{div}(\underline{\underline{\sigma}}) + \underline{f}_d = -\rho\omega^2 \underline{u}. \tag{1.8}$$

The transition from the time domain to the Fourier domain is done by the Fourier transform $\tilde{r}(f)$, which is defined as:

$$\tilde{r}(f) = \mathscr{F}(r) = \int_{-\infty}^{+\infty} r(t) e^{+i2\pi ft} dt, \tag{1.9}$$

while the inverse Fourier transform is defined as:

$$r(t) = \mathscr{F}^{-1}(\tilde{r}) = \frac{1}{2\pi} \int_{-\infty}^{+\infty} \tilde{r}(f) e^{-i2\pi ft} df. \tag{1.10}$$

1.4. Numerical methods to model elastic wave propagation in soils

There exist different methods to model site effects. The principle is to evaluate the response of a basin to the propagation of seismic waves. Each method has its advantages and limitations, and is more or less adapted to a certain type of problem. Depending on the geometric complexity of the medium, the material characteristics of the soil layers, the frequency content of the seismic signals, and on the computational ressources at hand, one method is more appropriate than another.

Several benchmarks and projects [45, 38] in the scientific community have been performed to evaluate the relevance of the use of these methods. In what follows, the most common methods are briefly presented: the finite element method (FEM), the discontinuous Galerkin method (DGM), the spectral element method (SEM) and the boundary element method (BEM).

1.4.1. Finite Element Method

The finite element method is based on a volume discretisation of the computational domain. It has the advantage to offer the possibility to treat domains with complex geometries, non-linearities and a large range of materials with complex constitutive laws. However, for large problems, the number of unknowns grows quickly, because the entire volume is meshed. In addition, it can suffer from dispersion and pollution effects [57] and it is not very well-suited to treat infinite or semi-infinite media. One has to artificially truncate the computational domain. However, it is not a strong limitation since there exist methods to overcome this issue such as the use of non-reflecting boundary conditions or PMLs [42, 37, 19, 2, 3].

Recent works, based on the use of the FEM have been conducted in the community to evaluate site effects. The work on the Abruzzo site in Italy [52] can be cited for example. This work has demonstrated the importance to take into account the lithological effects of the basin. In the work, the modelling was limited in 2D due to the complexity of the geologic situation. The work by Restrepo & al. [55] on the simulation of seismic wave propagation in the metropolitan area of Medellín in the Aburrá Valley can also be mentionned. It is an earthquake-pone region of the

Colombian Andes that exhibits moderate to strong topographic irregularities [55]. They show how realistic topography greatly modifies the ground response.

1.4.2. Discontinuous Galerkin Method

The Discontinuous Galerkin method (DGM) was introduced by Reed and Hill in 1973 [54] to solve the neutron transport equation. This method is quite similar to the finite element method, with the difference that the continuity of the unknowns at the nodes is not imposed [36]. The method relies on piecewise continuous shape functions per element. The main advantages of this method are: (i) the simplicity to generate a mesh since unstructured meshes can be used, (ii) the fact that models with strong heterogeneities can be easily treated and (iii) it is particularly well-suited for parallelisation. However, the discontinuity of the unknowns at the nodes considerably increases the size of the system to solve.

The method is currently used by different groups world-wide. The work in the group of Warburton [48] that concentrates on the massively parallel computing aspects of the method can be mentioned. The method has also been applied for realistic configurations, see e.g. the application to the Nice basin [53]. In addition, the results of the DGM [27] have been compared to the results of the spectral element method (SEM) and finite differences method (FDM) in the framework of the E2VP project [46, 13] to simulate a virtual $M1.3$ event. DGM results have shown a good fit with SEM and FDM results. Finally, the method is also applied to consider non-linear problem, see e.g. in [6].

1.4.3. Spectral Element Method

The spectral element method combines the flexibility of the finite element method with the high accuracy of spectral methods. As a results, it overcomes the problem of numerical dispersion, thanks to the high-order approximation of the variational problem in elastodynamics [59]. Similarly to the finite element method, it is not very well-suited to model infinite media. However, a lot of works are related to the use of special elements such as Perfectly Matched Layers [2, 15, 19, 39] to avoid this drawback. The main drawback of the method is the mesh generation since it is formulated for hexahedral mesh. In practice, it is sometimes hard to mesh a complex geological structure or a realistic topography with hexahedra. Nevertheless, some works are trying to overcome this difficulty [63, 40].

The method has been used for example for the quantification of site effects at the Matsuzaki site in Japan [51] or for the quantitative assessment of site effects in the Volvi Basin in the E2VP project [46]. The method is also used to model wave propagation in non-linear media [50] and to evaluate the "source-to-site" seismic scenarios for strong ground motion prediction [29, 30]. Very recently, the method has been coupled with the FEM to model soil-structure interaction [64].

The main challenge is to couple two methods with very different polynomial degrees in the shape functions.

1.4.4. Boundary Element Method

The Boundary Element Method (BEM) is based on the discretisation of a boundary integral equation expressed on the boundary of the domain. As a result, only the boundary of the domain is discretised, leading to a drastic reduction of the number of unknowns of the problem and of the difficulties related to the meshing of the volume of a complex geometry [4]. The unknowns of the system to solve are defined on the surface of the domain and possibly its interfaces. The BEM is well suited to study wave propagation in infinite media, since the radiation conditions are intrinsically taken into account in the formulation. The BEM also avoids the numerical dispersion that can appear in the simulation with the finite element method. However, one of the drawbacks of the BEM is the computational cost to assembly the fully-populated matrix of the system. If the mesh is composed of N DOFs on the boundary, the cost to assembly and store this matrix is of the order of $\mathcal{O}(N^2)$.

The method has been used for example in the study of site effects in the Nice basin [58]. Amplification factors up to 16 times in seismic spectral ratios in the free surface at low frequencies, compared to a reference of a homogeneous half-space have been identified. This study highlights the good quality of the results of the BEM for the study and the quantification of site effects. However, this study has been limited to 2D site effects due to the very large computational costs of the method. The BEM was also used to study the 3D amplification of the seismic waves in canonical problems [47]. In this case, the BEM solution was accelerated by the fast multipole method to allow the simulation of 3D configurations. It has highlighted the importance of the velocity contrast and the asymmetry of the basin in the amplification of the waves at the free surface.

The BEM is also used in an industrial context at EDF R&D. The substructure method is available for SSI calculations with *Code_Aster* : while the structure is modeled by FE, the soil is modeled with boundary elements using MISS3D software [18].

1.4.5. Conclusions

In many cases and whatever numerical method is used, as in the project E2VP [45], the studies are either done in 2D (which represents a simplification of the model), or they are limited to low frequencies because of the high computational cost. However, seismic signals have generally a non-zero frequency spectra over frequencies in the order of $0 - 20Hz$. In addition, the basin geometries can not always be represented in 2D, because they may represent lateral heterogeneities which must be considered in models. It is therefore important to develop a numerical solver to simulate propagation problems for complex models (lithology, topography ...).

One of the recent advances in this area has been the application of the fast multipole method (FMM) to accelerate the boundary element method [7] in 3D for higher frequencies in elastodynamics. With this fast BEM, it is possible to combine the flexibility of boundary elements to model complex geometries (without having to mesh inside the treated domains) with the acceleration of the resolution of the system offered by the fast multipole method. Indeed, one of the drawbacks of the standard (non accelerated) BEM is the cost of the solution of the system with an iterative solver of the order of $\mathcal{O}(N^2)$ per iteration. The fast multipole method allows to lower the cost to $\mathcal{O}(Nlog(N))$.

1.5. Main ingredients of the boundary element method

In what follows, the boundary integral equations are presented, as well as the corresponding numerical method: the boundary element method (BEM) in the Fourier domain.

1.5.1. Boundary integral equations

The reciprocity theorem. Let Ω be an elastic solid bounded in space, its boundary being $\partial\Omega$. The reciprocity theorem derives from the principle of virtual work and gives the relation between two elastodynamic states $(\underline{u}^{(1)}, \underline{\underline{\sigma}}^{(1)}, \underline{F}^{(1)})$ and $(\underline{u}^{(2)}, \underline{\underline{\sigma}}^{(2)}, \underline{F}^{(2)})$:

$$\int_{\partial\Omega} [\underline{T}^n(\underline{u}^{(1)}).\underline{u}^{(2)} - \underline{T}^n(\underline{u}^{(2)}).\underline{u}^{(1)}]dS = \rho \int_{\Omega} [\underline{F}^{(2)}.\underline{u}^{(1)} - \underline{F}^{(1)}.\underline{u}^{(2)}]dV \tag{1.11}$$

with $\underline{T}^n(\underline{u}) = \underline{\underline{\sigma}}.\underline{n}$ the vector of surface forces applied on the surface of outward normal $\underline{n}$.

Helmholtz fundamental solution for the free space. A boundary integral equation is defined by the use of some special solutions that are called fundamental solutions or Green's functions. To simplify, we first introduce the Helmholtz fundamental solution G. It is defined as the impulse response of an inhomogeneous linear differential equation for a specific domain, with defined boundary conditions. In the case of the Helmholtz equation, G is solution of the equation $\Delta G(\underline{x}, \underline{y}) + k^2 G(\underline{x}, \underline{y}) + \delta(\underline{y} - \underline{x}) = 0$, where δ is the unit impulse. When the studied domain is the free space, the solution of the equation is simply given by:

$$G(|\underline{y} - \underline{x}|, k) = \frac{e^{ik|\underline{y}-\underline{x}|}}{4\pi|\underline{y} - \underline{x}|}.$$

Fundamental solutions for an elastic free space. A fundamental solution is by definition a solution of the equation (1.8) (displacement $U_i^k(x, y, k)$ and stress tensor $\Sigma_{ij}^k(x, y, k)$) associated to a unitary punctual force load applied in a fixed point $\underline{x}$: $\rho\underline{F}(\underline{y}) = \delta(\underline{y} - \underline{x})\underline{e}_k$; $k \in \{1, 2, 3\}$[4]. It depends on the geometry of the domain and the boundary conditions of the problem.

In the following, the fundamental solution of the free space formulated by Yoshida [61] is used. The

advantage of this formulation is that each term can be expressed in terms of partial derivates of the Helmholtz fundamental solution G, allowing to extend existing work to 3D elastodynamics:

$$U_i^k(\underline{x},\underline{y},k_p,k_s) = \frac{1}{k_s^2\mu}[(\delta_{qs}\delta_{ik}-\delta_{qk}\delta_{is})\frac{\partial}{\partial x_q}\frac{\partial}{\partial y_s}G(|\underline{y}-\underline{x}|,k_s)+\frac{\partial}{\partial x_i}\frac{\partial}{\partial y_k}G(|\underline{y}-\underline{x}|,k_p)] \tag{1.12}$$

$$T_i^k(\underline{x},\underline{y},k_p,k_s) = C_{ijhl}\frac{\partial}{\partial y_l}U_h^k(\underline{x},\underline{y},k_p,k_s)n_j(\underline{y}) \tag{1.13}$$

with T_i^k the vector of surface forces applied on the surface of outward normal $\underline{n}$, hence $T_i^k = \Sigma_{ij}^k n_j$, and C_{ijhl} the terms of the stiffness tensor.

Integral representation. Using the reciprocity theorem (1.11), taking as first elastodynamic state the unknowns of the problem and as second elastodynamic state the fundamental solution, the displacement is expressed in all points $\underline{x} \notin \partial\Omega$ as follows:

$$c\ u_k(\underline{x}) = \int_{\partial\Omega}[t_i(\underline{y})U_i^k(\underline{x},\underline{y},k_p,k_s) - u_i(\underline{y})T_i^k(\underline{x},\underline{y},k_p,k_s)]dS_y + \int_\Omega \rho F_i(\underline{y})U_i^k(\underline{x},\underline{y},k_p,k_s)dV_y \tag{1.14}$$

with $c = 1$ if $\underline{x} \in \Omega$, $c = 0$ otherwise.

Thanks to this, in the absence of volume forces, it is possible to evaluate in all points the displacement (and to deduce the stresses and deformations) from boundary conditions on the boundary of the domain. It remains to define an equation to obtain unknowns on the boundary. In the following, the problem in the absence of body forces is considered.

Boundary integral equation. When $\underline{x} \in \partial\Omega$, a singularity occurs in $\underline{x} = \underline{y}$. With the help of a limiting process, the singular elastodynamic integral equation can be expressed as an equation linking unknowns on the boundary $\partial\Omega$ [7]:

$$c_{ik}(\underline{x})u_i(\underline{x}) = \int_{\partial\Omega} t_i(\underline{y})U_i^k(\underline{x},\underline{y},k_p,k_s)dS_y - (PV)\int_{\partial\Omega} u_i(\underline{y})T_i^k(\underline{x},\underline{y},k_p,k_s)dS_y \tag{1.15}$$

where (P.V.) indicates a Cauchy principal value singular integral [4] and $c_{ik} = \frac{1}{2}\delta_{ik}$ if the boundary is smooth enough around $\underline{x}$ [4]. The integral representation and the boundary integral equation are valid for both internal and external problems [7]. This method is based on the knowledge of the fundamental solution and the reciprocity theorem. The fact that the method relies on the fundamental solution implies that it can only be used to solve linear problems. This formulation is well-suited to study infinite or semi-infinite elastodynamic medium because the radiation condition at infinity is implicitly taken into account in the formulation (with the fundamental solution).

1.5.2. The boundary element method (BEM)

Thanks to the integral representation, one needs to solve the problem only on the boundary of the domain, to then be able to evaluate the displacements everywhere in the volume. There

exist different approach to discretise the boundary integral equation. In this work the collocation approach is used. It consists in enforcing the integral equation to be verified exactly in a finite number of collocation points [4].

The numerical solution of the boundary integral equation is based on a boundary element discretization of the surface $\partial\Omega$ and boundary unknowns $(\underline{u}, \underline{t})$. It leads to a linear system of the kind:

$$\underline{\underline{H}}\ \underline{u} + \underline{\underline{G}}\ \underline{t} = \underline{0}. \tag{1.16}$$

In this work, $\underline{u}$ is the displacement vector evaluated at nodes (i.e. linear interpolation of the displacements) and $\underline{t}$ is the vector of surfaces forces evaluated per element (i.e. piecewise constant interpolation of the displacements). Matrices $\underline{\underline{H}}$ and $\underline{\underline{G}}$ are fully-populated.

Taking into account the boundary conditions, and separating known displacements and forces from unknowns, the system can be assembled in the following way:

$$\underline{\underline{K}}\ \underline{v} = \underline{f} \tag{1.17}$$

where $\underline{v}$ represents the vector of unknowns and $\underline{f}$ the vector of specified boundary conditions.

1.5.3. Conclusions

Advantages of the BEM. The boundary element method relies on a discretisation of the surface of the domain only, leading to a drastic reduction of the number of unknowns of the system. This also makes it possible to simplify the mesh in the case of complicated models. This method is also suitable for the modelling of infinite media. Finally, the radiation condition is implicitly taken into account in the formulation.

Drawbacks of the BEM. The method is limited to the solution of linear problems because of the use of a fundamental solution. The system gives a costly, non-symmetric matrix to assemble and store (complexity $\mathcal{O}(N^2)$). However, these drawbacks are not absolute limits of the method. There exist accelerated methods to avoid the memory and computation time limits that could appear using the standard BEM. Among these methods, the fast multipole method applied to integral equations [7, 9], as well as the hierarchical matrix method [20, 11] have been shown to be efficient methods to model elastic waves. The acceleration of BEM by FMM or by H-matrix being recent, there has not yet been a exhaustive comparison between the performance of the two methods in elastodynamics. Some previous partial comparisons [26] conclude that the FMM is somehow less expensive in terms of CPU time and in memory.

1.6. Fast multipole accelerated boundary element method

In this section, the foundations of the fast multipole method applied to integral boundary equations are presented. Then, two variants of the fast multipole method: single-level and multi-level are presented. Finally, the advantages and drawbacks of the method are discussed.

1.6.1. Foundations of the fast multipole method

The fast multipole method (FMM) was introduced by Greengard and Rokhlin [33]. It is based on a reformulation of the fundamental solutions in term of a product of functions depending of only $\underline{x}$ or $\underline{y}$. This variable separation vectorises the solution. The integrals that depend on $\underline{y}$ are computed once and for all and reused when the collocation point $\underline{x}$ is changed, thus decreasing the complexity of the matrix assembly that was of $\mathcal{O}(N^2)$.

This method comes as a response to one of the limitations of the BEM, which is the computational cost in terms of CPU time and memory. Applying this method to the BEM (see Section 1.5) permits to accelerate the solution of elastodynamic problems by reducing the cost of computing the integrals.

The fundamental solutions being written as partial derivatives of the Helmholtz fundamental solution (see Section 1.5), they can be expressed with the plane wave decomposition of $G(\underline{r}, k)$ [7]:

$$G(|\underline{r}|, k) = \lim_{L\to\infty} \int_{\underline{\hat{s}}\in S} e^{ik\underline{\hat{s}}.(\underline{y}-\underline{y}_0)} \mathcal{G}_L(\underline{\hat{s}}, \underline{r}_0, k) e^{-ik\underline{\hat{s}}.(\underline{x}-\underline{x}_0)} d\underline{\hat{s}} \tag{1.18}$$

where L is a truncation parameter, k the wave number, and the vectors $\underline{x}_0$ and $\underline{y}_0$ are two poles close enough from $\underline{x}$ and $\underline{y}$ respectively: $\underline{r} = \underline{y} - \underline{x}$ and $\underline{r}_0 = \underline{y}_0 - \underline{x}_0$ (Figure 1.8). S represents the unit sphere and $\underline{\hat{s}}$ a quadrature point for the integral on the latter [7]. Importantly, in Equation (1.18), the components $\underline{x}$ and $\underline{y}$ are separated.

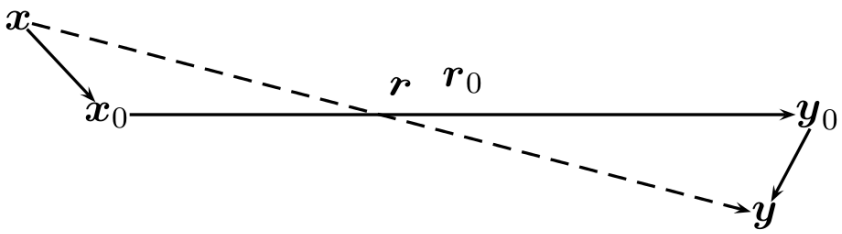

Figure 1.8.: *FMM: illustration of the position of points and of poles.*

The function G_L is defined in terms of Legendre polynomials P_n and the spherical Hankel functions

of the first kind $h_n^{(1)}$:

$$\mathcal{G}_L(\underline{\hat{s}}, \underline{r}_0, k) = \frac{ik}{16\pi^2} \sum_{n=0}^{L} (2n+1) i^n h_n^{(1)}(k|\underline{r}_0|) P_n(cos(\underline{\hat{s}}, \underline{r}_0)). \tag{1.19}$$

From there, the fundamental solutions can be expressed on the basis of this decomposition:

$$\begin{aligned} U_i^k(\underline{x}, \underline{y}, k) = &\lim_{L\to\infty} \int_{\underline{\hat{s}}\in S} e^{ik_p \underline{\hat{s}}.(\underline{y}-\underline{y}_0)} \mathcal{U}_{i,L}^{k,p}(\underline{\hat{s}}, \underline{r}_0) e^{-ik_p \underline{\hat{s}}.(\underline{x}-\underline{x}_0)} d\underline{\hat{s}} + \\ &\lim_{L\to\infty} \int_{\underline{\hat{s}}\in S} e^{ik_s \underline{\hat{s}}.(\underline{y}-\underline{y}_0)} \mathcal{U}_{i,L}^{k,s}(\underline{\hat{s}}, \underline{r}_0) e^{-ik_s \underline{\hat{s}}.(\underline{x}-\underline{x}_0)} d\underline{\hat{s}} \end{aligned} \tag{1.20}$$

$$\begin{aligned} T_i^k(\underline{x}, \underline{y}, k) = &\lim_{L\to\infty} \int_{\underline{\hat{s}}\in S} e^{ik_p \underline{\hat{s}}.(\underline{y}-\underline{y}_0)} \mathcal{T}_{i,L}^{k,p}(\underline{\hat{s}}, \underline{r}_0) e^{-ik_p \underline{\hat{s}}.(\underline{x}-\underline{x}_0)} d\underline{\hat{s}} + \\ &\lim_{L\to\infty} \int_{\underline{\hat{s}}\in S} e^{ik_s \underline{\hat{s}}.(\underline{y}-\underline{y}_0)} \mathcal{T}_{i,L}^{k,s}(\underline{\hat{s}}, \underline{r}_0) e^{-ik_s \underline{\hat{s}}.(\underline{x}-\underline{x}_0)} d\underline{\hat{s}} \end{aligned} \tag{1.21}$$

The transfer functions of the fundamental solutions are expressed as a combination of partial derivatives of the transfer function $\mathcal{G}_L$:

$$\mathcal{U}_{i,L}^{k,p}(\underline{\hat{s}}, \underline{r}_0) = \frac{\gamma^2}{\mu} \hat{s}_i \hat{s}_k \mathcal{G}_L(\underline{\hat{s}}, \underline{r}_0, k_p) \tag{1.22}$$

$$\mathcal{T}_{i,L}^{k,p}(\underline{\hat{s}}, \underline{r}_0) = \frac{ik_s\gamma^3}{\mu} C_{ijhl} \hat{s}_l \hat{s}_h \hat{s}_k \mathcal{G}_L(\underline{\hat{s}}, \underline{r}_0, k_p) n_j(\underline{y}) \tag{1.23}$$

$$\mathcal{U}_{i,L}^{k,s}(\underline{\hat{s}}, \underline{r}_0) = \frac{1}{\mu} (\delta_{ik} - \hat{s}_i \hat{s}_k) \mathcal{G}_L(\underline{\hat{s}}, \underline{r}_0, k_s) \tag{1.24}$$

$$\mathcal{T}_{i,L}^{k,s}(\underline{\hat{s}}, \underline{r}_0) = \frac{ik_s}{\mu} (\delta_{hk} - \hat{s}_h \hat{s}_k) C_{ijhl} \hat{s}_l \mathcal{G}_L(\underline{\hat{s}}, \underline{r}_0, k_s) n_j(\underline{y}) \tag{1.25}$$

where indices p and s designate the functions specific to the P and S waves, respectively.

This development is valid only if the points $\underline{x}$ and $\underline{y}$ are far enough. With fundamental solutions thus formulated, it is not possible to assemble the matrix of the system explicitly: only the matrix-vector product is evaluated $\underline{\underline{K}}.\underline{v}$. This implies that the system can only be solved by an iterative solver. Finally, this formulation of the FMM is not very accurate in the low frequency regime due to the divergence of the spherical Hankel functions of the first kind $h_p^{(1)}(k|\underline{r}_0|)$ when $k|\underline{r}_0| \to 0$. This plane wave decomposition of the fundamental solution is used in the following two versions of the FMM.

1.6.2. The single level FMM

To drive the evaluation of the matrix-vector product, a regular decomposition of the domain with cubic cells is introduced in the single-level FMM. The poles $\underline{x}_0$ et $\underline{y}_0$ in the reformulation of the fundamental solutions are defined as the centres of the cubes. Since the plane wave expansion is

valid only if $\underline{x}$ and $\underline{y}$ are far enough, the adjacent cells (close to each other) are distinguished from those that are not (see Figure 1.9). Adjacent cells are composed of cells that share at least one point in common. The FMM is only applied between two points $\underline{x}$ and $\underline{y}$ belonging to non-adjacent cells.

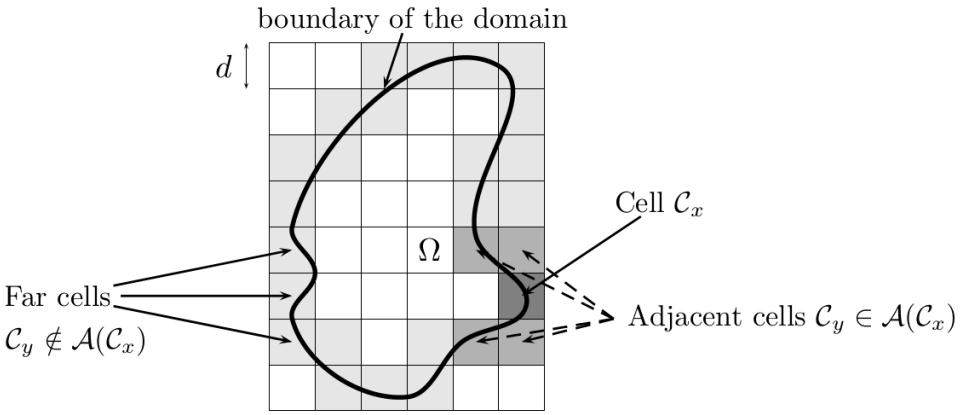

Figure 1.9.: *FMM: definition of the adjacent cells [7].*

For adjacent cells, the standard BEM is applied. This is equivalent to write that for each collocation point $\underline{x}$:

$$(\underline{\underline{K}}.\underline{u})(\underline{x}) = (\underline{\underline{K}}.\underline{u})^{FM}(\underline{x}) + (\underline{\underline{K}}.\underline{u})^{near}(\underline{x}) \tag{1.26}$$

$$\underline{f}(\underline{x}) = \underline{f}^{near}(\underline{x}) + \underline{f}^{FM}(\underline{x}) \tag{1.27}$$

The parts $\underline{f}^{near}$ and $(\underline{\underline{K}})^{near}$ are assembled by the standard BEM method once and for all (i.e. for all the iterations of the iterative solver). These two operations are not very expensive because the adjacent cells of a given cell correspond to a small portion of the cells. The remaining contributions are assembled by the FMM. The term $\underline{f}^{FM}(\underline{x})$ is assembled once and for all by the FMM. The evaluation of the term $(\underline{\underline{K}}.\underline{u})^{FM}(\underline{x})$ is reevaluated at each iteration of the iterative solver.

The advantage of the FMM is that it reduces the number of elementary operations performed to solve the system: instead of going through all the points of integration, each time we want to evaluate the system in one point $\underline{x}$, the performed operations are vectorized and re-used later.

The single-level FMM consists of three basic steps as it can be seen in Figure 1.10. For a given cell C_x and a cell C_y non-adjacent to C_x, the information contained in the integration points included in C_y are first factorised in the center of C_y (at the point $\underline{y}_0$). Then the information is transferred to the cell C_x (and more precisely to its center $\underline{x}_0$). Finally, from there, a last transfer of information to the collocation points of the C_x cell is made. In the following, a case where surface forces are imposed and displacements are unknown, is considered to illustrate the complete algorithm.

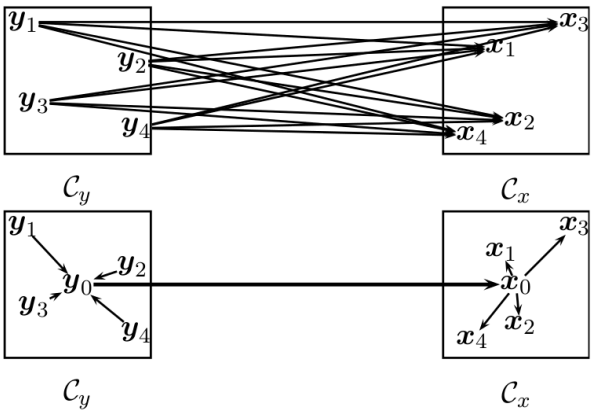

Figure 1.10.: *Comparaison of necessary elementary operations between FM-BEM and classical BEM [7].*

The first step of the single-level FMM is to compute the *multipole moments* for all the cells C_y:

$$\mathcal{R}_k^{s,u}(\underline{\hat{s}}, C_y) = -ik_s[\delta_{ik}\hat{s}_j + \delta_{jk}\hat{s}_i - 2\hat{s}_i\hat{s}_j\hat{s}_k] \int_{\partial\Omega\cap C_y} u_i(\underline{y}) n_j(\underline{y}) e^{ik_s\underline{\hat{s}}.(\underline{y}-\underline{y}_0)} dS_y \tag{1.28}$$

$$\mathcal{R}_k^{p,u}(\underline{\hat{s}}, C_y) = -ik_s\gamma^3[\frac{2\nu}{1-2\nu}\delta_{ij} + 2\hat{s}_i\hat{s}_j] \int_{\partial\Omega\cap C_y} u_i(\underline{y}) n_j(\underline{y}) e^{ik_p\underline{\hat{s}}.(\underline{y}-\underline{y}_0)} dS_y \tag{1.29}$$

$$\mathcal{R}_k^{s,t}(\underline{\hat{s}}, C_y) = \frac{1}{\mu}[\delta_{ka} - \hat{s}_a\hat{s}_k] \int_{\partial\Omega\cap C_y} t_a(\underline{y}) e^{ik_s\underline{\hat{s}}.(\underline{y}-\underline{y}_0)} dS_y \tag{1.30}$$

$$\mathcal{R}_k^{p,t}(\underline{\hat{s}}, C_y) = \frac{\gamma^2}{\mu} \int_{\partial\Omega\cap C_y} \hat{s}_a t_a(\underline{y}) e^{ik_p\underline{\hat{s}}.(\underline{y}-\underline{y}_0)} dS_y \tag{1.31}$$

Next, local expansions are computed for each cell C_x by going through all the non-adjacent cells of C_x:

$$\mathcal{L}_k^{s,u}(\underline{\hat{s}}, C_x) = \sum_{C_y\notin\mathcal{A}(C_x)} \mathcal{G}_L(\underline{\hat{s}}, \underline{r}_0, k_s)\mathcal{R}_k^{s,u}(\underline{\hat{s}}, C_y) \tag{1.32}$$

$$\mathcal{L}_k^{p,u}(\underline{\hat{s}}, C_x) = \sum_{C_y\notin\mathcal{A}(C_x)} \mathcal{G}_L(\underline{\hat{s}}, \underline{r}_0, k_p)\mathcal{R}_k^{p,u}(\underline{\hat{s}}, C_y) \tag{1.33}$$

$$\mathcal{L}_k^{s,t}(\underline{\hat{s}}, C_x) = \sum_{C_y\notin\mathcal{A}(C_x)} \mathcal{G}_L(\underline{\hat{s}}, \underline{r}_0, k_s)\mathcal{R}_k^{s,t}(\underline{\hat{s}}, C_y) \tag{1.34}$$

$$\mathcal{L}_k^{p,t}(\underline{\hat{s}}, C_x) = \sum_{C_y\notin\mathcal{A}(C_x)} \mathcal{G}_L(\underline{\hat{s}}, \underline{r}_0, k_p)\mathcal{R}_k^{p,t}(\underline{\hat{s}}, C_y) \tag{1.35}$$

The contribution of the FMM can now be computed by approaching the integral on the unit sphere by a quadrature rule of Q quadrature points $\underline{\hat{s}}_q \in S$. Note w_q the weights of the quadrature points.

$$(\underline{\underline{K}}.\underline{u})_k^{FM}(\underline{x}) \approx \sum_{q=1}^{Q} w_q[e^{-ik_s\underline{\hat{s}}_q.(\underline{x}-\underline{x}_0)}\mathcal{L}_k^{s,u}(\underline{\hat{s}}_q, C_x) + e^{-ik_p\underline{\hat{s}}_q.(\underline{x}-\underline{x}_0)}\mathcal{L}_k^{p,u}(\underline{\hat{s}}_q, C_x)] \tag{1.36}$$

$$\underline{f}^{FM}(\underline{x}) \approx \sum_{q=1}^{Q} w_q [e^{-ik_s \hat{\underline{s}}_q \cdot (\underline{x}-\underline{x}_0)} \mathcal{L}_k^{s,t}(\hat{\underline{s}}_q, C_x) + e^{-ik_p \hat{\underline{s}}_q \cdot (\underline{x}-\underline{x}_0)} \mathcal{L}_k^{p,t}(\hat{\underline{s}}_q, C_x)] \tag{1.37}$$

This method reduces the complexity of the computation of a matrix-vector product (i.e. at each iteration) from $\mathcal{O}(N^2)$ to $\mathcal{O}(N^{3/2})$.

1.6.3. The multi-level FMM

The goal is to optimise the previously presented method by having the smallest possible adjacent cells and the largest possible non-adjacent cells. This can be done by subdividing the space, not with only one level, but rather in several levels with a decreasing cell size (see Figure 1.11). With this improvement, the complexity of the computation of a matrix-vector product (i.e. at each iteration) reduces from $\mathcal{O}(N^2)$ to $\mathcal{O}(N \log(N))$. This time, for the computation of the contributions of the

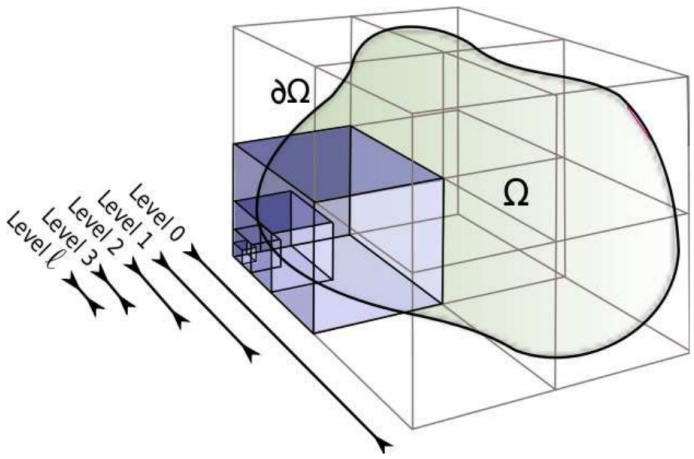

Figure 1.11.: *Multi-level subdivision of the domain [32].*

FMM part, the information is transmitted between several different levels. We note in the following $C_y^{(l)}$ the cell C_y of the level l and $\bar{l}$ the level at the smallest cell size (leaf level of the tree). The steps to compute $(\underline{\underline{K}}.\underline{u})^{FM}(\underline{x})$ at each iteration are the following:

• *Initialization:* Multipole moments for the cells at level $\bar{l}$ are first computed.

• *Upward pass:* Multipole moments are recursively computed for all cells from the bottom, up to level 2, ie:

$$\mathcal{R}_k^{s,u}(\hat{\underline{s}}, C_y^{(l)}) = \sum_{C_y^{(l+1)} \in \mathcal{S}(C_y^{(l)})} e^{ik_s \hat{\underline{s}}.(\underline{y}_0^{(l+1)} - \underline{y}_0(l)} \mathcal{R}_k^{s,u}(\hat{\underline{s}}, C_y^{(l+1)}) \tag{1.38}$$

$$\mathcal{R}_k^{p,u}(\hat{\underline{s}}, C_y^{(l)}) = \sum_{C_y^{(l+1)} \in \mathcal{S}(C_y^{(l)})} e^{ik_p \hat{\underline{s}}.(\underline{y}_0^{(l+1)} - \underline{y}_0(l)} \mathcal{R}_k^{p,u}(\hat{\underline{s}}, C_y^{(l+1)}) \tag{1.39}$$

• *Transfer:* The first terms of the local expansions for each cell of a given level l are computed for

$2 \leq l \leq \bar{l}$. The interaction list $\mathcal{I}(C)$ of a C cell is defined as the set of cells that are not adjacent but whose parents were adjacent to the parent cell of C.

$$\mathcal{L}_k^{s,u}(\hat{\underline{s}}, C_x^{(l)}) = \sum_{C_y^{(l)} \in \mathcal{I}(C_x^{(l)})} \mathcal{G}_L(\hat{\underline{s}}, \underline{r}_0, k_s) \mathcal{R}_k^{s,u}(\hat{\underline{s}}, C_y^{(l)}) \tag{1.40}$$

$$\mathcal{L}_k^{p,u}(\hat{\underline{s}}, C_x^{(l)}) = \sum_{C_y^{(l)} \in \mathcal{I}(C_x^{(l)})} \mathcal{G}_L(\hat{\underline{s}}, \underline{r}_0, k_p) \mathcal{R}_k^{p,u}(\hat{\underline{s}}, C_y^{(l)}) \tag{1.41}$$

• *Downward pass:* For each level l such that $3 \leq l \leq \bar{l}$, the local expansion is added to the contribution of the parent levels.

$$\mathcal{L}_k^{s,u}(\hat{\underline{s}}, C_x^{(l)}) = \mathcal{L}_k^{s,u}(\hat{\underline{s}}, C_x^{(l)}) + e^{-ik_s \hat{\underline{s}}.(\underline{x}_0^{(l-1)} - \underline{x}_0(l)} \mathcal{L}_k^{s,u}(\hat{\underline{s}}, C_x^{(l-1)}) \tag{1.42}$$

$$\mathcal{L}_k^{p,u}(\hat{\underline{s}}, C_x^{(l)}) = \mathcal{L}_k^{p,u}(\hat{\underline{s}}, C_x^{(l)}) + e^{-ik_p \hat{\underline{s}}.(\underline{x}_0^{(l-1)} - \underline{x}_0(l)} \mathcal{L}_k^{p,u}(\hat{\underline{s}}, C_x^{(l-1)}) \tag{1.43}$$

When the level $\bar{l}$ is reached, the contributions of the FMM part are computed with Formula (1.36).

1.6.4. Conclusions

Advantages of the FMM: This method allows to lower the algorithmic complexity of the method from a complexity of $\mathcal{O}(N^2)$ for the classical BEM, to a complexity of $\mathcal{O}(N^{\frac{3}{2}})$ for the single-level FMM, and finally to a complexity of $\mathcal{O}(Nlog(N))$ for the multi-level FMM.

This reduces the computational time compared to a classical BEM approach. In addition, memory requirements are less important than using the standard BEM. Thus, not only the FMM algorithm has a lower complexity than the conventional BEM, but also there is no need to store the matrix $\underline{\underline{K}}$ because only the matrix-vector product is computed. All this makes the method very interesting to simulate elastic wave propagation in large infinite or semi-infinite media.

Drawbacks of the FMM: The previously presented formulation of the FMM is not very adapted to the low frequency regime due to the divergence of the spherical Hankel functions of the first kind $h_p^{(1)}(k|\underline{r}_0|)$ when $k|\underline{r}_0| \to 0$. Thus, at low frequencies, it is advantageous to use the standard BEM, knowing that in this frequency ange, models do not need high mesh refinement, which gives relatively small size systems.

1.7. Aim and outline of this work

This work was initiated in a post-Fukushima context, from a wish of EDF R&D to improve its modeling of the site effects in the seismic hazard assessment in order to have a better knowledge of the margins in the design of its nuclear power plants. So far, EDF R&D had at hand a numerical method to model the structural response to an earthquake in the case of a stratified soil, through a

classical boundary element method coupled with the finite element method. This approach offered moderate possibilities in terms of complexity of the geometry, size of the problem and frequency range of interest. These limitations were mainly due to the rapid increase of the computational cost with the number of degrees of freedom. The site effects were also often decoupled from soil-structure interaction computations, because of the large-scale characteristics of the considered domains. The aim of this thesis is to go beyond these limitations and to open the possibility to perform numerical soil-structure interaction analysis which take into account the site effects (i.e. including the geometry of the site and its lithological properties) all of this within a reasonable computational cost. The proposed computational strategy consists in a combination of the acceleration of the boundary element method offered by the fast multipole method to model wave propagation in infinite media and the flexibility of the finite element method to model the structure and materials.

This thesis is organised as follows. Its main contents are divided into six chapters.

This first chapter has introduced the context of site effects and its importance in the soil-structure interaction analysis. The different causes of site effects that are sought to be taken into account in this thesis have been detailed and the different numerical methods to model site effects have been briefly presented. The theoretical aspects of the boundary element method have then been presented, followed by the fast multipole method.

The second chapter is about the evaluation of the impact of the modelling parameters on the accuracy and efficiency of the fast multipole method (FM) in an industrial context. The parameters studied are the acceleration offered by the fast multipole method, compared to the classical BEM, the choice of space discretisation criterion and the impact of the truncation radius of the free-surface on the accuracy of the results and the computational cost. Finally, a method to speed-up the multi-frequency analysis is proposed and results in the time domain are presented by using Fourier synthesis.

The third chapter presents a variational formulation of Soil-Structure Interaction within the scope of application of this work. The chosen strategy for the coupling of *Code_Aster* and *Coffee* is detailed.

The fourth chapter the coupling strategy (i.e., the impedance operator and the seismic forces) is numerically validated. The validation adresses canonical problems of surface and embedded footing in homogeneous basins and basins with a material contrast. The results are compared with reference solutions.

The fifth chapter adresses the use of the proposed coupling to study the impact of site effects on the response of a structure with an embedded cylindrical footing in the case of a soil composed of a hemispherical basin in a homogeneous half-space. The influence of the shape of the hemispherical basin is studied with respect to the velocity ratio, and results are compared to the case of a stratified soil. The impact of the angle of incidence of the waves is then analysed.

The sixth chapter concerns the application of the coupling to a more realistic basin. The chosen basin

is the Grenoble basin, which presents an interesting geometry with a topography, a stratigraphy and a non-planar bedrock. Results for the response of the Grenoble basin to a plane incident wave with and without a structure are presented and discussed.

Chapter 2

Capabilities of the fast multipole accelerated boundary element method to model elastic soils

Contents

2.1. Analysis of the numerical efficiency: benefits of the FM-BEM 24
2.2. Transition between the BEM and the FM-BEM 25
2.3. Choice of the density of points in an industrial context 26
2.4. Effects of the artificial truncation of the free surface 28
2.5. Speed-up of the multi-frequency computations 30
2.6. Fourier synthesis to obtain results in the time domain 31
2.7. Conclusions 33

The FM-BEM for elastodynamics is already developed and implemented in *Coffee* [7]. In this chapter, the impact of the modeling parameters on the accuracy and numerical efficiency of the FM-BEM, in an industrial context, is evaluated. The test case consists of a hemisperical basin embedded in an infinite elastic half-space (Figure 2.1). Both media have the same mechanical characteristics. This models presents two main advantages: (i) analytical solutions for the propagation of plane waves in a homogeneous elastic half-space are known in the time-harmonic domain; (ii) it contains two discretized domains, which offers the possibility to test the multi-domain (piecewise homogeneous) configuration.

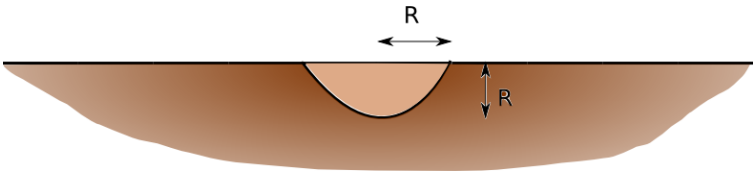

Figure 2.1.: *Hemispherical basin in a elastic half-space.*

This chapter is organised as follows. In Section 2.1, the gain of the fast multipole method compared to the classical boundary element method is quantified, both in term of computational time and memory requirements. The performances are compared to the expected theoretical ones. Since the FM-BEM formulation used here is not suitable for low frequencies, the Section 2.2 aims at defining an empirical criterion to determine the domain of validity of the FMM. In Section 2.3, a meshing criterion for the space discretisation is defined. The criterion is a compromise between an acceptable accuracy and a low computational cost, in an industrial context. The FM-BEM formulation used in *Coffee* is a reformulation of the fundamental solutions of the full-space [7]. To solve a problem of the propagation of a seismic wave in a elastodynamic half-space, the fundamental solution of the half-space which takes into account the free surface in its formulation is either used, or the fundamental solution of the free-space is used but implies the necessity to mesh the free surface far enough to have a model accurate enough. In Section 2.4, the accuracy of different models with different truncation radius of the free surface are compared, to determine the effect of this parameter on the accuracy of the FM-BEM solutions. After determining the optimal parameters to use the FM-BEM, Section 2.5 presents a way to accelerate the solution by taking benefit of the iterative solver. Section 2.6 presents results in the time-domain obtained by a Fourier synthesis.

2.1. Analysis of the numerical efficiency: benefits of the FM-BEM

In the following, the computational costs of BEM and FM-BEM are compared, in terms of time and memory requirements, with respect to the number of degrees of freedom.

Figure 2.2 reports the computational time per iteration to solve the problem of the propagation of a seismic plane wave in the hemispherical domain in an infinite half-space defined in Figure 2.1. In this simplified example, both media have the same mechanical properties ($C_s = 870\ m/s,\ C_p =$

1727 m/s, $\nu = 0.33$). The aim is to compare the efficiency of the FM-BEM and BEM, for an increasing number of degrees of freedom.

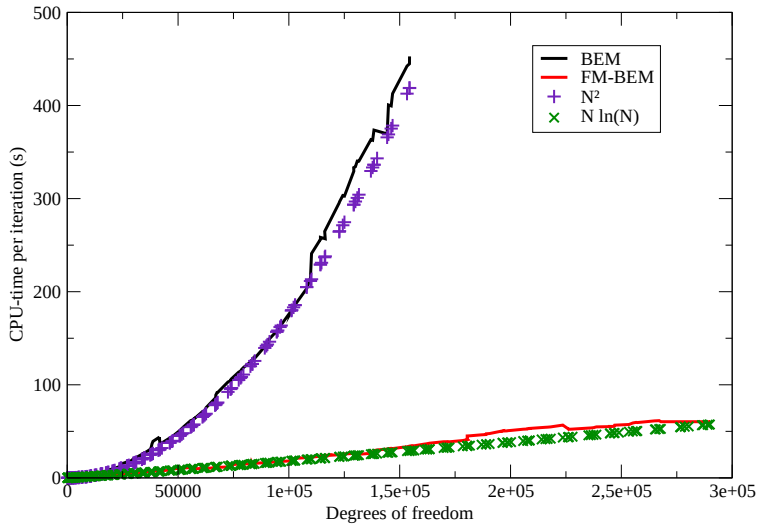

Figure 2.2.: *Computational time per iteration with respect to the number of degrees of freedom for the standard and Fast Multipole accelerated BEM.*

Figure 2.2 shows the impact of the FMM on the computational time. The BEM solution has a theoretical complexity of $\mathcal{O}(N^2)$ per iteration, while the FM-BEM has a complexity of $\mathcal{O}(N \log N)$ per iteration. These theoretical complexities are numerically found as can be seen in Figure 2.2. The use of a BEM solver can easily cost up to ten times more than with the FM-BEM. For problems with more than 30 000 DOFs, the BEM computational cost becomes too important to be viable while the FM-BEM computations can easily exceed 100 000 DOFs. Given that the cost given in the figure 2.2 is relative to a single iteration, the gain in terms of computational time is more important as the number of iterations increases, which is always the case in higher frequencies. It is clear that the FM-BEM is a very interesting alternative to solve seismic wave propagation problems. It allows to solve problems in larger domains or for a larger frequency range.

2.2. Transition between the BEM and the FM-BEM

One of the limitations of the FMM formulation used in this work is that it is not accurate in the low frequency regime due to the divergence of the spherical Hankel functions of the first kind $h_p^{(1)}(k|\underline{r}_0|)$, when $k|\underline{r}_0| \to 0$ (see Section 1.6). In an industrial context, there is a need to determine accurately the transition zone between the BEM and the FM-BEM. The criterion should consist of an empirical non-dimensional frequency to determine where the accuracy of the FM-BEM is acceptable. To assess the accuracy of the FM-BEM, results obtained with FM-BEM are compared to the results obtained with the classical BEM. The reference model used is again a hemispherical basin of radius $R = 100$ m in a homogeneous half-space (Figure 2.1). To simplify this study, both media have the same mechanical characteristics ($C_s = 870\ m/s,\ C_p = 1727\ m/s,\ \nu = 0.33$). Two

configurations are considered: the propagation of incident plane P- or SV-waves.

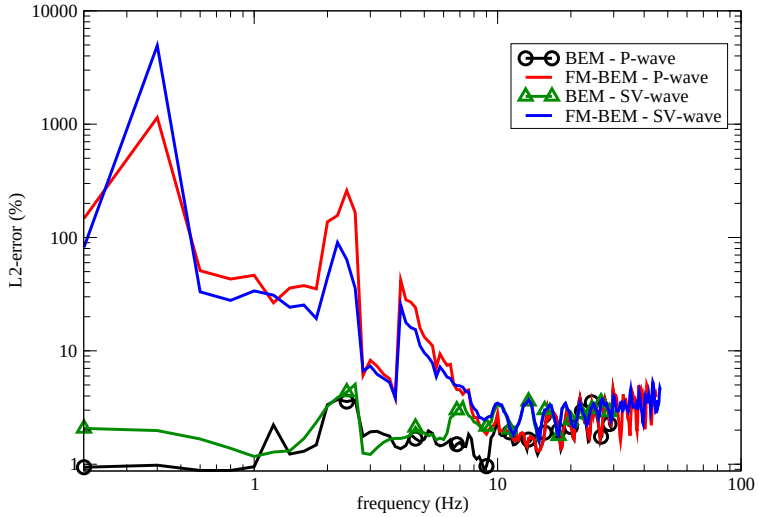

Figure 2.3.: *Relative errors with respect to the analytic solution for the FM-BEM (red and blue lines) and BEM (black and green symbols) to solve incident plane wave propagation problems.*

Relative errors with respect to the analytical solution are plotted in Figure 2.3: red and blue lines if the FM-BEM is used or black and green symbols if the standard BEM is used. It can be noticed that the error of the FM-BEM solver is high up to 7Hz, it can exceed 100% for some frequencies. This is clearly the effect of the divergence of the spherical Hankel functions. For frequencies higher than 7Hz, i.e. $\frac{\lambda_s}{R} = 1.25$ (λ_s being the wavelength of the SV-wave and R being the radius of the hemisphere), the difference of the error between FM-BEM and BEM is smaller than 1%. Throughout the rest of this work, the standard BEM is used for non-dimensional frequencies smaller than $\frac{\lambda_s}{R} = 1.25$.

2.3. Choice of the density of points in an industrial context

The aim of this section is to determine a meshing criterion, i.e. a good compromise between the accuracy of the results and the computational time. The criterion is based on numerical experiments. The reference model used is a hemispherical basin of radius $R = 100$m in a homogeneous half-space (Figure 2.1). Both media have the same mechanical characteristics ($C_s = 870\ m/s,\ C_p = 1727\ m/s,\ \nu = 0.33$). Problems are solved in the time-harmonic domain with the FM-BEM. Each problem is solved for a specific frequency. The frequency range of interest is $[7Hz, 25.Hz]$ with a frequency step $\Delta f = 0.2Hz$. Two levels of discretization are compared: a model where the geometry is meshed with a criterion of six points per S-wavelength and a model where the geometry is meshed with a criterion of ten elements per S-wavelength. The relative error of each model is compared with the analytical solution of an incident vertical plane P- or SV-wave in a homogeneous infinite elastic half-space. The relative errors computed for each model are given in Figure 2.4 for the two meshing criteria.

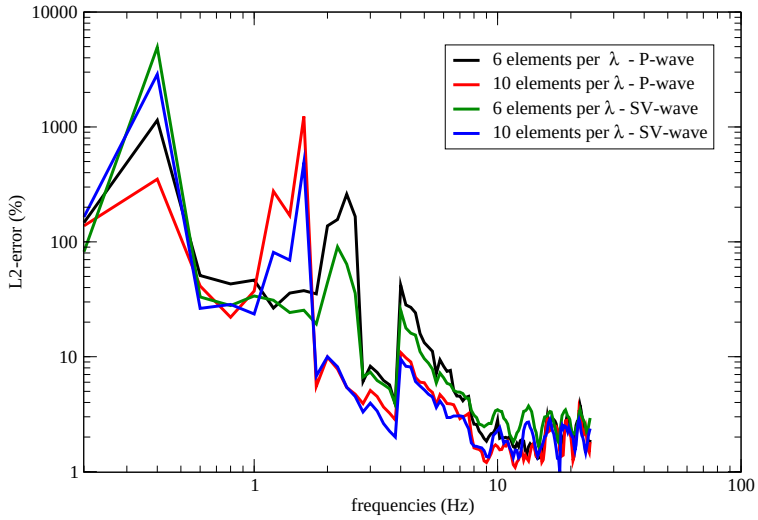

Figure 2.4.: *Relative errors for different meshing criterion.*

In this example, the errors introduced by the FMM for all frequencies are reported even though it was seen that this acceleration method should not be used for low frequencies. Importantly, it is noticed that the discrepancy between the results obtained with the two meshes is always of the order of few percents for the frequencies of interest. However the computation cost is almost double if the density of points goes from six to ten points per S-wavelength (see Figure 2.5). This result is in agreement with the theoretical complexity of the FMM of the order of $\mathcal{O}(N \log N)$. Another interesting remark is that the accuracy or computational time does not depend on the kind of incident plane wave.

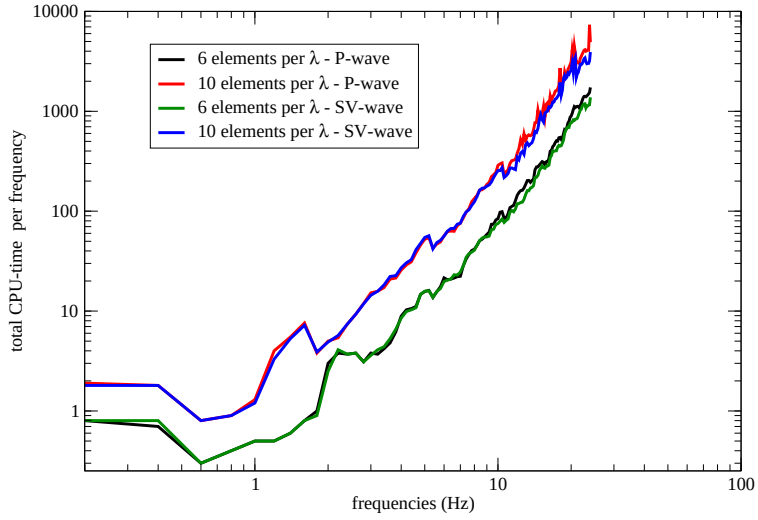

Figure 2.5.: *Total computational time per computation for the two meshing criteria: six or ten points per S-wavelength.*

Finally, if the total computational time depends naturally on the meshing criterion (and thus on the number of degrees of freedom), it seems from Figure 2.6 that the number of iterations depends also

on the frequency but is not sensitive to the number of degrees of freedom. This result is in agreement

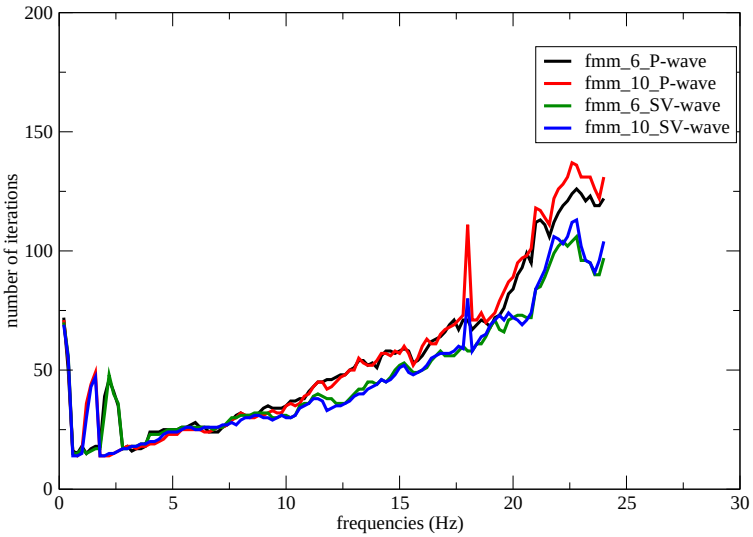

Figure 2.6.: *Number of iterations with respect to the frequency for the two meshing criteria: six or ten points per S-wavelength.*

with theoretical results given by Darbas and Le Louer [23]. In order to avoid the dependency with respect to the frequency, an efficiency preconditioner should be used. But this problem is still an open question in the context of the FMM. The issue is that the system matrix is not assembled to reduce the computational cost and memory requirements. It is thus difficult to define an efficient preconditioner. Tentative to use an algebraic preconditioner using only the small part of the matrix assembled has shown moderate efficiency [12] and cannot remove the dependency to the frequency. On the other hand, analytical preconditioners [10] are extremely efficient but have not yet been proposed for piecewise homogeneous domains.

It can be concluded from these tests that a meshing criterion of six points per S-wavelength is a good compromise between accuracy and computational cost in our industrial context. In the following, this criterion is respected. In addition, since the mechanical parameters of the soil are always polluted with some errors, it is not necessary to spent too much time to obtain an accurate solution to an inaccurate model.

2.4. Effects of the artificial truncation of the free surface

The truncation of the free surface is an important parameter in modelling wave propagation problems using the current FM-BEM formulation, which relies on a reformulation of the fundamental solution of the elastic full space. This would not be an issue if the elastic half-space fundamental solution was used. However the development of an efficient FMM solver is not an easy task (see the preliminary work [8])

To evaluate the impact of the truncation radius on the accuracy of the solution, computations are

performed for the case of a hemispherical domain in an infinite half-space defined in Figure 2.1, subjected to a vertically incident plane P- or SV-wave. Both media have the same mechanical properties ($C_s = 870\ m/s,\ C_p = 1727\ m/s,\ \nu = 0.33$). The frequency range of interest is [0, 2Hz,24Hz], which is equivalent to a S-wave length of range [36, 25m,4350m] . The value of the truncation radius is a function of the radius of the hemisphere. Results for truncation radius values equal to $3R,\ 4R,\ 5R$ are compared to analytical solutions (R being the radius of the hemisphere). Figure 2.7 reports the relative error for each model with respect to the frequency. The error is compared to the analytical solution for the propagation of an incident plane wave in an elastic homogeneous half-space.

The L_2 relative error is computed as

$$\sqrt{\frac{\int_\Gamma (\underline{u}_h - \underline{u}_{ana})^2}{\int_\Gamma \underline{u}_{ana}^2}},$$

where $\underline{u}_h$ is the displacement solution computed by *Coffee*, $\underline{u}_{ana}$ is the analytical displacement solution, and Γ is the boundary interface of the discretised problem.

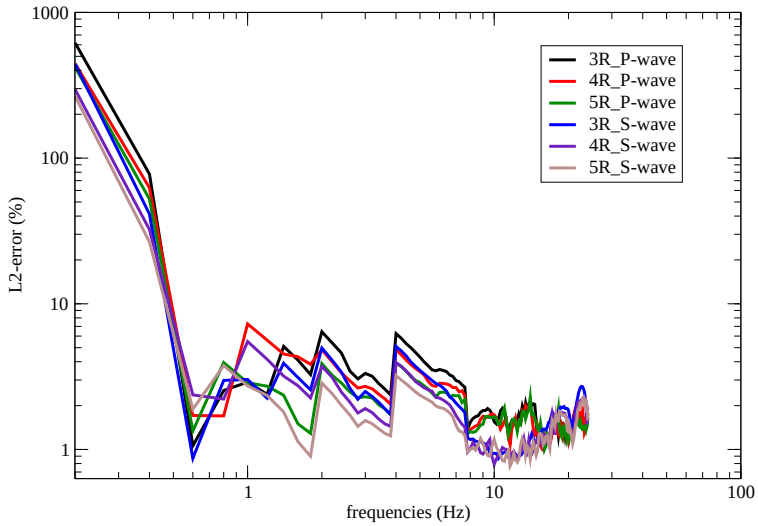

Figure 2.7.: *Relative error for different truncation error.*

Again, the FM-BEM is used for all the frequencies even though it should not be used in the low frequency regime. It would be more accurate (and not very more expensive) to use the standard BEM in that regime. It seems that the truncation radius does not influence much the results.

On the other hand, the increase of the size of the meshed free surface is very expensive in terms of computational time (see Fig. 2.8). Thus, it drastically increases the number of degrees of freedom of the problem. The truncation radius is chosen to be fixed to 4 times the characteristic size of the basin, in order to take into account other effects, such as the velocity contrast and the topography, not modeled in this comparison.

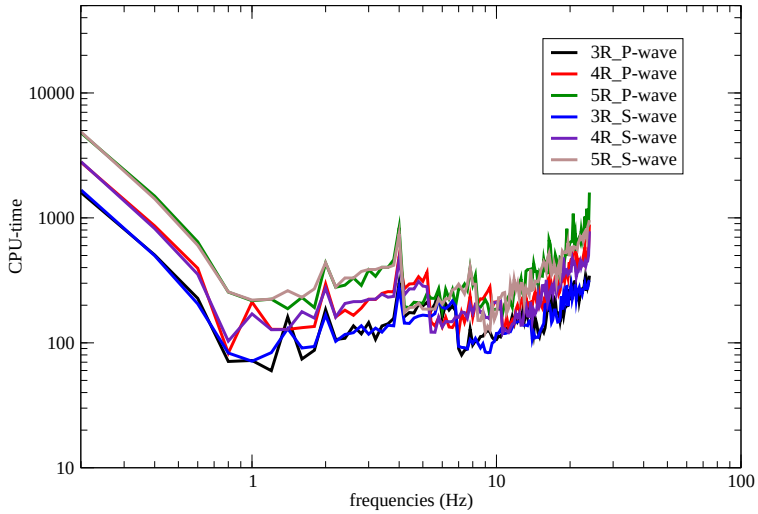

Figure 2.8.: *Total computational time per computation, with respect to the frequency for different size of the free surface.*

2.5. Speed-up of the multi-frequency computations

The FMM is intrinsically based on the use of an iterative solver, GMRES [56] in this work. Since our goal is to obtain results in the time domain with a Fourier synthesis, there is a need to perform many computations in the frequency domain. The use of an iterative solver is an advantage in this context. If a direct solver was used, each solution would be expensive and independent. On the other hand, an iterative solver is very efficient. The main limitation could be the growing number of iterations while the frequency increases. It is proposed to use the solution of the previous computation as an initial guess of the iterative solver while sweeping through the frequencies. This method supposes that, given a small enough frequency step, the solution at any point of the mesh is smooth with respect to the frequency. This method leads to a reduction of the number of iterations and thus a reduction of the computational time. Figure 2.9 reports the number of iterations to converge GMRES to a tolerance of 10^{-3} while activating or not the use of a zero initial guess (red lines) or an appropriate initial guess based on the solution at the previous frequency (black lines). Again, the case of a hemispherical basin of radius $R = 100$ m in a homogeneous half-space (Figure 2.1) is considered. Both media have the same mechanical characteristics ($C_s = 870\ m/s,\ C_p = 1727\ m/s,\ \nu = 0.33$). The slopes presented on Figure 2.9 are probably problem dependent, it is not the important result. The aim of this method is to minimise the computational cost by limiting the increase of the number of iterations increases with the frequency. This preconditioning method allows to run computations with 50 000 DOFs with an average CPU-time of seven minutes per frequency, for a total of 120 frequencies, while the computations without initializations took 35 minutes of CPU-time on average per frequency. Computations were run on the EDF intern cluster "ASTER5".

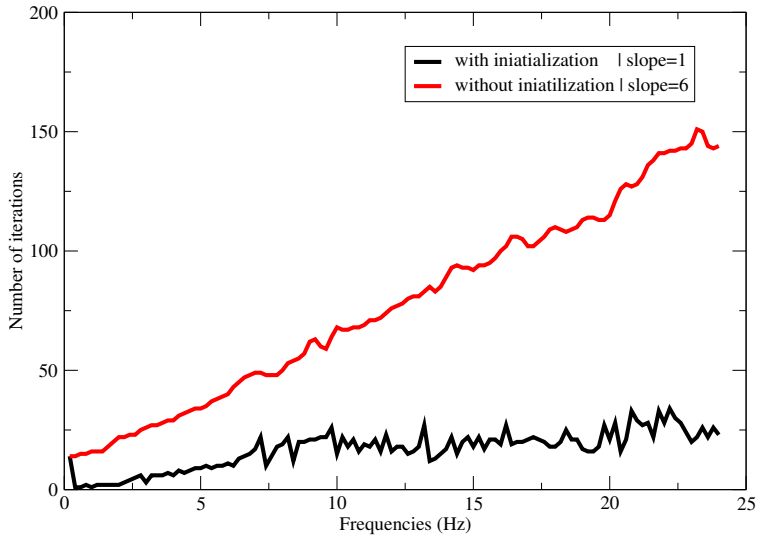

Figure 2.9.: *Impact of the use of an initial guess on the number of iterations.*

2.6. Fourier synthesis to obtain results in the time domain

In the following, the accuracy of the Fourier synthesis to obtain results in the time domain is checked.

Again, the hemispherical basin with radius $R = 80$m (Fig. 2.10) is considered. In agreement with previous numerical evidences, the free surface is truncated at a distance equal to $4R$ and the standard (non-accelerated) BEM is used for the low frequency regime, i.e. frequencies smaller than 7 Hz.

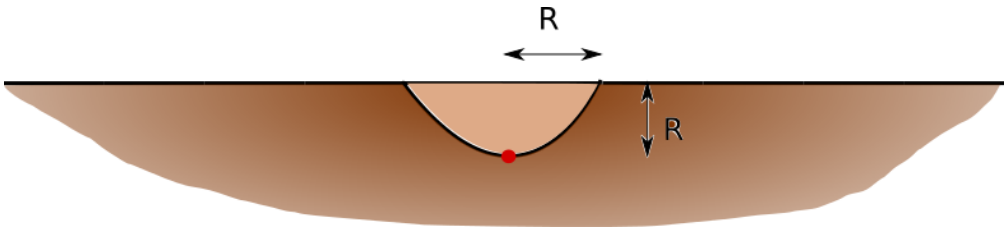

Figure 2.10.: *Test case considered to check the accuracy of the Fourier synthesis to obtain results in the time domain. The point in red corresponds to the point where the surface displacement is evaluated.*

A wave front of plane waves is imposed (Figure 2.11), whose amplitude takes the form of a Ricker signal $\underline{u} = r(t - \frac{z}{c})\underline{e}_z$. The frequency range of interest is set to $[0.2Hz, 19.Hz]$ with a frequency step of $\Delta f = 0.2$ Hz, and a time step $\Delta t = 0.01$ s.

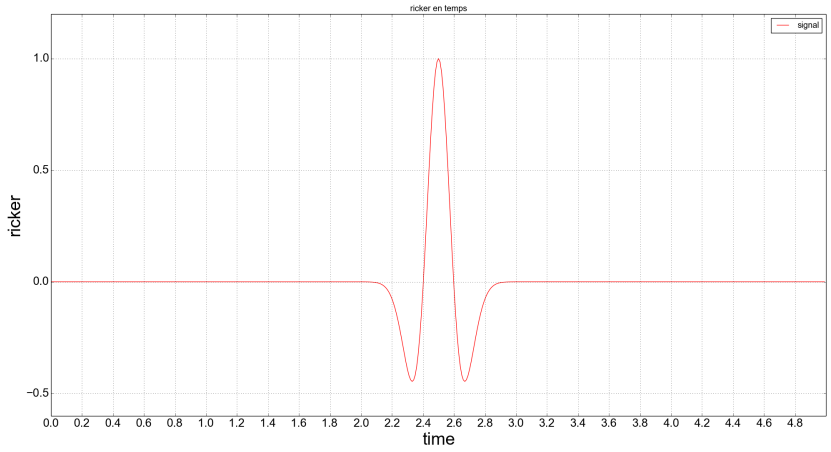

Figure 2.11.: *Input Ricker signal for the Fourier synthesis.*

Figures 2.12 and 2.13 present the vertical displacement obtained with *Coffee* at a point located at a depth equal to $R = 80$ m (Fig. 2.10) and denoted post-processing point in the following. It is compared to the analytical solution of an incident vertical P-wave in a homogeneous medium (see Appendix A).

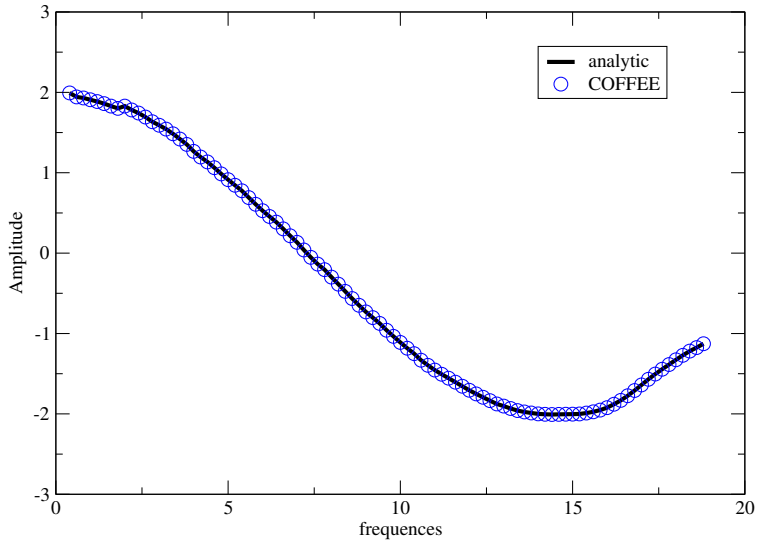

Figure 2.12.: *Amplitude of the vertical displacement at the post-processing with respect to the frequency.*

Figure 2.13 reports the vertical displacement obtained by Fourier synthesis at the post-processing point. The results provided by *Coffee* both in the frequency and in the time domain are in very good agreement with the analytical solution, validating the numerical method.

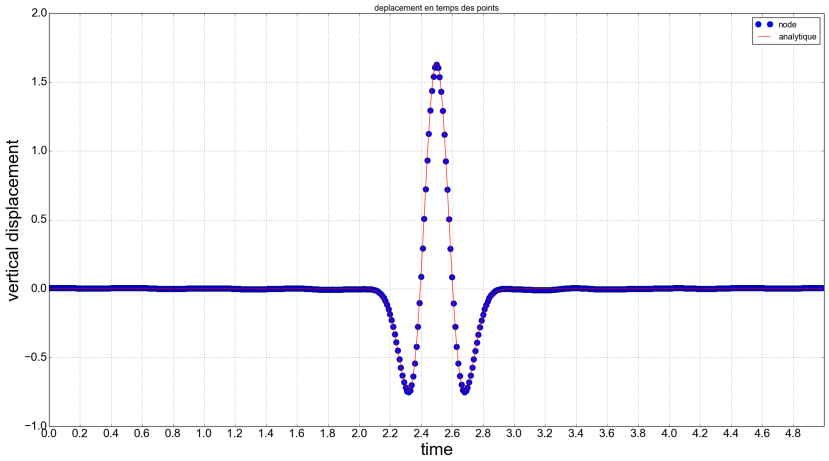

Figure 2.13.: *Amplitude of the vertical displacement at the post-processing point with respect to time.*

2.7. Conclusions

In this chapter, the computational efficiency and accuracy of the FM-BEM to model elastic wave propagation in an industrial context has been checked. The theoretical complexities of the FM-BEM ($\mathcal{O}(N \log N)$) and the standard BEM ($\mathcal{O}(N^2)$) are numerically recovered. The acceleration offered by the FM-BEM allows a way faster solution of problems compared to the standard BEM.

An empirical criterion has been proposed to determine the transition between the BEM and the FM-BEM. This transition is needed because the FMM formulation used in this work is not accurate in the low frequency regime. The criterion retained is $\frac{\lambda_s}{R} = 1.25$ (λ_s being the wavelength of the SV-wave and R the a characteristic length of the model).

In addition, since the FM-BEM is based on a reformulation of the fundamental solutions of the free-space, it is necessity to mesh the free surface. A parametric study on the impact of the truncation radius on the accuracy of the solution has been performed. The retained criterion is to truncate the free surface at a distance equal to four times the characteritic length of the basin.

The FM-BEM relying on an iterative solver, it is taken benefit of. The solution at a given frequency is used as an initial guess for the iterative solution at the next frequency. It has been shown to reduce the number of iterations and to limit the increase of the number of iterations as the frequency increases.

Finally, results in the time-domain obtained by Fourier synthesis have been presented for a simple problem, and compared to the reference solution.

Chapter 3

Fast methods to model Soil-Structure Interaction

Contents

3.1. Coupling between fast BEMs and FEM 36

3.2. Variational formulation of Soil-Stucture Interaction 37

3.3. Efficient computation of Soil-Structure Interaction problems 40

In the previous Chapter, the impact of the use of an accelerated BEM to solve wave propagation in elastodynamic media is assessed in terms of computational efficiency and expected accuracy. The aim of this chapter is to present a strategy of coupling of fast BEM with FEM. Different works that were interested in coupling fast-BEM with FEM for soil-structure interaction or structure–acoustic field interaction are first presented briefly. A variational formulation of Soil-Structure Interaction is then presented within the scope of application of this work. Finally, the chosen strategy for the coupling of *Code_Aster* and *Coffee* is detailed and explained.

3.1. Coupling between fast BEMs and FEM

In this Section are presented different works that aimed to couple fast BEM and FEM. This is not intended to be comprehensive but rather to give an overview of the different approaches for these kind of techniques.

The closest work to this thesis is that of Eva Grasso [32] who proposed an approach to couple the finite element method and the fast-multipole boundary element method to model three-dimensional time-harmonic visco-elastodynamics problems in unbounded domains. The work presented two strategies of coupling the FM-BEM with FEM. The first one is an iterative procedure based on a sequential interface relaxation method, such that at each iteration of the algorithm, a smoothing procedure is applied on the boundary conditions transmitted between the FEM domain and the FM-BEM domain in order to guarantee and speed up the convergence. This method was tested on simple geometries with homogeneous materials. The second developped strategy was a simultaneous approach. The algorithm is based on the fast solution of the BEM global system of equations and by an implicit condensation of the FEM internal degrees of freedom performed at each global iteration of the iterative solver. The simultaneous approach algorithm proved to be stable for models with simple shapes.

Always in the time-harmonic elastodynamics, a coupling of finite element and fast boundary element methods for the solution of dynamic soil–structure interaction problems was proposed in [21]. The application of hierarchical matrices in the boundary element formulation was used to accelerate the resolution of the BEM part in order to allow considering much larger problems compared to classical methods. Three coupling methodologies were presented and their computational performance assessed through numerical examples, namely direct, iterative and monolithic coupling strategies. It was shown that the direct coupling approach was less efficient than the iterative one, as it requires the assembly of a dynamic soil stiffness matrix, while the computation time remained quasi independent of the wave velocity ratio in the case of problems with differents mechanical characteristics between the FEM and BEM parts, but increases with frequency. The computational efficiency of the iterative coupling schemes, on the other hand, showed a much stronger correlation with the wave velocity ratio between materials of the FEM part and the BEM part. The monolithic coupling scheme was also relatively insensitive to the value of the wave velocity ratio, but the overall computational

performance of this methodology showed poor performance compared to the iterative algorithms.

In the domain of the simulation of structure–acoustic field interaction, Fischer and Gaul [28] proposed a coupling algorithm based on Lagrange multipliers [28] in the time-harmonic domain. The resulting system is solved by an iterative procedure in which the matrix–vector products of the boundary element operators are evaluated efficiently by the fast multipole boundary element method, the presented mortar coupling algorithm for structure–acoustic field interaction allowing the coupling of non-conforming discretizations. This method was tested on canonical examples and compared to an analytic series solution, giving satisfactory results. The method was also tested on a practical case of the vibration of a box made from steel sheets in a water pool and compared to experimental results, showing good correlation between the principal behaviour of simulation and experiment, with noticeable differences between numerical and experimental results.

In the following, a method for coupling boundary element method accelerated by fast multipole method with finite element method is presented. The choice is made to use *Coffee* for the FM-BEM part and *Code_Aster* for the FEM part, the aim being to choose the least intrusive method of coupling in terms of changes in both codes.

3.2. Variational formulation of Soil-Stucture Interaction

Soil-Structure Interaction problems can be solved either by a monolithic approach [41] which consists in applying a single approach (generally the finite element method) to the complete problem and thus necessitating to use a non-reflecting boundary condition in the soil to ensure the radiation condition. Alternatively, a substructuring approach [16, 49] (which is similar to a domain decomposition method) can be applied, where the whole computational domain is subdivided into several subdomains, which allows to apply in each subdomain the method that is best suited to it.

In this work, the latter method is used. In the present case of Soil-Structure Interaction problems, the subdomains are in general (a) a bounded domain Ω_b containing the building and possibly a portion of the soil (surrounding close-range environment) and (b) an unbounded domain (the soil modelled as a linear elastic medium). The two domains are connected through the shared interface Γ (Fig. 3.1). Moreover, the unbounded domain Ω_s is assumed to coincide with a homogeneous elastic half-space Ω_0 having a planar boundary Γ_0 except possibly in a finite neighbourhood of Ω_b (so that in particular the surfaces Γ_s and Γ_0 coincide except possibly in a finite region). It is then natural to use the finite element method (FEM) to model the bounded domain Ω_b and boundary element method (BEM) to model the unbounded domain Ω_s.

So far within EDF, the subregion approach for solving SSI problems was implemented by means of the code Miss3D, developped during the PhD thesis of D. Clouteau [16], for solving wave propagation problems by using the boundary element method, coupled with *Code_Aster*.

In this work, an association of *Code_Aster* with an accelerated fast multipole BEM is proposed,

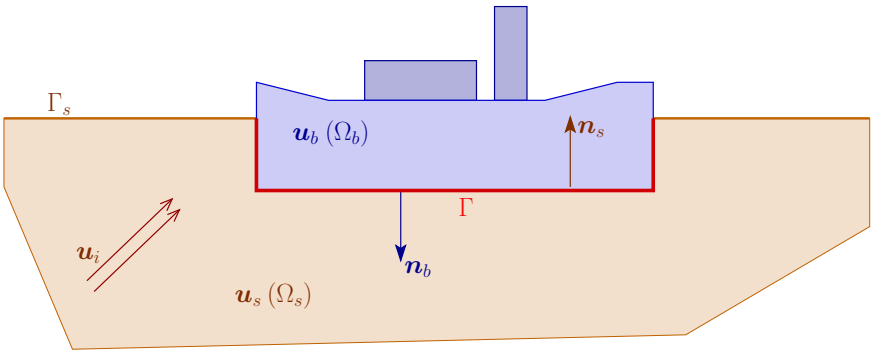

Figure 3.1.: *Subdomain method: schematic and notation.*

using for that purpose the code *Coffee* that resulted from S. Chaillat's thesis [7]. The aim is to exceed the well-known limitations, in terms of memory requierement and computational time, of non-accelerated BEM solvers, such as Miss3D, induced by the fully-populated nature of the integral operators in the classical BEM.

The finite element approximation of Ω_b is based on the following weak formulation, written in the frequency domain:

$$\int_{\Omega_b} \boldsymbol{\sigma}_b(\boldsymbol{u}_b) : \boldsymbol{\varepsilon}(\boldsymbol{w}) dV - \omega^2 \int_{\Omega_b} \rho_b \boldsymbol{u}_b . \boldsymbol{w} dV = F(\boldsymbol{w}) + \langle \boldsymbol{t}_{\boldsymbol{n}_b}(\boldsymbol{u}_b), \boldsymbol{w} \rangle_\Gamma, \quad \forall \boldsymbol{w} \in \mathcal{W} \tag{3.1}$$

where $\boldsymbol{u}_b$ is the displacement vector in Ω_b, $\mathcal{W}$ is the space of kinematically admissible virtual displacements in Ω_b, $\boldsymbol{\sigma}_b(\boldsymbol{u}_b)$ is the stress tensor associated to $\boldsymbol{u}_b$ by means of the chosen constitutive model in Ω_b, and $\boldsymbol{t}_{\boldsymbol{n}_b}$ represents the stress vector relative to Ω_b on Γ ($\boldsymbol{t}_{\boldsymbol{n}_b}(\boldsymbol{u}_b) = \boldsymbol{\sigma}_b(\boldsymbol{u}_b).\boldsymbol{n}_b$). The linear functional $F : \mathcal{W} \to \mathbb{R}$ synthesizes all loadings applied to Ω_b outside of the interface Γ.

The field $\boldsymbol{u}_s$ in Ω_s, corresponding to the displacement in the soil, satisfies the homogeneous equation of elastodynamics $\mathrm{div}\,(\boldsymbol{\sigma}_s(\boldsymbol{u}_s)) + \rho_s \omega^2 \boldsymbol{u}_s = \boldsymbol{0}$ (the constituve relation $\boldsymbol{u}_s \to \boldsymbol{\sigma}_s(\boldsymbol{u}_s)$ assumed to be linear elastic), as well as the free surface condition $\boldsymbol{t}_{\boldsymbol{n}_s}(\boldsymbol{u}_s) = \boldsymbol{0}$ on Γ_0 ($\Gamma_0 = \partial\Omega_s \setminus \Gamma$). The kinematic and dynamic compatibility conditions linking the solutions in both domains Ω_s and Ω_b are the transmission conditions

$$\boldsymbol{u}_b = \boldsymbol{u}_s, \quad \boldsymbol{t}_{\boldsymbol{n}_b}(\boldsymbol{u}_b) + \boldsymbol{t}_{\boldsymbol{n}_s}(\boldsymbol{u}_s) = \boldsymbol{0} \qquad \text{on } \Gamma.$$

To solve the above-described coupled problem, the displacement in Ω_s is additively decomposed as $\boldsymbol{u}_s = \boldsymbol{u}_i + \boldsymbol{u}_r + \boldsymbol{u}_c$, where:

(i) $\boldsymbol{u}_i$ is a given incident field, which implies that it is solution of the equation $\mathrm{div}\,(\boldsymbol{\sigma}_s(\boldsymbol{u}_i)) + \rho_s \omega^2 \boldsymbol{u}_i = \boldsymbol{0}$ in Ω_0 (in the absence of any lithologic or topographic perturbation), satisfying $\boldsymbol{t}_{\boldsymbol{n}_s}(\boldsymbol{u}_i) = \boldsymbol{0}$ on Γ_0.

(ii) $\boldsymbol{u}_r$ satisfies $\mathrm{div}\,(\boldsymbol{\sigma}_s(\boldsymbol{u}_r)) + \rho_s \omega^2 \boldsymbol{u}_r = \boldsymbol{0}$ in Ω_s, $\boldsymbol{u}_i + \boldsymbol{u}_r = \boldsymbol{0}$ on Γ and $\boldsymbol{t}_{\boldsymbol{n}_s}(\boldsymbol{u}_r) = \boldsymbol{0}$ on Γ_s; this field represents the diffraction of the incident field $\boldsymbol{u}_i$ due to lithologic and topographic

perturbations, and depends linearly on the trace of $\boldsymbol{u}_i$ on Γ through the above equations.

(iii) $\boldsymbol{u}_c$ is the radiated displacement in Ω_s resulting from the motion of Ω_b, transmitted through the interface Γ: the condition $\boldsymbol{u}_i + \boldsymbol{u}_r = \boldsymbol{0}$ on Γ imply that the trace of $\boldsymbol{u}_b$ and $\boldsymbol{u}_c$ on Γ are equal.

The term $\langle \boldsymbol{t}_{\boldsymbol{n}_b}(\boldsymbol{u}_b), \boldsymbol{w}\rangle_\Gamma$ in (3.1) is now expanded by taking into account the decomposition of $\boldsymbol{u}_s$ and the compatibility of the solutions between Ω_s and Ω_b:

$$\begin{aligned}\langle \boldsymbol{t}_{\boldsymbol{n}_b}(\boldsymbol{u}_b), \boldsymbol{w}\rangle_\Gamma = -\langle \boldsymbol{t}_{\boldsymbol{n}_s}(\boldsymbol{u}_s), \boldsymbol{w}\rangle_\Gamma = -\langle \boldsymbol{t}_{\boldsymbol{n}_s}(\boldsymbol{u}_i + \boldsymbol{u}_r), \boldsymbol{w}\rangle_\Gamma - \langle \boldsymbol{t}_{\boldsymbol{n}_s}(\boldsymbol{u}_c), \boldsymbol{w}\rangle_\Gamma \\ = \langle \boldsymbol{f}_s, \boldsymbol{w}\rangle_\Gamma - \langle \boldsymbol{t}_{\boldsymbol{n}_s}(\boldsymbol{u}_c), \boldsymbol{w}\rangle_\Gamma, \quad (3.2)\end{aligned}$$

having introduced the *seismic force density* $\boldsymbol{f}_s := -\boldsymbol{t}_{\boldsymbol{n}_s}(\boldsymbol{u}_i + \boldsymbol{u}_r)$ on Γ resulting from the incident field. This seismic force reflects the presence of a given incident field $\boldsymbol{u}_i$ in Ω_s: it depends linearly on $\boldsymbol{u}_i$, and thus in particular vanishes if $\boldsymbol{u}_i = \boldsymbol{0}$.

The auxilliary problem defining the field $\boldsymbol{u}_s = \boldsymbol{u}_s[\boldsymbol{v}]$ in Ω_s resulting from a prescribed displacement $\boldsymbol{v}$ on the interface is introduced as well:

$$\operatorname{div}(\boldsymbol{\sigma}_s(\boldsymbol{u}_s)) + \rho_s\omega^2\boldsymbol{u}_s = \boldsymbol{0} \ \text{ (in } \Omega_s), \quad \boldsymbol{t}_{\boldsymbol{n}_s}(\boldsymbol{u}_s) = \boldsymbol{0} \ \text{ (on } \Gamma_s), \quad \boldsymbol{u}_s = \boldsymbol{v} \ \text{ (on } \Gamma). \tag{3.3}$$

With this definition, we have in particular that $\boldsymbol{u}_r = -\boldsymbol{u}_s[\boldsymbol{u}_i]$. The computation of the seismic force $\boldsymbol{f}_s$ then requires the solution of (3.3) with $\boldsymbol{v} = -\boldsymbol{u}_i$.

The force density $\boldsymbol{t}_{\boldsymbol{n}_s}(\boldsymbol{u}_s[\boldsymbol{v}])$ created on Γ by $\boldsymbol{u}_s[\boldsymbol{v}]$ depends linearly on the displacement data $\boldsymbol{v}$. Accordingly, let $\mathcal{Z}$ be the linear impedance operator such that

$$\boldsymbol{t}_{\boldsymbol{n}_s}(\boldsymbol{u}_s[\boldsymbol{v}]) = \mathcal{Z}(\omega)\boldsymbol{v} \qquad \text{on } \Gamma. \tag{3.4}$$

The operator $\mathcal{Z}(\omega)$ operates the condensation of the unbounded soil region Ω_s on the interface Γ.

With these definitions, and since $\boldsymbol{u}_b = \boldsymbol{u}_c$ on Γ, (3.2) becomes

$$\langle \boldsymbol{t}_{\boldsymbol{n}_b}(\boldsymbol{u}_b), \boldsymbol{w}\rangle_\Gamma = \langle \boldsymbol{f}_s, \boldsymbol{w}\rangle_\Gamma - \langle \mathcal{Z}(\omega)\boldsymbol{u}_b, \boldsymbol{w}\rangle_\Gamma. \tag{3.5}$$

Equation (3.1) can be rewritten, by incorporating (3.5), in the condensed form

$$\mathcal{K}(\boldsymbol{u}_b, \boldsymbol{w}) + \omega^2\mathcal{M}(\boldsymbol{u}_b, \boldsymbol{w}) + \langle \mathcal{Z}(\omega)\boldsymbol{u}_b, \boldsymbol{w}\rangle_\Gamma = F(\boldsymbol{w}) + \langle \boldsymbol{f}_s, \boldsymbol{w}\rangle_\Gamma. \tag{3.6}$$

An approximation space in the form of $\mathcal{W}_h = Vect\big((\boldsymbol{\Phi}_i)_{1\le i\le n}\,,\, (\boldsymbol{\Psi}_j)_{1\le j\le m} \big) \subset \mathcal{W}$ is then considered, such that each (vector) basis function $\boldsymbol{\Phi}_i$ has a vanishing trace on Γ. To evaluate the contribution of $\langle \boldsymbol{t}_{\boldsymbol{n}_b}(\boldsymbol{u}_b), \boldsymbol{w}\rangle_\Gamma$ to the weak formulation (3.1), we approximate $\boldsymbol{u}_b$ on Γ as $\boldsymbol{u}_b = \sum_j u_b^j \boldsymbol{\Psi}_j$, while

virtual displacements $\boldsymbol{w}$ are chosen as $\boldsymbol{w} = \boldsymbol{\Psi}_k$ $(1 \leq k \leq m)$, which gives

$$\langle \mathcal{Z}(\omega)\boldsymbol{u}_b, \boldsymbol{w}\rangle_\Gamma = \sum_j u_b^j \langle \boldsymbol{t}_{\boldsymbol{n}_s}(\boldsymbol{\Psi}_j), \boldsymbol{\Psi}_k\rangle_\Gamma = \sum_j u_b^j \langle \mathcal{Z}\boldsymbol{\Psi}_j, \boldsymbol{\Psi}_k\rangle_\Gamma = \sum_j u_b^j Z_{kj}, \tag{3.7}$$

which defines the coefficients Z_{kj} of the projection of the impedance operator $\mathcal{Z}$ on the subspace $Vect\big((\boldsymbol{\Psi}_i)_{1\leq i\leq m}\big)$, and

$$\langle \boldsymbol{f}_s, \boldsymbol{w}\rangle_\Gamma = \langle \boldsymbol{f}_s, \boldsymbol{\Psi}_k\rangle_\Gamma = \langle -\boldsymbol{t}_{\boldsymbol{n}_s}(\boldsymbol{u}_i + \boldsymbol{u}_r), \boldsymbol{\Psi}_k\rangle_\Gamma = f_{sk}, \tag{3.8}$$

which defines the coefficients f_{sk} asociated with the corresponding projection of the seismic force $\boldsymbol{f}_s$.

The evaluation of the coefficients Z_{kj} requires the solution of m problems (3.3) corresponding to $\boldsymbol{v} = \boldsymbol{\Psi}_i$ $(1 \leq i \leq m)$.

The numerical resolution of the weak formulation (3.6) by the finite element method requires the computation of the impedance operator $\mathcal{Z}$ and the seismic force $\boldsymbol{f}_s$ projected on $\mathcal{W}_h$, which means that the Z_{kj} coefficients defined by (3.7) and f_{sk} coefficients defined by (3.8) have to be evaluated numerically. This entails the numerical solution of $m+1$ problems of the type (3.3) in Ω_s. In this work, the choice is made to solve these problems with the fast multipole accelerated boundary element method, which is well adapted to the modelling of infinite media and applicable to cases where the finite element discretization of Ω_b would generate a high number of degrees of freedom on Γ.

3.3. Efficient computation of Soil-Structure Interaction problems

As it was concluded in Section 3.2, a substructuring method was used to solve the problem through the computation of the impedance operator and the seismic force. The computation of those requieres the construction of an approximation space in the form of $\mathcal{W}_h = Vect\big((\boldsymbol{\Phi}_i)_{1\leq i\leq n}\,,\,(\boldsymbol{\Psi}_j)_{1\leq j\leq m}\big)$, such that $\boldsymbol{\Phi}_i$ is equal to zero on Γ.

For an efficient resolution of the soil-structure interaction problem, the approximation space $\mathcal{W}_h$ must be optimal. One way of ensure this is to reduce the number of the $m+1$ required computations of problems of the type (3.3), with the construction of a reduced basis of the problem through a Rayleigh-Ritz procedure [43].

There are different methods to solve dynamic substructuring method through a reduced basis based of a Rayleigh-Ritz procedure, such as the method proposed by Macneal [44] where the reduction basis consists of free interface modes to represent the dynamics inside the substructure and the attachment modes which are the response of the substructure corresponding to a unit force applied at the interface, but also the method proposed by Craig and Bampton [1], the dynamics inside the substructure are defined with a fixed interface condition, completed with the constraint modes

which consists of producing a unit displacement for one degree of freedom of the interface at a time, the others being blocked. The reduced Craig-Bampton basis produces nearly diagonal matrices and thus leads to an efficient method to solve problems with the finite element method [24].

In the construction of $\mathcal{W}_h = Vect\big((\mathbf{\Phi}_i)_{1\leq i\leq n}\,,\, (\mathbf{\Psi}_j)_{1\leq j\leq m} \big)$, the vectors $\mathbf{\Phi}_i$ are null at the interface. The Craig-Bampton method is compatible with this condition and the choice is made to use it to build the approximation space $\mathcal{W}_h$. The reduced basis is then composed of dynamic modes $(\mathbf{\Phi}_i)_{1\leq i\leq n}$ built on the eigenmodes of Ω_b with a fixed interface Γ, and of constraint modes $(\mathbf{\Psi}_j)_{1\leq j\leq m}$ which describes the interface kinematics with producing each time a unit displacement for each degree of freedom and blocking the others. Consequently, there are as many constraint modes m as degrees of freedom in the interface. Even if this method reduces the size of the approximation space $\mathcal{W}_h$, the number of degrees of freedom at the interface Γ can be large, and thus makes the computation of the impedance and the seismic forces costly and potentially leads to a large discrezized impedance operator. The strategy consisis then in reducing the size of $\mathcal{W}_h$ while focusing on building a reduced basis of the constraint modes. The reduced basis of the constraint modes will be computed as the eigenmodes of the dynamic system composed of the stiffness and mass matrix condensated at the DOFs of the interface [5].

In conclusion, the SSI problem can be solved with a substructuring method through a Craig-Bampton procedure. The domain Ω_b is modelled with the FEM though *Code_Aster*, and an approximation space is constructed based on a reduced basis composed of dynamic modes $(\mathbf{\Phi}_i)_{1\leq i\leq n}$ and constraint modes $(\mathbf{\Psi}_j)_{1\leq j\leq m}$. The impedance operator and the seismic forces are then computed by solving $m+1$ problem of type (3.3) in Ω_s with FM-BEM through *Coffee*. In the following diagram, the procedure of coupling *Code_Aster* with *Coffee* is schematically explained.

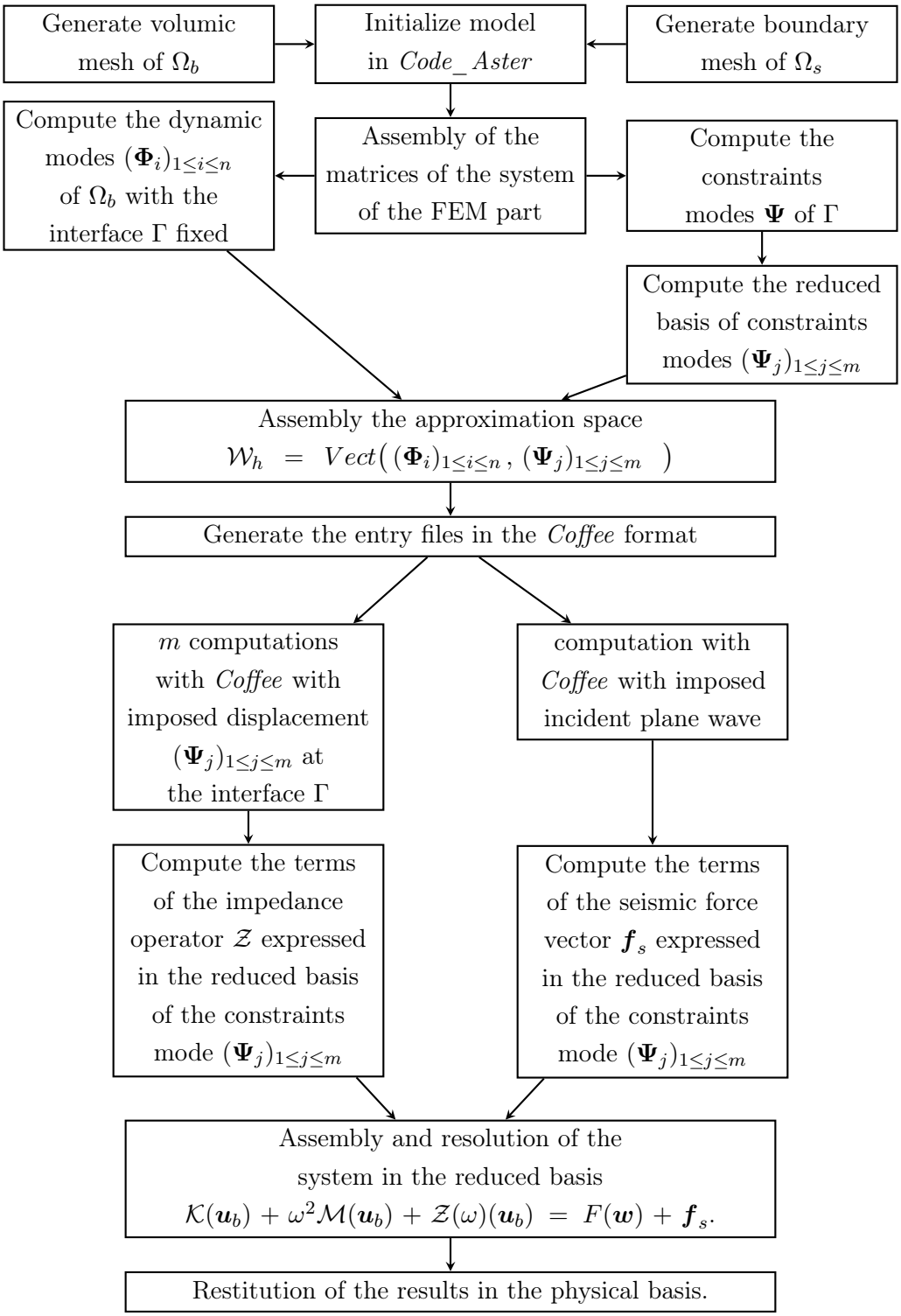
Generate volumic mesh of Ω_b
Initialize model in *Code_Aster*
Generate boundary mesh of Ω_s
Compute the dynamic modes $(\mathbf{\Phi}_i)_{1\leq i\leq n}$ of Ω_b with the interface Γ fixed
Assembly of the matrices of the system of the FEM part
Compute the constraints modes $\mathbf{\Psi}$ of Γ
Compute the reduced basis of constraints modes $(\mathbf{\Psi}_j)_{1\leq j\leq m}$
Assembly the approximation space $\mathcal{W}_h = Vect\big((\mathbf{\Phi}_i)_{1\leq i\leq n}, (\mathbf{\Psi}_j)_{1\leq j\leq m}\big)$
Generate the entry files in the *Coffee* format
m computations with *Coffee* with imposed displacement $(\mathbf{\Psi}_j)_{1\leq j\leq m}$ at the interface Γ
computation with *Coffee* with imposed incident plane wave
Compute the terms of the impedance operator $\mathcal{Z}$ expressed in the reduced basis of the constraints mode $(\mathbf{\Psi}_j)_{1\leq j\leq m}$
Compute the terms of the seismic force vector $\boldsymbol{f}_s$ expressed in the reduced basis of the constraints mode $(\mathbf{\Psi}_j)_{1\leq j\leq m}$
Assembly and resolution of the system in the reduced basis $\mathcal{K}(\boldsymbol{u}_b) + \omega^2\mathcal{M}(\boldsymbol{u}_b) + \mathcal{Z}(\omega)(\boldsymbol{u}_b) = F(\boldsymbol{w}) + \boldsymbol{f}_s.$
Restitution of the results in the physical basis.

Chapter 4

Validation of the impedance operator and seismic force for reference case studies

Contents

4.1. Evaluation of the impedance operator in the case of a homogeneous half-space 44

4.1.1. Mode basis considered: rigid body modes 45

4.1.2. Numerical validations: circular surface footing on a homogeneous elastic half-space 45

4.1.3. Numerical validation: impedance for an interface in a bounded domain . . 52

4.1.4. Numerical validation: embedded cylindrical footing in a homogeneous half-space 53

4.2. Impedance operator for hemispherical basin in half-space with material contrasts 59

4.2.1. Circular surface footing 61

4.2.2. Embedded cylindrical footing 68

4.3. Seismic force for a homogeneous basin 71

4.3.1. Circular surface footing 72

4.4. Seismic force in the case of a heterogeneous basin 73

4.4.1. Circular surface footing 74

4.4.2. Embedded cylindrical footing 76

4.5. Conclusion 77

The aim of this chapter is to validate the evaluation of impedance operator and the seismic force with the FM-BEM (see Chapter 3). Two cases are addressed: the case when the hemispherical basin and the half-space have the same mechanical properties (i.e. homogeneous half-space), and the case where there is a contrast of two between the wave velocity of the hemispherical basin and the homogeneous half-space. The terms of the impedance operator for a circular surface footing and an embedded cylindrical footing in a homogeneous half-space are first compared to other references in Section 4.1. The impedance for a circular surface footing and an embedded footing in a medium composed of a hemispherical basin in a homogeneous half-space are then presented in Section 4.2. These results are compared to impedances computed with the FEM (i.e. *Code_Aster*). The validation of the seismic force is addressed in Section 4.3. Seismic forces computed with FM-BEM in the case of a circular footing are compared to results computed with the standard BEM. In Section 4.4, seismic forces computed with the FM-BEM in the case of a surface circular footing or an embedded cylindrical footing in a medium composed of a hemispherical basin in a homogeneous half-space are compared to seismic forces computed with the FEM.

4.1. Evaluation of the impedance operator in the case of a homogeneous half-space

The impedance operator (Section 3.2) is computed numerically using the FM-BEM in the case of a surface or an embedded footing (Figure 4.1). In the following, the numerical results obtained with FM-BEM are compared to reference numerical solutions available in the literature, namely impedance operators from the book *Manuel des fonctions d'impédance* of Sieffert and Cevaer [60] and the validation test cases of the standard BEM code Miss3D [17]. These solutions are already used at EDF, and considered as accurate solutions, available as Verification & Validation test cases for *Code_Aster*. Note that these are only reference approximate solutions, not exact analytic solutions.

Figure 4.1.: *Illustration of the two configurations considered for the validation of the impedance operator for a homogeneous half-space: surface (right) and embedded (left) footings.*

The impedances are plotted against the non-dimensional circular frequency defined by $a_0 = \omega R/C_s$, where C_s is the S-wave velocity, ω the angular frequency and R the radius of the footing.

4.1.1. Mode basis considered: rigid body modes

Throughout Section 4.1, only rigid body modes of the footing are taken into account. They consist in kinematically admissible displacements with no deformation of the footing: the three possible translations and the three rotations for an underformable body. More precisely, the following rigid body modes are considered:

- Horizontal mode: displacement along the horizontal axis $\underline{e}_x$ or $\underline{e}_y$. All the degrees of freedom of the footing are blocked except the horizontal direction ($\underline{e}_x$ or $\underline{e}_y$) where a unit displacement is imposed (Figure 4.2a);
- Vertical mode: displacement along the vertical axis $\underline{e}_z$. All the degrees of freedom of the footing are blocked except the vertical direction where a unit displacement is imposed (Figure 4.2b);
- Rocking mode: unit rotation of the undeformable footing around the horizontal axes $\underline{e}_x$ or $\underline{e}_y$ (Figure 4.2c);
- Torsion mode: unit rotation of the undeformable footing around the vertical axis $\underline{e}_z$ (Figure 4.2d).

In the following, results obtained with FM-BEM are validated with respect to the reference solutions by comparing the values of the impedance operator projected on a reduced basis composed of these rigid body modes [22]. Only the diagonal terms are presented.

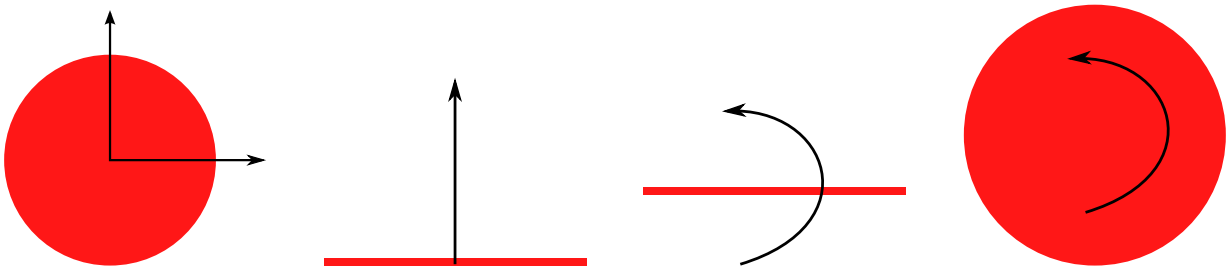

(a) *horizontal mode* ***(b)*** *vertical mode* ***(c)*** *rocking mode* ***(d)*** *torsion mode*

Figure 4.2.: *Illustration of the rigid body modes of a circular surface footing.*

4.1.2. Numerical validations: circular surface footing on a homogeneous elastic half-space

The case of a circular surface footing is considered. The footing has a radius of $R = 0.5m$ (Figure 4.3), the free surface is truncated at a distance equal to $4R$. The mechanical properties of the soil are: $\mu = 1.\ (N/m^2)$, $\rho = 1.\ (kg/m^3)$, $\nu = 0.33$. The frequency range of interest is [0.05Hz, 1.6Hz], such that $a_0 \in [0.15,\ 5.02]$.

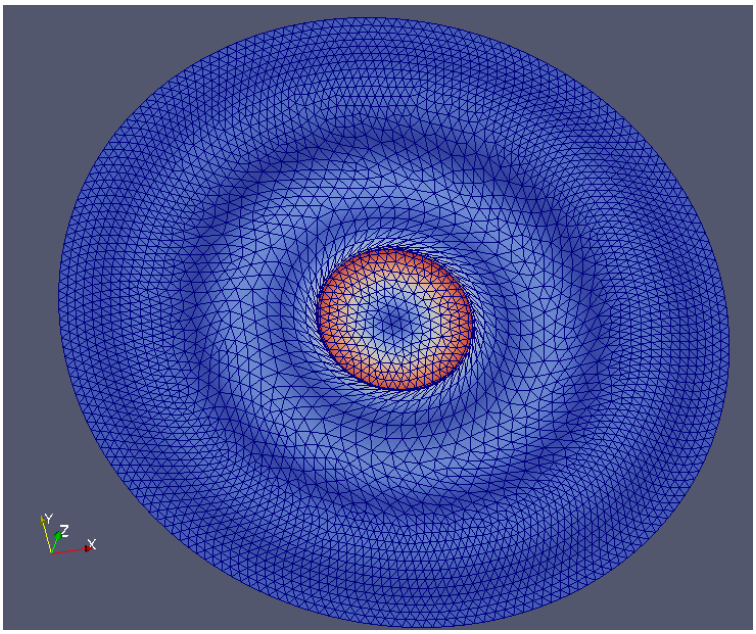

Figure 4.3.: *Example of a mesh of a surface circular footing on a homogeneous half-space.*

Table 4.1.: *Static stiffness of a circular surface footing of radius R on a homogeneous half-space of Poisson's ratio ν.*

Mode	Vertical	Horizontal	Rocking	Torsion
Static stiffness	$K_{33} = \frac{4\mu R}{1-\nu}$	$K_{11} = \frac{8\mu R}{2-\nu}$	$K_{44} = \frac{8\mu R^3}{3(1-\nu)}$	$K_{66} = \frac{16\mu R^3}{3}$

The impedance operator (Eq 3.7) values presented in the following are normalized by the static stiffness (see Table 4.1) relevant for each body mode of the interface, the purpose being to compare simulations performed with different configurations (i.e. material properties and dimensions). In the book *Manuel des fonctions d'impédance* and in Miss3D, the same quantities are used to obtain non-dimensional impedances. The values of the impedance operator being complex numbers, the real part, imaginary part, modulus and argument of these complex numbers are presented in Figures 4.4, 4.5, 4.6 and 4.7. It is known that the imaginary part of the impedance for both the rocking and torsion modes stands for the radiation damping caused by the energy dissipation of the radiated displacement resulting from the motion of the structure.

For the case of the horizontal mode, the results obtained with *Coffee* are close to both references (Figure 4.4). Nevertheless, oscillations are observed in the real part of the solution obtained with *Coffee*. These oscillations are less apparent in the imaginary part, the modulus and the argument, mainly due to the scale factor. The oscillations would be then much more apparent if the figures were normalized by the maximum value of each parameter.

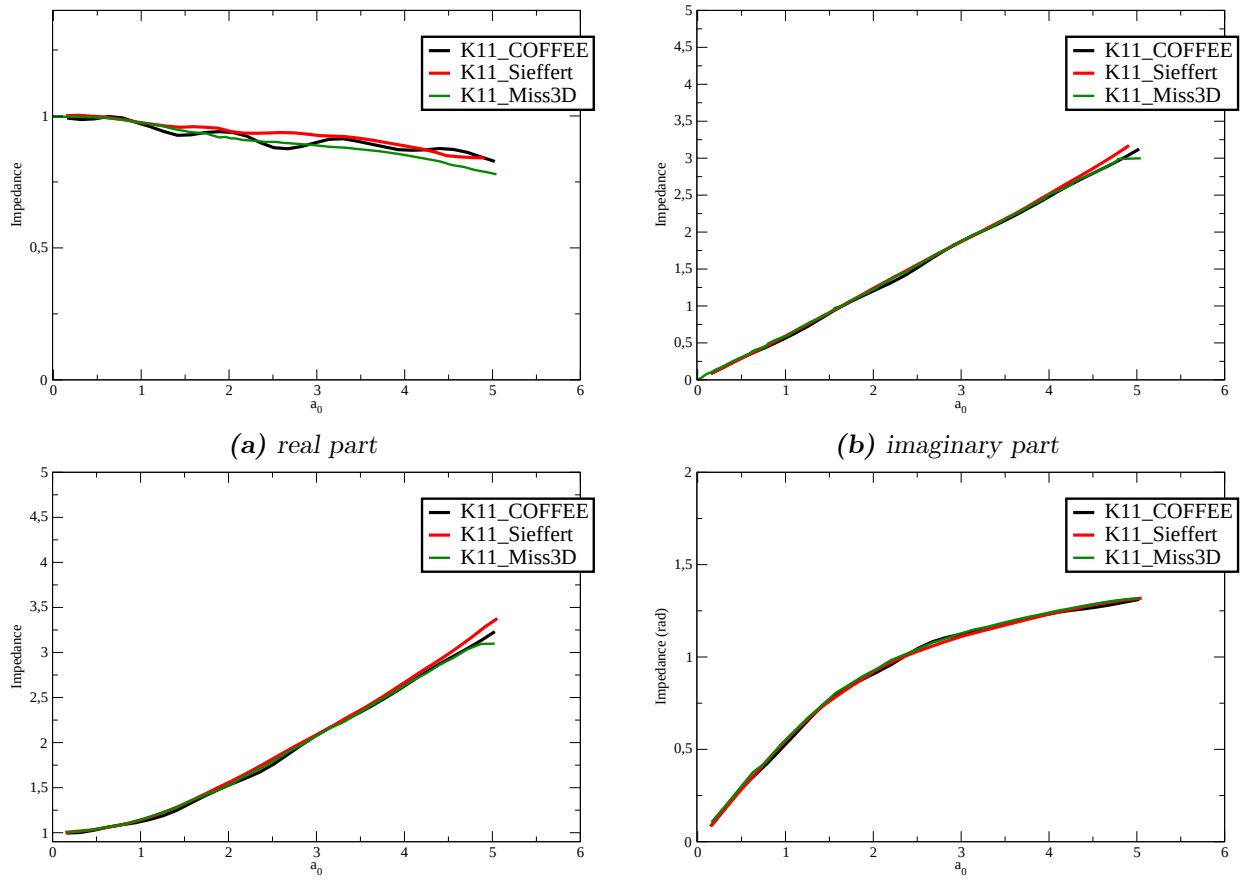

(a) *real part* ***(b)*** *imaginary part*

(c) *modulus* ***(d)*** *argument*

Figure 4.4.: *Circular surface footing on a homogeneous half-space: Validation of the computation of the impedance of the horizontal mode K_{11} (Eq 3.7): comparison between the FM-BEM solution (denoted COFFEE), the solution given by the standard BEM using Miss3D code (denoted Miss3D) and the solution extracted from [60] (denoted Sieffert).*

It is worth noting that both "references" are simplified numerical solutions. As a result, it is difficult to assess the absolute accuracy of any of these references. However, in the case of a surface circular footing in a homogeneous half-space, analytical solutions in the quasi-static regime are available (see Table 4.1). Since the results obtained with the FM-BEM are normalized by the static stiffness, the real part of the normalized impedances should be close to 1 in the low-frequency limit.

For the case of the vertical mode (Figure 4.5), results present the same pattern as for the horizontal mode: oscillations for the real part of the impedance while being in good agreement with the reference solutions. Note that since the two reference solutions are issued from simplified computations, differences between the results with Miss3D and the results of [60] are also observed. For both the horizontal and vertical modes, the low-frequency limit of the real part of the impedance is close to 1, as expected.

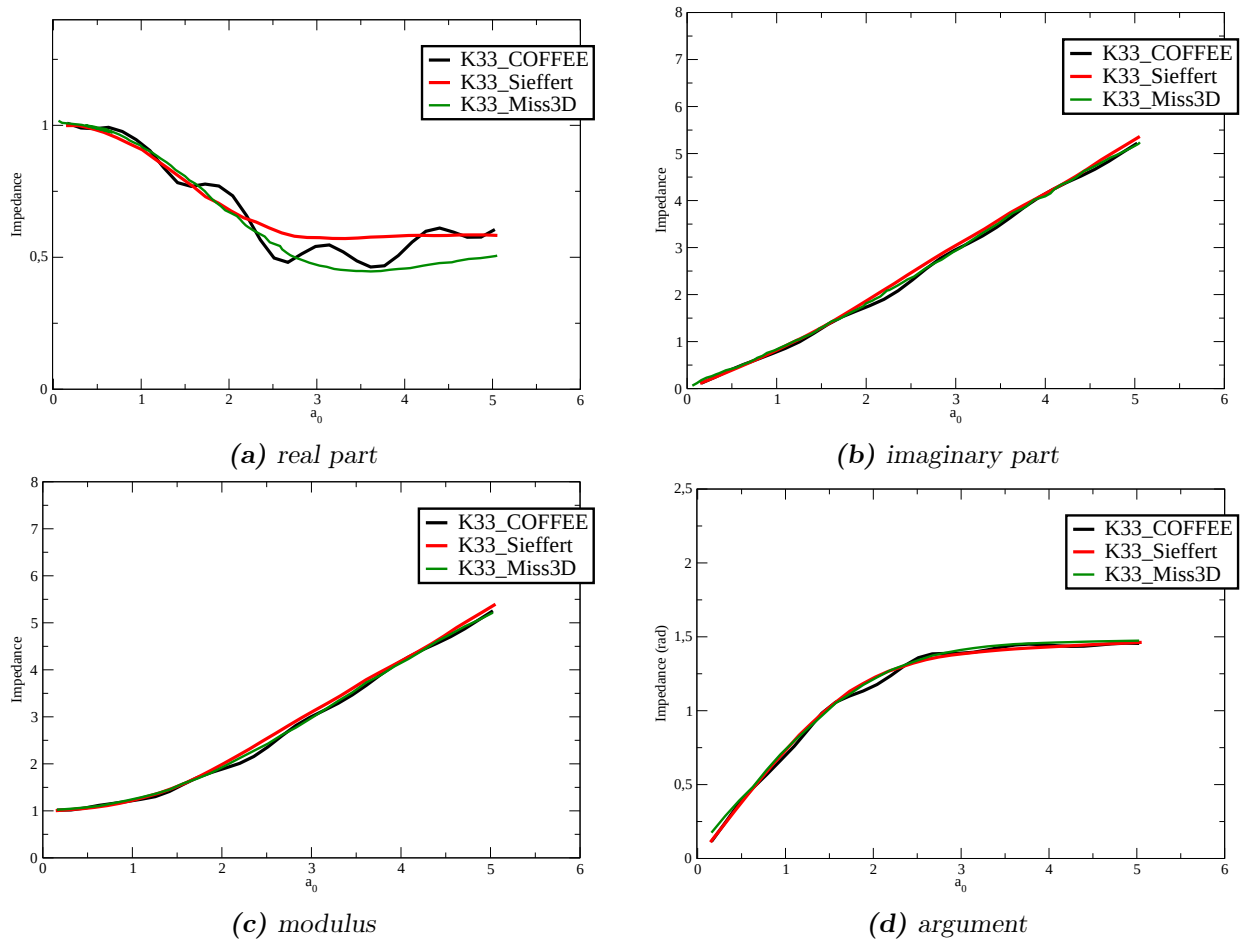

(a) *real part* **(b)** *imaginary part*

(c) *modulus* **(d)** *argument*

Figure 4.5.: *Circular surface footing on a homogeneous half-space: Validation of the computation of the impedance of the vertical mode K_{33s} (Eq 3.7): comparison between the FM-BEM solution (denoted COFFEE), the solution given by standard BEM using Miss3D code (denoted Miss3D) and the solution extracted from [60] (denoted Sieffert).*

For the rocking (Figure 4.6) and torsion (Figure 4.7) modes, the discrepancies between the impedance computed with FM-BEM and both references become more important. But all the solutions follow the same pattern of evolution with respect to the frequency. The oscillations are also less pronounced compared to the horizontal and vertical modes. Since the impedance is normalized by the static stiffness, the real part and modulus of the impedance are again expected to be close to one in the quasi-static regime. The quasi-static value of the impedance for the rocking mode exhibits a significant gap of about 10% with the analytical static stiffness. This problem has also been observed in some results in the reference book of Miss3D (i.e., with standard BEM). To overcome this problem, more complex elements have been introduced in Miss3D. The same improvement can be done in *Coffee* but it is has not been considered in this work due to time constraints.

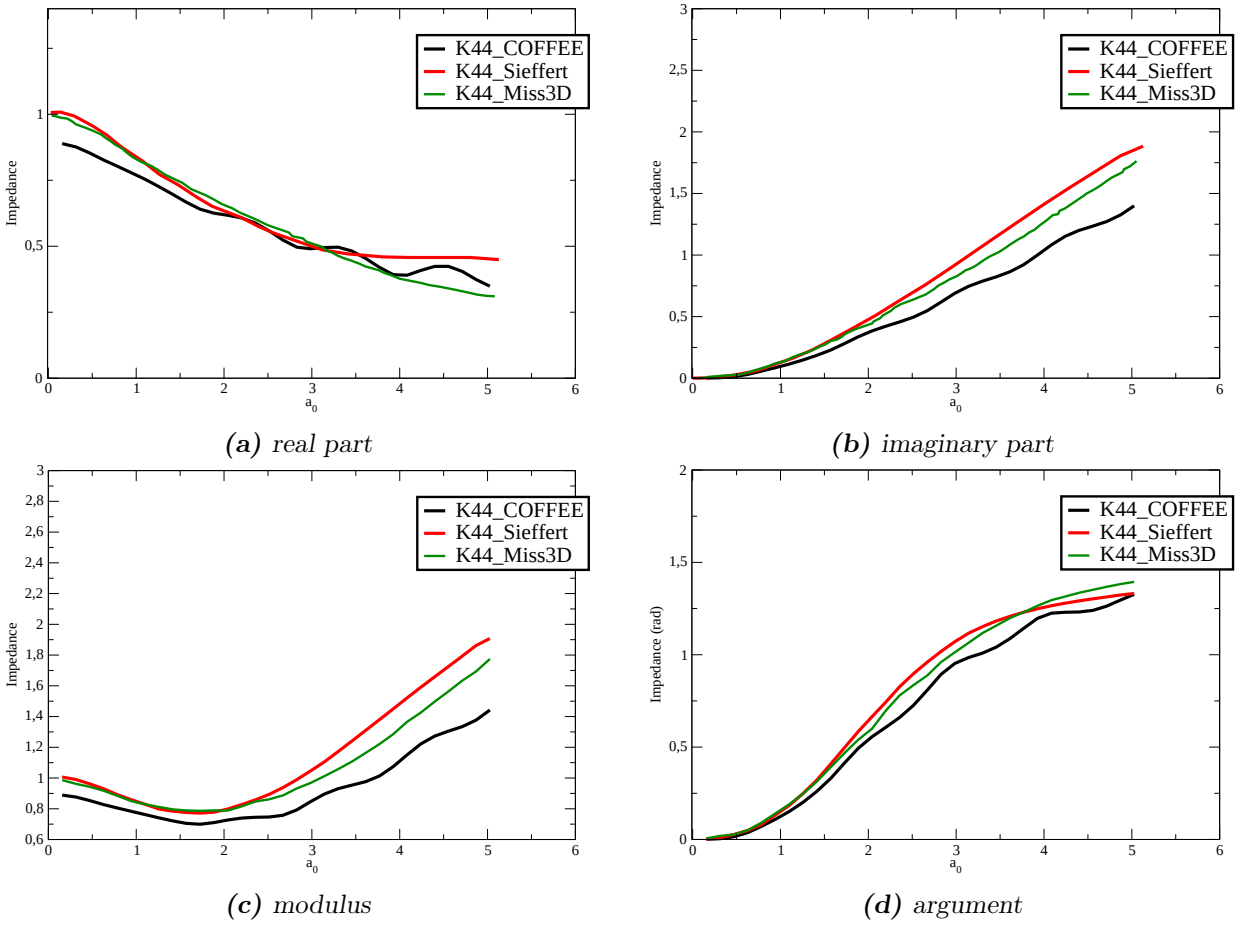

(a) *real part* ***(b)*** *imaginary part*

(c) *modulus* ***(d)*** *argument*

Figure 4.6.: *Circular surface footing on a homogeneous half-space: Validation of the computation of the impedance of the rocking mode K_{44} (Eq 3.7): comparison between the FM-BEM solution (denoted COFFEE), the solution given by standard BEM using Miss3D code (denoted Miss3D) and the solution extracted from [60] (denoted Sieffert).*

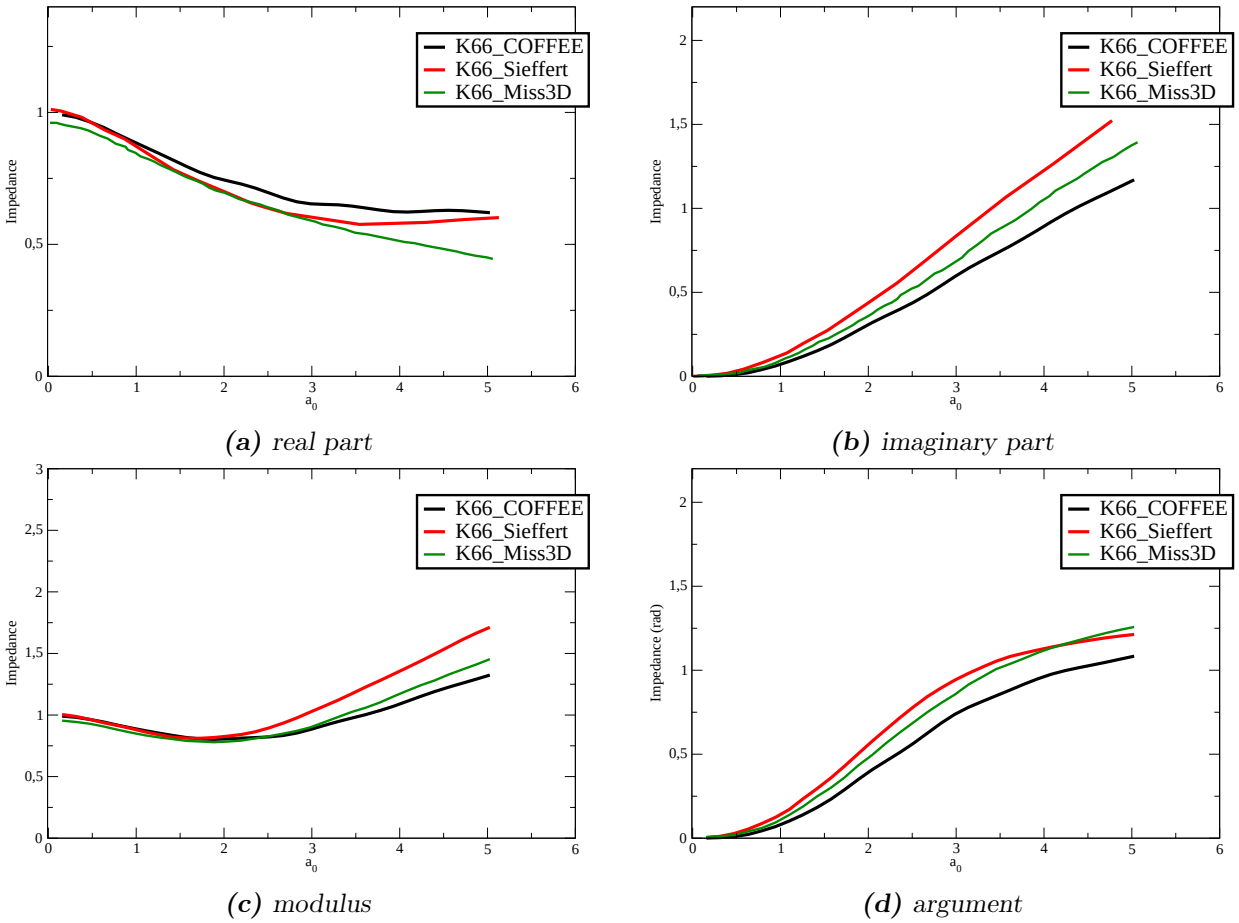

(a) *real part*

(b) *imaginary part*

(c) *modulus*

(d) *argument*

Figure 4.7.: *Circular surface footing on a homogeneous half-space: Validation of the computation of the impedance of the torsion mode K_{66} (Eq 3.7): comparison between the FM-BEM solution (denoted COFFEE), the solution given by standard BEM using Miss3D code (denoted Miss3D) and the solution extracted from [60] (denoted Sieffert).*

The numerical results obtained with the FM-BEM are considered to be accurate enough in an industrial context. The impedances follow the general pattern of the evolution of the reference solutions with respect to the frequency.

To understand the oscillations in the FM-BEM solution, a parametric study is performed. The sensitivity of the results to the truncation radius is checked. Figure 4.8 reports the impedance for the horizontal mode of a surface circular footing in a homogeneous half-space. The impedance is again normalized by the static stiffness and represented with respect to the non-dimensional frequency a_0. The results for different radius of truncation radius (ie $1.5R$, $2R$, $4R$, $10R$, $15R$, R being the radius of the circular footing) are compared to the reference solution extracted from [60]. It is noted that the frequency of the oscillations increases while the amplitude decreases when the truncation of the free surface radius is increased.

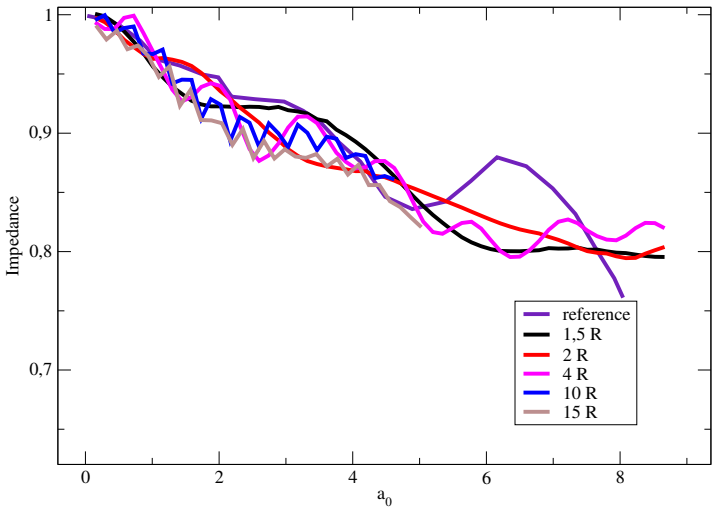

Figure 4.8.: *Influence of the truncation radius on the oscillations reported in the impedance computed with the FM-BEM.*

One possible explanation of the oscillations between standard BEM and FM-BEM solutions is the used of different fundamental solutions. In the standard BEM, the fundamental solution of a stratified half-space is used, while in the FM-BEM, the fundamental solution of the full-space is used. As a result, it is thus necessary to mesh the free surface up to a certain distance where it is truncated. The oscillations in the impedances might be caused by the reflection of surface waves at the artificial truncation of the free surface. Such phenomenon are observed in other fields where BEM is used for elastic wave propagation in half-space, e.g. nanophotonics [62]. To validate this assumption, the impedance of an interface in a bounded domain is computed next, using FM-BEM, in Subsection 4.1.3.

4.1.3. Numerical validation: impedance for an interface in a bounded domain

Previous results for an unbounded domain have shown oscillations of the FM-BEM solutions around the reference solutions. A parametric study of the variation of the results with respect to the truncation radius allowed to conclude that the frequency of the oscillations increases while the amplitude decreases when the truncation radius of the free surface is increased.

Another way to validate that these oscillations are caused by the truncation of the free surface is to compute the impedance of an interface in a bounded domain. In that case, the truncation of the free surface is avoided. The impedance computed with the FM-BEM is compared with an impedance computed with the FEM (i.e. with *Code_Aster*). The computation of the impedance of the interface is equivalent to the computation of the Schur complement of the DOFs outside the interface of the global dynamic matrix of the finite element model, expressed in the eigenmodes basis. Let $\underline{\underline{K}}$ and $\underline{\underline{M}}$ be respectively the stiffness and the mass matrix of the finite element model and $\underline{\underline{Z}} = \underline{\underline{K}} - \omega^2 \underline{\underline{M}}$ the global dynamic matrix of the finite element mode. The DOFs on the interface are denoted by an index *int* and the DOFs outside the interface are denoted by an index *out*. The $\underline{\underline{Z}}$ matrix can be written in blocks separating the DOFs inside and outside the interface as follows:

$$\underline{\underline{Z}} = \left[\begin{array}{c|c} \underline{\underline{Z}}_{int,int} & \underline{\underline{Z}}_{int,out} \\ \hline \underline{\underline{Z}}_{out,int} & \underline{\underline{Z}}_{out,out} \end{array}\right]$$

The Schur complement $\underline{\underline{S}}$ of the block $\underline{\underline{Z}}_{out,out}$ of $\underline{\underline{Z}}$ is defined as $\underline{\underline{S}} = \underline{\underline{Z}}_{int,int} - \underline{\underline{Z}}_{int,out} . \underline{\underline{Z}}^{-1}_{out,out} . \underline{\underline{Z}}_{out,int}$. The i, j term of the impedance expressed in a reduced basis corresponding to the $\underline{\Phi}_i$ and $\underline{\Phi}_j$ eigenmodes is computed as ${}^t\underline{\Phi}_i . \underline{\underline{S}} . \underline{\Phi}_j$.

The model considered consists in a cube with an edge of 100 m. The cube is homogeneous, visco-elastic with isotropic constitutive properties defined by $C_s = 870\ m/s$, $\rho = 2710\ kg/m^3$, $\nu = 0.33$, $\beta_p = \beta_s = 5\%$. Damping is used in this model to avoid the division by zero at the resonance frequencies, i.e. to regularize the evaluation. The model (Figure 4.9) is fixed at the base. The

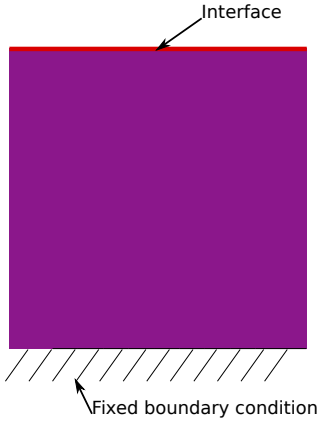

Figure 4.9.: *Impedance for an interface in a bounded domain: model considered.*

impedance is computed on the upper face of the cube with both the FM-BEM and the FEM, for the horizontal and vertical modes.

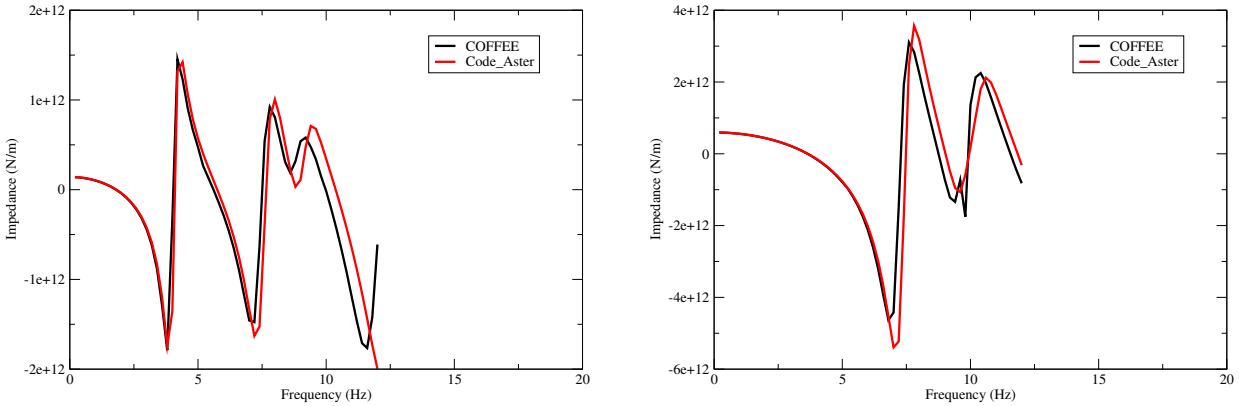

(a) *Real part of the horizontal mode* ***(b)*** *Real part of the vertical mode*

Figure 4.10.: *Computation of the impedance for the horizontal and the vertical modes of an interface in a bounded domain. Comparison of the solution with FM-BEM (denoted COFFEE) and FEM (denoted Code_ Aster).*

Figure 4.10 presents the real part of the impedance (horizontal and vertical modes) of the interface obtained with both the FM-BEM and the FEM. Results with both methods are consistent. In this bounded configuration, the impedance computed with the FM-BEM does not present the artificial oscillations. This observation supports the hypothesis that the origin of the oscillations is the artificial truncation of the free surface. It is therefore expected that these oscillations will disappear by using a version of the FM-BEM that is based on the half-space fundamental solution, as proposed in [8]. Since it is an involved task, it is not considered in this thesis and is left as future work, which should result in improved accuracy for the impedance evaluation.

4.1.4. Numerical validation: embedded cylindrical footing in a homogeneous half-space

Now that the case of a circular surface footing is validated and the cause of the oscillations identified, the case of a cylindrical embedded footing in a homogeneous half-space is considered. Results with the FM-BEM are compared to reference solutions. The footing has a radius of $R = 100$ m and a depth $D = 200$ m (Figure 4.11). The free surface is truncated at a distance of $4R$. Mechanical properties of the homogeneous visco-elastic soil are: $C_s = 870m/s, \rho = 2710kg/m^3, \nu = 0.25, \beta_p = 1\%, \beta_s = 0.5\%$. Impedances presented in the following are normalized by values of the same dimension, because there is no known analytical static stiffness of the impedance corresponding to the rigid body modes, and so was the choice in Miss3D and the book of Sieffert. Hence, impedances for the horizontal and vertical modes are normalized by μR (i.e. $K_{11}/(\mu R)$, $K_{22}/(\mu R)$ and $K_{33}/(\mu R)$), impedances for the rocking and torsion modes are normalized by μR^3 (i.e. $K_{44}/(\mu R^3)$, $K_{55}/(\mu R^3)$ and $K_{66}/(\mu R^3)$). Impedances for coupling between horizontal and rocking are no longer

negligible due to the lose of the symmetries, are normalized by μR^2 (i.e. $K_{15}/(\mu R^2)$). Values presented for Miss3D are extracted from the validation test cases of the code, with a maximum value for $a_0 = 3,5$ as in the validation test case.

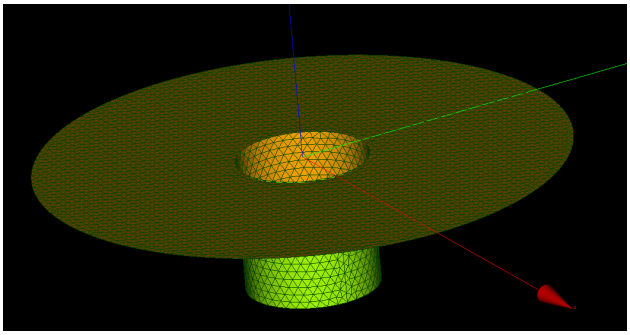

Figure 4.11.: *Example of a mesh of an embedded cylindrical footing on a homogeneous half-space.*

The results for the horizontal and vertical modes (Figures 4.12 and 4.13) are similar to those obtained in the case of a surface circular footing. The reference solutions and impedances obtained with the FM-BEM are in good agreement. Again, the real part of the impedance exhibits oscillations, as observed in the case of a surface circular footing.

The results for the horizontal mode (see Figure 4.12) show an important gap in the real part of the impedance for the three values compared (results of FM-BEM, results of classical BEM and results from [60]), while the imaginary part of the impedance of the three values are in good agreement. The real part of the impedance of the horizontal mode exhibits important amplitude of oscillations.

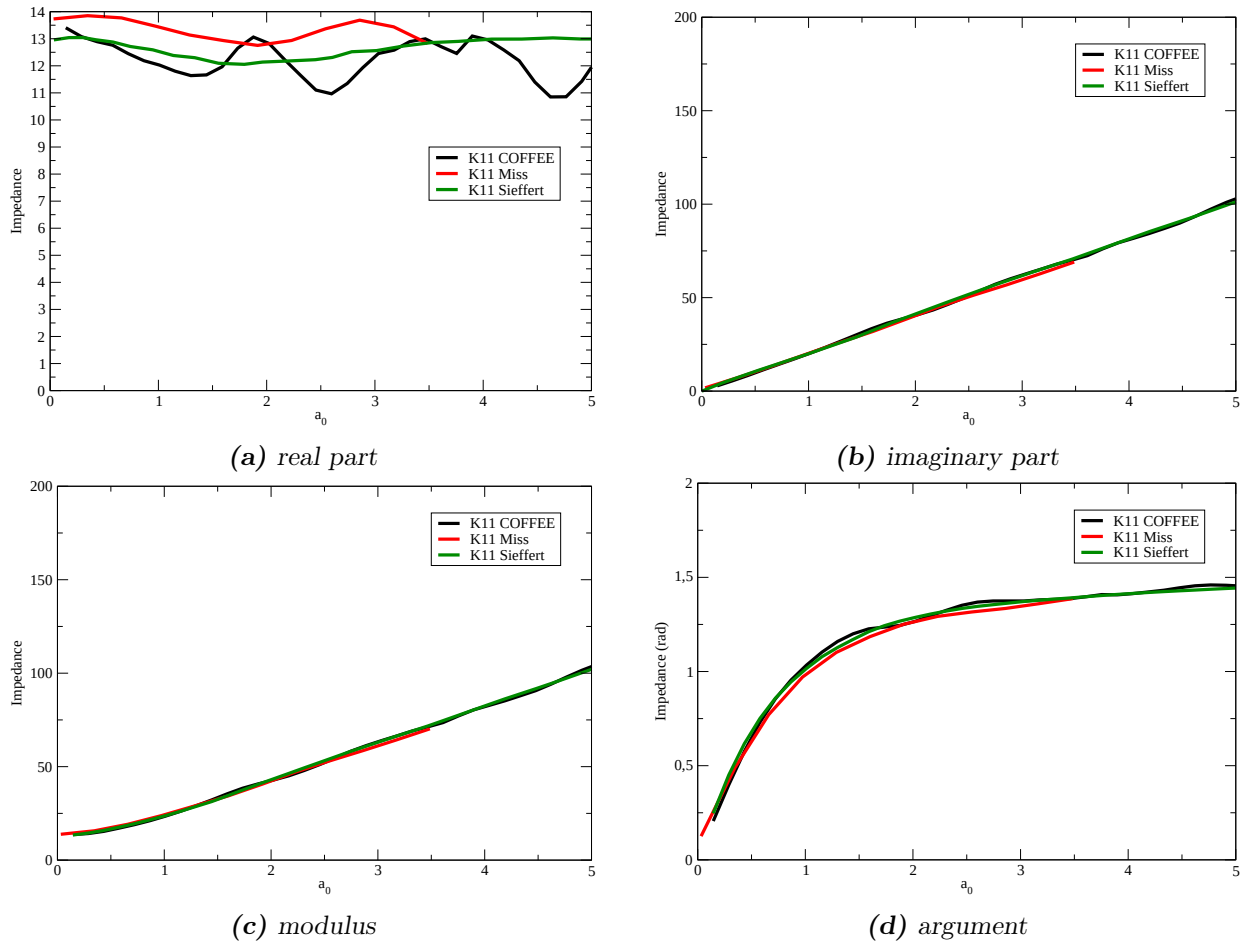

(a) *real part* **(b)** *imaginary part*

(c) *modulus* **(d)** *argument*

Figure 4.12.: *Embedded cylindrical footing: Validation of the computation of the impedance of the horizontal mode K_{11} (Equation 3.7): comparison between the FM-BEM solution (denoted COFFEE), the solution given by standard BEM using Miss3D code (denoted Miss) and the solution extracted from [60] (denoted Sieffert).*

The results for the vertical mode (see Figure 4.13) are similar to those obtained in the case of a surface circular footing. Again, the real part of the impedance exhibits oscillations, as observed in the surface circular footing. However it can be considered that the reference solutions and impedances obtained with FM-BEM are in good agreement, because even if there is oscillations, the values of the impedances are of the same magnitude.

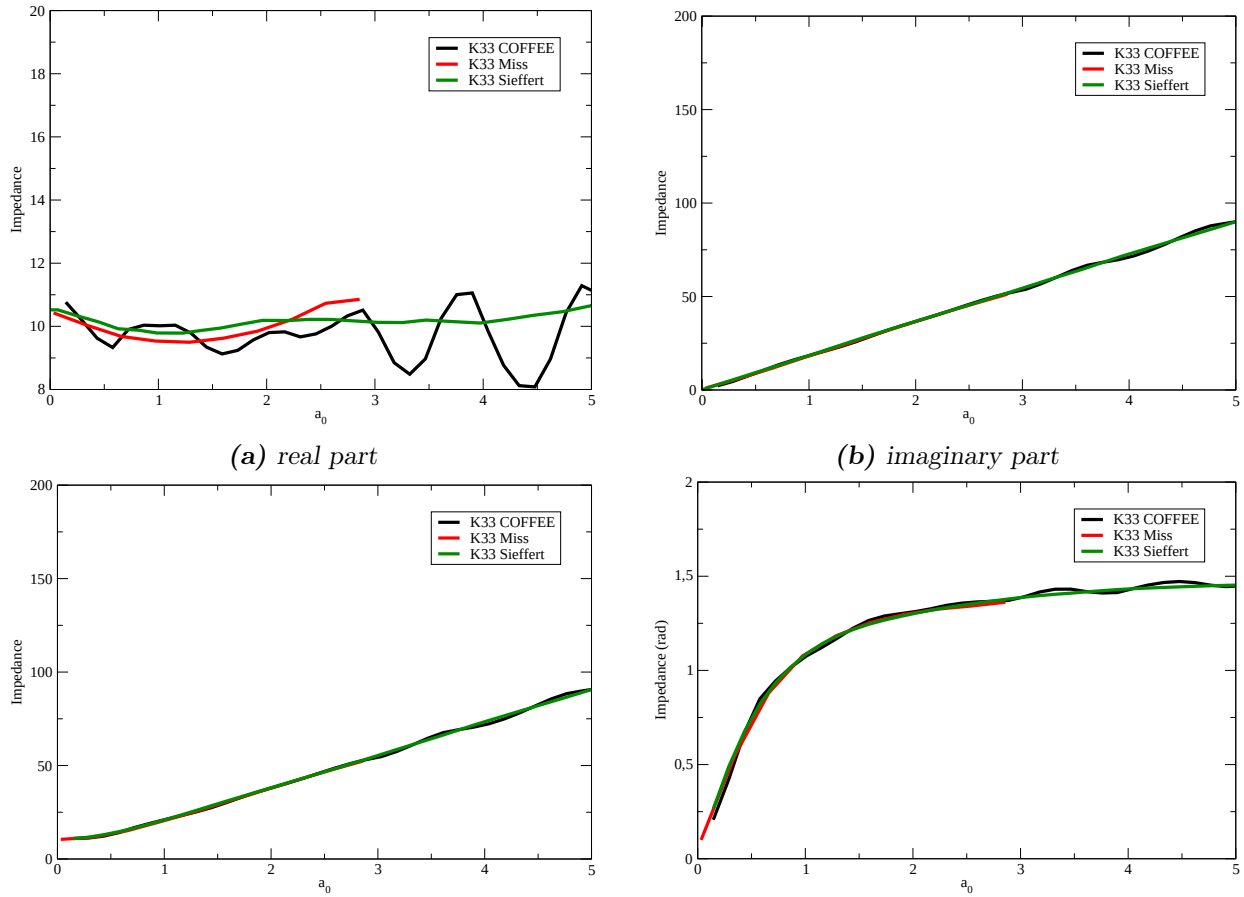

(a) *real part* **(b)** *imaginary part*

(c) *modulus* **(d)** *argument*

Figure 4.13.: *Embedded cylindrical footing: Validation of the computation of the impedance of the vertical mode K_{33} (Equation 3.7): comparison between the FM-BEM solution (denoted COFFEE), the solution given by standard BEM using Miss3D code (denoted Miss) and the solution extracted from [60] (denoted Sieffert).*

Results for the rocking (Fig. 4.14) and torsion (Fig. 4.15) modes evaluated with the FM-BEM exhibit oscillations similarly to the case of a surface circular footing. In addition, they both significantly deviate from the two references for the real part of the impedance. This deviation can be explained by the scaling factor of the problem. Both reference solutions have been obtained for canonical models, i.e. with unitary mechanical properties ($\mu = 1.$, $\rho = 1.$, $\nu = 0.25$) and a radius of the footing of 0.5 m. The FM-BEM results are normalized by μR for horizontal and vertical modes, and by μR^3 for rocking and torsion modes. These terms do not correspond to the static impedance, as it is the case for the circular surface footing. They are just used to have comparable non-dimensional impedances.

Similarly, the reference solutions and impedances obtained by FM-BEM are in good agreement for the imaginary part, with a greater slope of the imaginary part of the impedance for the rocking mode computed with FM-BEM compared to references.

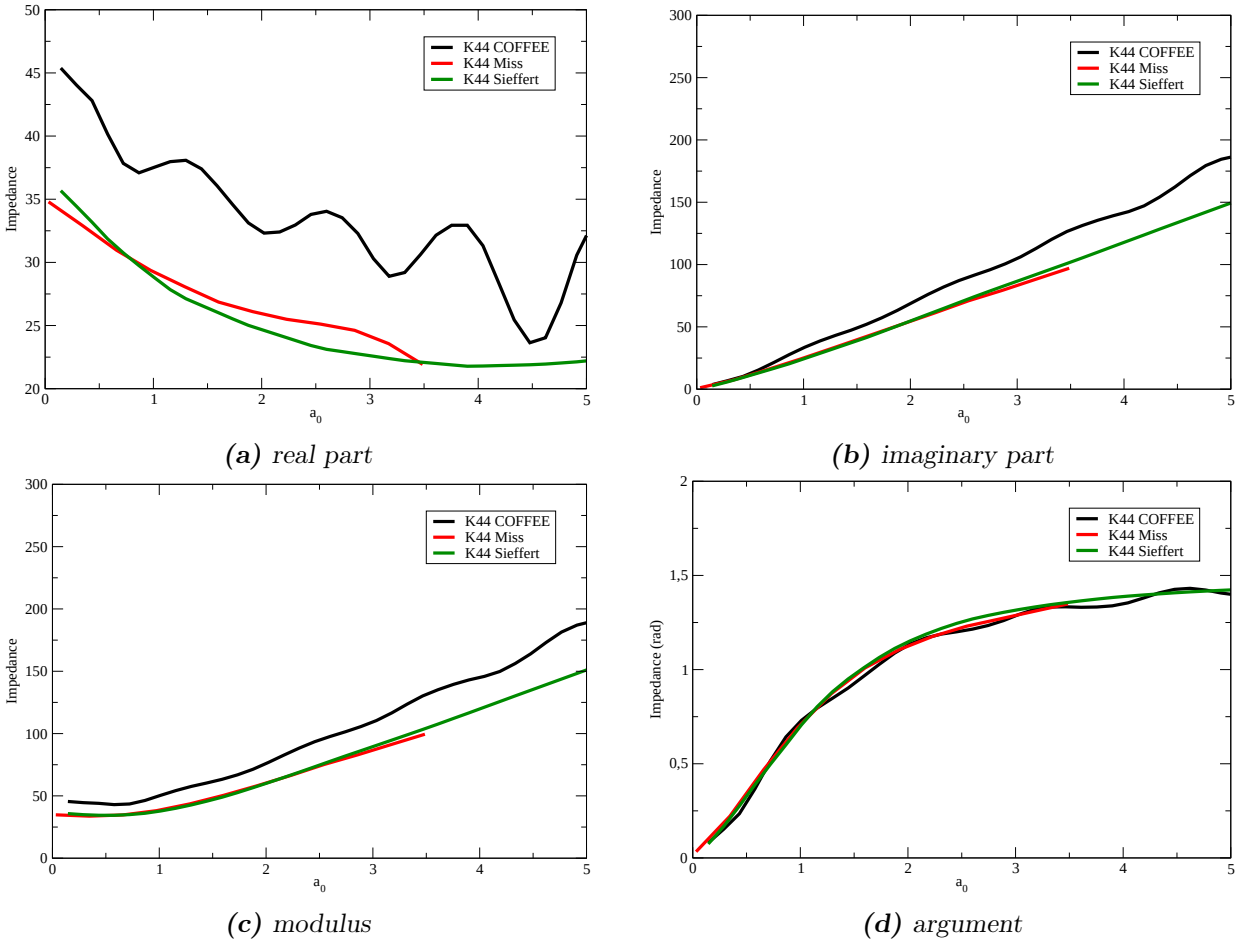

(a) *real part*

(b) *imaginary part*

(c) *modulus*

(d) *argument*

Figure 4.14.: *Embedded cylindrical footing: Validation of the computation of the impedance of the rocking mode K_{44} (Eq 3.7): comparison between the FM-BEM solution (denoted COFFEE), the solution given by standard BEM using Miss3D code (denoted Miss) and the solution extracted from [60] (denoted Sieffert).*

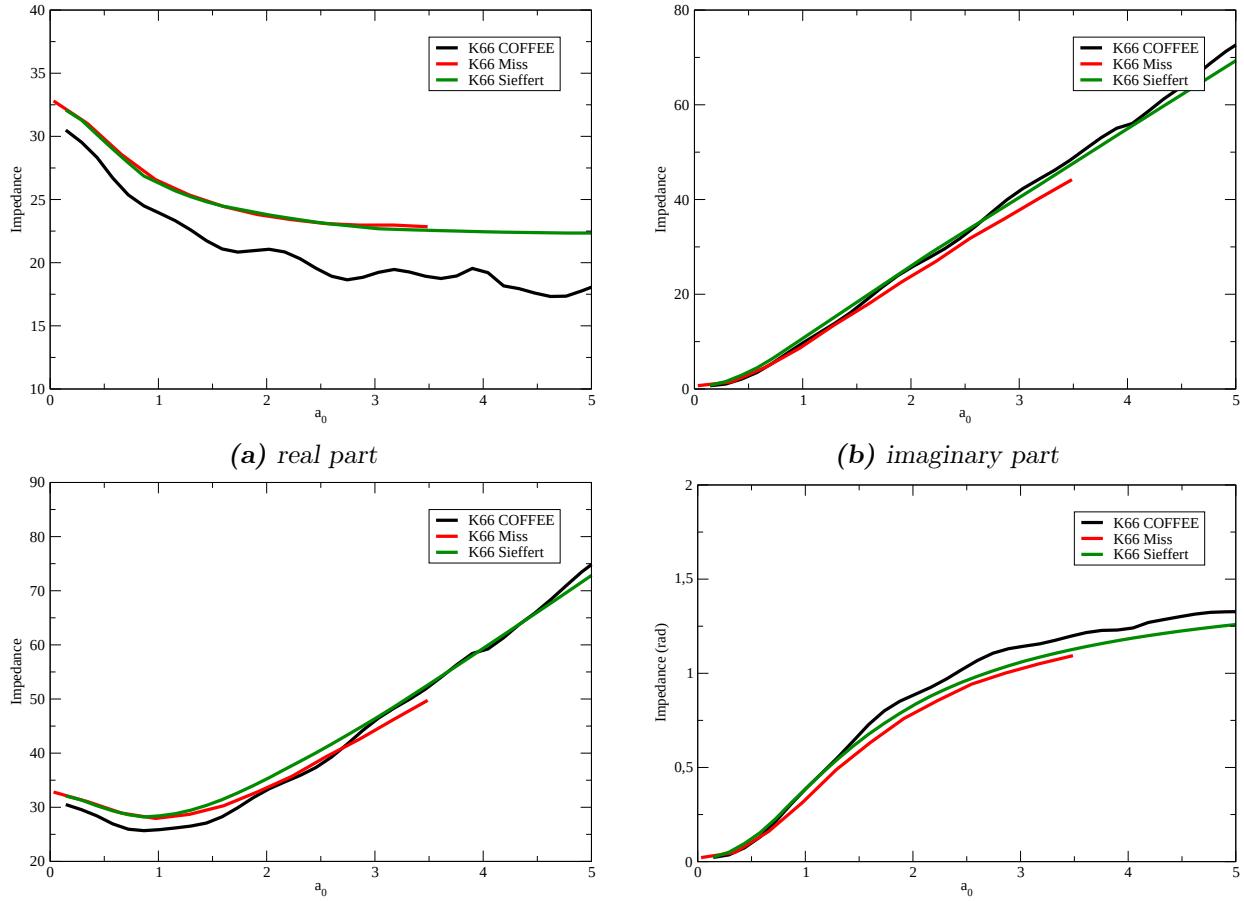

(a) *real part*

(b) *imaginary part*

(c) *modulus*

(d) *argument*

Figure 4.15.: *Embedded cylindrical footing: Validation of the computation of the impedance of the torsion mode K_{66} (Eq 3.7): comparison between the FM-BEM solution (denoted COFFEE), the solution given by standard BEM using Miss3D code (denoted Miss) and the solution extracted from [60] (denoted Sieffert).*

The impedance term associated with the coupling between the horizontal mode and the rocking mode (Fig. 4.16) exhibits the same pattern as the horizontal mode and the rocking mode, since it is a combination of both modes: oscillations with respect to the non-dimensional frequency and a shift in the value of the impedance compared with both references.

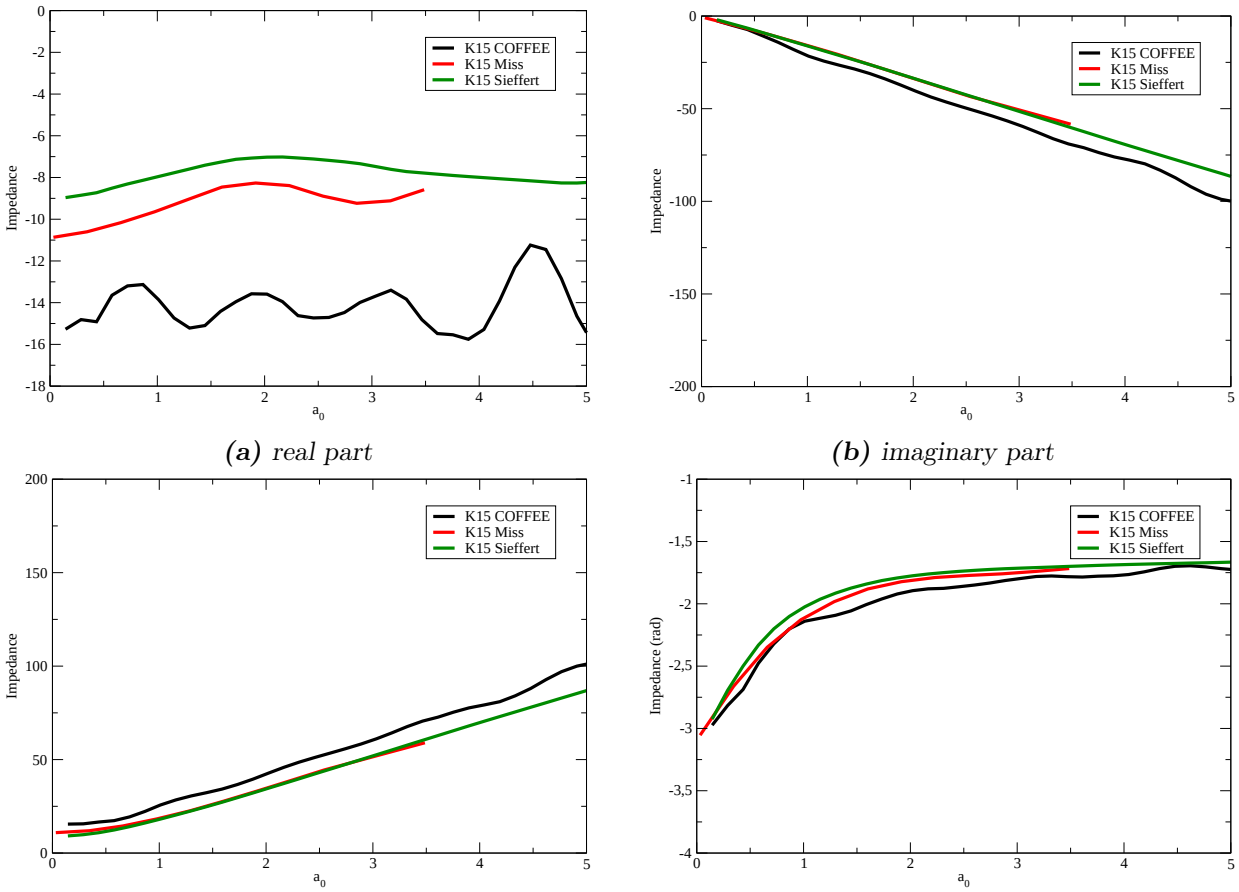

(a) *real part* **(b)** *imaginary part*

(c) *modulus* **(d)** *argument*

Figure 4.16.: *Embedded cylindrical footing: Validation of the computation of the impedance of the coupling of the rocking mode and the torsion mode K_{15} (Eq. 3.7): comparison between the FM-BEM solution (denoted COFFEE), the solution given by standard BEM using Miss3D code (denoted Miss) and the solution extracted from [60] (denoted Sieffert).*

4.2. Impedance operator for hemispherical basin in half-space with material contrasts

This section concerns the validation of impedances computed with the FM-BEM in the case of multi-domain basins. The model consists of a hemispherical basin in an infinite half-space (Figure 4.17). Two cases are studied: (i) a case where both domains have the same mechanical characteristics, which is equivalent to a homogeneous half-space, and (ii) a case with a velocity contrast, such that the hemispherical domain has wave velocities equal to half the corresponding velocities of the

half-space material. Two kinds of footings are studied: a surface circular footing and an embedded circular footing. The interface for which the impedance is computed is the footing (red line in Fig. 4.17).

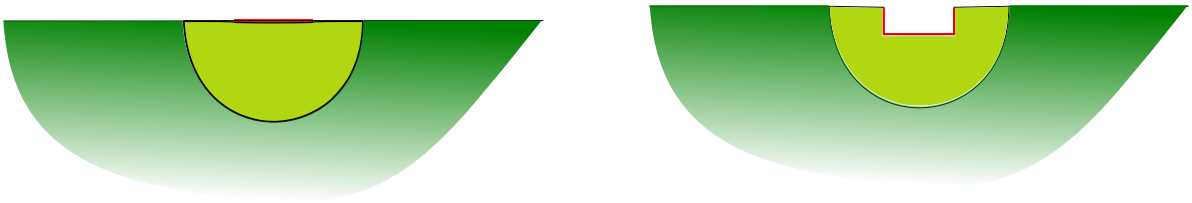

Figure 4.17.: *Surface and embedded circular footings in the case (i) of a hemispherical basin in a half-space.*

The goal of the case (i) is to validate impedances computed with FM-BEM in the case of a multi-domain model (basin embedded in a half-space) where both media have the same mechanical characteristics. This case corresponds to the previous configuration validated but allows to check the accuracy of the handling of multi-domain problems. The mechanical characteristics of the basin and half-space in the homogeneous case are $C_s = 1740\ m/s$, $C_p = 3455\ m/s$, $\nu = 0.33$.

The goal of the model (ii) with a velocity contrast is to validate the computation of impedances with the FM-BEM in the case of a multi-domain model (basin embedded in a half-space) with a velocity contrast. The mechanical characteristics of the two domains are:

- characteristics of the hemispherical basin: $C_s = 870\ m/s$, $C_p = 1727\ m/s$, $\nu = 0.33$;
- characteristics of the half-space: $C_s = 1740\ m/s$, $C_p = 3455\ m/s$, $\nu = 0.33$.

Since the coupling between the FEM (i.e. *Code_Aster*) and the standard BEM (i.e. *Miss3D*) has already been extensively validated at EDF, the FM-BEM results are compared with these results. It is worth noting that the standard BEM used at EDF is based only on the layered half-space fundamental solutions, such that it is not possible to use only the BEM (i.e. *Miss3D*) to consider configurations with hemispherical basins. On the other hand, the FM-BEM uses the full-space fundamental solutions, so that it is not necessary to couple the FM-BEM with the FEM to consider basin problems. Figure 4.18 presents the strategy adopted to define the FEM-BEM coupling solution: the hemispherical basin is modelled with the FEM (blue domain in the figure), while the half-space is modelled with the BEM (black domain in the figure). The FEM/BEM interface is the interface between the hemispherical basin and the half-space (orange line in the figure). The impedance of the footing (red line in the figure) is then computed as the force resulting from the application of a unitary displacement corresponding to the different rigid body modes.

The elements used in the finite element volume mesh of the hemispherical basin are linear hexahedra, meshed with a density of six elements per S-wavelength. The hexahedra, albeit hard to generate, are necessary in this case. It is observed that the use of tetrahedra generates a global model stiffer than it should be. Hence, for the evaluation of the impedance of a surface circular footing in the quasi-static case, for which an analytical solution is available (see Table 4.1), the model with tetrahedra

gives quasi-static stiffness overestimated up to three times compared to the value of the analytical solution. On the other hand, the model with the hexahedra give results in good agreement with the analytical solutions.

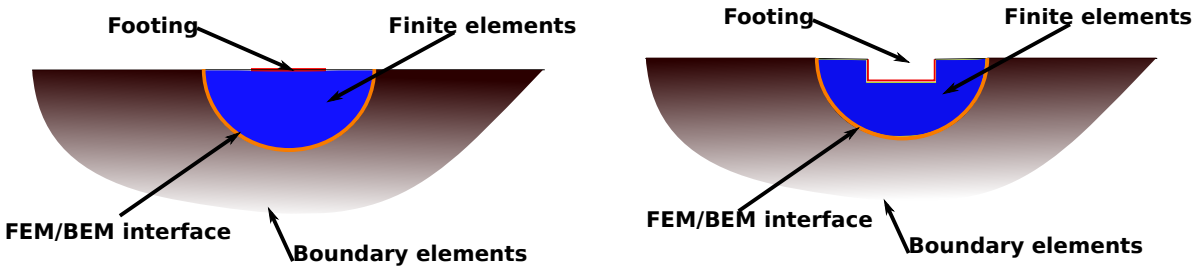

Figure 4.18.: *Coupling FEM-BEM strategy for the case of a surface or embedded footings (case of a hemispherical basin in a half-space).*

The hemispherical basin has a radius of 100 m. The free surface is truncated at a distance equal to four times the radius of the hemispherical basin. The surface footing has a radius of $30m$. The embedded cylindrical footing has a radius of 30 m and a depth of 21 m. The frequency range of interest is $[0.2\text{ Hz}, 24\text{ Hz}]$. The motivation behind the use of these dimensions and frequency range is to have a model that can be treated at the same time by the FM-BEM (i.e. *Coffee*) and the FEM-BEM coupling (i.e. *Code_Aster*), so that there is a way to compare both results. The model used in *Coffee* consists of $20,000$ DOFs, i.e. a relatively small problem for the FM-BEM. The interface between FEM and BEM elements in the model used in *Code_Aster* contains $3,000$ DOFs. Again, the FM-BEM has the capabilities to solve problems much larger problems than the one treated here, but the main hindrance would be the ability to compare the results with other numerical codes.

4.2.1. Circular surface footing

Results for impedance of circular surface footing are presented, for both the homogeneous case (i) and the case with a velocity contrast (ii). The impedances are plotted with respect to the non-dimensional circular frequency defined by $a_0 = \omega R/C_s$ and are normalized by the static stiffness of a surface circular footing in a homogeneous half-space (Table 4.1).

Homogeneous half-space. This case has already been validated in the previous section. A fictitious new domain is now added. The goal is to check the accuracy of the code in the case of a multi-domain instead of a homogeneous domain. Results are compared to impedances operators from the book of Sieffert and Cevaer [60].

Impedances computed with the FM-BEM (i.e. with *Coffee*) and with the FEM-BEM coupling (i.e. *Code_Aster*) for the horizontal, vertical, rocking and torsion modes are presented in Figures 4.19, 4.20, 4.21 and 4.22. They show a good agreement with the analytical static stiffness, except the impedance of the rocking mode obtained with the FEM-BEM, which presents 13% of relative error to the analytical static stiffness.

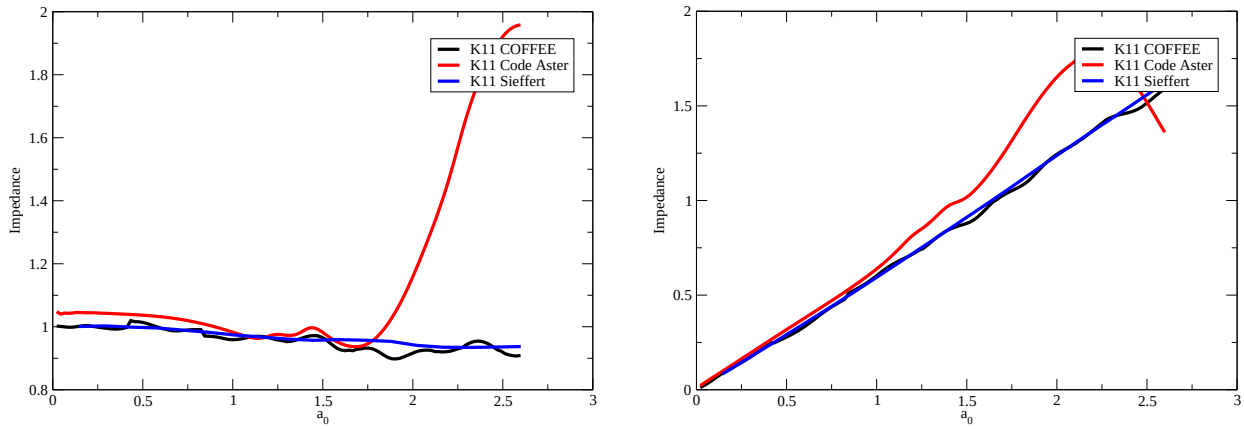

(a) *real part* **(b)** *imaginary part*

Figure 4.19.: *Circular surface footing on a homogeneous half-space. Validation of the computation of the impedance of the horizontal mode K_{11} (Eq 3.7): comparison between the FM-BEM solution (denoted COFFEE), the solution given by the FEM-BEM coupling (Code_Aster) and the solution extracted from [60] (denoted Sieffert).*

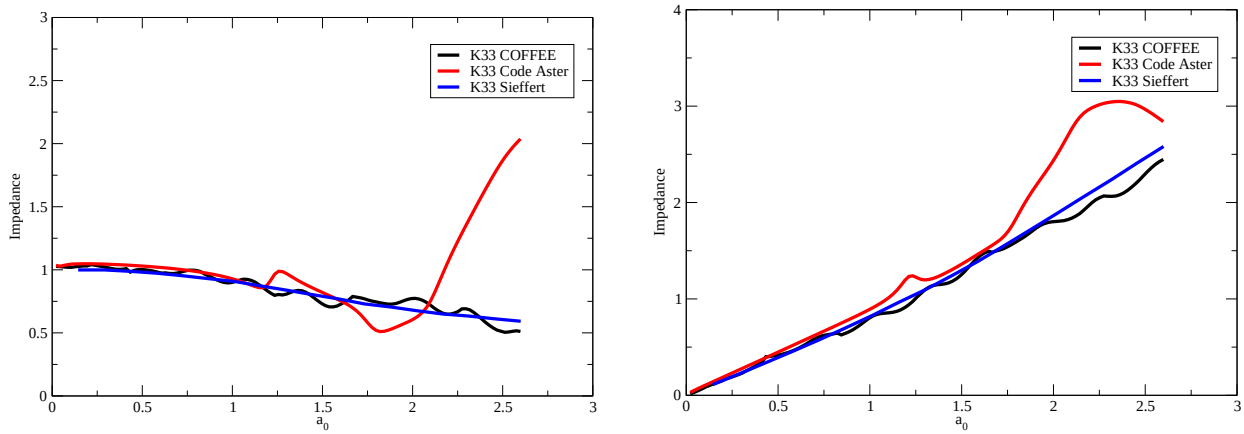

(a) *real part* **(b)** *imaginary part*

Figure 4.20.: *Circular surface footing on a homogeneous half-space. Validation of the computation of the impedance of the vertical mode K_{33} (Eq 3.7): comparison between the FM-BEM solution (denoted COFFEE), the solution given by the FEM-BEM coupling (Code_Aster) and the solution extracted from [60] (denoted Sieffert).*

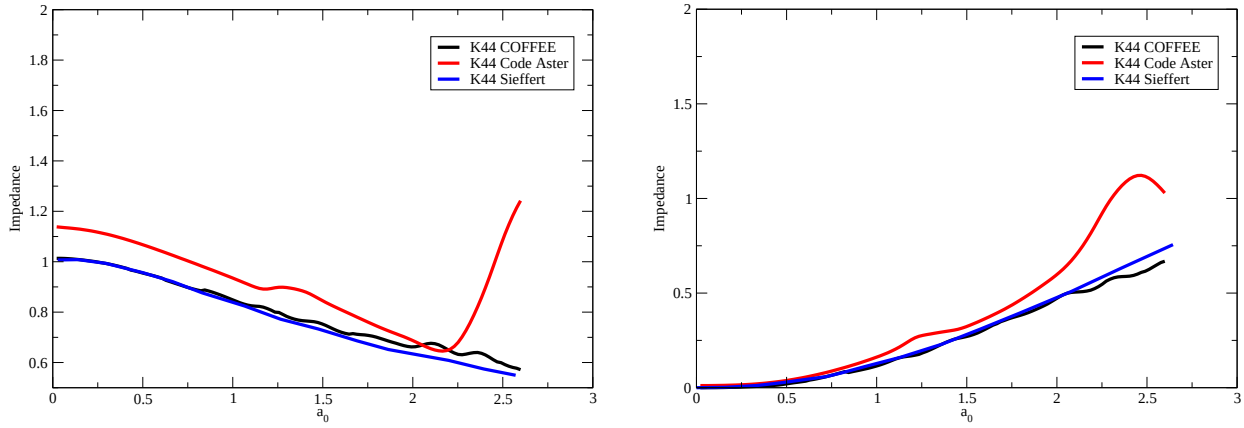

(a) *real part* **(b)** *imaginary part*

Figure 4.21.: *Circular surface footing on a homogeneous half-space. Validation of the computation of the impedance of the rocking mode K_{44} (Eq 3.7): comparison between the FM-BEM solution (denoted COFFEE), the solution given the FEM-BEM coupling (Code_Aster) and the solution extracted from [60] (denoted Sieffert).*

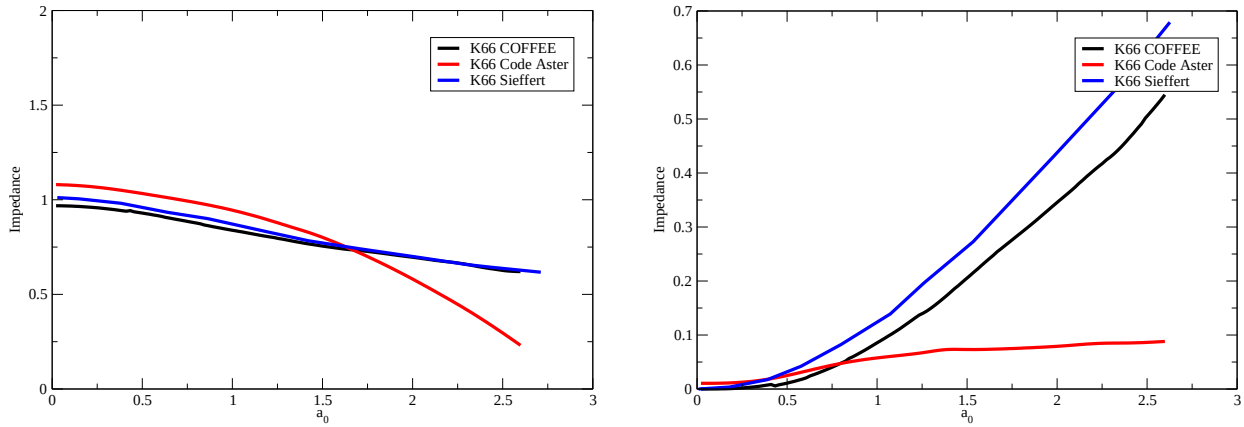

(a) *real part* **(b)** *imaginary part*

Figure 4.22.: *Circular surface footing on a homogeneous half-space. Validation of the computation of the impedance of the torsion mode K_{66} (Eq 3.7): comparison between the FM-BEM solution (denoted COFFEE), the solution given by the FEM-BEM coupling (Code_Aster) and the solution extracted from [60] (denoted Sieffert).*

Impedances computed with the FM-BEM for the horizontal and vertical modes are conform to the reference impedance operator from [60], while impedances for the horizontal, vertical and rocking modes computed with the FEM-BEM (i.e. *Code_Aster*) coupling are conform to the reference up to a frequency that depends on the mode. Then they tend to diverge from the reference. This might be explained by the eingenmodes of the hemispherical basin modelled with the FEM.

To check this hypothesis, computations are performed with FEM-BEM (i.e *Code_Aster*) on two models with the same geometry as in Section 4.2 which consists of a homogeneous half-space, but with different mechanical characteristics: one with mechanical characteristics such that $C_s = 870\ m/s$, $C_p = 1727\ m/s$ and $\nu = 0.33$ and another one wih mechanical characteristics such that $C_s = 1740\ m/s$, $C_p = 3455\ m/s$ and $\nu = 0.33$. Both results are compared in Figure 4.23, where the impedance of the vertical mode is presented with respect to the frequency (in Hz) without being normalized. Both models have the same mesh. The only change is in the mechanical characteristics. The aim is to check if the divergence that occurs in the impedance of the FEM-BEM model is due to the eigenmodes of the hemispherical basin, and not to some numerical errors. This will be verified if the frequency where the divergence occurs is divided by two when the wave-velocity is also divided by two.

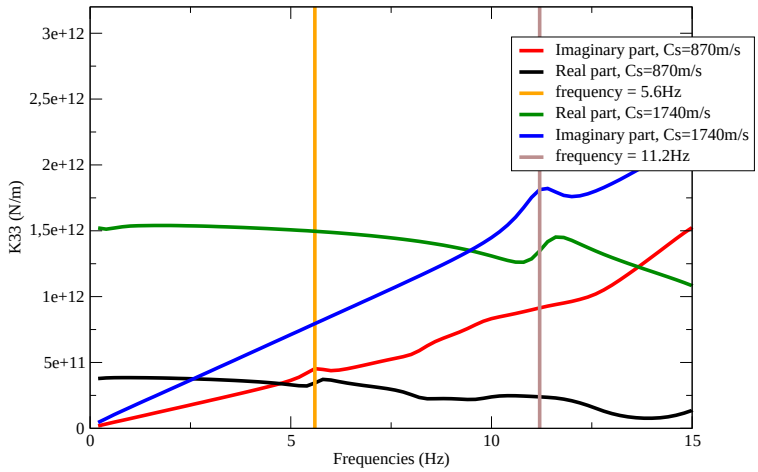

Figure 4.23.: *Comparison of K_{33} for two different wave velocities.*

Figure 4.23 shows that, as expected, by dividing the velocity of the hemispherical basin by two, the frequency range for which the perturbation in the impedance occurs is also divided by two. This confirm the hypothesis that this frequency corresponds to one of the eigenmodes of the hemispherical basin.

In addition, It can be seen on Figure 4.22 that the real part of the impedance for the torsion mode computed with the FEM-BEM coupling (i.e. *Code_Aster*) is in agreement with the reference up to a certain frequency, then it diverges from the reference, while the imaginary part is different from the reference. This approach to compute the impedance operator with the FEM-BEM coupling is not accurate to represent the torsion mode. It might be due to the type of elements used (linear hexahedra elements). The use of quadratic hexahedra might allow more flexibility to the finite

element model. All these results show the interest of replacing the current FEM-BEM approach with a purely FM-BEM approach. This new approach is accurate for all frequencies of interest in our industrial context.

Basin with material contrast. Once the simulated homogeneous domain (i.e. two domains with the same mechanical parameters) validated, a basin with two domains is considered. The impedances computed with the FM-BEM and the FEM-BEM coupling are normalized by the static stiffness of an infinite half-space presenting the mechanical characteristics of the hemispheric basin. Thus, the purpose is to compare the stiffness in the quasi-static regime, i.e. it is supposed to be close to 1 in the normalized values of the impendance. The impedances for a circular surface footing in homogeneous half-space, extracted from [60], are plotted along with the results to assess the impact of the velocity contrast on the impedance.

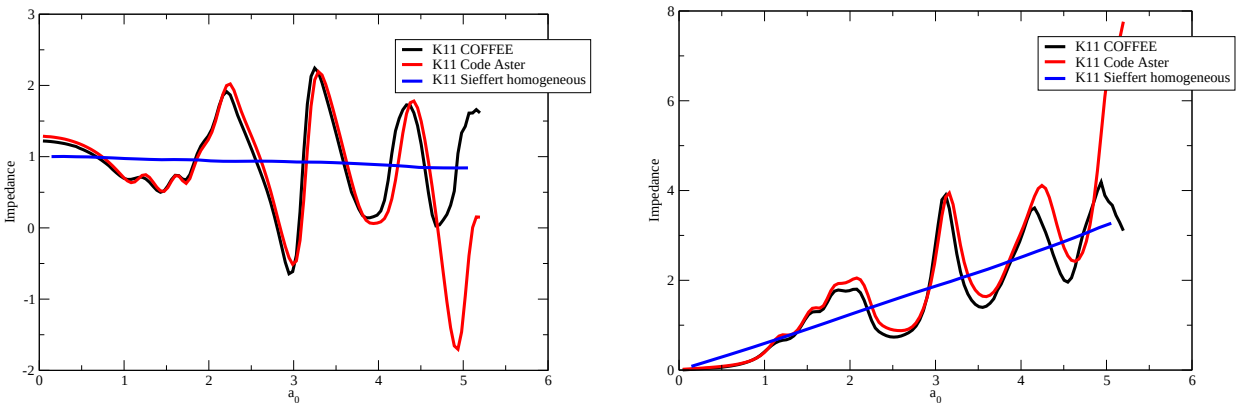

(a) *real part* ***(b)*** *imaginary part*

Figure 4.24.: *Circular surface footing on a multi-domain basin. Validation of the computation of the impedance of the horizontal mode K_{11} (Eq 3.7): comparison between the FM-BEM solution (denoted COFFEE), the solution given by the FEM-BEM coupling (Code_Aster) and the solution extracted from [60] (denoted Sieffert homogeneous) in the case of a homogeneous half-space.*

Impedances computed with the FM-BEM (i.e. with *Coffee*) and with the FEM-BEM coupling (i.e. *Code_Aster*) for the horizontal, vertical, rocking and torsion modes are presented in Figures 4.24, 4.25, 4.26 and 4.27. Results show a good agreement between the impedances computed with the FEM-BEM coupling and the FM-BEM. Similarly to the case of a homogeneous medium, the torsion mode is not properly handled by the FEM-BEM coupling. Impedances of the horizontal, vertical and rocking modes oscillate around the corresponding impedances for the homogeneous case, for both the real part and the imaginary part of the impedance. The oscillations can reach up to twice the value of the impedance of the homogeneous case. They correspond to the resonance of the hemispherical basin. The presence of these peaks permits to determine on the figures the resonance frequencies of the hemispherical basin.

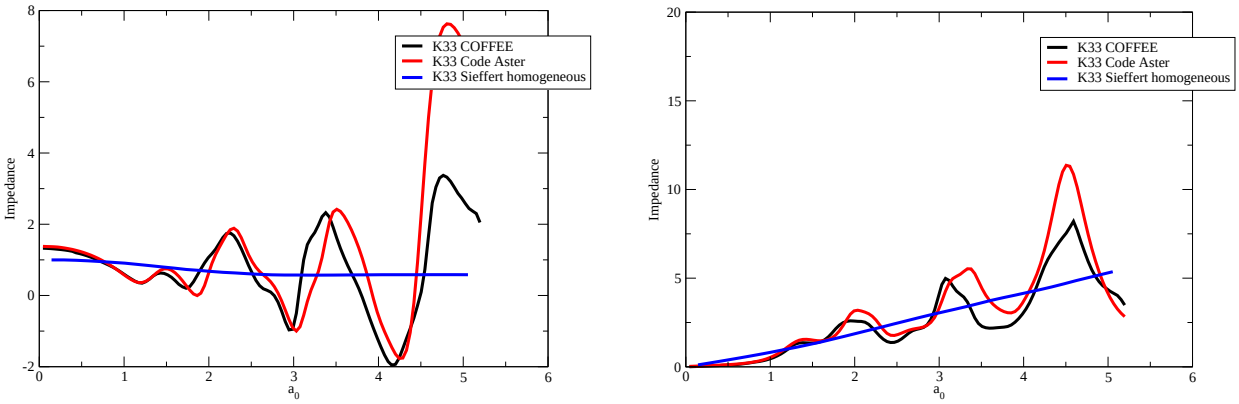

(a) *real part* **(b)** *imaginary part*

Figure 4.25.: *Circular surface footing on a multi-domain basin. Validation of the computation of the impedance of the vertical mode K_{33} (Eq 3.7): comparison between the FM-BEM solution (denoted COFFEE), the solution given by the FEM-BEM coupling (Code_ Aster) and the solution extracted from [60] (denoted Sieffert homogeneous) in the case of a homogeneous half-space.*

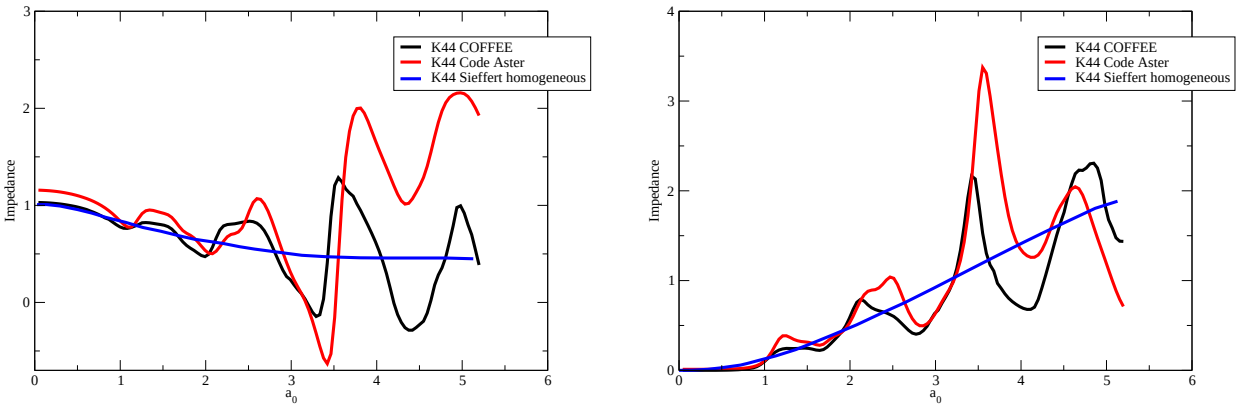

(a) *real part* **(b)** *imaginary part*

Figure 4.26.: *Circular surface footing on a multi-domain basin. Validation of the computation of the impedance of the rocking mode K_{44} (Eq 3.7): comparison between the FM-BEM solution (denoted COFFEE), the solution given by the FEM-BEM coupling (Code_ Aster) and the solution extracted from [60] (denoted Sieffert homogeneous) in the case of a homogeneous half-space*

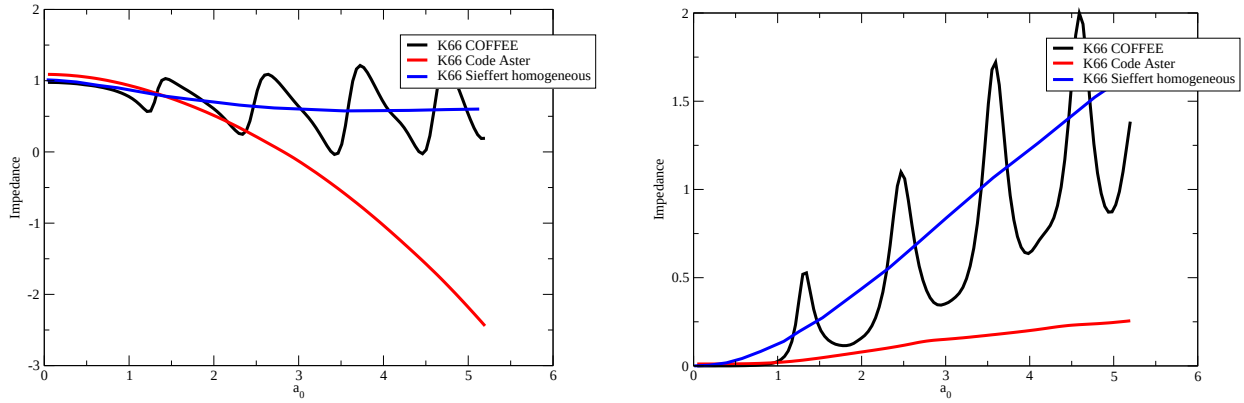

(a) *real part* **(b)** *imaginary part*

Figure 4.27.: *Circular surface footing on a multi-domain basin. Validation of the computation of the impedance of the horizontal mode K_{66} (Eq 3.7): comparison between the FM-BEM solution (denoted COFFEE), the solution given by the FEM-BEM coupling (Code_Aster) and the solution extracted from [60] (denoted Sieffert homogeneous) in the case of a homogeneous half-space*

4.2.2. Embedded cylindrical footing

Finally, the case of embedded cylindrical footing is considered for both the homogeneous case (i) and the case with a velocity contrast (ii). The impedances are not normalized because there is no analytical static solution. In addition, both models presented in the figures (i.e. impedances computed with *Coffee* and *Code_Aster*) correspond to identical configurations with the same geometries and the same mechanical properties. There is no need to normalize the results before comparing them.

Homogeneous half-space. Figures 4.28, 4.29, 4.30 and 4.31 present the impedances for the horizontal, vertical, rocking and torsion modes.

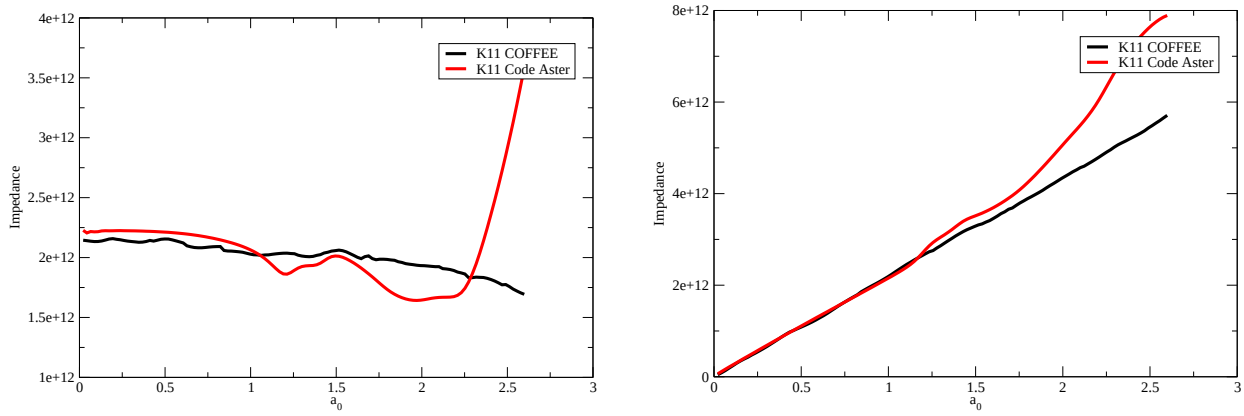

(a) *real part* ***(b)*** *imaginary part*

Figure 4.28.: *Embedded cylindrical footing on a homogeneous half-space. Validation of the computation of the impedance of the horizontal mode K_{11} (Eq 3.7): comparison between the FM-BEM (denoted COFFEE), FEM-BEM coupling (Code_Aster) solutions.*

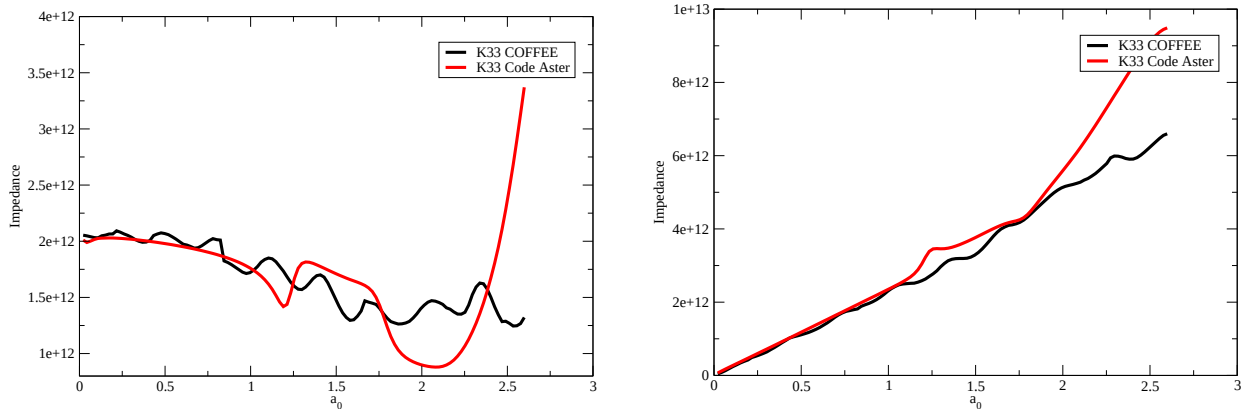

(a) *real part* ***(b)*** *imaginary part*

Figure 4.29.: *Embedded cylindrical footing on a homogeneous half-space. Validation of the computation of the impedance of the vertical mode K_{33} (Eq 3.7): comparison between the FM-BEM (denoted COFFEE), FEM-BEM coupling (Code_Aster) solutions.*

Results for the horizontal, vertical and rocking modes between the FM-BEM and the FEM-BEM coupling are in agreement, below the frequency that corresponds to the eigenmodes of the hemispherical basin. The impedance of the torsion mode, similarly to the case of the surface footing, differs from the others. The impedance of the rocking mode computed with the FEM-BEM coupling is largely influenced by the resonance of the eigenmodes of the hemispheric basin for a_0 greater than 1. Values of the impedance of the rocking mode computed with *Code_Aster* will not be taken into consideration for a_0 greater than 1.

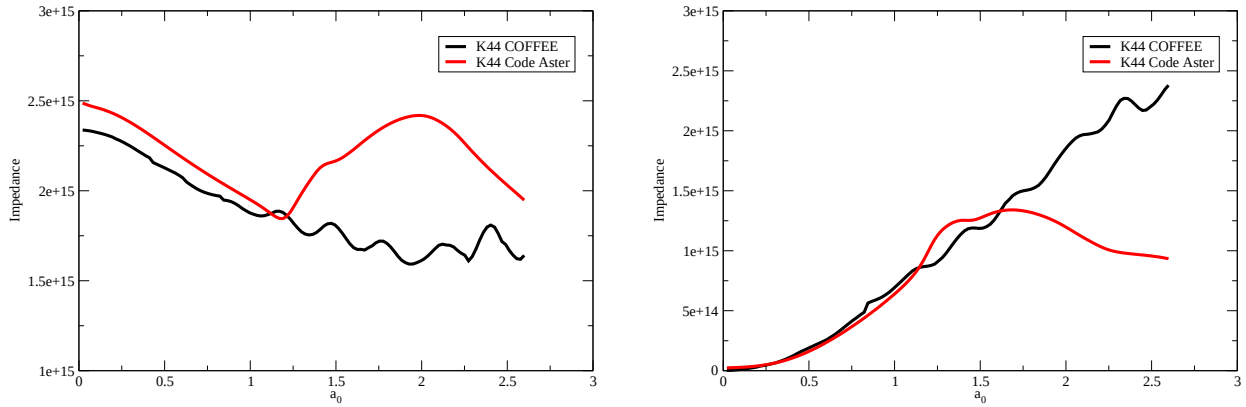

(a) *real part* ***(b)*** *imaginary part*

Figure 4.30.: *Embedded cylindrical footing on a homogeneous half-space. Validation of the computation of the impedance of the rocking mode K_{44} (Eq 3.7): comparison between the FM-BEM solution (denoted COFFEE), the solution given by the FEM-BEM coupling (Code_Aster).*

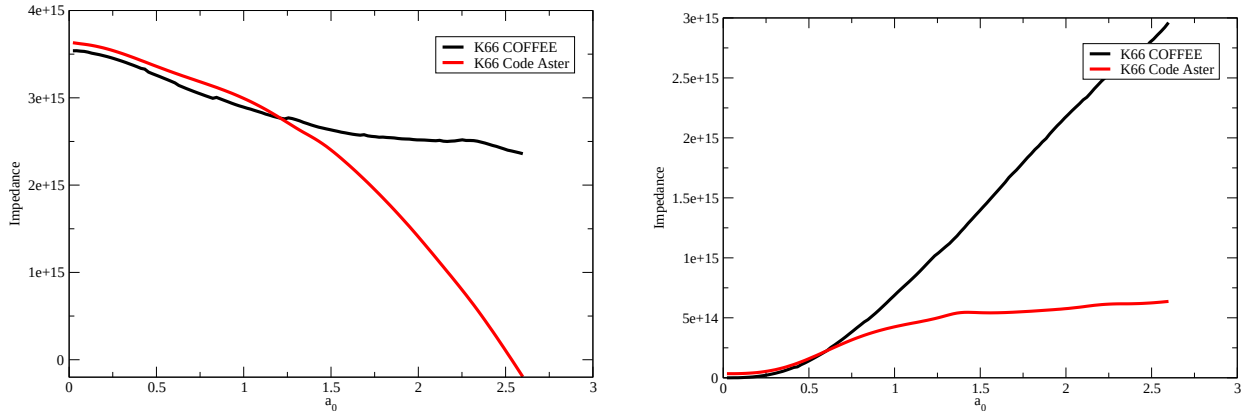

(a) *real part* ***(b)*** *imaginary part*

Figure 4.31.: *Embedded cylindrical footing on a homogeneous half-space. Validation of the computation of the impedance of the torsion mode K_{66} (Eq 3.7): comparison between the FM-BEM solution (denoted COFFEE), the solution given by the FEM-BEM coupling (Code_Aster).*

Basin with a material contrast. Figures 4.32, 4.33, 4.34 and 4.35 present the impedances for the horizontal, vertical, rocking and torsion modes. Results observed are similar to the homogeneous

case: while the horizontal and vertical modes show a good agreement between the impedances computed with the FM-BEM and the FEM-BEM coupling, differences are observed in the rocking mode for a_0 greater than 1. The torsion mode shows similar results than for the homogeneous case.

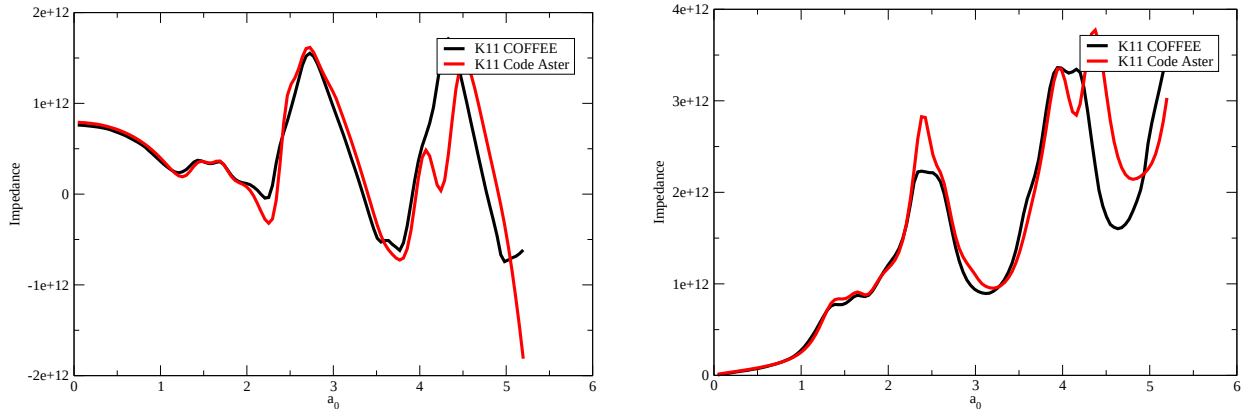

(a) *real part* **(b)** *imaginary part*

Figure 4.32.: *Embedded cylindrical footing on a multi-domain basin. Validation of the computation of the impedance of the horizontal mode K_{11} (Eq 3.7): comparison between the FM-BEM (denoted COFFEE) and the FEM-BEM coupling (Code_Aster) solutions.*

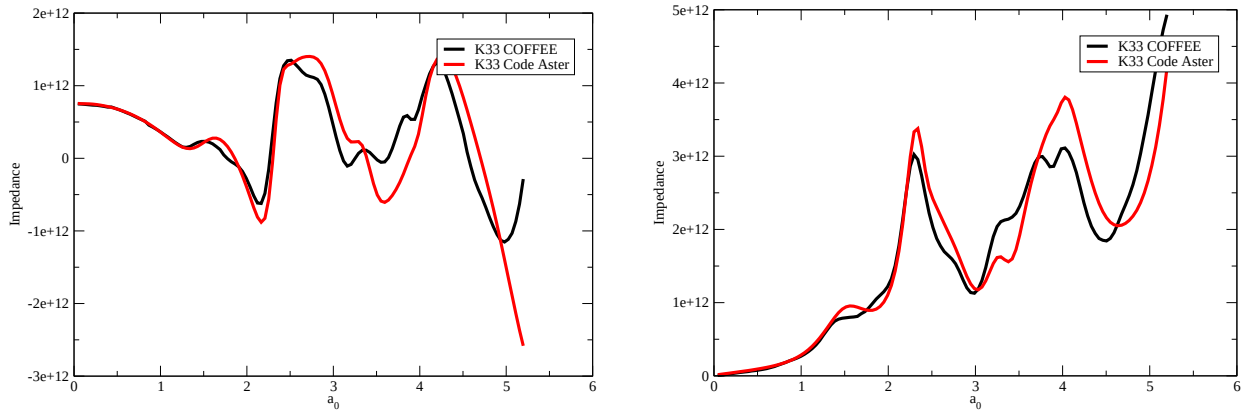

(a) *real part* **(b)** *imaginary part*

Figure 4.33.: *Embedded cylindrical footing on a multi-domain basin. Validation of the computation of the impedance of the vertical mode K_{33} (Eq 3.7): comparison between the FM-BEM (denoted COFFEE) and the FEM-BEM coupling (Code_Aster) solutions.*

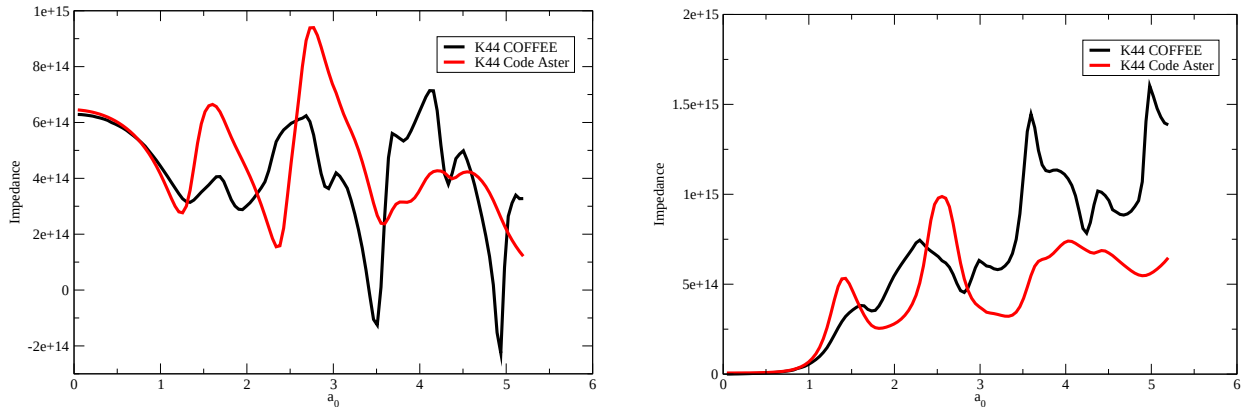

(a) *real part* **(b)** *imaginary part*

Figure 4.34.: *Embedded cylindrical footing on a multi-domain basin. Validation of the computation of the impedance of the rocking mode K_{44} (Eq 3.7): comparison between the FM-BEM (denoted COFFEE) and the FEM-BEM coupling (Code_Aster) solutions.*

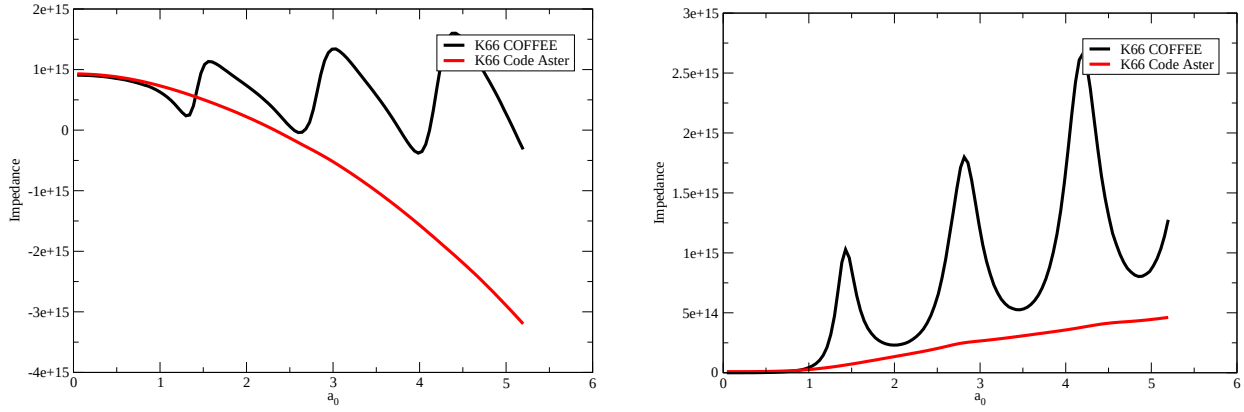

(a) *real part* **(b)** *imaginary part*

Figure 4.35.: *Embedded cylindrical footing on a multi-domain basin. Validation of the computation of the impedance of the torsion mode K_{66} (Eq 3.7):comparison between the FM-BEM (denoted COFFEE) and the FEM-BEM coupling (Code_Aster) solutions.*

4.3. Seismic force for a homogeneous basin

This section concerns the validation of the computation of the seismic forces (as defined in Chapter 3 after eq. (3.2)) performed by the coupling of the FM-BEM (i.e. *Coffee*) with the FEM (i.e. *Code_Aster*) for Soil-Structure Interaction computations. The reference solutions are now computed with the FEM (i.e. with *Code_Aster*). Each term of the seimic force corresponds to a type of wave (P or SV or SH) and a single mode. Hence, if the number of interface modes is m, each term of the seismic force f_{ij} corresponds to a given wave $j \in P, SV, SH$ and a given mode $i \in 1 \dots m$. As a result, the number of terms of the seismic force is equal to three (corresponding to three kinds of waves) times the number of modes.

The validation is performed with (i) a homogeneous half-space (constituted by a single medium) and

(ii) a multi-domain half-space formed by a hemispherical basin embedded in an infinite half-space. Results are compared to the seimic forces computed with the standard (non accelerated) BEM only by means of the Miss3D module available in with *Code_Aster*.

4.3.1. Circular surface footing

First, results for the computation of the seismic forces in the case of a circular surface footing on a homogeneous half-space are presented. The mechanical characteristics of the soil are defined by $C_s = 870\ m/s$, $C_p = 1727\ m/s$, $\nu = 0.33$ and the footing has a radius of 100 m (Fig. 4.36). The results of the FM-BEM are compared to the seismic forces computed with classical BEM code Miss3D in Figures 4.37 and 4.38.

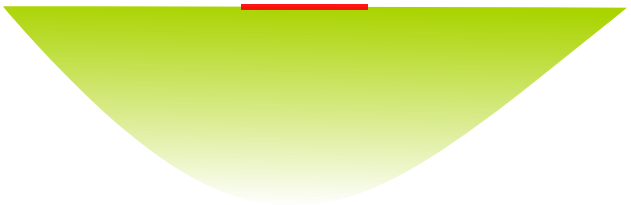

Figure 4.36.: *Surface footing on a homogeneous half-space.*

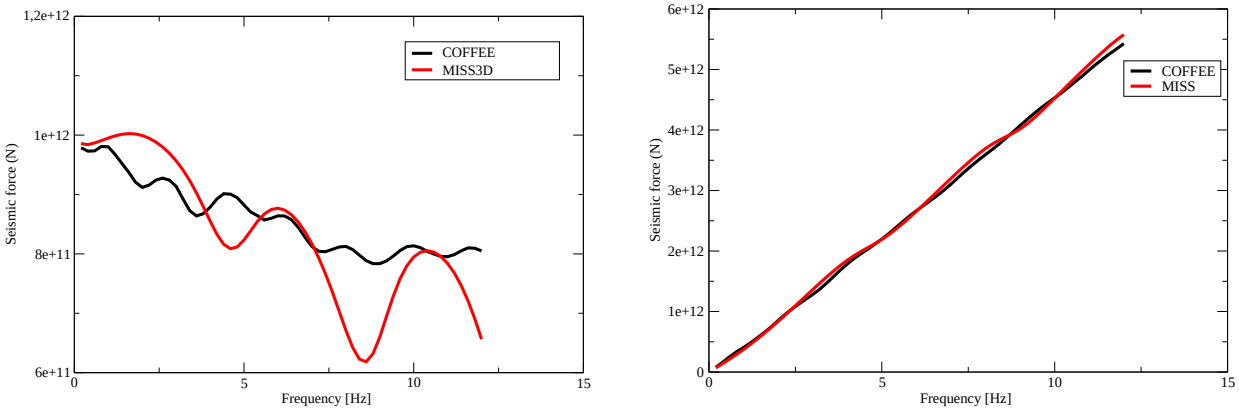

(a) *real part* ***(b)*** *imaginary part*

Figure 4.37.: *Validation of the computation of the seismic force for the coupling of SV-wave with the horizontal mode f_{11}: comparison between the FM-BEM solution (denoted COFFEE) and the solution given by classical BEM (denoted Miss3D).*

Each time, the real and imaginary parts of the seismic force are presented. A good agreement between the results of the FM-BEM and of the standard BEM are observed. Nevertheless, oscillations are observed in the seismic force corresponding to the real parts of the seismic forces computed with the standard BEM, due to the reflection of surface waves in the border of the meshed model. The results obtained with Miss3D involved the tuning of some empirical parameters of the code to obtain the best result. The computations presented here have shown an important sensitivity to the chosen parameters. However, for a fair comparison, we need to say that the model here is not favorable to

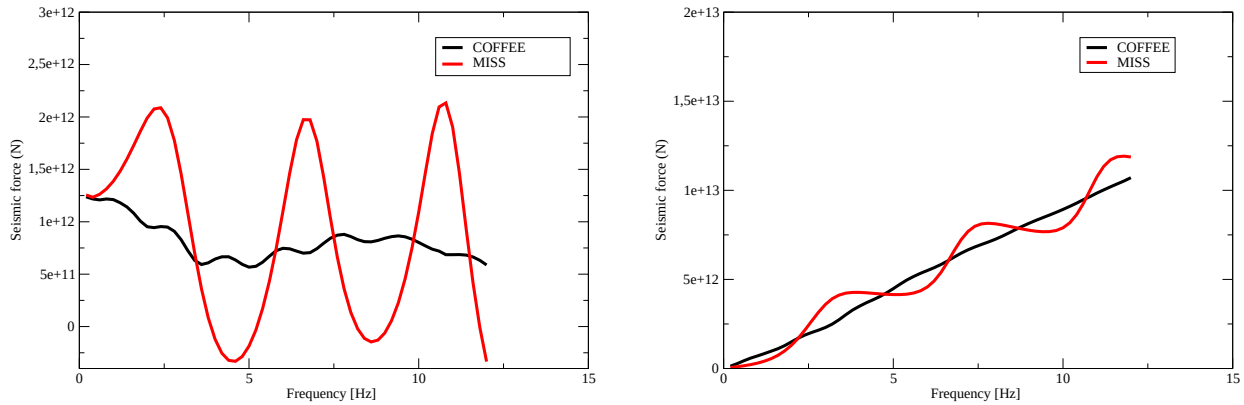

(a) *real part* **(b)** *imaginary part*

Figure 4.38.: *Validation of the computation of the seismic force for the coupling of P-wave with the vertical mode f_{33}: comparison between the FM-BEM solution (denoted COFFEE) and the solution given by classical BEM (denoted Miss3D).*

Miss3D as the sensitivity of the results to the parameters is more important for homogeneous cases, while for stratified soils with velocity contrasts it is a lot less sensitivity.

4.4. Seismic force in the case of a heterogeneous basin

This Section concerns the validation of the seismic forces computed with the FM-BEM in the case of multi-domain basin. The model consists of a hemispherical basin in an infinite half-space (Figure 4.39). The model features a velocity contrast, such that the hemispherical domain has wave velocities equal to half the velocities of the half-space. The cases of a surface footing and a embedded footing are studied. The mechanical characteristics of the soil are:

- characteristics of the hemispherical basin: $C_s = 870\ m/s$, $C_p = 1727\ m/s$, $\nu = 0.33$;
- characteristics of the half-space: $C_s = 1740\ m/s$, $C_p = 3455\ m/s$, $\nu = 0.33$.

The hemispheric basin has a radius of 100 m. The free surface is truncated at a distance equal to four times the radius of the hemispherical basin. The surface footing has a radius of 30 m. The embedded cylindrical footing has a radius of 30 m and a depth of 21 m. The frequency range of interest is $[0.2\ \text{Hz}, 24\ \text{Hz}]$.

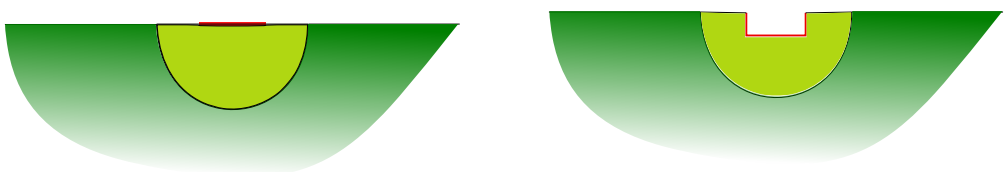

Figure 4.39.: *Surface and embedded footings in the case of a hemispherical basin in half-space.*

The reference solution consists in computing the seismic forces with a FEM-BEM coupling in *Code_Aster*, i.e. by modelling the half-space with the BEM and the hemispherical basin with the FEM (see Figure 4.40).

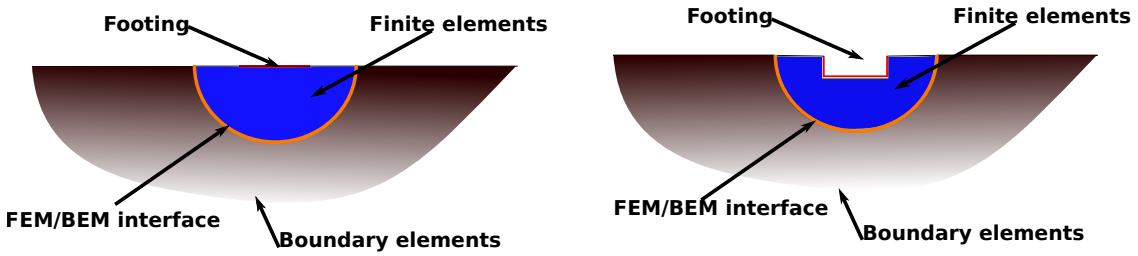

Figure 4.40.: *Surface and embedded footings in the case of a hemispherical basin in half-space.*

4.4.1. Circular surface footing

Results on Figures 4.41 and 4.42 for the circular surface footing show a good agreement between the FM-BEM and the FEM-BEM coupling. Besides the amplitude of certain eigenmodes is different, both curves follow the same tendance globally. For frequencies lower than 5Hz, the real part of the seismic forces are constant with respect to the frequency while the imaginary close to zero. The model exhibits the behaviour of a quasi-static system. There is no energy dissipated due to the radiated waves. These waves are reflected in large parts on the boundary between the hemispherical basin and the soil, due to the velocity contrast between the two media.

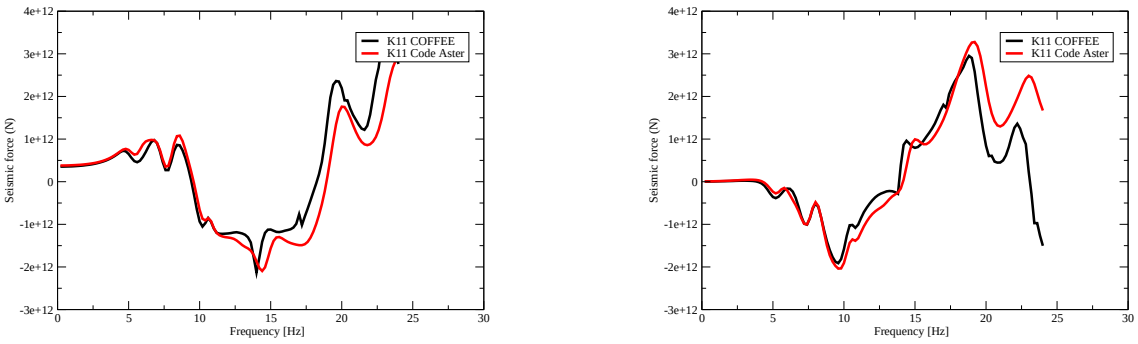

(a) *real part* ***(b)*** *imaginary part*

Figure 4.41.: *Validation of the computation of the seismic force for the coupling of SV-wave with the horizontal mode f_{11}: comparison between the FM-BEM solution (denoted COFFEE) and the solution given by the FEM-BEM coupling (Code_Aster).*

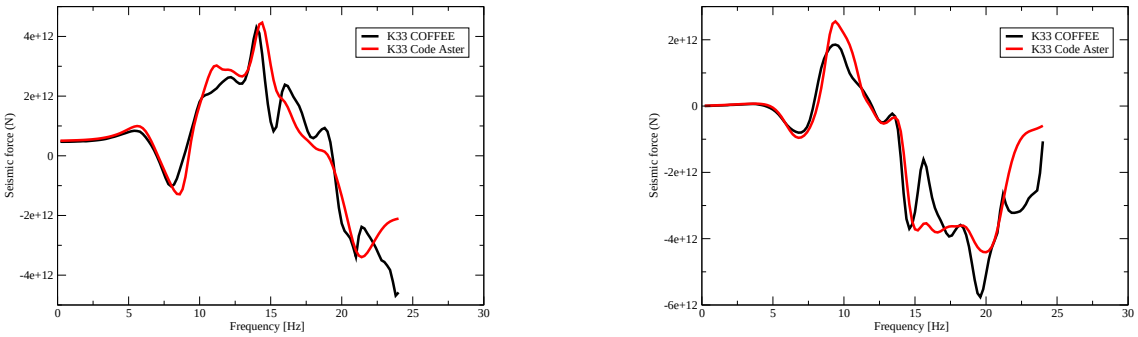

(a) *real part* ***(b)*** *imaginary part*

Figure 4.42.: *Validation of the computation of the seismic force for the coupling of P-wave with the vertical mode f_{33}: comparison between the FM-BEM solution (denoted COFFEE) and the solution given by the FEM-BEM coupling (Code_ Aster).*

In order to confirm the previous results, the homogeneous case is studied. The seismic forces are computed in the case of a homogeneous half-space with the following mechanical characteristics: $C_s = 1740\ m/s$, $C_p = 3455\ m/s$, $\nu = 0.33$. As seen in Figures 4.43 and 4.44, the system starts to dissipate energy from the first frequencies, as expected in the case of a homogeneous infinite half-space respecting the condition of radiation, which validates the used model with a material contrast.

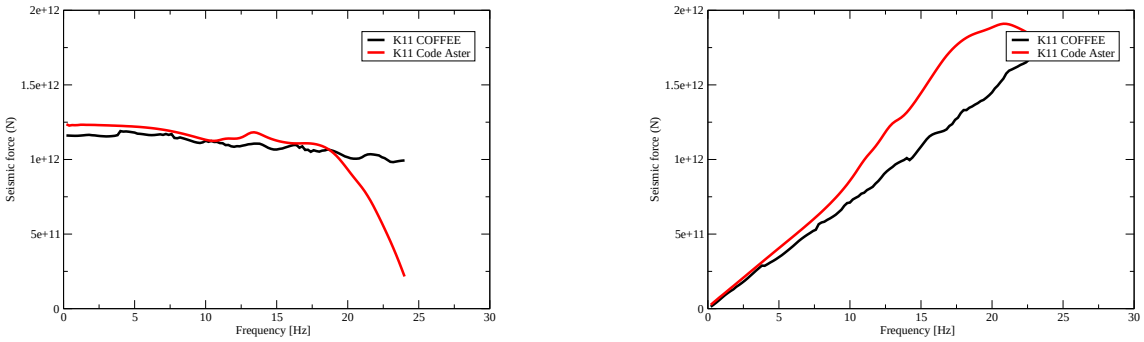

(a) *real part* ***(b)*** *imaginary part*

Figure 4.43.: *Validation of the computation of the seismic force for the coupling of SV-wave with the horizontal mode f_{11}: comparison between the FM-BEM solution (denoted COFFEE), the solution given by Code_ Aster.*

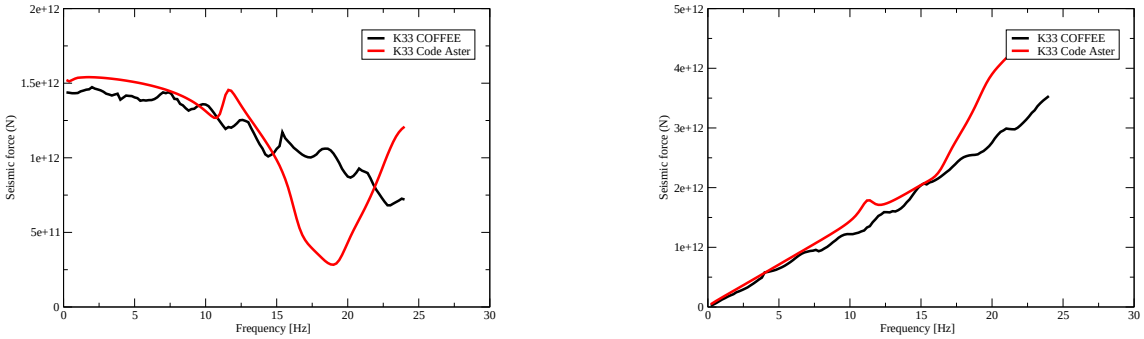

(a) *real part* ***(b)*** *imaginary part*

Figure 4.44.: *Validation of the computation of the seismic force for the coupling of P-wave with the horizontal mode f_{33}: comparison between the FM-BEM solution (denoted COFFEE), the solution given by Code_Aster.*

4.4.2. Embedded cylindrical footing

Results of the embedded cylindrical footing presented in Figures 4.45 and 4.46 are similar to the results of the circular surface footing. Both methods of computation of the seismic forces are in good agreement with some differences in the amplitude of the eigenmodes of the system. Similarly to the surface case, the system behaves as in quasi-static for frequencies lower than 5Hz.

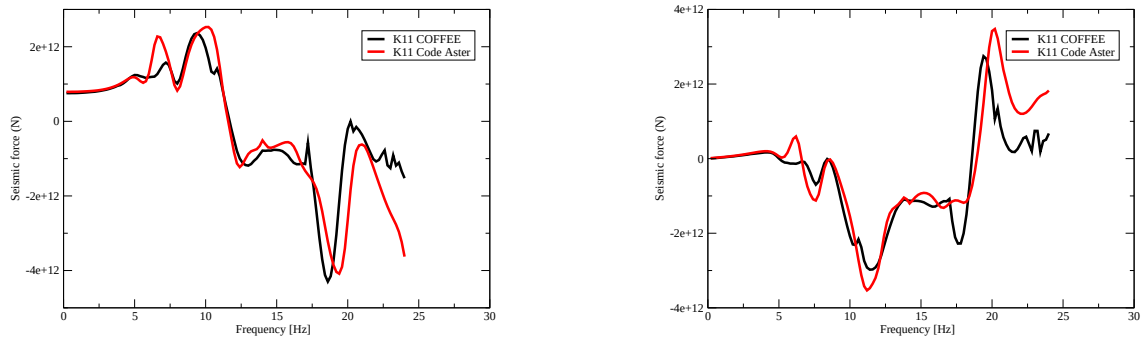

(a) *real part* ***(b)*** *imaginary part*

Figure 4.45.: *Embedded cylindrical footing. Validation of the computation of the seismic force for the coupling of SV-wave with the horizontal mode f_{11}: comparison between the FM-BEM (denoted COFFEE) and the FEM-BEM coupling (Code_Aster) solutions.*

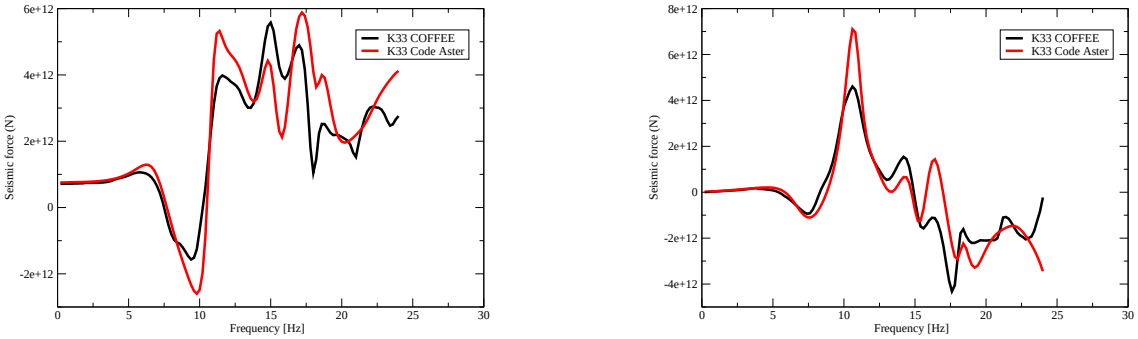

(a) *real part* ***(b)*** *imaginary part*

Figure 4.46.: *Embedded cylindrical footing. Validation of the computation of the seismic force for the coupling of SV-wave with the horizontal mode f_{33}: comparison between the FM-BEM (denoted COFFEE) and the FEM-BEM coupling (Code_Aster) solutions.*

4.5. Conclusion

The coupling strategy between the FEM and the FM-BEM outlined in Chapter 3 has been validated in this chapter. The computation of impedance operator and seismic forces have been compared to reference solutions for various models. The validation cases included surface and embedded footings, in homogeneous soils and soils with a velocity contrast between the infinite half-space and the hemispheric basin. In general, results computed with the FM-BEM are in good agreement with the reference solutions. The oscillations observed in the homogeneous cases are not observed in case of multi-domain models with velocity contrasts.

Chapter 5

Structural response for piecewise homogeneous media

Contents

5.1. Definition of the test case 80
5.2. Influence of the basin shape on the response of the structure 84
5.2.1. SV-wave 85
5.2.2. SH-wave 88
5.2.3. P-wave 90
5.3. Effect of an obliquely incident wave on the response of the structure . 92
5.3.1. SV-wave 92
5.3.2. SH-wave 97
5.3.3. P-wave 100
5.4. Conclusion 104

In this Chapter, results on the evaluation of site effects in the soil-structure interaction, using the coupling method of Chapter 3, are presented. In Chapter 4, the approach has been validated by comparisons with existing solutions. In this Chapter, the capabilities of this method coupling fast BEM and FEM are used to study the site effects on a building on top of a sedimentary basin.

5.1. Definition of the test case

Choice of sedimentary basin. Two different kind of soils (Figure 5.1) are used in this Chapter. The case (a) is a hemispherical basin in a homogeneous half-space. The radius of the hemisphere is $R = 100$ m. The case (b) is a horizontally stratified basin with two layers, the upper layer having a thickness of 100 m. It is clear that the larger the radius of the hemispherical basin is, the closer to the case of a stratified basin the response should be. The problem (a) is solved with the coupling of the FM-BEM (code *Coffee*) with the FEM (code *Code_Aster*). Since the FM-BEM uses the full-space fundamental solutions, the mesh must include a truncated free surface, which is truncated at a distance equal to $4R$. The problem (b) is solved with the coupling of the standard BEM (code *Miss3D* based on the layered half-space fundamental solutions) with the FEM (code *Code_Aster*).

In both cases, a circular embedded footing (with a 30 m radius and a 21.21 m depth) is placed in the sedimentary basin (Fig. 5.1).

Figure 5.1.: *Types of basin used: Case (a) hemispherical basin in homogeneous half-space (left) and Case (b) horizontally stratified basin (right).*

Modeling of the structure. The structure of interest is a six-story building (with a 42.3 m height) which is modelled by a concentrated mass in each floor, with an equivalent one-dimensional beam connecting the concentrated masses (Fig. 5.1). The interest of modeling the building with an equivalent one-dimensional structure with concentrated masses is to approach the structure by a quite simple model, with few degrees of freedom (six degrees of freedom per concentrated mass: three translations and three rotations), which nevertheless gives enough informations about the response of the structure. The response of the structure at each floor can then be used to later model each floor separately.

The approach presented in Chapter 3 relying on a reduced basis. In this Chapter, the selected reduced basis consists of eigenmodes of the structure that represents up to 80% of the total mass of

the structure, and the six rigid body modes of the footing. To achieve this criterion, the effective mass is relied upon: it represents the mass moved by a mode in a certain direction (in this case: the X,Y and Z direction). The unit effective mass $\mu(\Phi, d)$ of the Φ mode in the direction d for the case of a structure of total mass m_t is computed as

$$\mu(\Phi, d) = \frac{({}^t\underline{\Phi}.\underline{\underline{M}}.\underline{D})^2}{{}^t\underline{\Phi}.\underline{\underline{M}}.\underline{\Phi}}.\frac{1}{m_t}.$$

In this specific case, the structure is characterised by the eigenmodes presented in Tables 5.1, 5.2 and 5.3.

Table 5.1.: *Frequencies, unit effective mass and cumulated effective mass for the eigenmodes in u_x direction. The most important modes in this direction are indicated in blue.*

Frequencies (Hz)	Unit effective mass	Cumulated unit effective mass
1.28601E+00	8.42591E-33	8.42591E-33
1.46002E+00	5.86449E-01	5.86449E-01
3.05322E+00	1.45367E-37	5.86449E-01
3.50889E+00	1.47033E-01	7.33482E-01
3.94676E+00	3.60907E-33	7.33482E-01
5.49576E+00	1.72825E-32	7.33482E-01
6.82155E+00	3.16887E-02	7.65171E-01
7.12905E+00	9.95722E-35	7.65171E-01
8.06154E+00	1.55499E-02	7.80721E-01
8.16988E+00	2.85748E-32	7.80721E-01
9.33858E+00	2.50355E-02	8.05756E-01
9.78819E+00	3.44869E-34	8.05756E-01
1.06265E+01	6.57818E-39	8.05756E-01
1.48843E+01	8.46278E-33	8.05756E-01
1.93325E+01	1.53139E-34	8.05756E-01

Table 5.2.: *Frequencies, unit effective mass and cumulated effective mass for the eigenmodes in u_y direction. The most important modes in this direction are indicated in blue.*

Frequencies (Hz)	Unit effective mass	Cumulated unit effective mass
1.28601E+00	5.79638E-01	5.79638E-01
1.46002E+00	8.94693E-34	5.79638E-01
3.05322E+00	1.44059E-01	7.23697E-01
3.50889E+00	5.22772E-31	7.23697E-01
3.94676E+00	6.86120E-29	7.23697E-01
5.49576E+00	4.32442E-02	7.66941E-01
6.82155E+00	2.41801E-32	7.66941E-01
7.12905E+00	5.47312E-03	7.72415E-01
8.06154E+00	3.75832E-32	7.72415E-01
8.16988E+00	3.25206E-02	8.04935E-01
9.33858E+00	2.15027E-35	8.04935E-01
9.78819E+00	2.44724E-33	8.04935E-01
1.06265E+01	1.07710E-03	8.06012E-01
1.48843E+01	1.80911E-33	8.06012E-01
1.93325E+01	1.30421E-33	8.06012E-01

Table 5.3.: *Frequencies, unit effective mass and cumulated effective mass for the eigenmodes in u_z direction. The most important modes in this direction are indicated in blue.*

Frequencies (Hz)	Unit effective mass	Cumulated unit effective mass
1.28601E+00	6.16785E-35	6.16785E-35
1.46002E+00	2.20294E-33	2.26462E-33
3.05322E+00	5.09186E-33	7.35648E-33
3.50889E+00	8.92100E-33	1.62775E-32
3.94676E+00	7.07028E-01	7.07028E-01
5.49576E+00	3.88665E-32	7.07028E-01
6.82155E+00	1.16674E-34	7.07028E-01
7.12905E+00	1.45962E-39	7.07028E-01
8.06154E+00	1.44076E-33	7.07028E-01
8.16988E+00	4.39184E-32	7.07028E-01
9.33858E+00	2.54579E-33	7.07028E-01
9.78819E+00	3.17257E-02	7.38754E-01
1.06265E+01	8.92598E-34	7.38754E-01
1.48843E+01	4.01711E-02	7.78925E-01
1.93325E+01	2.68998E-02	8.05825E-01

This footing has geometrical characteristics (i.e. 30 m radius) that are of significant magnitude in comparison with the geometrical characteristic length of the sedimentary basin (ie 100 m). This may allow to show the impact of the site effects concerning the shape of the basin.

Parametric study. The mechanical characteristics of the soil are modified in order to see the interactions between site effects (due to material contrasts and by the geometry of the basin) and the response of the structure. The mechanical characteristics of the inner basin (light green in Figure 5.1) are fixed in all examples to $C_s = 870$ m/s, $C_p = 1727$ m/s and $\nu = 0,33$, while the characteristics of the outer soil are varied to achieve a given contrast with respect to the inner soil parameters. The incident fields considered are a unit harmonic plane wave, P-waves, SH-waves or SV-waves. The angle of incidence of each of the three waves is varied such that it takes the following values: 0^o, 10^o, 20^o and 30^o. The range of frequencies of interest is $[0.2Hz, 20Hz]$, with a step of 0.2Hz.

In the following, the quantities of interest are the displacements along each of the directions of the base of the structure, in time-harmonic domain. Such quantities will be called transfer functions in the following. The response of the point of interest in the structure to the incident field is reported in each case. The results are presented as functions of the frequency, which is normalized by the first resonance frequency of the upper layer of the stratified basin. It is well known that the resonance frequency of the n-th mode of a layered soil, in the case of an incident plane wave with a velocity V, is equal to $f_n = (2n-1)V/4h$, with h the thickness of the layer. As a result, the first resonance frequency is equal to $f_s = C_s/4h$ when considering an incident SV-wave or SH-wave, while it is equal to $f_p = C_p/4h$ when considering an incident P-wave. The modes of the structure corresponding to

the direction of interest are also plotted in the figures with the quantities of interest: they correspond to the frequencies with significant effective unit mass shown (in blue) in Tables 5.1, 5.2 and 5.3.

5.2. Influence of the basin shape on the response of the structure

This section considers the influence of the basin shape on the response of the structure. The characteristic length of the basin is close enough to the size of the basin for the site effects to have a significant effect on the response of the structure.

In this section, the structure is laid on two type of soils (Figure 5.2): a hemispherical basin in a homogeneous half-space (case a) and a horizontally stratified soil (case b). The case (a) is solved with the coupling of the FM-BEM code *Coffee* with the FEM code *Code_Aster*, the model consists of 4644 nodes and 9334 elements (the mesh of the free surface included). The case (b) is solved with the coupling of the standard BEM code Miss3D with the FEM code *Code_Aster*, the model consists of 887 nodes and 1268 elements, as only the interface between the BEM part and the FEM part is meshed, since the BEM formulation used is based on the layered half-space fundamental solutions.

The hemispherical basin has a $R = 100$ m radius, and the upper layer of the stratified soil has a thickness of 100 m. Results are presented for velocity contrasts $C_s^2/C_s^1 = C_p^2/C_p^1 = 1, 2$ and 4. In both cases, a circular embedded footing of a radius of 30 m and a depth of 21.21 m is placed in the sedimentary basin. The FM-BEM/FEM interface and the BEM-FEM interface are the circular embedded footing (shown in red in Fig. 5.2).

Figure 5.2.: *Types of basin used: Case (a) hemispherical basin in homogeneous half-space (left) and Case (b) horizontally stratified basin (right).*

Excitation by plane waves, namely a SV-wave, a SH-wave and a P-wave of unit amplitude, are imposed. Results are presented separately for each type of wave. The P-wave and SV-wave propagate in the XZ-plane (Fig. 5.3). The SH-wave is orthogonal to both other waves (Fig. 5.3).

For the layered soil, the plane waves are expected to cause displacement only in the direction of their respective polarization.

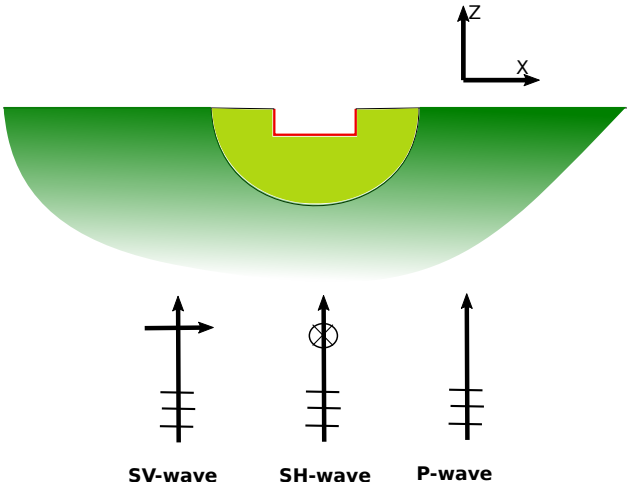

Figure 5.3.: *Polarization of the plane waves.*

In the following, for each type of wave (SV-wave, SH-wave and P-wave), the free-field at the bottom center of the footing (i.e. the displacement in the absence of structure) and the displacement at the base of the structure are shown. The displacement being complex-valued, its modulus is chosen as a representative value.

5.2.1. SV-wave

Figures 5.4(**b**) (**d**) and (**f**) present the results for the horizontal displacement along the X-direction, the horizontal displacement along the Y-direction and the vertical displacement along the Z-direction at the base of the structure. Figures 5.4(**a**) (**c**) and (**e**) present the results of the horizontal displacement along the X-direction, the horizontal displacement along the Y-direction and the vertical displacement along Z-direction at the bottom of the cylinder, in the absence of the structure. The aim of presenting the free-field displacement is to evaluate its influence on the response of the structure. Those displacements result from imposing a unit plane SV-wave in vertical incidence.

The largest component of the displacement is along the X-direction, which is expected since the polarization of the SV-wave is along the same direction. Concerning the free-field, displacement along Y-direction and Z-direction are expected to vanish for both the stratified and the hemispherical basin, due to the symmetries of the problem. However, the free field in the Y-direction and Z-direction shows non-negligible values, this might be due to numerical errors caused by the approximation due to the tolerance of the iterative solver (here fixed at 0.005), the geometrical error due to the discretization of the mesh with triangular linear elements and the truncation of the free surface.

In the following, the only quantity of interest is the displacement along the X-direction. The comparison of the results for the homogeneous case of the hemispherical basin and the stratified basin shows good correspondance as expected and validates the modelization, for both results of

the free-field and the response at the base of the structure.

The response of the structure in the X-direction is driven by the horizontal eigenmodes of the structure at frequencies close to corresponding eigenfrequencies, while it is driven by the free-field for frequencies relatively far from the eigenfrequencies in the X-direction.

The amplitude of the response at the base of the structure when driven by the eigemodes of the structure are relatively small (always lower than 1) compared to the values of the amplitude of the response when driven by the free-field that can reach values up to 18 (velocity ratio of 4) and up to 3 (velocity ratio of 2) for the case of the hemispherical basin and values up to 4 (velocity ratio of 4) and up to 2 (velocity ratio of 2) for the case of the stratified basin. The peaks of the response correspond to the peaks of the response of the free-field.

The transfer function of the structure in the hemispherical basin have globally larger values than that of the stratified basin. Also, both the stratified basin and the hemispherical basin exhibited an increase of the transfer function caused by an increase of the velocity contrast, however the increase of the transfer function caused by an increase in the velocity ratio in the case of the hemispherical basin is more important than that of the stratified basin, due to the 3D shape of the hemispherical basin.

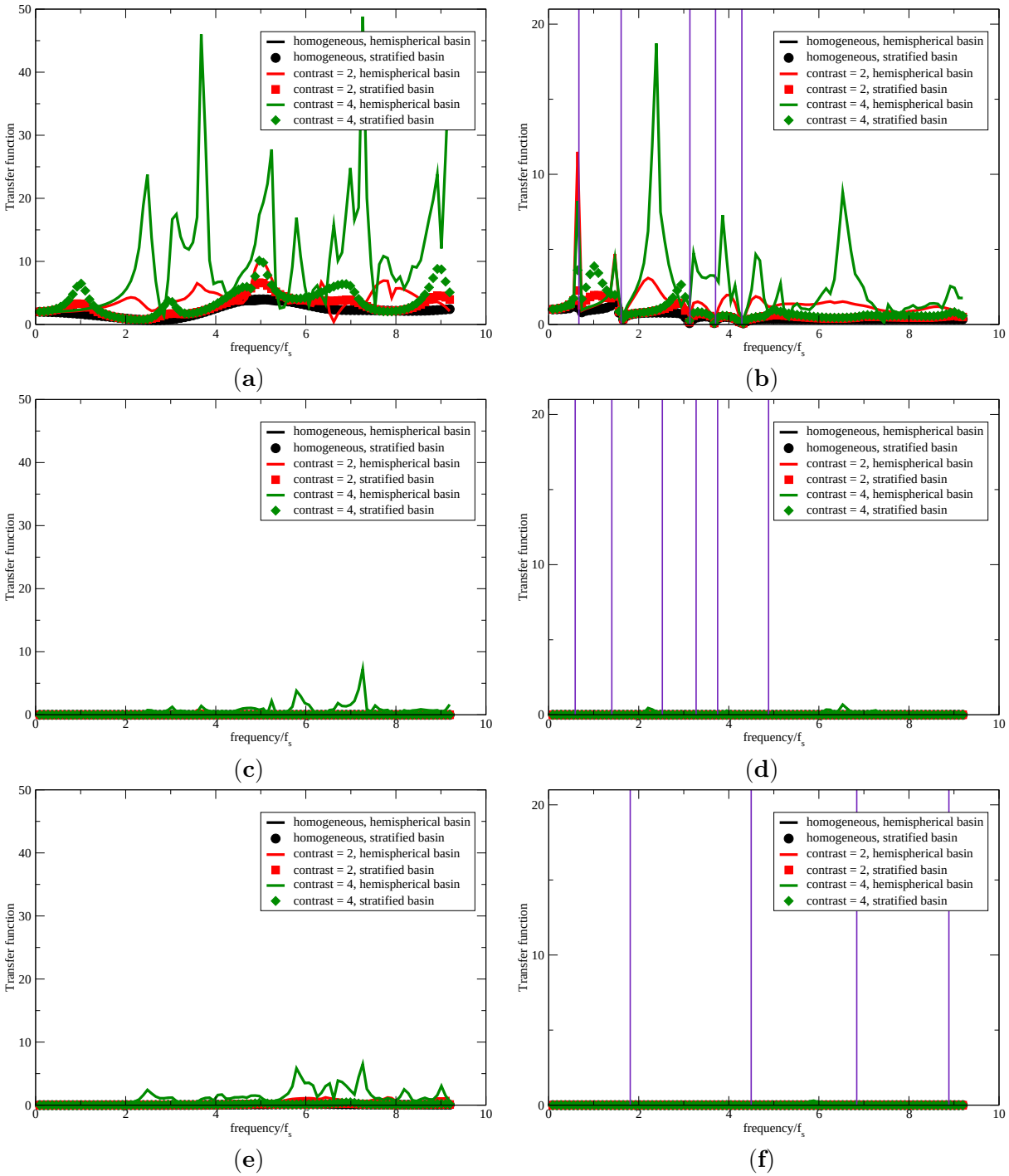

Figure 5.4.: *Free field displacements along the* (**a**) *X-,* (**c**) *Y- and* (**e**) *Z-direction; and displacements along the* (**b**) *X-,* (**d**) *Y- and* (**f**) *Z-direction at the base of the structure. A vertical incident unit plane SV-wave is imposed as a loading.*

5.2.2. SH-wave

Figures 5.5(**b**) (**d**) and (**f**) present the results of the horizontal displacement along the X-direction, the horizontal displacement along the Y-direction and the vertical displacement along the Z-direction at the base of the structure. Figures 5.5(**a**) (**c**) and (**e**) present the results of the horizontal displacement along the X-direction, the horizontal displacement along the Y-direction and the vertical displacement along Z-direction at the bottom of the cylinder. In the absence of the structure, the aim of presenting the free-field displacement is to evaluate its influence on the response of the structure. Those displacements result from imposing a unit plane SH-wave in vertical incidence.

The largest component of the displacement is along the Y-direction, which is expected since the polarization of the SH-wave is along the same direction. In the following, the only quantity of interest considered is the displacement along the Y-direction.

The comparison of the results for the homogeneous case of the hemispherical basin and the stratified basin shows good correspondance as expected and validates the modelization, for both results of the free-field and the response at the base of the structure.

Similarly to the case where an SV-wave was imposed, the response of the structure in the Y-direction is mainly driven by the eigenmodes of the structure at frequencies close to corresponding eigenfrequencies, and it is driven by the free-field for frequencies relatively far from the eigenfrequencies in the Y-direction. Also, the amplitude of the response at the base of the structure when driven by the eigenmodes of the structure is relatively small (always lower than 1) compared to the values of the amplitude of the response when driven by the free-field that can reach values up to 20 for the case of the hemispherical basin and values up to 4 for the case of the stratified basin. The peaks of the response correspond to the peaks of the response of the free-field. As it was the case when applying an SV-wave, the transfer function of the structure in the hemispherical basin have globally larger values than that of the stratified basin. Also, both the stratified basin and the hemispherical basin exhibit an increase of the transfer function caused by an increase of the velocity contrast.

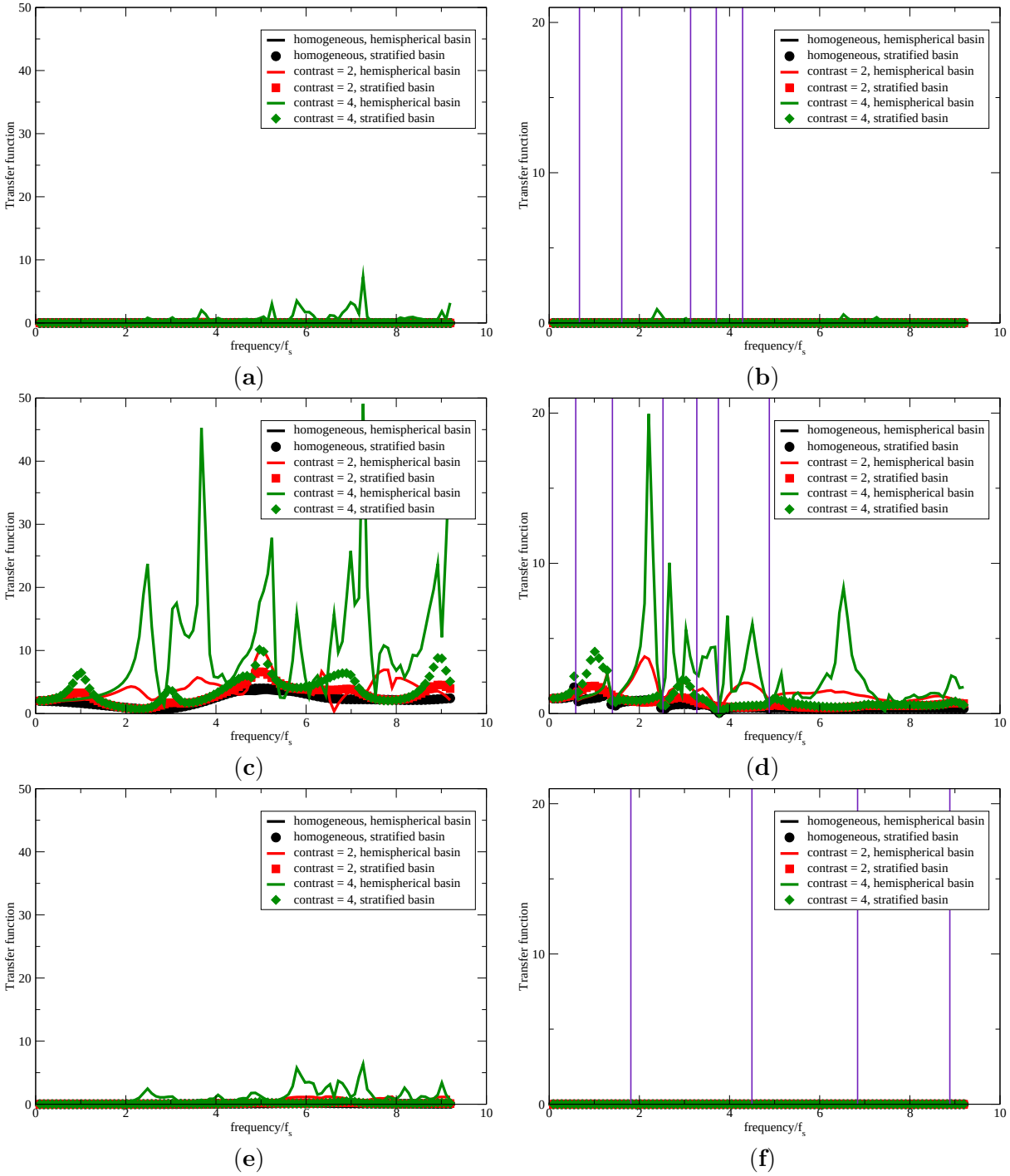

Figure 5.5.: *Free field displacements along the* (**a**, **b**) *X-,* (**c**, **d**) *Y- and* (**e**, **f**) *Z-direction. A vertical incident unit plane SH-wave is imposed as a loading.*

5.2.3. P-wave

Figures 5.6(**b**) (**d**) and (**f**) present the results of the horizontal displacement along the X-direction, the horizontal displacement along the Y-direction and the vertical displacement along the Z-direction at the base of the structure. Figures 5.6(**a**) (**c**) and (**e**) present the results of the horizontal displacement along the X-direction, the horizontal displacement along the Y-direction and the vertical displacement along Z-direction at the bottom of the cylinder, in the absence of the structure. As before, the aim of presenting the free-field displacement is to evaluate its influence on the response of the structure. Those displacements result from imposing a unit plane P-wave in vertical incidence.

The largest component of the displacement is along the Z-direction, which is expected since the polarization of the P-wave is along the same direction. In the following, the only quantity of interest considered is the displacement along the Z-direction.

The comparison of the results for the homogeneous case of the hemispherical basin and the stratified basin shows good correspondance as expected and validates the modelization, for both results of the free-field and the response at the base of the structure.

Similarly to the case where an SV-wave was imposed, the response of the structure in the Z-direction is mainly driven by the eigenmodes of the structure at frequencies close to corresponding eigenfrequencies, and it is driven by the free-field for frequencies relatively far from the eigenfrequencies in the Z-direction. Also, the amplitude of the response at the base of the structure when driven by the eigenmodes of the structure are relatively small (always lower than 1) compared to the values of the amplitude of the response when driven by the free-field that can reach values up to 10 for the case of the hemispherical basin and values up to 12 for the case of the stratified basin. The peaks of the response correspond to the peaks of the response of the free-field. As it was the case when applying an SV-wave, the transfer function of the structure in the hemispherical basin have globally larger values than that of the stratified basin. Also, both the stratified basin and the hemispherical basin exhibited an increase of the transfer function caused by an increase of the velocity contrast.

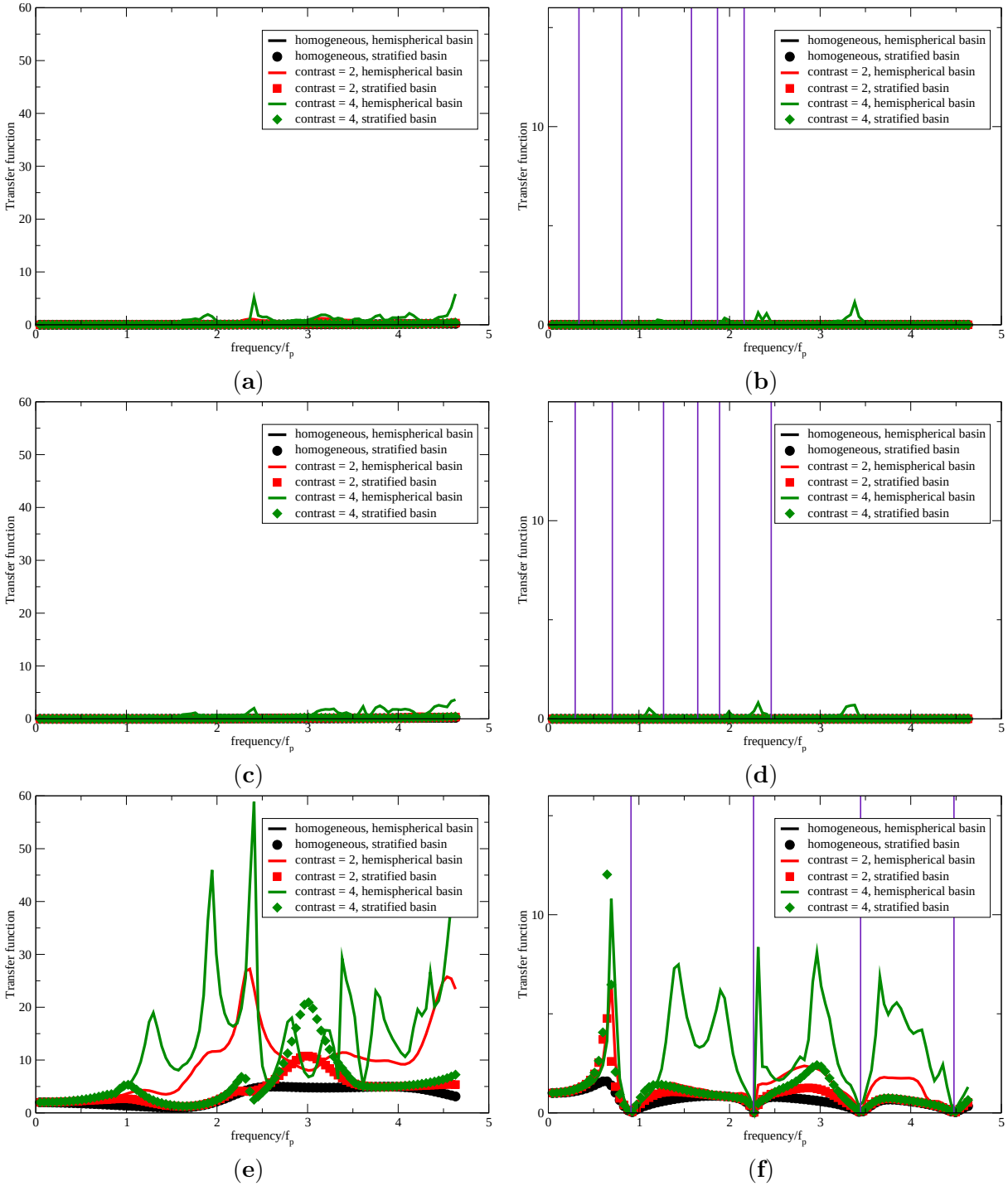

Figure 5.6.: *Free field displacements along the (**a**) X-, (**c**) Y- and (**e**) Z-direction; and displacements along the (**b**) X-, (**d**) Y- and (**f**) Z-direction at the base of the structure. A vertical incident unit plane P-wave is imposed as a loading.*

5.3. Effect of an obliquely incident wave on the response of the structure

This section examines the influence of the angle of incidence of an incident plane wave on the response of the structure, more specifically on the base of the structure, in the case of the hemispherical basin in a homogeneous half-space. Three kind of waves are used separately: SV-wave, SH-wave and P-wave (Figure 5.3). The angles of incidence considered are $\theta = 0^o, 10^o, 20^o$ and 30^o (Figure 5.7).

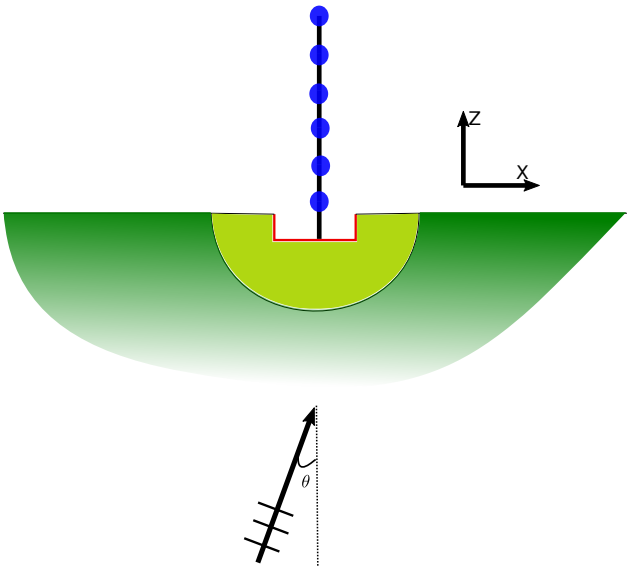

Figure 5.7.: *Oblique incident plane wave.*

The problem is solved with the coupling of the FM-BEM code *Coffee* with the FEM code *Code_Aster*, the model consists of 4644 nodes and 9334 elements (the mesh of the free surface included).

The hemispherical basin has a radius of $R = 100$ m, a circular embedded footing with a radius 30 m and a depth of 21.21 m is placed in the sedimentary basin. The FM-BEM/FEM interface is the circular embedded footing (in red in Figure 5.7). Results are presented for velocity contrasts $C_s^2/C_s^1 = C_p^2/C_p^1 = 1, 2, 4$.

5.3.1. SV-wave

Figures 5.8, 5.9, 5.10 and 5.11 present the results of the horizontal displacement along the X-direction, the horizontal displacement along the Y-direction, the vertical displacement along Z-direction and the total displacement norm defined as $\| u_t \| = \sqrt{| u_x |^2 + | u_y |^2 + | u_z |^2}$. Those are the resulting displacements of imposing a unit plane SV-wave.

The first remark is that the displacement in the Y-direction is almost null: imposing a SV-wave in the XZ-plane does not generate displacement outside of this plane.

Concerning the displacement along X and Z: the transfer functions of the three different velocity ratios ($C = 1, 2, 4$) exhibits similar pattern for the four angles of incidence. The transfer functions are also driven by the eigenmodes for frequencies close to the eigenfrequencies and driven by the free-field when not close to the eigenfrequencies. Globally, the incidences of $\theta = 0^o, 10^o$ and 20^o have similar transfer functions while the incidence of $\theta = 30^o$ is globally more important than the latters. Important maximum amplifications are observed for the velocity contrast of $C = 2, 4$, with values up to 19 in the X-direction for a velocity ratio of two and 27 for a velocity ratio of 4, but for different frequencies, probably because of the shift in the eigenfrequencies of the hemispherical basin due to the change in the velocity ratio. Maximum amplifications in the Z-directions for velocity ratios of 2 and 4 reached values of 2 and 9 respectively.

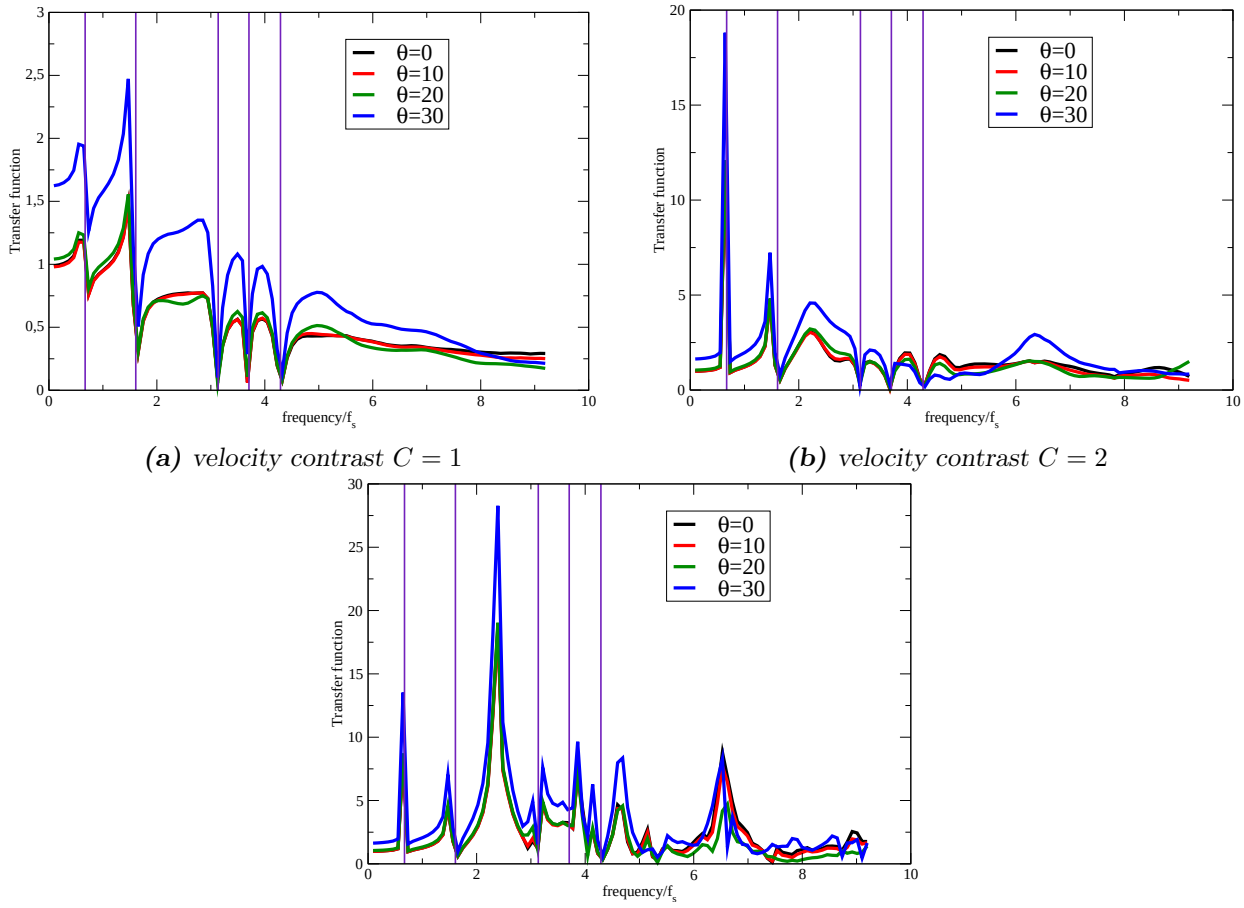

(a) *velocity contrast $C = 1$*

(b) *velocity contrast $C = 2$*

(c) *velocity contrast $C = 4$*

Figure 5.8.: *Horizontal displacement along the X-direction at the base of the structure. An incident unit plane SV-wave is imposed as a loading for various angle of incidence.*

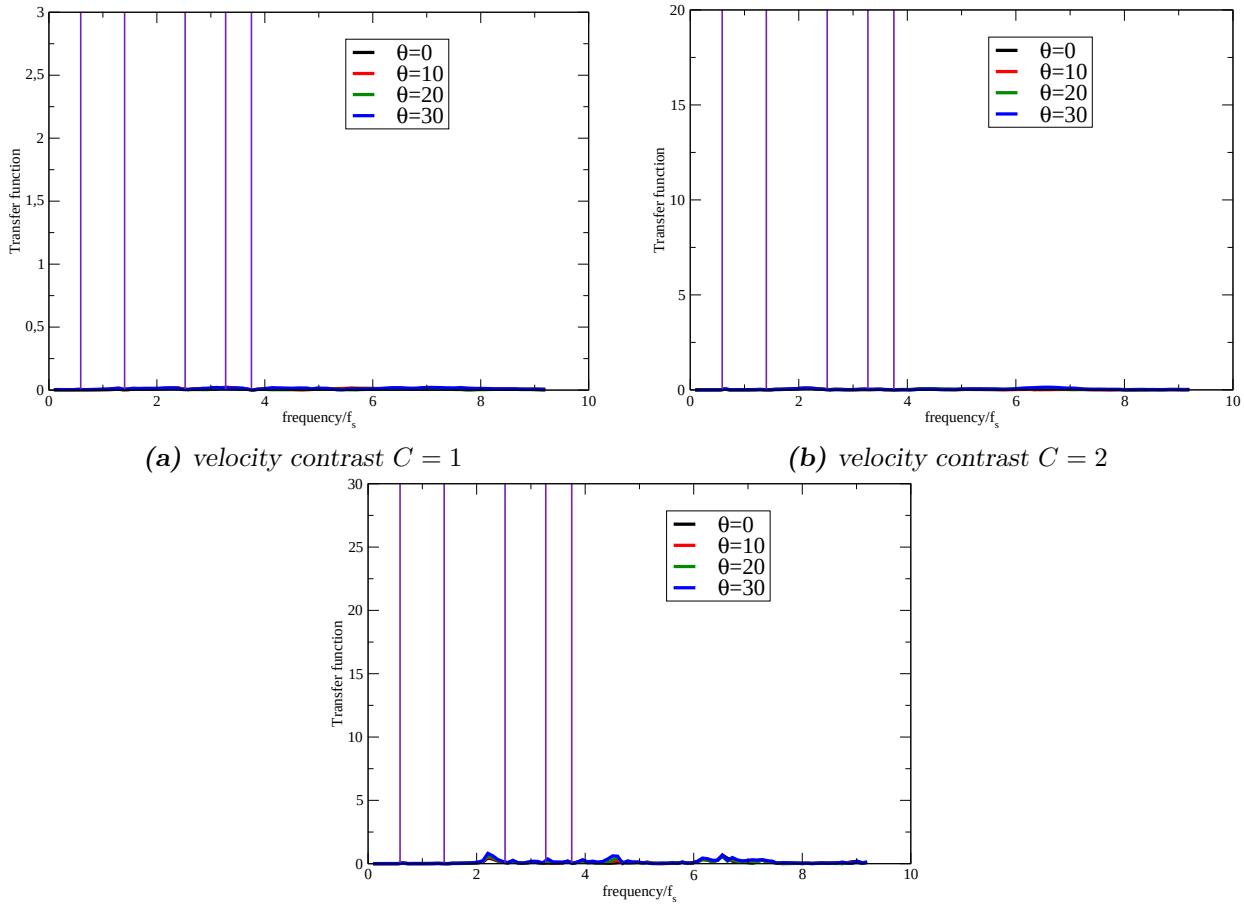

(a) *velocity contrast* $C = 1$

(b) *velocity contrast* $C = 2$

(c) *velocity contrast* $C = 4$

Figure 5.9.: *Horizontal displacement along the Y-direction at the base of the structure. An incident unit plane SV-wave is imposed as a loading for various angle of incidence.*

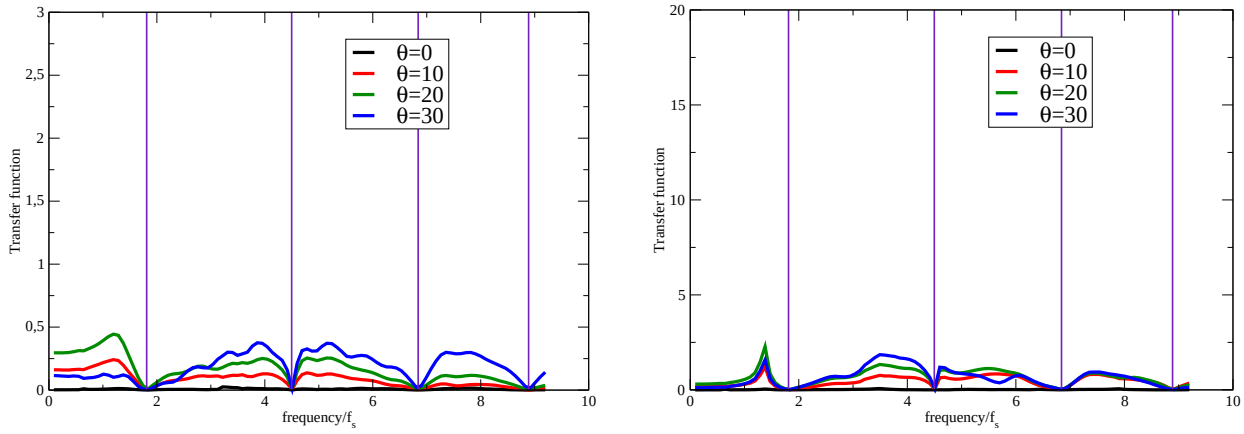

(a) *velocity contrast* $C = 1$

(b) *velocity contrast* $C = 2$

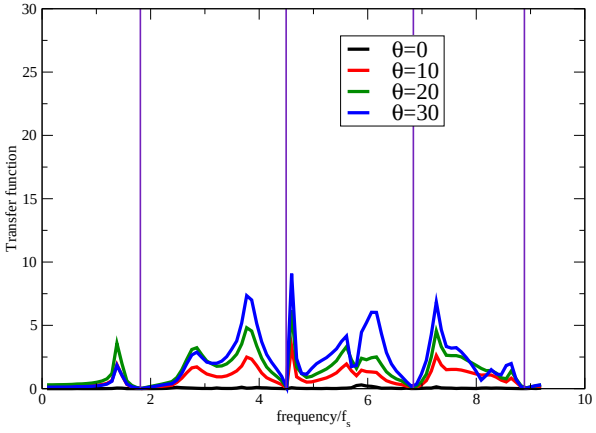

(c) *velocity contrast* $C = 4$

Figure 5.10.: *Vertical displacement along the Z-direction at the base of the structure. An incident unit plane SV-wave is imposed as a loading for various angle of incidence.*

An important quantity to look into is the total displacement, since the incident wave has now non-null components along the X-direction and Z-direction, it is hard to determine if the increase of displacement along the Z-direction with the angle, was due to the increase to the component of the incident SV-wave along the Z-direction, or due to other phenomena.

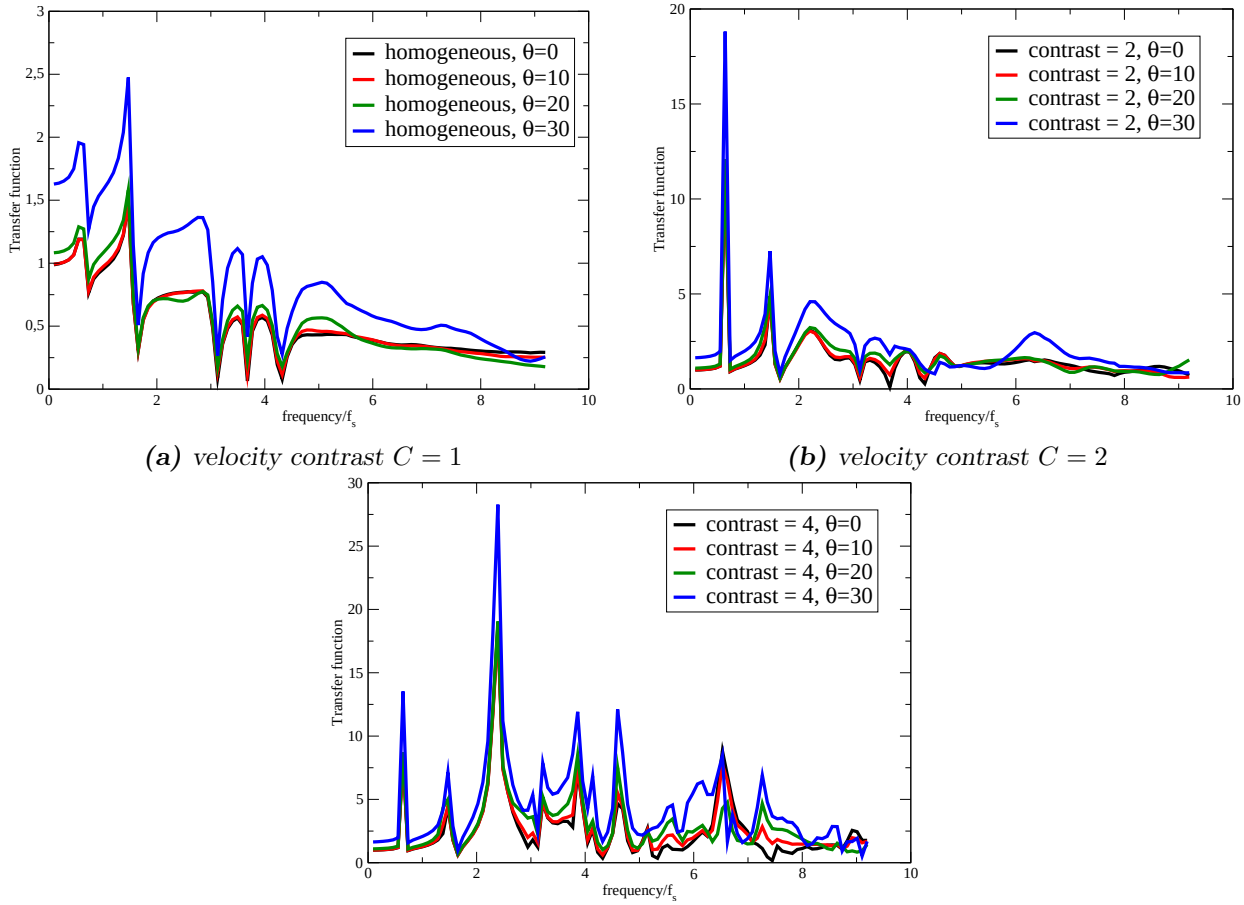

(a) *velocity contrast* $C = 1$

(b) *velocity contrast* $C = 2$

(c) *velocity contrast* $C = 4$

Figure 5.11.: *Total displacement at the base of the structure. An incident unit plane SV-wave is imposed as a loading for various angle of incidence.*

Figure 5.11 shows the evolution of the total displacement for various incidence angles and a fixed velocity contrast. The transfer function is again seen to increase as the incidence angle increases, for all velocity contrasts. The gap between the different angles get more important with the increase of the angle: tranfer functions for the vertical angle are similar to the transfer function of the case of the incident angle of $\theta = 10^o$ while the difference between the transfer functions of the wave with the incident angle of $\theta = 20^o$ and the transfer functions of the wave with the incident angle of $\theta = 30^o$ are noticeable.

The total displacement also exhibits the tendency of transfer functions becoming smoother as the velocity contrast increases, the eigenmodes of the structure becoming less noticeable.

5.3.2. SH-wave

Figures 5.12, 5.13, 5.14 and 5.15 present the results of the horizontal displacement along the X-direction, the horizontal displacement along the Y-direction, the vertical displacement along Z-direction and the total displacement norm defined as $u_t = \sqrt{u_x^2 + u_y^2 + u_z^2}$. Those are the resulting displacement of imposing a unit plane SH-wave.

The first remark is that the displacement in the X-direction and Z-direction is almost null: this is consistent with Section 5.2. Only the displacement along the Y-direction is non-null.

The different angles shows similar results at fixed velocity contrast, as well as an increase of the maximum amplification with the increase of the velocity ratio. The total displacement confirms this tendency since there is no other components besides the displacement along the Y-direction.

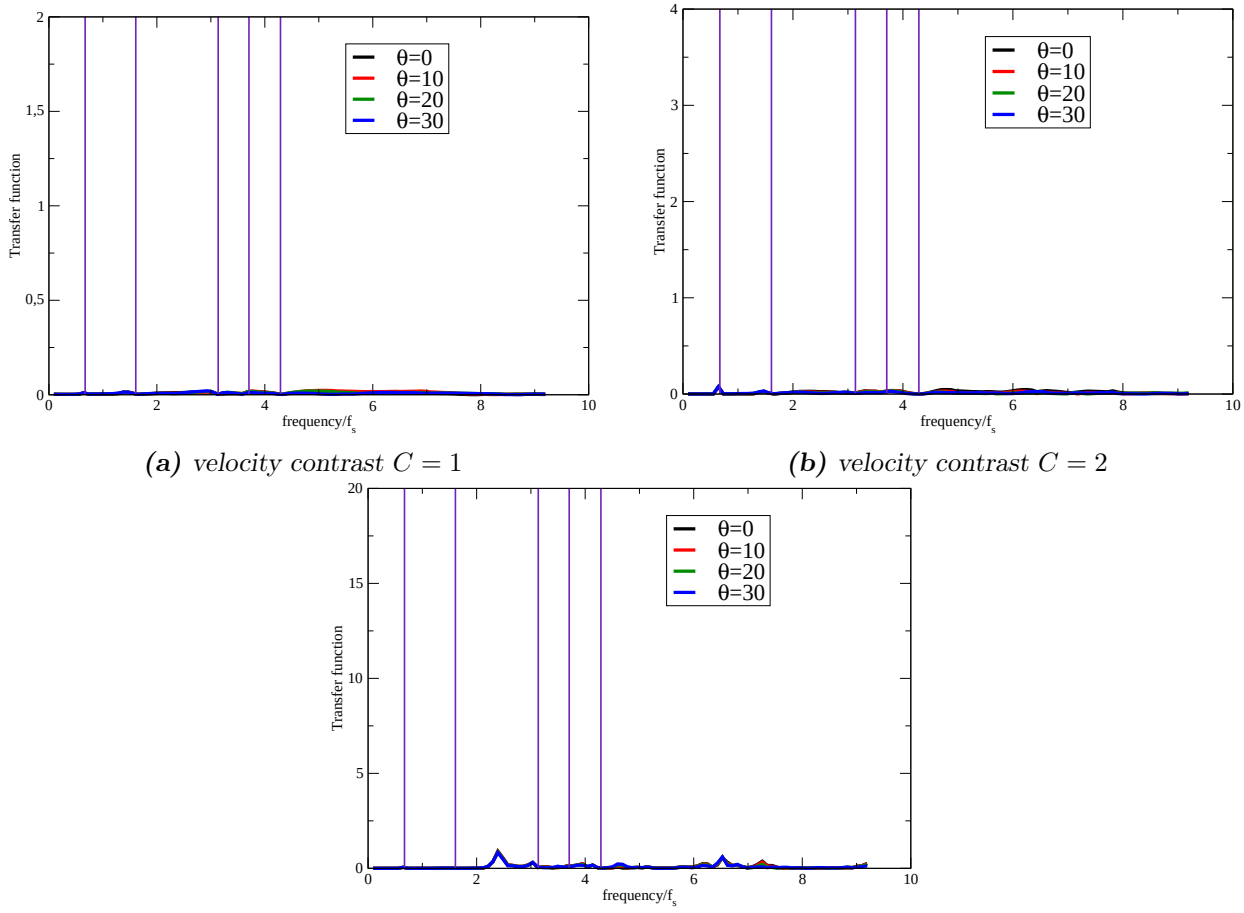

(a) *velocity contrast $C = 1$*

(b) *velocity contrast $C = 2$*

(c) *velocity contrast $C = 4$*

Figure 5.12.: *Horizontal displacement along the X-direction at the base of the structure. An incident unit plane SH-wave is imposed as a loading for various angle of incidence.*

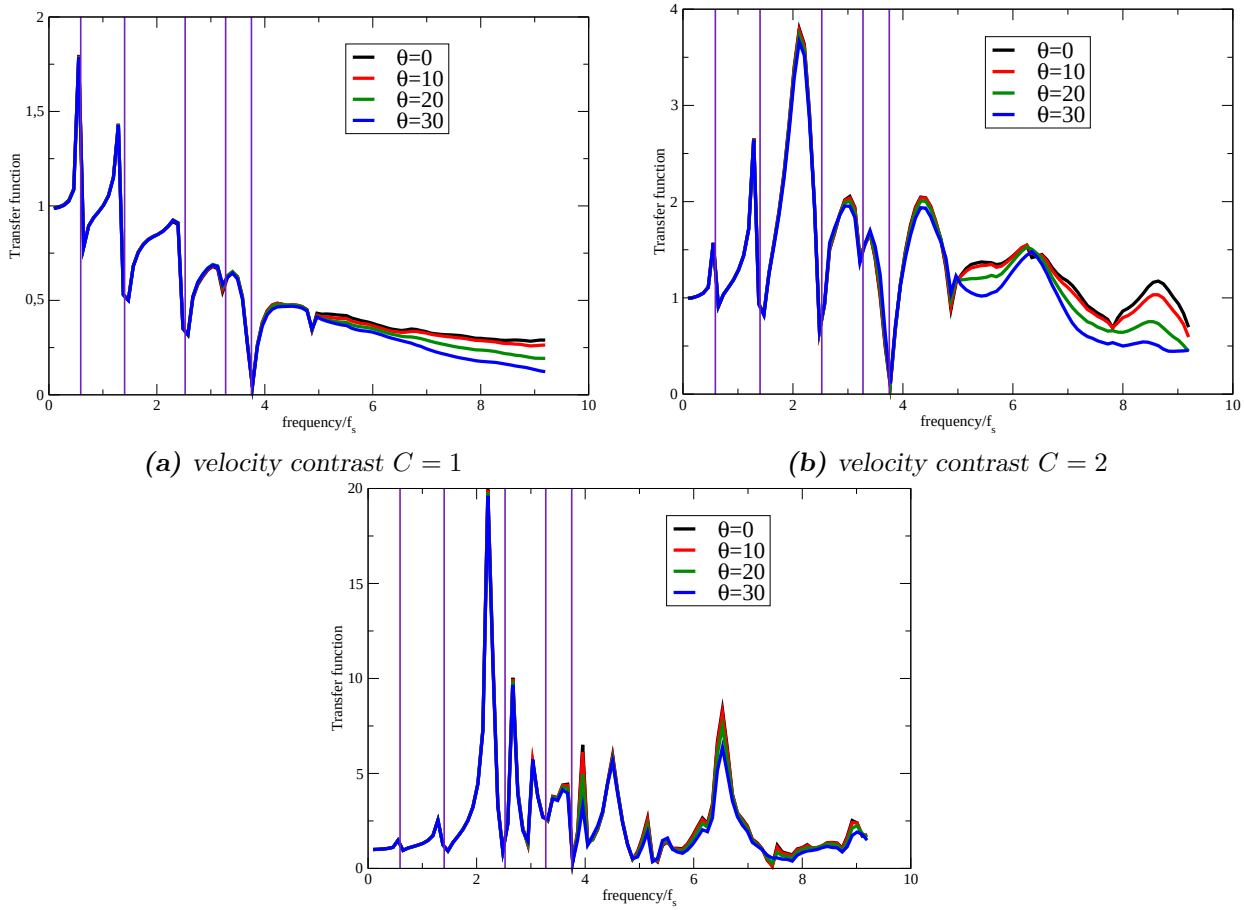

(a) *velocity contrast* $C = 1$

(b) *velocity contrast* $C = 2$

(c) *velocity contrast* $C = 4$

Figure 5.13.: *Horizontal displacement along the Y-direction at the base of the structure. An incident unit plane SH-wave is imposed as a loading for various angle of incidence.*

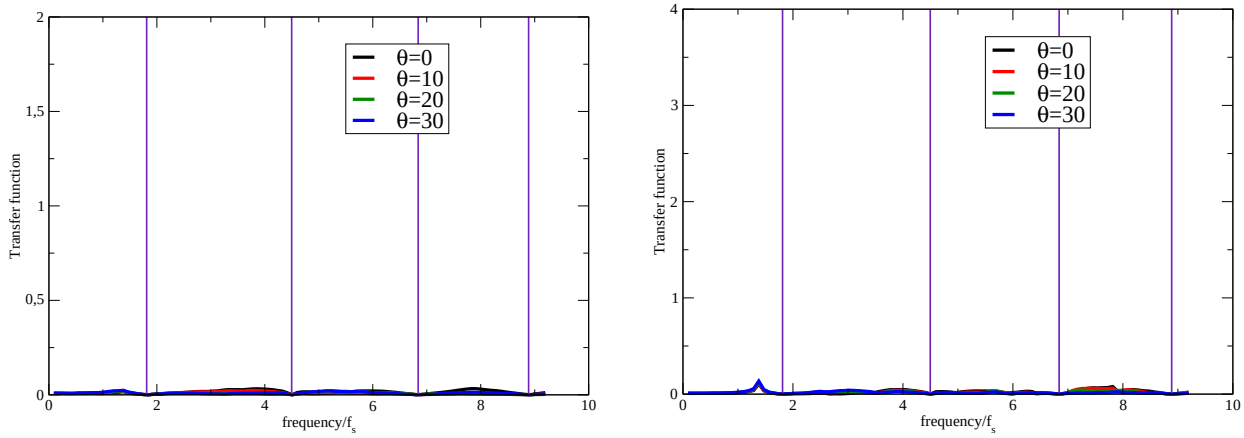

(a) *velocity contrast* $C = 1$ ***(b)*** *velocity contrast* $C = 2$

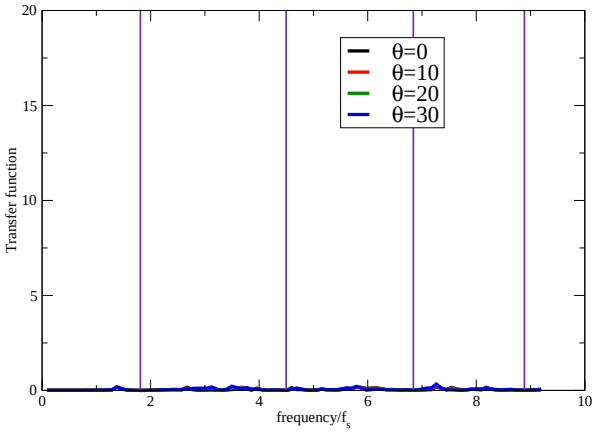

(c) *velocity contrast* $C = 4$

Figure 5.14.: *Vertical displacement along the Z-direction at the base of the structure. An incident unit plane SH-wave is imposed as a loading for various angle of incidence.*

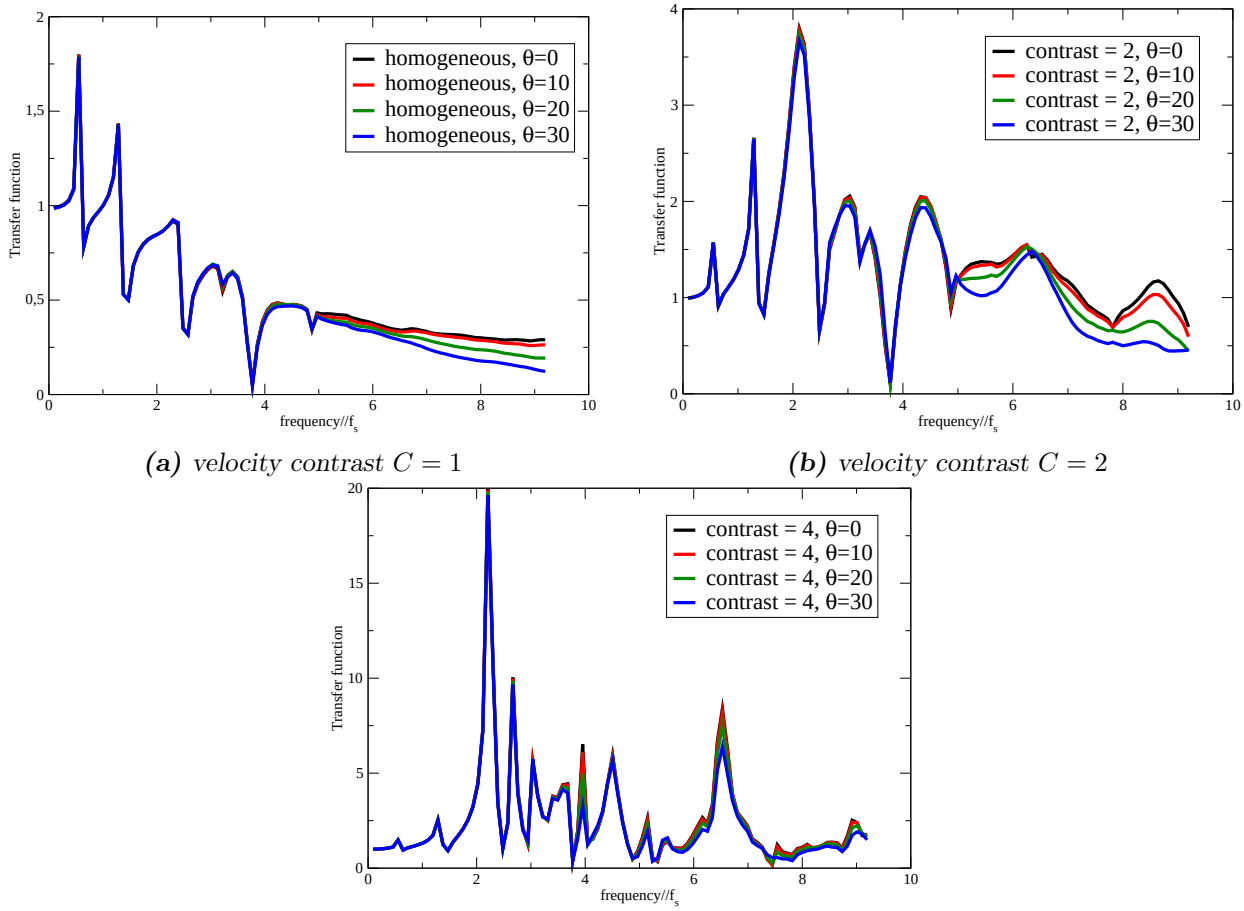

(a) *velocity contrast* $C = 1$

(b) *velocity contrast* $C = 2$

(c) *velocity contrast* $C = 4$

Figure 5.15.: *Total displacement at the base of the structure. An incident unit plane SH-wave is imposed as a loading for various angle of incidence.*

5.3.3. P-wave

Figures 5.16, 5.17, 5.18 and 5.19 present the results of the horizontal displacement along the X-direction, the horizontal displacement along the Y-direction, the vertical displacement along Z-direction and the total displacement norm defined as $u_t = \sqrt{u_x^2 + u_y^2 + u_z^2}$. Those are the resulting displacement of imposing a unit plane P-wave.

The first remark is that the displacement in the Y-direction is almost null: imposing a P-wave in the XZ-plane does not generate displacement outside of this plane. Also, the transfer functions for other components are driven by the eigenmodes for frequencies close to the eigenfrequencies and by the free-field other frequencies.

Concerning the displacement along X: it is noticeable that the transfer functions increase with the angle, for all the velocity ratios, which can be explained by the increase of the component of the incident wave in the X-direction with the increase of the angle. The maximum amplification of the

transfer function also increases with the increase of the velocity ratio: up to $5,5$ for the velocity contrast of 2 and up to 9 for the velocity contrast of 4, which is to be expected as the wave is amplified with the increase of the velocity contrast.

Concerning the displacement along Z: changing the angle of incidence does not seem to influence much on the transfer function, while the velocity contrast influences much more the amplitude of the transfer function and the maximum amplifications observed, with an increase of the latters with the velocity ratio, which is expected. The low influence of changing the angle on the response of the structure must be due to the cylindrical shape of the footing and its size compared with the size of the hemispherical basin.

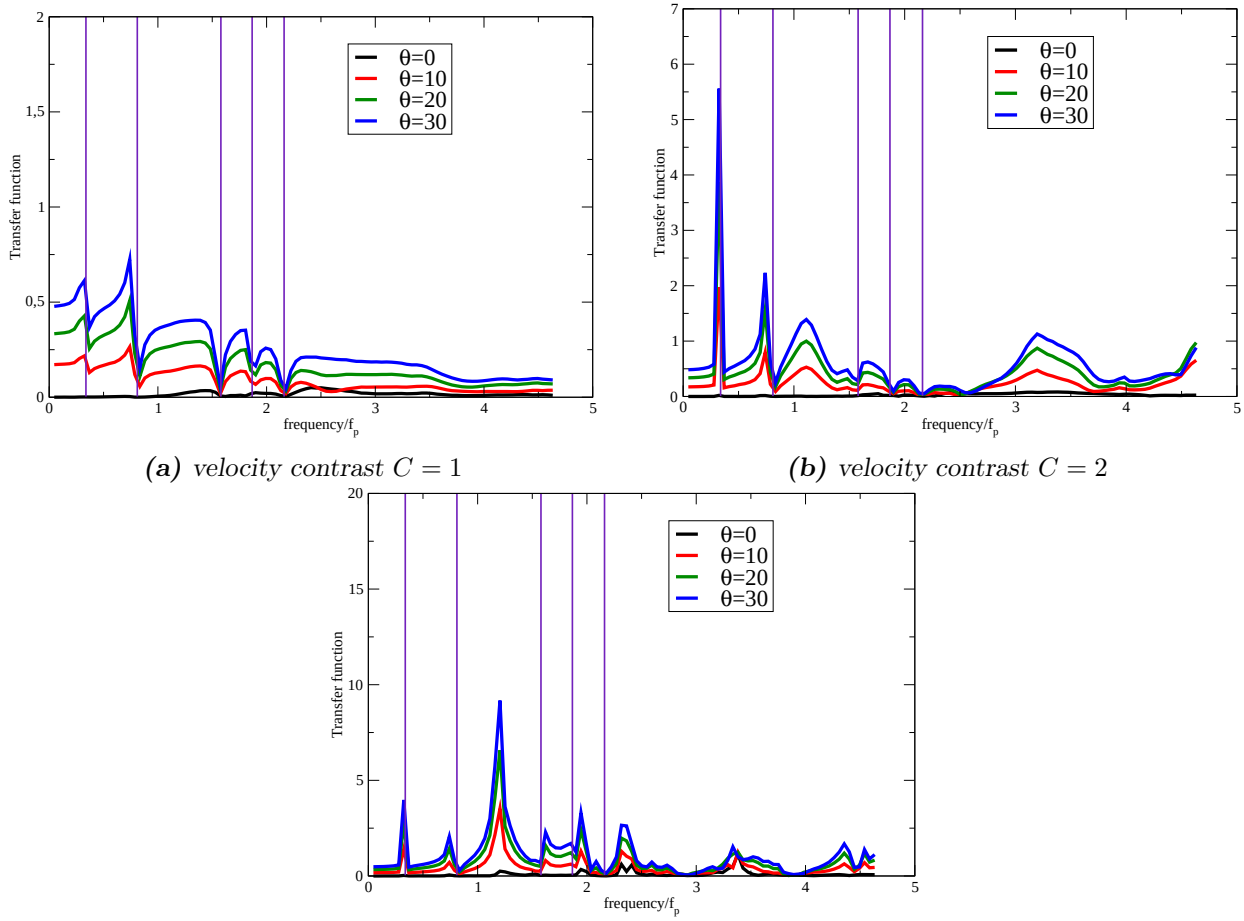

(a) *velocity contrast* $C = 1$

(b) *velocity contrast* $C = 2$

(c) *velocity contrast* $C = 4$

Figure 5.16.: *Horizontal displacement along the X-direction at the base of the structure. An incident unit plane P-wave is imposed as a loading for various angle of incidence.*

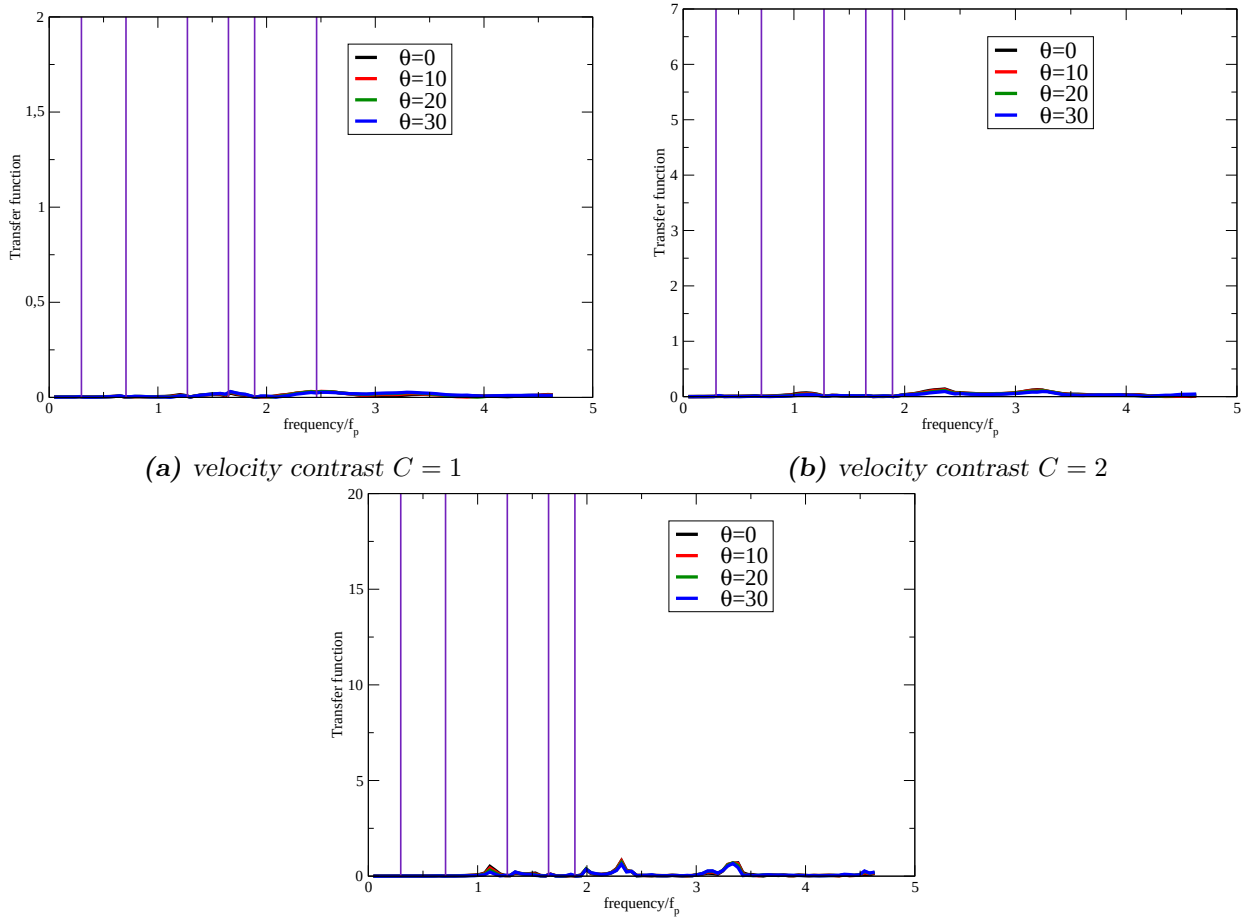

(a) *velocity contrast $C = 1$*

(b) *velocity contrast $C = 2$*

(c) *velocity contrast $C = 4$*

Figure 5.17.: *Horizontal displacement along the Y-direction at the base of the structure. An incident unit plane P-wave is imposed as a loading for various angle of incidence.*

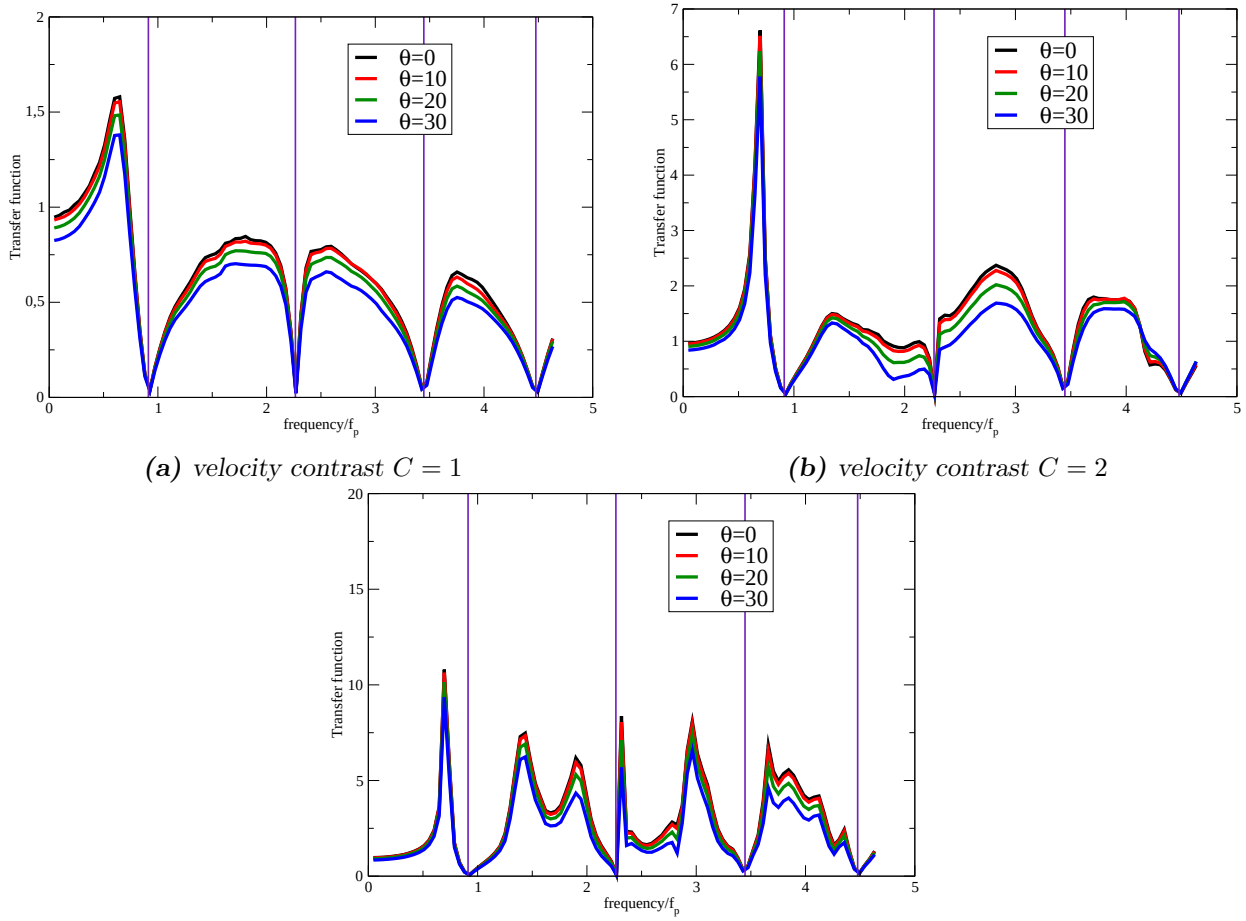

(a) *velocity contrast* $C = 1$

(b) *velocity contrast* $C = 2$

(c) *velocity contrast* $C = 4$

Figure 5.18.: *Vertical displacement along the Z-direction at the base of the structure. An incident unit plane P-wave is imposed as a loading for various angle of incidence.*

The total displacement has globally the same pattern as the transfer function of the Z-direction, with the difference of an added peak of amplification of the transfer functions of the velocity contrasts of 2 and 4 due to peak caused by the first eigenfrequency in the X-direction.

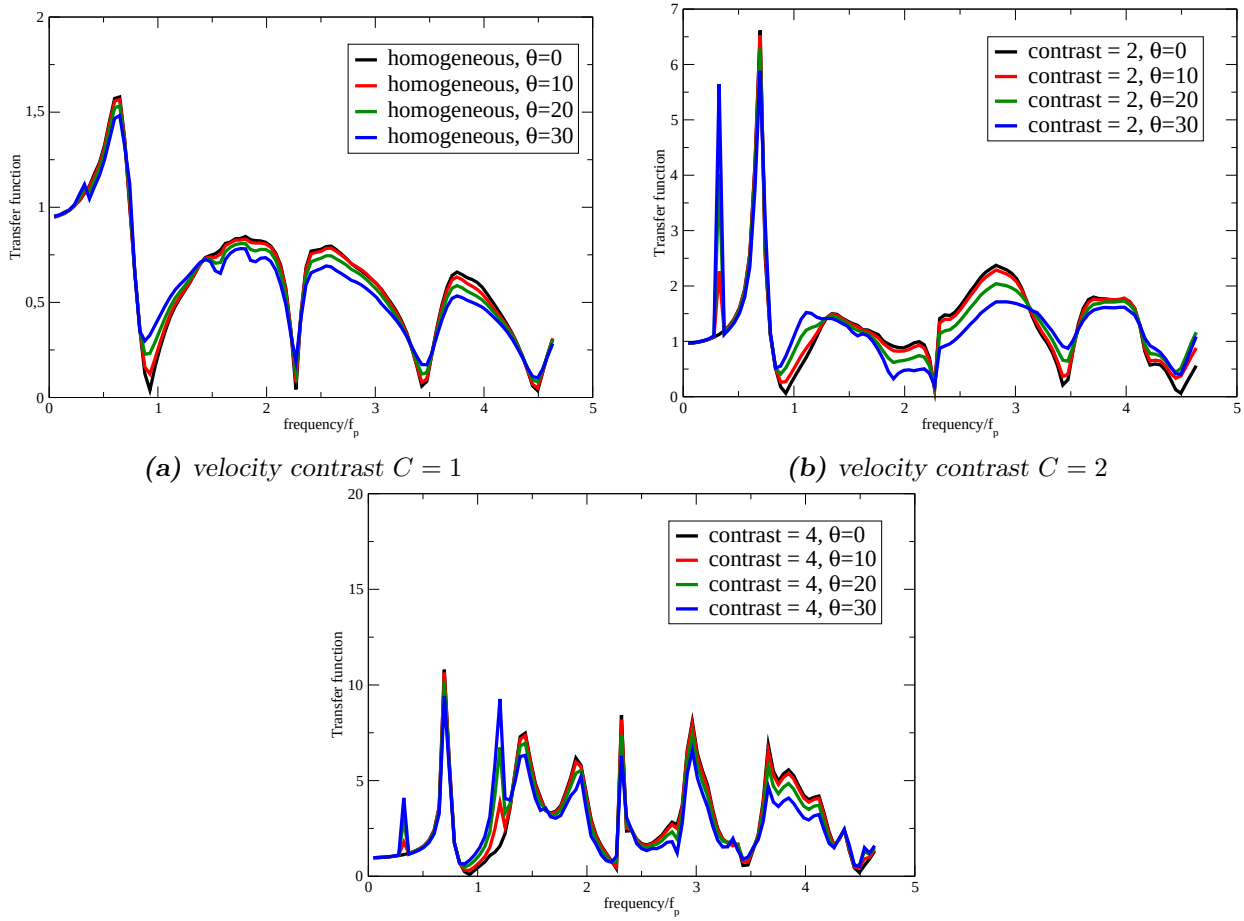

(a) *velocity contrast* $C = 1$

(b) *velocity contrast* $C = 2$

(c) *velocity contrast* $C = 4$

Figure 5.19.: *Total displacement at the base of the structure. An incident unit plane P-wave is imposed as a loading for various angle of incidence.*

5.4. Conclusion

The following conclusions can be reached from Chapter 5:

- applying an SV-wave or a P-wave does not generate displacements outside of the plane in the Y-direction, and similarly, the application of an SH-wave do not generate displacements in the X-direction of in the Z-direction;
- the response at the base of the structure is driven by the eigenmodes of the structure when the frequency is close to the eigenfrequencies of the structure, while it is driven by the free-field response for other frequencies;

- the velocity ratio between the bedrock and the hemispherical basin has a more important influence on the response of the structure than the angle of incidence;
- an increase of the velocity ratio was accompanied by an increase of the maximum amplitude of the transfer functions.

Chapter 6

Application on realistic configuration of Soil Structure Interaction

Contents

6.1. Modelling of the Grenoble valley 108
6.2. Illustration of site effects due to geological and topographical structure 110
6.3. Illustration of the site effects on the response in the presence of buildings116
6.4. Conclusion 120

The main goal of this work is to take into account site effects in the study of soil-structure interaction. In the previous chapters, academic examples were studied to assess the proposed numerical approach. Now that the method is validated, a more realistic configuration is considered: an Alpine valley (Grenoble). The Grenoble valley has the advantage to present three kinds of site effects (see Fig. 6.1): topographical effects due to the complex topography, lithological effects due to the different layers in the basin and the geometry of the interface between the bedrock and the sedimentary basin, and geometric effects due to the Y shape of the basin. It is therefore a good scenario to quantify the influence of site effects on the response of a building.

Two cases are treated. First, the response of the alluvial basin without any structure is considered, in order to quantify the site effects. Then, the response of the basin with a structure is evaluated.

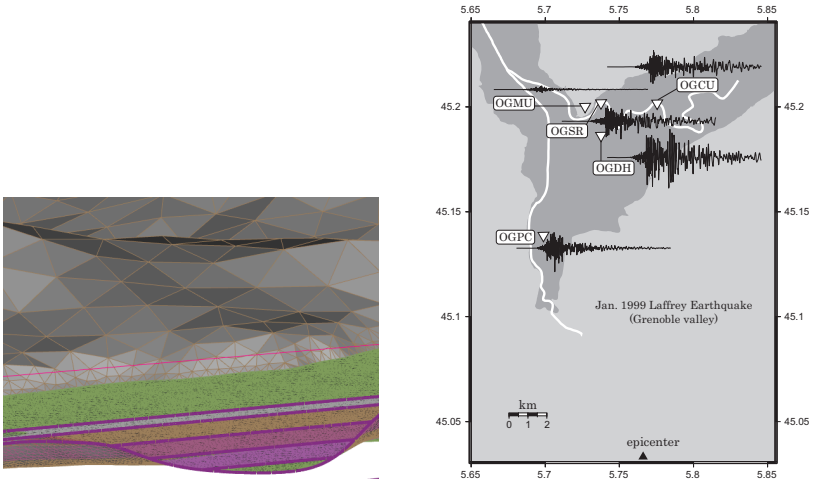

(a) *Layers in Grenoble basin.* **(b)** *Shape of the Grenoble basin.*

Figure 6.1.: *Grenoble basin: layers and shape of the basin.*

6.1. Modelling of the Grenoble valley

The mechanical parameters of the bedrock and sedimentary basin models are as proposed in [14]. For the bedrock, the P and S velocities and the density are set to constant values in four areas (see Table 6.1). In order to keep the number of degrees of freedom reasonable, the four different areas are not considered but only the first one.

Depth	ρ	c_s	c_p
0-3 km	2720	3200	5600
3-27 km	2720	3430	5920
27-35 km	2920	3810	6600
$>$ 35 km	3320	4450	8000

Table 6.1.: *Mechanical parameters used to model the layers of the bedrock.*

In the sedimentary basin, the velocity profile increases with the depth z. The proposed models are:

$$c_p(z) = 1450 + 1.2z, \quad c_s(z) = 300 + 19\sqrt{z}, \quad \rho = 2140 + 0.125z.$$

Since the use of a BEM imposes a piecewise homogeneous domain, the sedimentary basin is decomposed into five homogeneous layers of depth 100 or 200 m. The corresponding mechanical parameters are summarized in Table 6.2.

Layer	Depth	ρ	c_s	c_p
1	0-100	2146.25	434	1510
2	100-300	2165	568	1690
3	300-500	2190	680	1930
4	500-700	2215	765	2170
5	700-1000	2246.25	854	2470

Table 6.2.: *Mechanical parameters used to model the layers of the sedimentary basin.*

The BE mesh has been provided by Adrien Loseille from INRIA Saclay. Each homogeneous layer is meshed in order to have at least ten points per S-wavelength at the frequency of 1 Hz. Mesh conformity requirements at interfaces induce densities of about ten points per smallest S-wavelength on interfaces. As a result, the interface between layers 4 and 5 is adapted to domain 4 but is too dense for domain 5. This situation is sub-optimal for the FM-BEM [7]. The efficiency of the FM-BEM is based on the use of a uniform mesh with a moderate (about 10) density of points per wavelength. If the interface between the bedrock and the layer 5 is meshed to achieve ten points per S-wavelength in the layer 5, then the bedrock is about 4 times too dense. This results in a artificially "too" large matrix for the near contributions. In order to avoid this issue that is beyond the scope of this thesis and due to limited computational resources, the parameters of the bedrock are replaced by the parameters of the layer 5. It is known that this trick will reduce the site effects due to the material contrasts. But this is a preliminary attempt to model this realistic configuration. Some improvements on the FM-BEM are required to consider such large scale problems with high velocity contrasts.

The model consists of 890.000 DOFs. Difficulties were met when solving the problem: some frequencies required more than 5.000 iterations. Hence, the tolerance of the iterative solver was set to $0,01$ for all frequencies, besides the frequency $f = 0,8\ Hz$ where the tolerance was set to $0,15$ and the frequency $f = 0,9\ Hz$ where the tolerance was set to $0,10$. This tolerances for the latter frequencies are not sufficient for a modelling with an appropriate accuracy. The results for these frequencies should be analyzed with caution.

The Grenoble valley was previously treated and modeled with FM-BEM in [7]. The main differences with [7] is that the topography was not taken into account (as the free surface was considered horizontal), the sedimentary basin was homogeneous (while it is layered here) and the analysis was performed for two frequencies of $0,3$ Hz and $0,6$ Hz. In this work, the ambition is to better take

into account the topography and the layers inside the sedimentary basin, as well as treat higher frequencies.

The quantities of interest in the following are the modulus of the displacement in the three directions (X,Y and Z).

6.2. Illustration of site effects due to geological and topographical structure

In this section, the response of the sedimentary basin (without any building) to vertically incident plane P-, SV- or SH-waves is considered. For each configuration, the response for each frequency (from 0.1 Hz to 1Hz with a step of 0.1 Hz) is reported, at two locations called "center" and "border" (see Fig. 6.2). These two locations are chosen to illustrate two specific configurations. The center point is located in the middle of the basin (see Fig. 6.2). It is on top of the five layers, the stratification of the layers and their thickness is given in Table 6.3. It should illustrate the effects of the layers in the sedimentary basin. On the other hand, the border point is located near the bedrock, the stratification of the layers and their thickness is given in Table 6.4. It is chosen to check the sensitivity to the material discontinuity and the topography effect near the point (see Fig. 6.2).

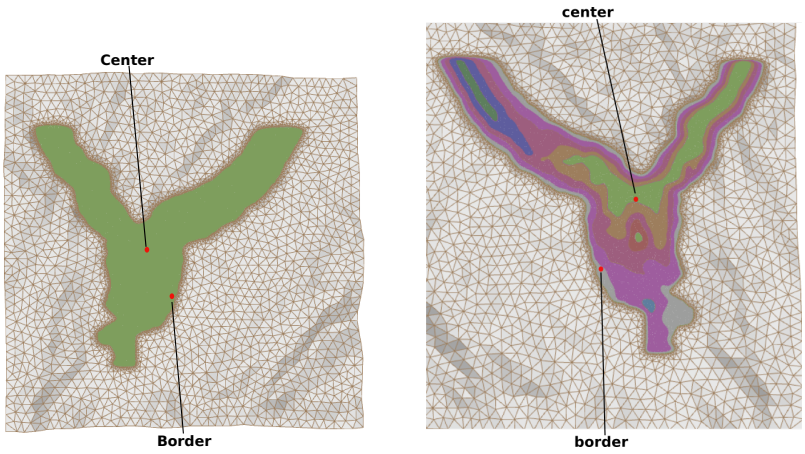

(a) *Top view of the mesh of Grenoble basin.*

(b) *Bottom view of the mesh of Grenoble basin.*

Figure 6.2.: *Top and bottom view of the mesh of Grenoble basin, with the chosen location for the center and border points are indicated in red.*

Layer	Thickness (m)
1	100
2	200
3	200
4	200
5	13

Table 6.3.: *Depth of the layer under the center point of the basin 6.2.*

Layer	Thickness (m)
1	100

Table 6.4.: *Depth of the layer under the border point of the basin 6.2.*

The displacement modulus at the border point and center point along the three directions (X,Y and Z) for each kind of wave is now presented, in the absence of the structure, for various cases of incident waves.

The displacement resulting from imposing a unit vertical incident SV-wave is plotted in Figure 6.3. Resonance of the basin at around $0,4$ Hz and $0,8$ Hz can be observed for both observation points. The maximum amplitude of the transfer function in the X-direction is about 5 while the other directions (Y and Z) have maximum amplitude of $2,5$.

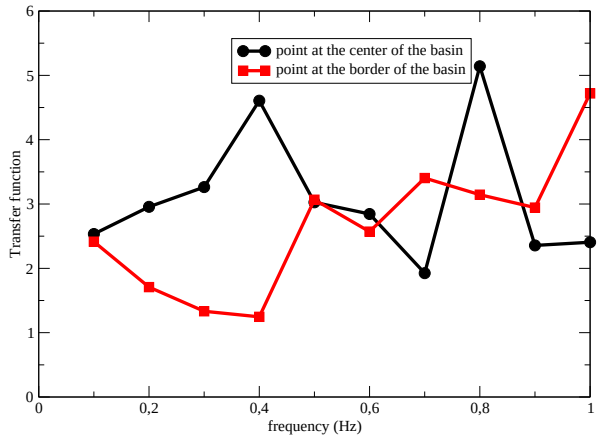

(a) Horizontal displacement along the X-direction

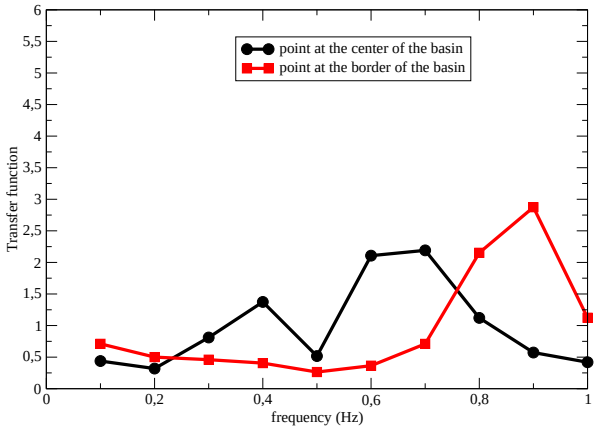

(b) Horizontal displacement along the Y-direction

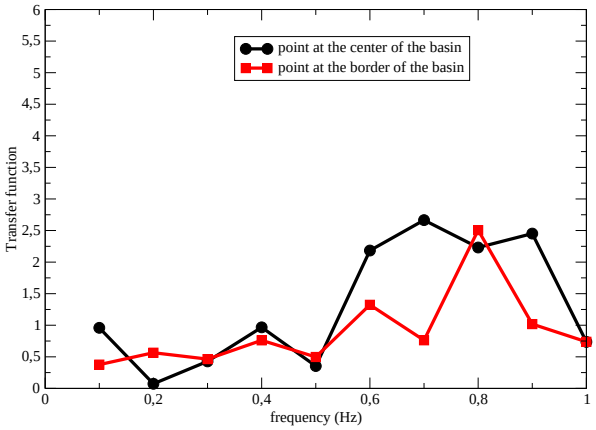

(c) Vertical displacement along the Z-direction

Figure 6.3.: *Displacement at the free surface of the basin. A vertical incident unit plane SV-wave is imposed as a loading.*

The displacement resulting from imposing a unit vertical incident SH-wave is plotted in Figure 6.4. Resonance of the basin at around $0,7$ Hz can be observed for both observation points. The maximum amplitude of the transfer function in the Y-direction is about $6,5$ while the other directions (X and Z) present amplitude about half the amplitude of the Y direction.

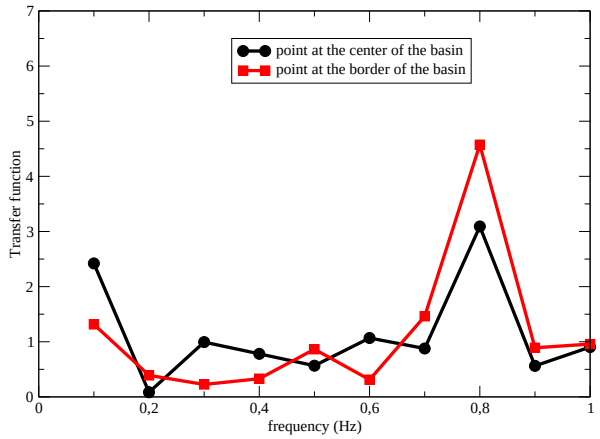

(a) *Horizontal displacement along the X-direction*

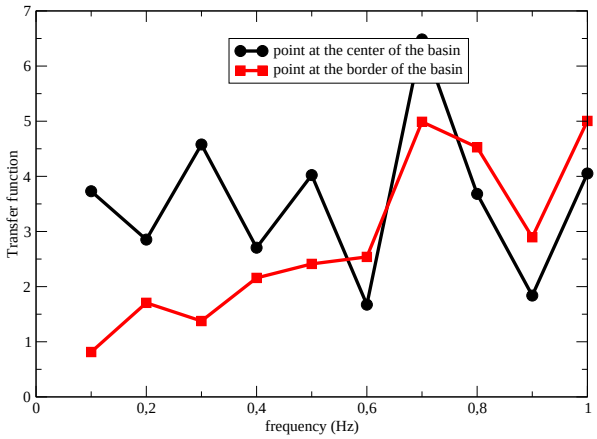

(b) *Horizontal displacement along the Y-direction*

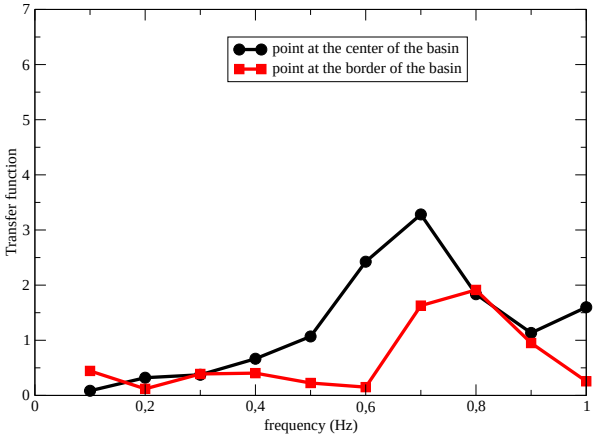

(c) *Vertical displacement along the Z-direction*

Figure 6.4.: *Displacement at the free surface of the basin. A vertical incident unit plane SH-wave is imposed as a loading.*

The displacement resulting from imposing a unit vertical incident P-wave is plotted in Figure 6.5. The transfer function of the Z-direction presents values of around 2 with a maximum of 5 at the frequency $0,8$ Hz, while transfer functions in other directions are globally lower than 2.

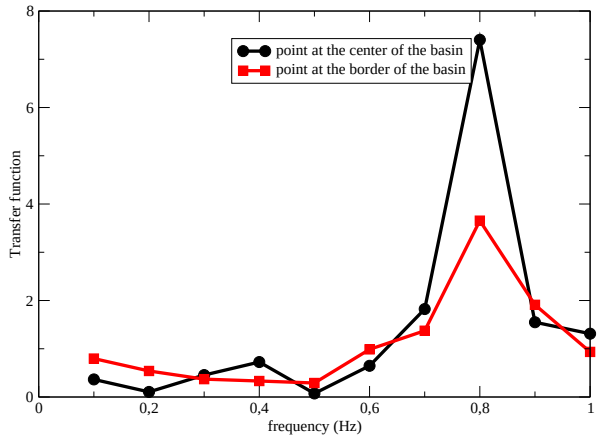

(a) Horizontal displacement along the X-direction

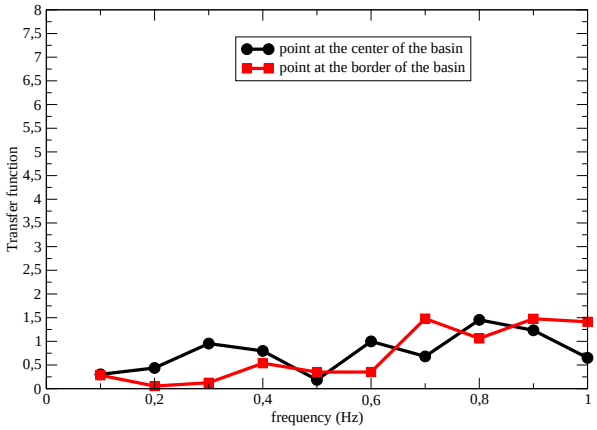

(b) Horizontal displacement along the Y-direction

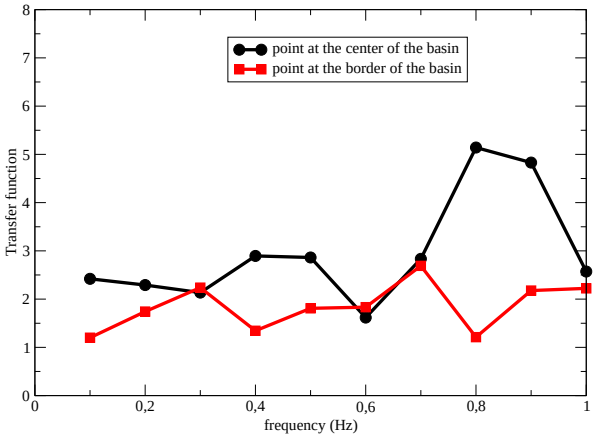

(c) Vertical displacement along the Z-direction

Figure 6.5.: *Displacement at the free surface of the basin. A vertical incident unit plane P-wave is imposed as a loading.*

Figures 6.6, 6.7 and 6.8 present the modulus of the amplitude of the displacement at the free-surface of the Grenoble basin, subjected respectively to a SV-wave, SH-wave and P-wave, for the frequency of $0,2$ Hz and the frequency of $0,6$ Hz. This displacements were computed with *Coffee*. The waveforms look smooth. Also, the observed wavelengths on the figures for the frequency of $0,6$ Hz are, as expected, smaller than the wavelengths for the frequency of $0,2$ Hz.

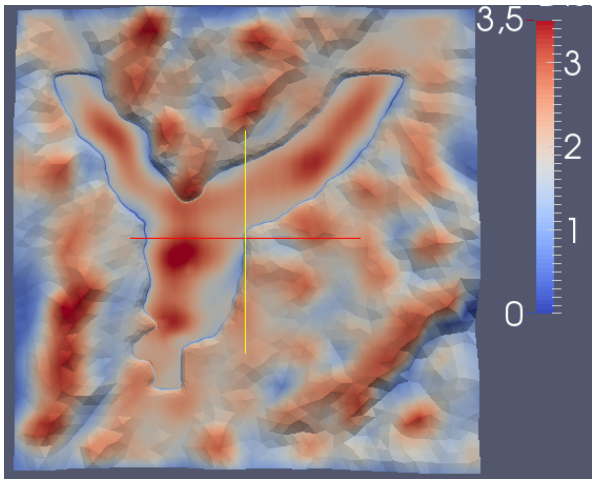

(a) *Grenoble basin harmonic response to a unit incident wave at frequency $f = 0,2Hz$.*

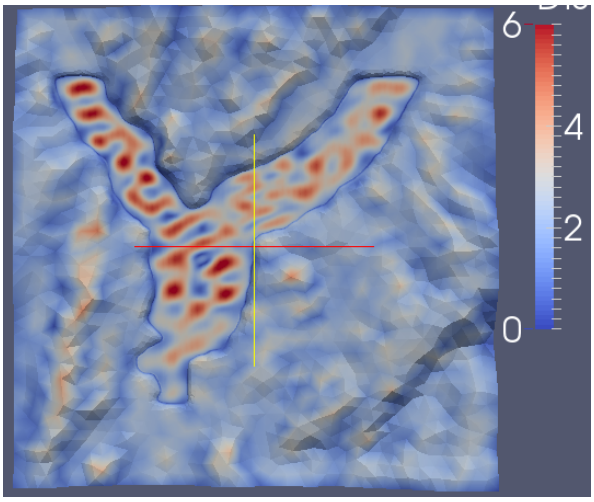

(b) *Grenoble harmonic response to a unit incident wave at frequency $f = 0,6Hz$.*

Figure 6.6.: *Displacement at the free surface of the basin in the X-direction. A vertical incident unit plane SV-wave is imposed as a loading.*

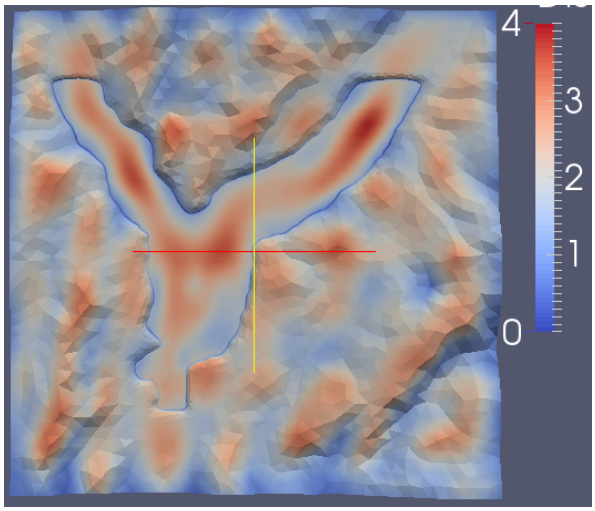

(a) *Grenoble basin harmonic response to a unit incident wave at frequency $f = 0,2Hz$.*

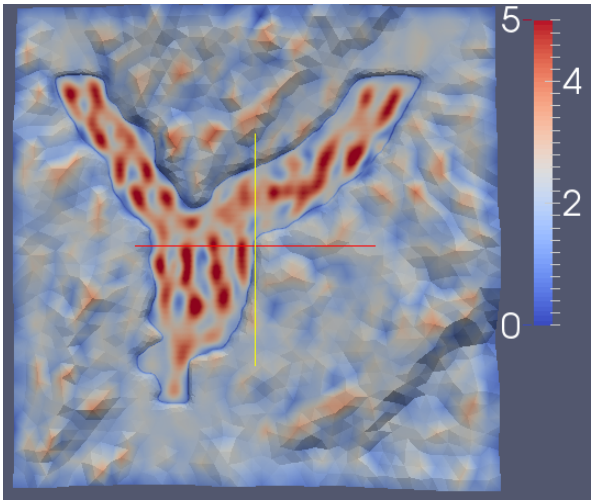

(b) *Grenoble basin harmonic response to a unit incident wave at frequency $f = 0,6Hz$.*

Figure 6.7.: *Displacement at the free surface of the basin in the Y-direction. A vertical incident unit plane SH-wave is imposed as a loading.*

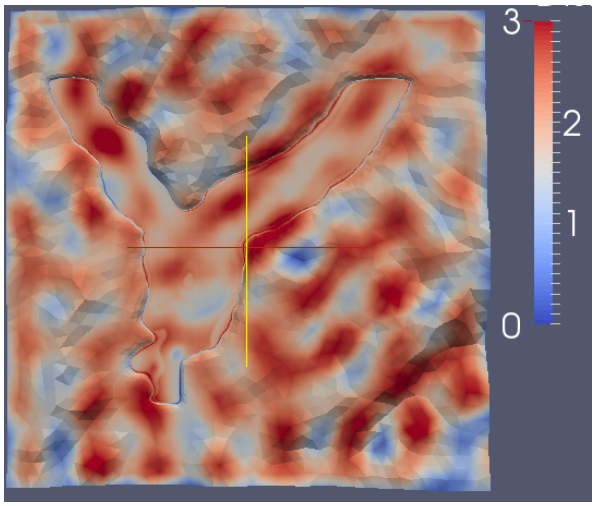

(a) Grenoble basin harmonic response to a unit incident wave at frequency $f = 0,2Hz$.

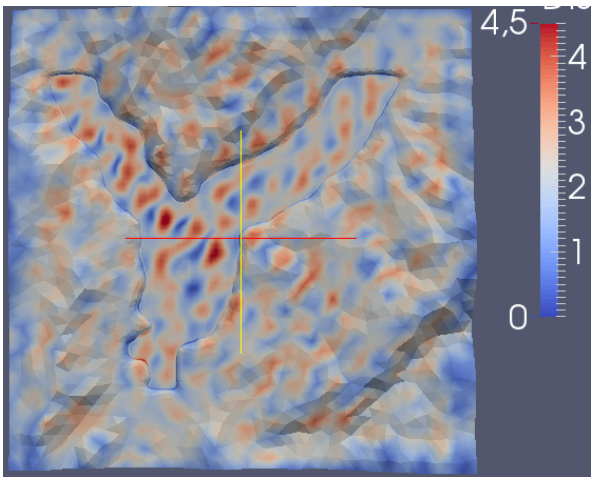

(b) Grenoble basin harmonic response to a unit incident wave at frequency $f = 0,6Hz$.

Figure 6.8.: *Displacement at the free surface of the basin in the Z-direction. A vertical incident unit plane P-wave is imposed as a loading.*

6.3. Illustration of the site effects on the response in the presence of buildings

In this section, the response of a structure in the sedimentary basin to vertical incident plane P-, SV- or SH-waves is considered. Two positions of the structure are considered: at the center of the basin and at the border of the basin (see Figure 6.2). For each configuration, the response for each frequency (from 0.1 Hz to 1Hz with a step of 0.1 Hz) is reported, at the two locations. The characteristics of the structure are represented by its eigenfrequencies presented in Tables 6.5, 6.6 and 6.7. The unit effective mass $\mu(\Phi, d)$ of the Φ mode in the direction d for the case of a structure of total mass m_t is computed as

$$\mu(\Phi, d) = \frac{({}^t\underline{\Phi}.\underline{\underline{M}}.\underline{D})^2}{{}^t\underline{\Phi}.\underline{\underline{M}}.\underline{\Phi}}.\frac{1}{m_t}.$$

A structure with such eigenfrequencies is not intended as a realistic case. Its use aims at demonstrating the feasibility of computing a Soil-Structure Interaction in a basin similar to Grenoble.

The displacement at the base of the structure resulting from imposing a unit vertical incident SV-wave is plotted in Figure 6.9. The displacement in the X-direction oscillates around 2 for the center location and around 1 for the border location. Displacements along the Y-direction and the Z-direction are globally smaller than 1.

Table 6.5.: *Frequencies, unit effective mass and cumulated effective mass for the eigenmodes in u_x direction.*

Frequencies (Hz)	Unit effective mass	Cumulated unit effective mass
1.39807E-01	1.45240E-01	1.45240E-01
1.65790E-01	5.02591E-01	6.47832E-01
3.23638E-01	9.16629E-04	6.48748E-01
3.83109E-01	1.02963E-01	7.51711E-01
3.94676E-01	2.28776E-22	7.51711E-01
5.60840E-01	2.62729E-03	7.54338E-01
5.86603E-01	2.67613E-06	7.54341E-01
7.36783E-01	3.70235E-02	7.91364E-01
8.49459E-01	2.79543E-04	7.91644E-01
9.31534E-01	1.43493E-02	8.05993E-01
9.78819E-01	2.17639E-23	8.05993E-01

Table 6.6.: *Frequencies, unit effective mass and cumulated effective mass for the eigenmodes in u_y direction.*

Frequencies (Hz)	Unit effective mass	Cumulated unit effective mass
1.39807E-01	4.53792E-01	4.53792E-01
1.65790E-01	1.42943E-01	5.96735E-01
3.23638E-01	1.15466E-01	7.12201E-01
3.83109E-01	1.00316E-03	7.13204E-01
3.94676E-01	6.56849E-24	7.13204E-01
5.60840E-01	9.06114E-04	7.14110E-01
5.86603E-01	4.55650E-02	7.59675E-01
7.36783E-01	2.76924E-05	7.59703E-01
8.49459E-01	4.30319E-02	8.02735E-01
9.31534E-01	1.37576E-03	8.04111E-01
9.78819E-01	3.65937E-23	8.04111E-01

Table 6.7.: *Frequencies, unit effective mass and cumulated effective mass for the eigenmodes in u_z direction.*

Frequencies (Hz)	Unit effective mass	Cumulated unit effective mass
1.39807E-01	2.09507E-24	2.09507E-24
1.65790E-01	1.06217E-23	1.27168E-23
3.23638E-01	1.68076E-22	1.80792E-22
3.83109E-01	1.53105E-21	1.71185E-21
3.94676E-01	7.07028E-01	7.07028E-01
5.60840E-01	2.85067E-24	7.07028E-01
5.86603E-01	3.22747E-23	7.07028E-01
7.36783E-01	1.10284E-24	7.07028E-01
8.49459E-01	5.06814E-25	7.07028E-01
9.31534E-01	1.61136E-23	7.07028E-01
9.78819E-01	3.17257E-02	7.38754E-01

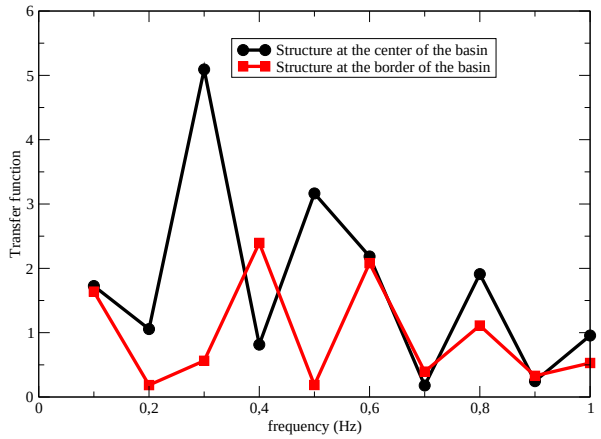

(a) Horizontal displacement along the X-direction

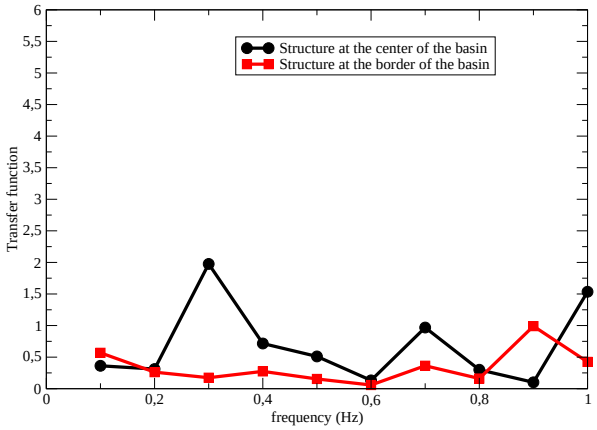

(b) Horizontal displacement along the Y-direction

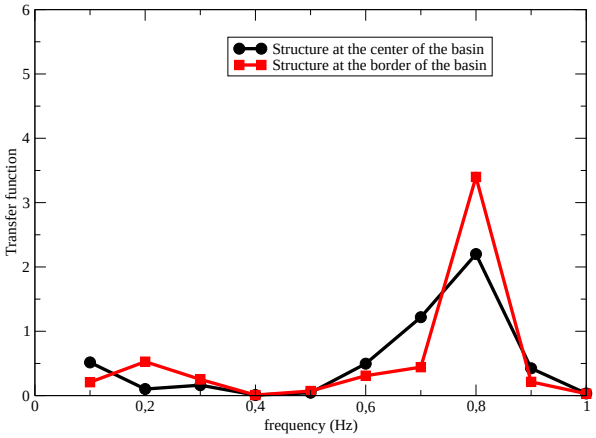

(c) Vertical displacement along the Z-direction

Figure 6.9.: *Displacement at the free surface of the basin. A vertical incident unit plane SV-wave is imposed as a loading.*

The displacement at the base of the structure resulting of imposing a unit vertical incident SH-wave is plotted in Figure 6.10. The results present similarities with the SV-wave case: the displacement along the Y-direction oscilated around 2 in the center position and around 1 in the border position, while displacement and X and Z-direction are globally smaller than 1.

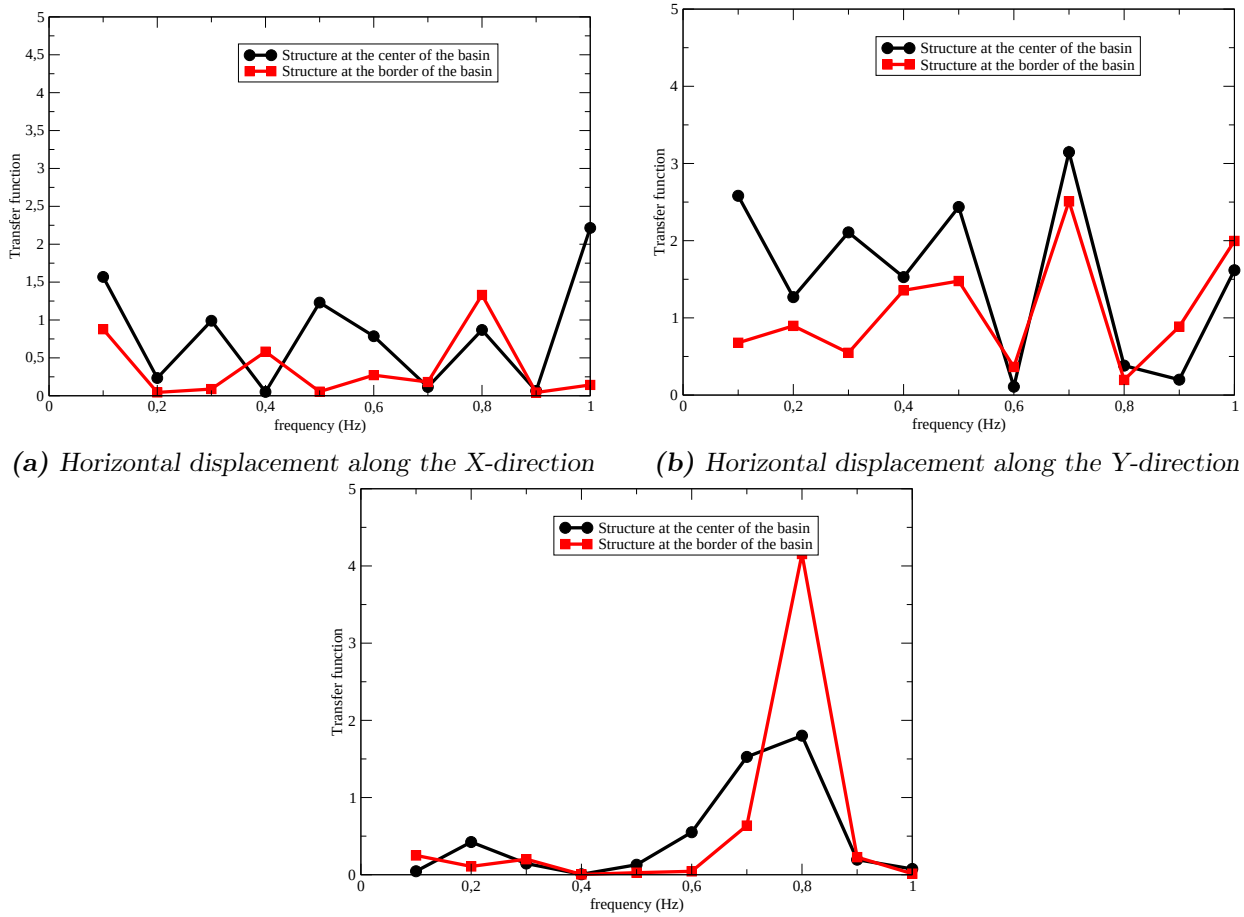

(a) *Horizontal displacement along the X-direction*

(b) *Horizontal displacement along the Y-direction*

(c) *Vertical displacement along the Z-direction*

Figure 6.10.: *Displacement at the free surface of the basin. A vertical incident unit plane SH-wave is imposed as a loading.*

The displacement at the base of the structure resulting of imposing a unit vertical incident P-wave is plotted in Figure 6.11. The transfer function along the Z-direction has a maximum of 5 at frequency $0,8$ Hz while other directions are globally smaller than 1.

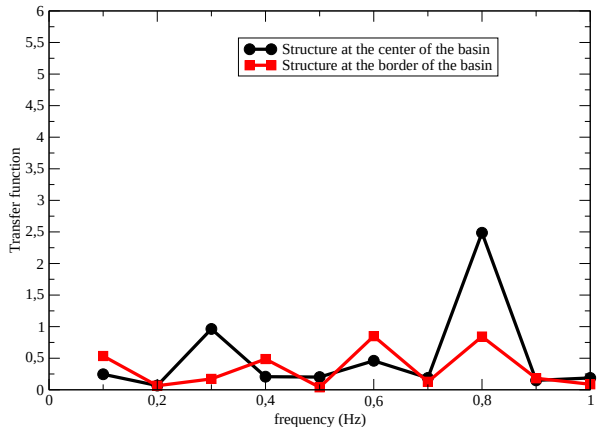

(a) Horizontal displacement along the X-direction

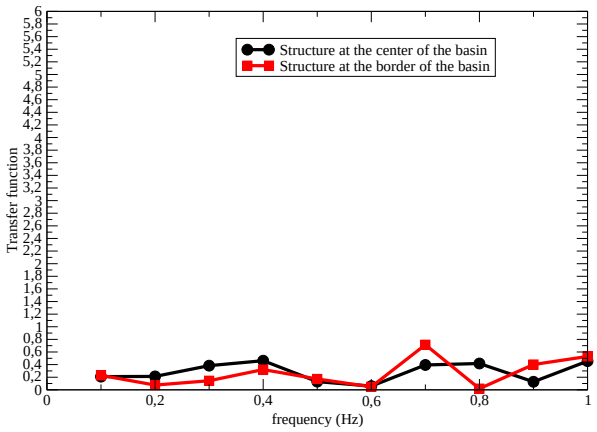

(b) Horizontal displacement along the Y-direction

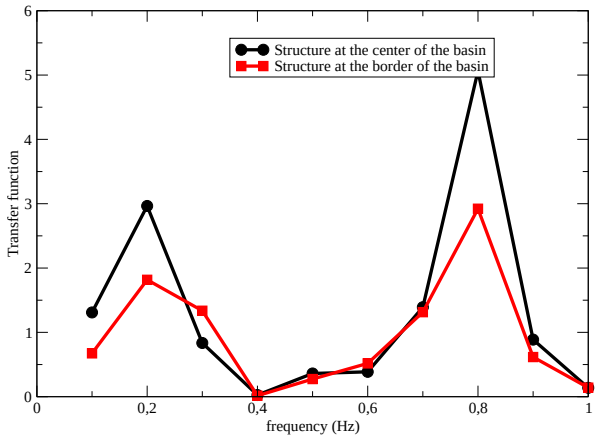

(c) Vertical displacement along the Z-direction

Figure 6.11.: *Displacement at the free surface of the basin. A vertical incident unit plane P-wave is imposed as a loading.*

6.4. Conclusion

In this section, the previously presented coupling method of FM-BEM with FEM for the modelling of Soil-Structure Interaction problems was used for the case of the Grenoble valley. It allowed to give results for a basin that would present extreme difficulties if it were to be solved with classical BEM. However, some difficulties were met when dealing with the mesh of the Grenoble valley and the convergence of the

In analyzingthe results, It is observed that, for our structure, the maximum amplitudes were met in the direction of the incident wave, namely in the X-direction for the SV-wave, Y-direction for the SH-wave and Z-direction for the P-wave. For each wave, the maximum amplification each time was of 5 times of the amplitude of the incident wave. It can also be observed that the response at the base of the structure was globally more important in the case of a structure at the center of the basin, compared with the case of the structure in the border of the basin.

Chapter 7

Conclusions and directions for future work

7.1. Conclusions

The main objective of this work was to develop a computational strategy to take into account site effects in the numerical simulation of Soil-Structure Interaction. This work is restricted to lithologic, topographic and geometric site effects. A requirement for the numerical model was to allow including several kilometres around the structure in the near-field region (modelled using the FEM) while being applicable to wide frequency ranges. The most important point is to choose the most appropriate numerical approach in this context, where wave propagation problems to be solved involve large media and large numbers of degrees of freedom.

In Chapter 1, the different kind of site effects that are taken into account are recalled and the main possible numerical methods to model wave propagation. The boundary element method (BEM) is used to model the soil. The main advantages are to rely on a discretisation of the domain boundary only (thus reducing drastically the number of degrees of freedom of the model) and to take into account the radiation condition implicitly in the formulation. The finite element method is used to model the structure. The drawbacks of the boundary element method, mainly in terms of computational times and memory requirements, are overcome by using the fast multipole method to accelerate the solution of the BEM system. The principles of the fast multipole accelerated boundary element method (FM-BEM) have then been presented, and the main advantages and drawbacks of the method explained.

After presenting the framework of this thesis, several numerical experiments have been conducted in Chapter 2 with the objective of evaluating the impact of the modelling parameters on the accuracy and efficiency of the acceleration offered by the fast multipole method. The complexity of the FM-BEM has been compared to the standard BEM and the theoretical complexities observed

numerically. Since the FM-BEM formulation is not appropriate for very low frequencies, an empirical parameter to determine the transition between the standard BEM and FM-BEM has been proposed. Discretisation parameters, namely the meshing criterion and the truncation of the free surface (necessary due to the use of a reformulation of the fundamental solution of the free-space in the fast multipole formulation) have then been determined in an industrial context as a compromise between the accuracy and the computational cost. A method for speeding up the solution of wave propagation problems in the case of multiple frequency studies (e.g. for solving transient problems by means of Fourier synthesis), consisting of initializing the iterative solver (GMRES in this work) by the solution of the previous frequency, has been proposed and its efficiency checked (in terms of the reduction of the number of iterations for reaching convergence). Since the FM-BEM used is based on the solution of time-harmonic elastodynamic problems, Fourier-synthesis analysis has been performed to obtain results in the time domain, which are compared to analytic solutions.

The parameters of the FM-BEM being validated for an industrial context, Chapter 3 has presented the proposed coupling of the FM-BEM with the FEM. The coupling is done through an impedance and a seismic force computed at the interface between the FM-BEM mesh and the FEM mesh. To keep computational costs within reasonable limits, the coupling strategy has been formulated in a reduced basis composed of the eigenmodes of the structure and the eigenmodes of the FM-BEM/FEM interface.

Chapter 4 was then dedicated to the validation of the evaluation of the impedances and seismic forces. These entities have been compared with simple canonical test cases solutions extracted from the bibliography. Also, more complex models composed of a hemispherical basin in a homogeneous half-space have been used to validate the impedances and seismic forces, in the case of wave velocity contrasts and surface or embedded footings. The comparison of the results to various references has shown a good overview of the quality of the results. Some differences between the computed results and reference ones have been discussed and explained.

The main entities of the coupling, namely the impedance and the seismic forces being validated at this point, Chapter 5 presented some soil-structure interaction computations. The configuration used was a simple FEM model for a building with 42.3 m height, and a circular footing with a radius of 30 m and a depth of 21.21 m. The structure was embedded in a soil composed of a hemispherical basin in a homogeneous half-space. Two studies were conducted. The first one aimed at studying the impact of the shape of the hemispherical basin on the response of the structure. This case has then been compared with a horizontally layered soil with the same velocity contrast between the two media. Various velocity ratios (1, 2 and 4) and types of plane waves (SV, SH and P) have been considered and the results compared in terms of amplification of the incident wave. The second study concerned the impact of the angle of incidence of the plane wave on the response of the structure. Various angles were used to apply the plane waves (SV, SH and P) and the impact on the response of the structure has been discussed. Results showed in general a more important impact of the shape of the basin than the incidence angle. The amplification due to the shape of the basin was in all the three type of waves more important than in the case of the horizontally

layered soil.

Finally, the coupling was used on a realistic configuration of soil-structure interaction on the Grenoble basin. Difficulties were encountered due to the high velocity contrast between the bedrock and the basin layers: the computation cost of the near contributions was too high. The mechanical characteristics of the bedrock have been modified to meet the mechanical characteristics of the lower layer of the basin. A first study was conducted to compare the response of the basin at two different points of the free-surface in the absence of structure. A second one was conducted to compare the site effects on the response of a structure positioned in two different points of the basin.

7.2. Directions for future work

This work was the first step towards the development of an efficient FM-BEM/FEM coupling to study soil-structure interaction. The results are encouraging in terms of accuracy and computational times. However, further work should be performed to improve the efficiency of the method to consider more realistic structures and basin geometries. Some possible directions for future work are briefly discussed.

Parallelisation of the FM-BEM. Since results in the time domain are considered, a first parallelisation has been performed by considering various frequencies at the same time. However, it should be possible to consider larger problems by parallelising the FM-BEM. One level of parallelism could be achieved by considering the various layers of a basin in parallel. The last level of parallelism is a more intrusive approach, it consists in parallelising the FM-BEM approach, i.e. by considering various cells in parallel.

Preconditioner. It has been observed numerically that the number of iterations to achieve convergence grows with the frequency, the number of degrees of freedom and the number of layers in a basin. In addition, since the FM-BEM is used in our context for a large frequency range to obtain results in the time domain, the largest frequency can require a prohibitive number of iterations before to converge, since the number of iterations necessary increases with the frequency. The definition of an optimal preconditioner is thus a crucial issue. In fact it can be the limiting factor to consider larger problems. An optimal preconditioner for the FM-BEM would allow to overcome this impediment. The issue is that the matrix of the system is not assembled to reduce the memory requirements. Some algebraic preconditioners using the matrix of the near contributions have been tested, and found to bring moderate improvement [12], typically reducing the computational cost by a factor of about 2-3, but not achieving frequency-insensitive iteration counts. On the other hand, analytic preconditioners, i.e. the definition of well conditioned integral equations have been shown to be very efficient to reduce the number of iterations [10], in particular by achieving iteration counts that are nearly independent on the working frequency. However these preconditioners are much more involved to implement, and for that reason have been so far applied only on Dirichlet problems in homogeneous domains. It would be interesting to understand more precisely why

algebraic preconditioners are not efficient while analytic preconditioners are close to be optimal and if it is possible to combine the two approaches.

Definition of an iterative solver for multiple right hand sides. The proposed strategy to model soil structure interaction is based on the computation of a seismic force and an impedance operator projected on a reduced basis of the eigenmodes of the interface. This approach, as presented here, is not yet optimal as it requires solving multiple systems with the same matrix but different right-hand sides. Using a iterative solver allowing for multiple right hand sides would be expected to reduce the overall computational cost of a coupled FM-BEM analysis.

Application of the H-matrices to the near contributions. An important enhancement of the method would be to get rid of the high computational time required by the near contributions when the velocity contrast is high. In such configurations, the FM-BEM is not optimal because the meshes in the two adjacent media are conforming and must be fine enough for the medium with the shortest wavelength. As a result the mesh is way too fine for the slower medium, and the computation of the near contributions is using up unnecessary large amounts of time and memory. In fact the FM-BEM is efficient for a constant density of points per S-wavelength. A possible strategy would be to accelerate the assembly of the near contributions by using the H-matrix approach [11].

Appendix A

Analytic solutions: diffraction of incident plane waves

A.1. Case of an incident plane P-wave

We consider the propagation of an incident harmonique P-wave in a isotropic homogeneous elastic half-space. We note θ the angle of incidence with respect to the vector $\underline{e_z}$ in the plane $\underline{e_x}, \underline{e_z}$. This wave has a unit amplitude. The elastic medium is determined by C_p, i.e. the velocity of the P-waves, C_s, i.e. the velocity of the S-waves and the ratio $\gamma = C_p/C_s$. We note (E, ν) the Young's modulus and the Poisson's ratio of the elastic soil.

The incident plane P-wave is reflected by the free surface and generates a P wave and a S-wave (Fig. A.1). The reflexion angle α of the S-wave is given by:

$$\frac{\sin\theta}{C_p} = \frac{\sin\alpha}{C_s}$$

The condition $\sin\alpha = \frac{C_s}{C_p}\sin\theta < 1$ is always satisfied. The P-wave does not generate out-of-plane displacements. The displacement components with respect to $\underline{e_y}$ are equal to zero. The other components for each wave are given by

$$\begin{cases} U_x^{ip} = \sin(\theta)\exp[ik_p(x\sin(\theta) + z\cos(\theta)] \\ U_z^{ip} = \cos(\theta)\exp[ik_p(x\sin(\theta) + z\cos(\theta)] \end{cases} \tag{A.1}$$

$$\begin{cases} U_x^{rp} = \quad R_p\sin(\theta)\exp[ik_p(x\sin(\theta) - z\cos(\theta)] \\ U_z^{rp} = -R_p\cos(\theta)\exp[ik_p(x\sin(\theta) - z\cos(\theta)] \end{cases} \tag{A.2}$$

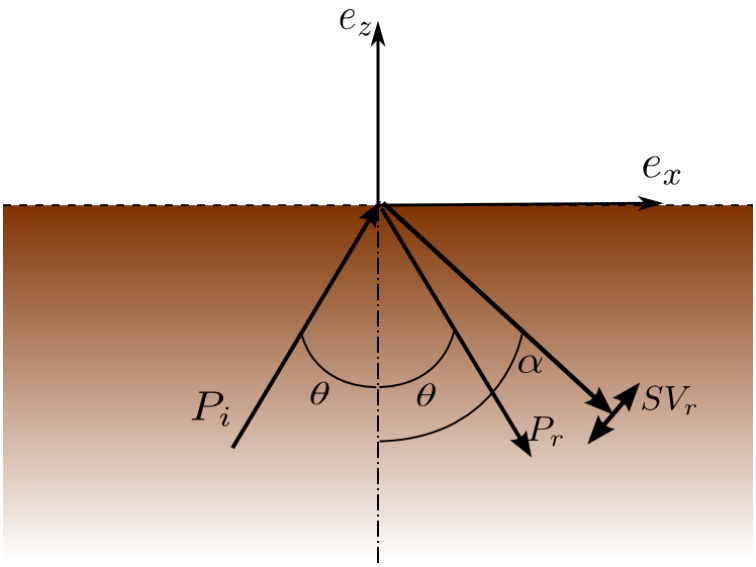

Figure A.1.: *Diffraction of an incident plane P-wave by a free surface.*

$$\begin{cases} U_x^{rs} = R_s \cos(\alpha) \exp[ik_s(x \sin(\alpha) - z \cos(\alpha)] \\ U_z^{rs} = R_s \sin(\alpha) \exp[ik_s(x \sin(\alpha) - z \cos(\alpha)] \end{cases} \tag{A.3}$$

Where we have denoted U^{ip} the incident plane P-wave, U^{rp} the reflected plane P-wave and the reflected plane S-wave. The total displacement is given by the sum of these three displacements:

$$\underline{U}_t = \underline{U}^{ip} + \underline{U}^{rp} + \underline{U}^{rs}.$$

To determine the constants R_p and R_s, we use the free surface condition. The stress tensor $\underline{\underline{\sigma}}$ is given by the Hooke law:

$$\underline{\underline{\sigma}} = \frac{E}{1+\nu}(\underline{\underline{\varepsilon}} + \frac{\nu}{1-2\nu} tr(\underline{\underline{\varepsilon}})\underline{\underline{I}}) \tag{A.4}$$

where the strain tensor $\underline{\underline{\varepsilon}}$ is equal to the symmetric gradient of the displacement vector.
The free surface condition $\underline{\underline{\sigma}}.\underline{n} = \underline{0}$ (with $\underline{n} = \underline{e}_z$ the normal to the free surface) is decomposed into three equations satisfied on any point of the free surface:

$$\begin{cases} \sigma_{xz} = 0, \\ \sigma_{yz} = 0, \\ \sigma_{zz} = 0. \end{cases} \tag{A.5}$$

The equation $\sigma_{yz} = 0$ is intrinsically satisfied. We now have two equations for the two unknowns

(R_p, R_s). Noting, $C = \frac{1-2\nu}{1-\nu} \frac{\sin(2\theta)\tan(2\alpha)}{2(\frac{\nu}{1-\nu}\sin^2(\theta)+\cos^2(\theta))}$ we obtain

$$\begin{cases} R_p = \frac{C-1}{C+1} \\ R_s = (1-R_p)\frac{\sin(2\theta)}{\gamma\cos(2\alpha)}. \end{cases} \tag{A.6}$$

A.2. Case of an incident plane SV-wave

We consider the propagation of an incident harmonique SV-wave in a isotropic homogeneous elastic half-space. We note θ the angle of incidence with respect to the vector $\underline{e_z}$ in the plane $\underline{e_x}, \underline{e_z}$. This wave has a unit amplitude. The elastic medium is determined by C_p, i.e. the velocity of the P-waves, C_s, i.e. the velocity of the S-waves and the ratio $\gamma = C_p/C_s$. We note (E, ν) the Young's modulus and the Poisson's ratio of the elastic soil.

The incident plane SV-wave is reflected by the free surface and generates a P wave and a S-wave (Fig. A.2). The reflexion angle α of the P-wave is given by:

$$\frac{\sin\theta}{C_s} = \frac{\sin\alpha}{C_p}.$$

Unlike the case of an incident plane P-wave, these exists a critical angle θ_c for which $\theta > \theta_c \Rightarrow \sin(\alpha) = \frac{C_p}{C_s}\sin(\theta) > 1$. In that case, surface waves are generated at the interface. In the following we assume that $\theta < \theta_c$

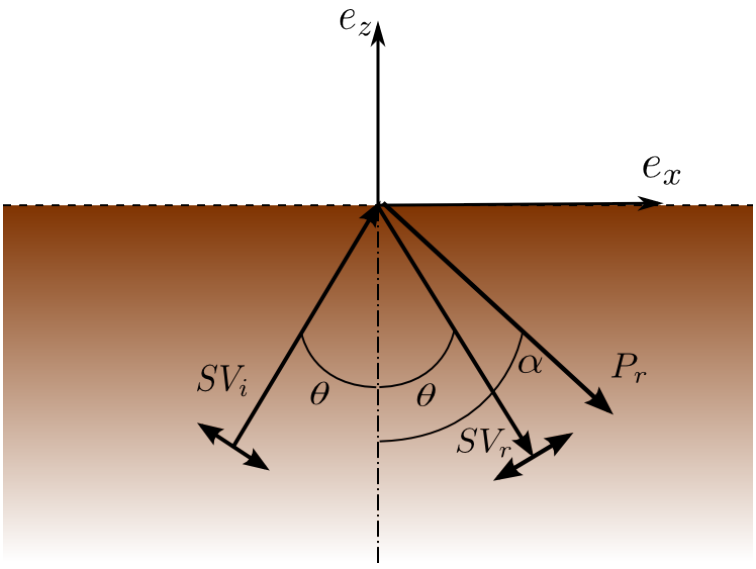

Figure A.2.: *Diffraction of an incident plane S-wave by a free surface.*

The incident S-wave does not generate out-of-plane displacements. The displacement components

with respect to $\underline{e_y}$ are equal to zero. The other components for each wave are given by

$$\begin{cases} U_x^{is} = \quad \cos(\theta) exp[ik_s(x\sin(\theta) + z\cos(\theta)] \\ U_z^{is} = -\sin(\theta) exp[ik_s(x\sin(\theta) + z\cos(\theta)] \end{cases} \tag{A.7}$$

$$\begin{cases} U_x^{rs} = R_s\cos(\theta) exp[ik_s(x\sin(\theta) - z\cos(\theta)] \\ U_z^{rs} = R_s\sin(\theta) exp[ik_s(x\sin(\theta) - z\cos(\theta)] \end{cases} \tag{A.8}$$

$$\begin{cases} U_x^{rp} = \quad R_p\sin(\alpha) exp[ik_p(x\sin(\alpha) - z\cos(\alpha)] \\ U_z^{rp} = -R_p\cos(\alpha) exp[ik_p(x\sin(\alpha) - z\cos(\alpha)] \end{cases} \tag{A.9}$$

Where we have denoted U^{is} the incident plane S-wave, U^{rs} the reflected plane S-wave and U^{rp} the reflected plane P-wave. The total displacement is given by the sum of these three displacements: $\underline{U}_t = \underline{U}^{is} + \underline{U}^{rs} + \underline{U}^{rp}$.

To determine the constants R_p and R_s, we use the free surface condition. The stress tensor $\underline{\underline{\sigma}}$ is given by the Hooke law:

$$\underline{\underline{\sigma}} = \frac{E}{1+\nu}(\underline{\underline{\varepsilon}} + \frac{\nu}{1-2\nu} tr(\underline{\underline{\varepsilon}})\underline{\underline{I}}) \tag{A.10}$$

where the strain tensor $\underline{\underline{\varepsilon}}$ is equal to the symmetric gradient of the displacement vector.
The free surface condition $\underline{\underline{\sigma}}.\underline{n} = \underline{0}$ (with $\underline{n} = \underline{e_z}$ the normal to the free surface) is decomposed into three equations satisfied on any point of the free surface:

$$\begin{cases} \sigma_{xz} = 0 \\ \sigma_{yz} = 0 \\ \sigma_{zz} = 0 \end{cases} \tag{A.11}$$

The equation $\sigma_{yz} = 0$ is intrinsically satisfied. We now have two equations for the two unknowns (R_p, R_s). Noting, $C = \frac{2\nu-1}{1-\nu}\frac{\tan(2\theta)}{2}\sin(2\alpha)(\frac{\nu}{1-\nu}\sin^2(\alpha) + \cos^2(\alpha))$ we obtain

$$\begin{cases} R_s = \frac{1+C}{1-C}, \\ R_p = -\gamma(R_s+1)\frac{2\nu-1}{1-\nu}\frac{\sin(2\theta)}{2(\frac{\nu}{1-\nu}\sin^2(\alpha)+\cos^2(\alpha))}. \end{cases} \tag{A.12}$$

Bibliography

[1] Mervyn CC Bampton and Roy R Craig Jr. Coupling of substructures for dynamic analyses. *Aiaa Journal*, 6(7):1313–1319, 1968. (cite p. 40)

[2] Ushnish Basu and Anil K Chopra. Perfectly matched layers for transient elastodynamics of unbounded domains. *International Journal for Numerical Methods in Engineering*, 59(8):1039–1074, 2004. (cite p. 8 et 9)

[3] Jean-Pierre Berenger. A perfectly matched layer for the absorption of electromagnetic waves. *Journal of computational physics*, 114(2):185–200, 1994. (cite p. 8)

[4] Marc Bonnet. *Boundary integral equations methods in solids and fluids*. John Wiley and sons, 1999. (cite p. 10, 11 et 12)

[5] Frédéric Bourquin and Frédéric d'Hennezel. Numerical study of an intrinsic component mode synthesis method. *Computer methods in applied mechanics and engineering*, 97(1):49–76, 1992. (cite p. 41)

[6] Simon Chabot, Nathalie Glinsky, Enrique Diego Mercerat, and LF Bonilla Hidalgo. A high-order discontinuous Galerkin method for 1D wave propagation in a nonlinear heterogeneous medium. *Journal of Computational Physics*, 355:191–213, 2018. (cite p. 9)

[7] Stéphanie Chaillat. *Méthode multipôle rapide pour les équations intégrales de frontière en élastodynamique 3-D. Application à la propagation d'ondes sismiques*. PhD thesis, Paris-Est University, 2008. (cite p. ix, 10, 12, 13, 14, 16, 17, 24, 38 et 109)

[8] Stéphanie Chaillat and Marc Bonnet. A new fast multipole formulation for the elastodynamic half-space green's tensor. *Journal of Computational Physics*, 258:787–808, 2014. (cite p. 28 et 53)

[9] Stéphanie Chaillat, Marc Bonnet, and Jean-François Semblat. A multi-level fast multipole BEM for 3-D elastodynamics in the frequency domain. *Computer Methods in Applied Mechanics and Engineering*, 197(49-50):4233–4249, 2008. (cite p. 13)

[10] Stéphanie Chaillat, Marion Darbas, and Frédérique Le Louër. Fast iterative boundary element methods for high-frequency scattering problems in 3d elastodynamics. *Journal of Computational Physics*, 341:429–446, 2017. (cite p. 28 et 123)

[11] Stéphanie Chaillat, Luca Desiderio, and Patrick Ciarlet. Theory and implementation of H-matrix based iterative and direct solvers for Helmholtz and elastodynamic oscillatory kernels. *Journal of Computational Physics*, 351:165–186, 2017. (cite p. 13 et 124)

[12] Stéphanie Chaillat, Jean-François Semblat, and Marc Bonnet. A preconditioned 3-d multi-region fast multipole solver for seismic wave propagation in complex geometries. *Communications in Computational Physics*, 11(2):594–609, 2012. (cite p. 28 et 123)

[13] Emmanuel Chaljub, Peter Moczo, Jozef Kristek, Pierre-Yves Bard, and Fabrice Hollender. Relevance of ground motion numerical simulations: What have we learned since the esgæ 2006 benchmark? In *Proceedings of the 4th IASPEI/IAEE International Symposium on Effects of Surface Geology on Seismic Motion*, 2011. (cite p. 9)

[14] Emmanuel Chaljub, Peter Moczo, Seiji Tsuno, Pierre-Yves Bard, Jozef Kristek, Martin Käser, Marco Stupazzini, and Miriam Kristekova. Quantitative comparison of four numerical predictions of 3d ground motion in the grenoble valley, france. *Bulletin of the Seismological Society of America*, 100(4):1427–1455, 2010. (cite p. 108)

[15] WC Chew and QH Liu. Perfectly matched layers for elastodynamics: A new absorbing boundary condition. *Journal of Computational Acoustics*, 4(04):341–359, 1996. (cite p. 9)

[16] Didier Clouteau. *Propagation d'ondes dans les milieux hétérogènes. Application á la tenue des ouvrages sous séismes*. PhD thesis, Ecole Centrale de Paris, 1990. (cite p. 37)

[17] Didier Clouteau. *Miss: Manuel Scientifique*. 2005. (cite p. 44)

[18] Didier Clouteau, D Broc, G Devésa, V Guyonvarh, and P Massin. Calculation methods of structure–soil–structure interaction (3si) for embedded buildings: Application to nupec tests. *Soil Dynamics and Earthquake Engineering*, 32(1):129–142, 2012. (cite p. 10)

[19] Francis Collino and Chrysoula Tsogka. Application of the perfectly matched absorbing layer model to the linear elastodynamic problem in anisotropic heterogeneous media. *Geophysics*, 66(1):294–307, 2001. (cite p. 8 et 9)

[20] Pieter Coulier, Stijn François, Geert Lombaert, and Geert Degrande. Application of hierarchical matrices to boundary element methods for elastodynamics based on green's functions for a horizontally layered halfspace. *Engineering Analysis with Boundary Elements*, 37(12):1745–1758, 2013. (cite p. 13)

[21] Pieter Coulier, Stijn François, Geert Lombaert, and Geert Degrande. Coupled finite element–hierarchical boundary element methods for dynamic soil–structure interaction in the frequency

domain. *International Journal for Numerical Methods in Engineering*, 97(7):505–530, 2014. (cite p. 36)

[22] Roy Craig and Mervyn Bampton. Coupling of substructures for dynamic analyses. *AIAA journal*, 6(7):1313–1319, 1968. (cite p. 45)

[23] Marion Darbas and Frédérique Le Louër. Well-conditioned boundary integral formulations for high-frequency elastic scattering problems in three dimensions. *Mathematical Methods in the Applied Sciences*, 38(9):1705–1733, 2015. (cite p. 28)

[24] Denis de Klerk, Daniel J Rixen, and Sven N. Voormeeren. General framework for dynamic substructuring: history, review and classification of techniques. *AIAA journal*, 46(5):1169–1181, 2008. (cite p. 41)

[25] Nicolas Delepine. *Numerical modeling for seismic site effects in sedimentary basins and influences of nonlinear soil behavior*. PhD thesis, Ecole des Ponts ParisTech, 2007. (cite p. ix, 4 et 5)

[26] Luca Desiderio. *H-matrix based Solver for 3D Elastodynamics Boundary Integral Equations*. PhD thesis, Université Paris-Saclay, 2017. (cite p. 13)

[27] Vincent Etienne, Emmanuel Chaljub, Jean Virieux, and Nathalie Glinsky. An hp-adaptive discontinuous galerkin finite-element method for 3-d elastic wave modelling. *Geophysical Journal International*, 183(2):941–962, 2010. (cite p. 9)

[28] Matthias Fischer and Lothar Gaul. Fast bem–fem mortar coupling for acoustic–structure interaction. *International Journal for Numerical Methods in Engineering*, 62(12):1677–1690, 2005. (cite p. 37)

[29] Filippo Gatti. *Forward physics-based analysis of "source-to-site" seismic scenarios for strong ground motion prediction and seismic vulnerability assessment of critical structures*. PhD thesis, Université Paris-Saclay, 2017. (cite p. 9)

[30] Filippo Gatti, Fernando Lopez-Caballero, Didier Clouteau, and Roberto Paolucci. On the effect of the 3-d regional geology on the seismic design of critical structures: the case of the kashiwazaki-kariwa nuclear power plant. *Geophysical Journal International*, 213(2):1073–1092, 2018. (cite p. 9)

[31] Louis Geli, Pierre-Yves Bard, and Beatrice Jullien. The effect of topography on earthquake ground motion: a review and new results. *Bulletin of the Seismological Society of America*, 78(1):42–63, 1988. (cite p. 3)

[32] Eva Grasso. *Modelling visco-elastic seismic wave propagation: a fast-multipole boundary element method and its coupling with finite elements*. PhD thesis, Paris-Est University, 2012. (cite p. ix, 18 et 36)

[33] Leslie Greengard and Vladimir Rokhlin. A fast algorithm for particle simulations. *Journal of Computational Physics*, 135(2):280–292, 1997. (cite p. 14)

[34] Yong Feng Gui and Wen-Bin Dou. A rigorous and completed statement on helmholtz theorem. *Progress in Electromagnetics Research*, 69:287–304, 2007. (cite p. 7)

[35] Polat Gülkan and Ray W Clough. *Developments in dynamic soil-structure interaction*, volume 390. Springer Science & Business Media, 2012. (cite p. 5)

[36] Jan S Hesthaven and Tim Warburton. *Nodal discontinuous Galerkin methods: algorithms, analysis, and applications*. Springer Science & Business Media, 2007. (cite p. 9)

[37] Robert L Higdon. Absorbing boundary conditions for elastic waves. *Geophysics*, 56(2):231–241, 1991. (cite p. 8)

[38] Heiner Igel. Quest: Quantitative estimation of earth's seismic sources and structure: a european initial training network. In *EGU General Assembly Conference Abstracts*, volume 12, page 8612, 2010. (cite p. 2 et 8)

[39] Dimitri Komatitsch and Jeroen Tromp. A perfectly matched layer absorbing boundary condition for the second-order seismic wave equation. *Geophysical Journal International*, 154(1):146–153, 2003. (cite p. 9)

[40] Michael Kremer, David Bommes, Isaak Lim, and Leif Kobbelt. Advanced automatic hexahedral mesh generation from surface quad meshes. In *Proceedings of the 22nd International Meshing Roundtable*, pages 147–164. Springer, 2014. (cite p. 9)

[41] ZP Liao. Dynamic interaction of natural and man-made structures with earth medium. *Earthquake Research in China*, 11(7):367–408, 1999. (cite p. 37)

[42] John Lysmer and Roger L Kuhlemeyer. Finite dynamic model for infinite media. *Journal of the Engineering Mechanics Division*, 95(4):859–878, 1969. (cite p. 8)

[43] J. K. L. MacDonald. Successive approximations by the rayleigh-ritz variation method. *Phys. Rev.*, 43:830–833, May 1933. (cite p. 40)

[44] Richard H MacNeal. A hybrid method of component mode synthesis. *Computers & Structures*, 1(4):581–601, 1971. (cite p. 40)

[45] Emeline Maufroy, Pierre-Yves Bard, Emmanuel Chaljub, and Fabrice Hollender. Validation of site-effect numerical predictions: New results from the euroseistest verification and validation project (e2vp). (cite p. 2, 8 et 10)

[46] Emeline Maufroy, Emmanuel Chaljub, Fabrice Hollender, et al. Earthquake ground motion in the mygdonian basin, greece: the e2vp verification and validation of 3d numerical simulation up to 4 hz. *Bulletin of the Seismological Society of America*, 105(3):1398–1418, 2015. (cite p. 9)

[47] Kristel C Meza-Fajardo, Jean-François Semblat, Stéphanie Chaillat, and Luca Lenti. Seismic-wave amplification in 3d alluvial basins: 3d/1d amplification ratios from fast multipole bem simulations. *Bulletin of the Seismological Society of America*, 106(3):1267–1281, 2016. (cite p. 10)

[48] Axel Modave, Amik St-Cyr, and Tim Warburton. GPU performance analysis of a nodal discontinuous Galerkin method for acoustic and elastic models. *Computers & Geosciences*, 91:64–76, 2016. (cite p. 9)

[49] Alex Nieto ferro. *Nonlinear Dynamic Soil-Structure Interaction in Earthquake Engineering*. PhD thesis, Ecole centrale de Paris, 2013. (cite p. 37)

[50] Elif Oral. *Multi-dimensional modeling of seismic wave propagation in linear and nonlinear media*. PhD thesis, Université Paris-Est, 2016. (cite p. 9)

[51] Roberto Paolucci, Ezio Faccioli, and Fabio Maggio. 3d response analysis of an instrumented hill at matsuzaki, japan, by a spectral method. *Journal of Seismology*, 3(2):191–209, 1999. (cite p. 9)

[52] Floriana Pergalani, Massimo Compagnoni, and V Petrini. Evaluation of site effects using numerical analyses in celano (italy) finalized to seismic risk assessment. *Soil Dynamics and Earthquake Engineering*, 28(12):964–977, 2008. (cite p. 8)

[53] Fabien Peyrusse, Nathalie Glinsky, Céline Gélis, and Stéphane Lanteri. A nodal discontinuous Galerkin method for site effects assessment in viscoelastic media—Verification and validation in the Nice basin. *Geophysical Journal International*, 199(1):315–334, 2014. (cite p. 9)

[54] William H Reed and TR Hill. Triangular mesh methods for the neutron transport equation. 1973. (cite p. 9)

[55] Doriam Restrepo, Jacobo Bielak, Ricardo Serrano, Juan Gómez, and Juan Jaramillo. Effects of realistic topography on the ground motion of the Colombian Andes. A case study at the Aburrá Valley, Antioquia. *Geophysical Journal International*, 204(3):1801–1816, 2016. (cite p. 8 et 9)

[56] Youcef Saad and Martin H Schultz. Gmres: A generalized minimal residual algorithm for solving nonsymmetric linear systems. *SIAM Journal on scientific and statistical computing*, 7(3):856–869, 1986. (cite p. 30)

[57] Jean-François Semblat and Patrick Dangla. Modélisation de la propagation d'ondes et de l'interaction solstructure: approches par éléments finis et éléments de frontière. *Bulletin des laboratoires des ponts et chaussées*, 256(257):163–178, 2005. (cite p. 8)

[58] Jean-François Semblat, Anne-Marie Duval, and Patrick Dangla. Numerical analysis of seismic wave amplification in nice (france) and comparisons with experiments. *Soil Dynamics and Earthquake Engineering*, 19(5):347–362, 2000. (cite p. 10)

[59] Jean François Semblat and Alain Pecker. *Waves and vibrations in soils: earthquakes, traffic, shocks, construction works*. Iuss Press, 2009. (cite p. ix, 2 et 9)

[60] Jean-Georges Sieffert and Franck Cevaer. *Manuel des fonctions d'impédance: fondations superficielles*. Quest Editions, 1992. (cite p. x, xi, xii, 44, 47, 48, 49, 50, 51, 54, 55, 56, 57, 58, 59, 61, 62, 63, 64, 65, 66 et 67)

[61] Kenichi Yoshida. *Applications of fast multipole method to boundary integral equation method*. PhD thesis, 2001. (cite p. 11)

[62] Lei Zhang, Jung Hoon Lee, Ardavan Oskooi, Amit Hochman, Jacob K White, and Steven G Johnson. A novel boundary element method using surface conductive absorbers for full-wave analysis of 3-d nanophotonics. *Journal of Lightwave Technology*, 29(7):949–959, 2011. (cite p. 51)

[63] Yongjie Zhang, Thomas JR Hughes, and Chandrajit L Bajaj. An automatic 3d mesh generation method for domains with multiple materials. *Computer methods in applied mechanics and engineering*, 199(5-8):405–415, 2010. (cite p. 9)

[64] Loic Zuchowski, Michael Brun, and Florent De Martin. Co-simulation coupling spectral/finite elements for 3D soil/structure interaction problems. *Comptes Rendus Mécanique*, In Press:1–15, 2018. (cite p. 9)

université PARIS-SACLAY
ÉCOLE DOCTORALE
Sciences mécaniques et énergétiques, matériaux et géosciences (SMEMAG)

Titre : Modélisation numérique tridimensionnelle des effets de site en Interaction Sol-Structure par une méthode adaptée aux problèmes sismiques de très grande taille

Mots clefs : Interaction Sol-Structure, Effets de site, Méthode des éléments de frontière, Méthode multipôles rapide, Méthode des éléments finis.

Résumé : Les études récentes ont montré l'influence de la géométrie et de la lithologie du site sur l'amplification de l'onde sismique incidente. Disposer d'outils de simulation est nécessaire pour l'analyse du risque sismique des ouvrages. Néanmoins, les effets de site sont souvent découplés des calculs d'interaction sol-structure vu la taille des domaines à considérer et de la complexité des modèles. L'objectif de cette thèse est de développer une stratégie de calcul numérique d'interaction sol-structure permettant de prendre en compte les effets de site dans un contexte industriel. Pour ce faire, un couplage entre la méthode des éléments finis (FEM) et la méthode des éléments de frontière accélérée par la méthode multipôle rapide (FM-BEM) est développé dans ce travail. La BEM permet de modéliser des problèmes dans des domaines de très grande taille ou infinis mais est gourmande en temps de calculs. Avec la méthode accélérée, il est possible de considérer des géologies plus complexes et d'accéder à des gammes de fréquences plus élevées par rapport à des approches classiques (purement FEM ou couplage BEM-FEM), grace à l'accélération du produit matrice-vecteur dans la résolution par un solveur itératif. La mise en place de cette approche s'appuie sur le code FEM industriel *Code_Aster* (EDF R&D) et le code FM-BEM *Coffee* (CNRS) développé par S. Chaillat.
La FM-BEM est d'abord utilisée pour la modélisation de cas de sols réalistes afin de valider ses paramètres pour une utilisation dans un cadre industriel. Une stratégie de couplage FM-BEM/FEM est ensuite développée à l'aide d'une technique de sous-structuration dynamique où la structure (et éventuellement le sol proche) est modélisée par la FEM, alors que le sol infini est représenté par un opérateur d'impédance et des forces sismiques, construits avec la méthode FM-BEM. L'opérateur d'impédance et les forces sismiques, qui sont calculés sur une base réduite afin d'en réduire le coût de calcul, sont validés sur des cas canoniques (demi-espace homogène, bassin à géométrie variable...). L'influence sur la réponse de la structure de la forme du bassin, de l'angle d'incidence des ondes ainsi que du rapport de célérité des ondes entre les couches est alors étudiée et la réponse de la structure comparée aux cas où les effets de site seraient absents. Enfin, la méthodologie de couplage mise en place est utilisée pour effectuer des calculs d'interaction sol-structure sur des structures dans le bassin de Grenoble.

Title : Three-dimensional numerical modeling of site effects in Soil-Structure Interaction for large scale seismic problems

Keywords : Soil-Structure Interaction, Site effects, Boundary element method, Fast multipole method, Finite element method.

Abstract : Recent studies have shown the influence of the geometry and lithology of the site on the amplification of the incident seismic wave. Having simulation tools is necessary to seismic risk analysis of structures. Nevertheless, site effects are often decoupled from soil-structure interaction computations given the size of the domains to be considered and the complexity of the models. The objective of this work is to develop a numerical method to simulate soil-structure interaction, that also takes into account site effects. To this aim, a coupling strategy between the finite element method (FEM) and the fast multipole accelerated boundary element method (FM-BEM) is proposed. The BEM is well suited to deal with large-scale or infinite domains but is very expensive in terms of memory requirements or computational time. Once accelerated with the Fast Multipole Method, the FM-BEM allows to model more complex geologies and to consider a higher frequency range compared to classical approaches (purely with the FEM or with a standard BEM-FEM coupling) thanks to the acceleration of the matrix-vector product needed in the iterative solver. The implementation of this strategy is based on the FEM code *Code_Aster* (EDF R&D) and the FM-BEM code *Coffee* (CNRS) developed by S. Chaillat.
In this work, FM-BEM is first used to model soils with realistic mechanical characteristics and to validate the parameters of the method in an industrial context. An FM-BEM/FEM coupling strategy is then proposed using a dynamic substructuring technique where the structure (and possibly the near soil) is modelled by the FEM, while the infinite soil is represented by an impedance operator and seismic forces, computed with the FM-BEM. The impedance operator and the seismic forces, which are computed on a reduced basis in order to reduce computational costs, are then validated on canonical cases (homogeneous half-space, basin with variable geometry ...). The influence on the response of the structure of the shape of the basin, the angle of incidence of the waves as well as the ratio of the wave velocities between the layers is then studied and the response of the structure is compared to cases where the site effects are absent. Finally, the proposed coupling methodology is used to simulate soil-structure interaction on a configuration such as structures in the Grenoble basin.